

SCHOOL OF SCIENCE

Department of Industrial Chemistry "Toso Montanari"

Corso di Laurea Magistrale/Master

## **Advanced Spectroscopy in Chemistry**

Classe LM-71 - Scienze e Tecnologie della Chimica Industriale

Gilded bronze conservation: assessment of protective treatments by accelerated ageing and of treatment removal procedures by laser cleaning

Experimental Master Thesis

### **CANDIDATE**

Oancea Andrei-Victor

### **TUTOR**

**Chiar.mo Prof.** Martini Carla

### **CO-TUTOR**

Dr. Chiavari Cristina

Prof. Bernardi Elena

Dr. Ospitali Francesca

Dr. Boromei Iuri

**Sessione I**

---

**Anno Accademico 2013-2014**

---



## Contents

Aim and background .....	1
1. Introduction .....	3
1.1. Bronze gilding methods .....	3
1.2. Gilded bronze corrosion.....	9
1.3. The Paradise Door by Ghiberti.....	28
1.4. Laser cleaning of bronzes/gilded bronzes.....	36
2. Materials and methods.....	71
2.1. Accelerated corrosion test.....	71
2.2. Tested material: quaternary gilded bronze and organosilane coating (PropS-SH +nanoparticles) 71	
2.3. Weathering method: dropping test.....	72
2.4. Artificial acid rain solution .....	74
2.5. Application of coating on pre-patinated samples.....	74
3. Accelerated ageing in runoff conditions for corrosion investigations of fire gilded bronzes and assessment of the protective efficiency of PropS-SH .....	76
3.1 Samples before corrosion testing .....	76
3.1.1 As gilded bronzes .....	76
3.1.2. As-gilded bronze coated with PropS-SH .....	78
3.2. Samples (as-gilded) after corrosion testing.....	80
3.2.1. Assessment of the ability of the accelerated ageing test to simulate real corrosion conditions.....	81
3.2.2. Evaluation of the influence of exposure time on corrosion morphologies .....	81
3.2.3. Case study (Our Lady of the Fire, 1707).....	83
3.2.4 Uncoated samples.....	87
3.2.5. PropS-SH coated sample .....	94

3.2.6.	Gravimetric measurements and metal release (as-gilded samples).....	102
3.3.	Samples (pre-patinated) after corrosion testing .....	105
3.3.1.	Surface and cross section analysis .....	105
3.3.2.	Gravimetric measurements and metal release (pre-patinated samples).....	122
3.4.	Conclusions .....	124
4.	Laser treatment for the removal of aged organosilane coatings .....	126
4.1	Materials and methods.....	126
4.2	Results .....	127
4.2.1.	Gilded bronze sample coated with PropS-SH+CeO.....	127
4.2.2.	Gilded bronze sample coated with PropS-SH .....	144
4.3.	Concluding remarks .....	158
References	.....	159

## **Aim and background**

Throughout the ages craftsmen and artists working on gold gilt bronze sculptures have produced some of the world's most remarkable masterpieces. At the same time however these masterpieces are also very fragile, their alteration leading to changes of surface but also of the bulk of the alloy that modify their original appearance. Corrosion damage on recent works of art may be hard to notice at first as much of the corrosion products are situated beneath the gold layer. The changes are quite visible when considering historic artifacts such as the Porta del Paradiso by Lorenzo Ghiberti from the Florence Baptistery where corrosion products have migrated to the surface of the gilding layer and pustules have formed leading to a flaking off of the gold. As such it is imperative that we take care and protect these masterpieces before their appearance is completely changed forever.

Difficult to produce, these masterpieces are difficult to preserve as well. The presence of the gold layer, which always contains defects and discontinuities due to the deposition technique, may galvanically stimulate corrosion of the bronze substrate. Then, the growth of corrosion products at the gold/bronze interface leads to blistering or break-up and loss of the gold layer. Any conservation plan and consequently any preservation treatment has to take into account all of these facts and also the particular exposure geometry of the artwork, when exposed to outdoor atmospheric environment, because it has been demonstrated that stagnant rainwater (in sheltered areas of the artifact) or runoff conditions (in unsheltered areas) have a different influence on corrosion of bronze monuments.

When talking about chemical protective treatments we must always consider that they respect the following requirements: they are able to diminish the effect of the corrosion process, they are non-toxic and any substances used are easily removable.

Using their knowledge in protecting copper statues, conservation experts currently use in the case of bronze artifacts a protective treatment involving double coatings consisting of benzotriazole (BTA) and acrylic resins or microcrystalline wax. While BTA has proven its

effectiveness in the protection of copper objects, in the case of bronze items its performance has been lower. The use of this class of compounds also comes in conflict with the second requirement as it is known to have toxic effects on the environment and BTA itself is believed to be carcinogenic.

In the current study, we analyze the effectiveness of an organosilane compound, 3-mercaptopropyl-tri-methoxy-silane (abbreviated PropS-SH), in the corrosion protection of fire-gilded bronzes. Firstly, the coating was applied on as-gilded bronze. Subsequently, it was also applied on pre-patinated bronze, because the substrate on which protective coatings are applied in real conservation interventions are corroded artifacts (cleaning procedures never remove all the corrosion products). Aiming to obtain results that simulate the situation of real artifacts, a dropping test that simulates outdoor exposure in runoff conditions (unsheltered areas of monuments) was employed in order to prepatinate the gilded bronze samples, which are the substrate for applying the protective coating. The preparation of the samples by applying the protective coating was performed in collaboration with the Corrosion Studies Centre “Aldo Daccò” from Ferrara University. After the artificial exposure cycles the samples underwent investigations through a variety of spectroscopic methods including SEM, Raman, FIB, AAS and color measurements.

In order to evaluate the possible removal of the organosilane coating, protected samples were subjected to laser cleaning tests and characterized by SEM/EDS so as to assess the changes in composition and morphology of the treated surfaces. The laser cleaning treatment was performed at the Institute of Applied Physics “Nello Carrara” (CNR Sesto Fiorentino (FI)). The morphology and chemical composition of the samples was observed before and after the operation in order to obtain information about the fluence and type of laser which are best suited to the removal of this type of coating.

## 1. Introduction

### 1.1. Bronze gilding methods

The application of a thin layer or coating of gold on the surface of another material, be it metal, ceramic, stone or wood, has been one of the most important technological processes in human history. While the original purpose of gilding was primarily esthetic, the decorative effect giving the impression that the object was being made of a more noble metal, gilding might also improve corrosion resistance (if the gold layer has no defect or discontinuity and is fully adherent to the substrate). The evolution of the gilding process is closely linked to the economic requirements that the object has to fulfill: the reduction of the production costs and the increase of the quality. This is why the major advances in this process depended on: the use of higher quality gold by improvements in the purification technique, the reduction in the amount of gold used by obtaining thinner but dense gold layers and the improvements of the adhesion of the gold layer to the underlying substrate.

Gold gilding first appears as the covering of an artifact with a thin gold foil followed by a mechanical attachment between the two. This was achieved either by folding the foil around the object, riveting it or, later, hammering the foil into grooves cut into the substrate [1]. An Egyptian ceramic vase displayed in the Louvre museum dating from approximately 4000 B.C [2] presents handles decorated with thick gold foil (figure 1).



Fig. 1. Vase from Nagada(Egypt).[2]

Subsequent technological developments by use of the hammering technique permitted the decrease in the size of the gold layer from several tens of  $\mu\text{m}$ (sheet) to that of several  $\mu\text{m}$ (foil), to less than  $1\mu\text{m}$ (leaf). In ancient times the gold foil was attached to the substrate by using an adhesive such as egg white or resin and drying oil as is mentioned by Pliny the Elder [1]. He also mentions that gold craftsmen were able to obtain thin gold leafs of a thickness evaluated to less than  $0.4\mu\text{m}$ .

As the thickness of the gold layer decreased over time, so did its strength and thus this technique encountered mechanical problems as the gold leaf could no longer be properly applied on the substrate mechanically. These problems would persist until the discovery of mercury which permitted artisans to avoid them.

Fire gilding or mercury or amalgam gilding as it is sometimes referred, was discovered during the 3<sup>rd</sup> century B.C. in China and by the 1<sup>st</sup> century B.C. in the western world. The process involves the formation of gold amalgam which has a pasty texture, obtained by dissolving small gold fragments in mercury. The amalgam is afterwards applied to the substrate and heated in order to evaporate the mercury. This is followed by burnishing with a hard and smooth agate tip instrument in order to obtain the desired shiny surface (due to compaction of the gold layer by plastic deformation).

Chemically, the formation of gold amalgam implies the interaction between gold and mercury, which leads to the formation of the gray  $\gamma\text{Au}_2\text{Hg}$  phase [1]. By using an excess of mercury, the craftsmen were able to obtain a paste of  $\text{Au}_2\text{Hg}$  particles in mercury. Depending on the requirements, the consistency of the amalgam paste could be modified either by adding or removing mercury. The substrate can then be covered with a thin coating of gold amalgam.



Fig. 2. Amalgam paste [3]



Fig.3.Silver amalgam applied to substrate [4]

In the case of copper and copper alloys, the application of the gold amalgam is difficult due to several problems. Fire gilding implies the heating of the object in order to evaporate the mercury. Due to the high temperature, the copper on the surface will oxidize to form copper oxides [1]. These corrosion products will not allow for a good adhesion of the gold layer and will have to be removed. Also mercury has a very low solubility in copper which leads to a very difficult wetting of the surface by the gold amalgam. Due to these problems, the substrate requires a thorough mechanical cleaning and also a removal of the corrosion products on the surface. Nowadays this is achieved by using a solution of dilute nitric acid while in the Middle Ages a solution of alum, rock salt and vinegar was employed as mentioned by Benvenuto Cellini[1].

The evaporation of mercury is performed at a temperature of 250-300°C for a short period of several minutes. This temperature is well below the boiling point of mercury which is of 356.73 °C. Not all mercury is removed in this stage and a large amount (ranging from 8 to 25% ) remains in the gold layer. As an outcome of this operation, a very irregular and porous surface with a matte appearance is obtained as can be seen in figures 4 and 5.

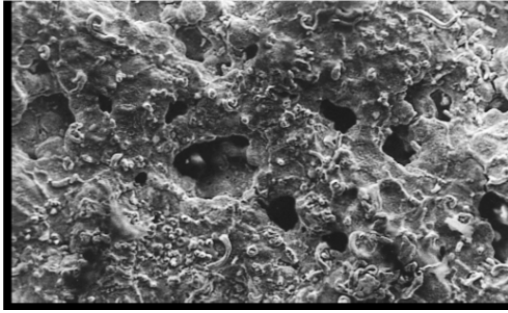


Fig. 4. A secondary electron image of the surface of an amalgam gilding replication sample before burnishing [1]

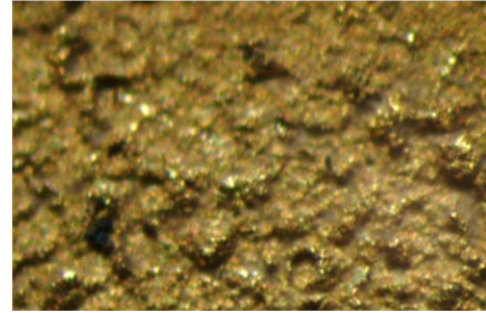


Fig. 5. Picture of the surface of an amalgam gilding replication before burnishing [3]

Using electron microprobe analysis, Anheuser [1] was able to monitor the mercury content of replicated fire gilding samples. Thus he was able to show that while the mercury content in the amalgam paste is very high at the beginning (80-90 wt. %), it decreases rapidly during the heating process by means of evaporation. The author explained the color change from gray to yellow using XRD analysis and demonstrated that a solid state reaction takes place after the evaporation of metallic mercury. The amount of mercury in the amalgam layer continues to decrease, leading the gray  $\gamma\text{Au}_2\text{Hg}$  phase to become the  $\zeta\text{Au}_3\text{Hg}$  gold amalgam. If the heating continues, combinations of  $\alpha$  and  $\zeta$  phases or just  $\alpha$  (Au-rich solid solution) were found, which is in agreement with the mercury-gold phase diagram presented in figure 6 [1].

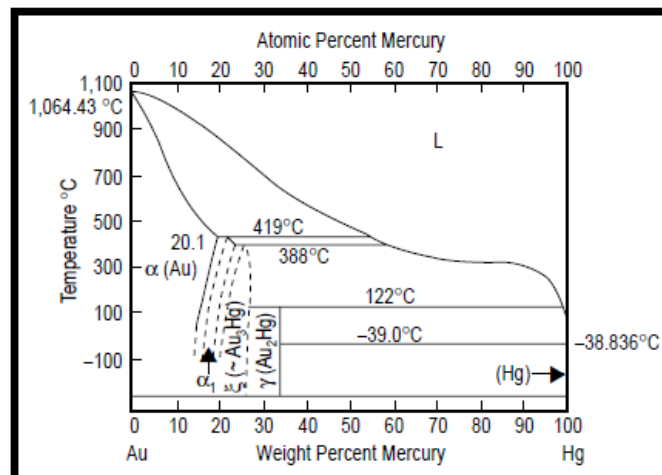


Fig. 6. The mercury-gold phase diagram [1]

Great caution must be taken when heating the bronze object covered with the amalgam paste, due to the fact that copper oxidizes in the presence of air at high temperatures. This can lead to the formation of a copper oxide layer that causes the gold layer to have a less adequate adhesion to the bronze substrate.

The next step in the fire gilding process is the burnishing of the gold surface. This is performed with a hard and smooth tip tool usually made of agate or steel. As a result, the structure of the gold layer is compacted and a part of the pores formed in the previous step are covered up. The surface presents at this point a brilliant shine and smoothness that is esthetically pleasing as can be seen from figure 8.

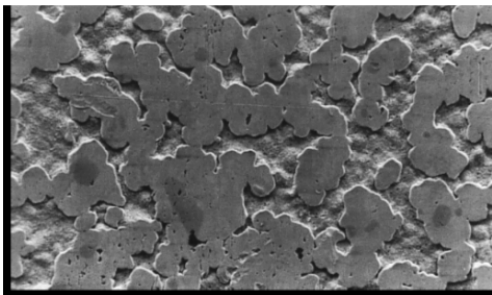


Fig. 7. A secondary electron image of the surface of an amalgam gilding replication sample after burnishing [1]

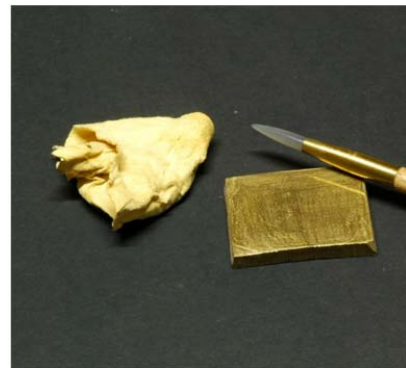


Fig. 8. Picture of an amalgam gilding replication sample after burnishing [3]

As can be seen in figure 7, the gold layer obtained after burnishing is not completely uniform and continues to have many irregularities. It continues to have porosities which allow atmospheric corrosion to take place.

The adhesion of the gold layer to the bronze substrate provided by fire gilding is much better compared to leaf gilding, and the thickness of the layer is much higher (up to an order of size). The craftsmanship of the artisan also plays an important role in thickness of the gold layer. It can vary greatly from item to item but also in different regions of the same object, as discussed in the experimental section of this thesis.

Due to the use of mercury, fire gilding poses major health risks. Fire gilding remained in use until the 19<sup>th</sup> century when it was replaced with electroplating, which is a much safer and much cheaper gilding method. Currently, fire gilding is employed only in restoration and heritage works.

As a conclusion, during the centuries many challenges in terms of manufacturing processes took place. The economy of gold and a better knowledge of gold-adhesion techniques to the surface of the object can explain the progressive evolution from the ancient mechanical gold foil gilding to the chemical layer deposition by mercury-gilding technique [5]. Alternative and short-lived recipes such as gilding by diffusion, or cold mercury gilding were also reported and can be seen as attempts to fulfill these preoccupations.

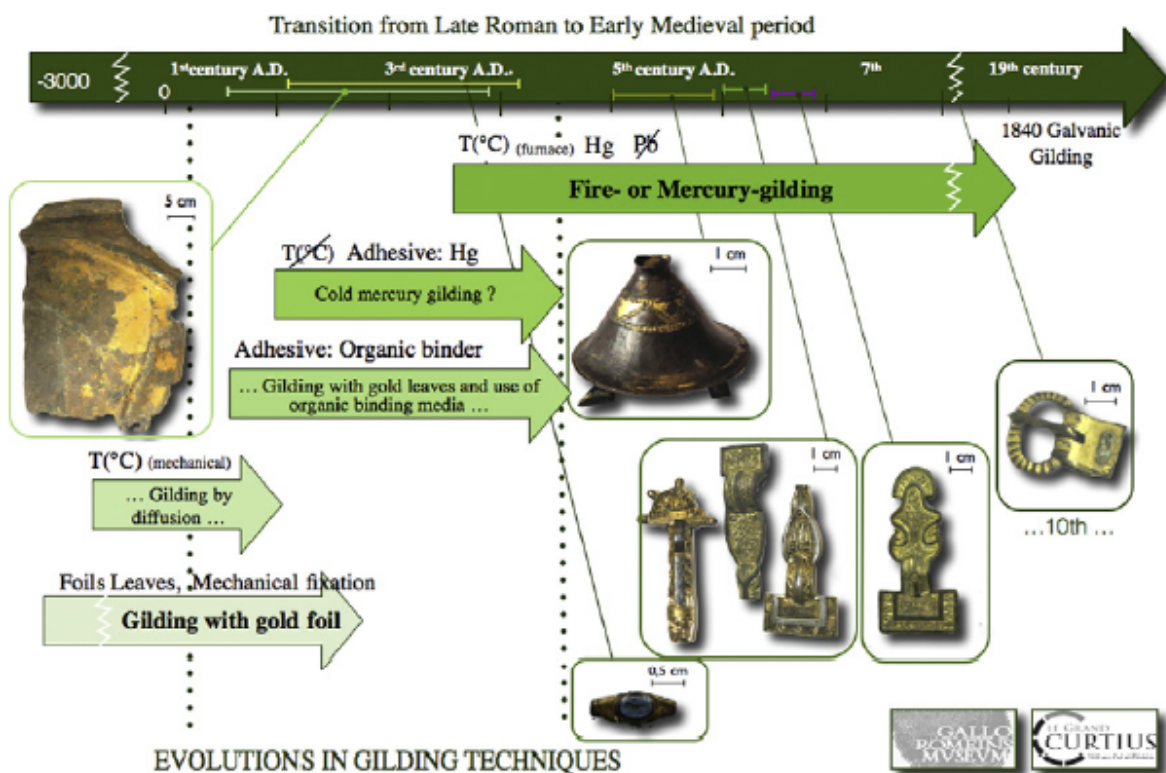


Fig. 9. Gilding techniques through ages [6]

## 1.2. Gilded bronze corrosion

### Bronze alloy

Bronze is an alloy that has been used in a wide range of applications over the course of history: from weapons to musical instruments, from cooking utensils to currency and from plumbing to decorative uses. Its discovery is so important in the developments of human society that it has given its name to a period of time in Antiquity, the Bronze Age.

Unlike pure copper which is softer, the alloying elements induce defects in the crystalline network of bronze giving it a higher resistance (solid solution strengthening). Furthermore, bronze corrosion resistance is higher than copper and here also the alloying elements determine the corrosion rate. While traditionally bronze is referred to alloys of copper with a high tin content, as opposed to brass which contains copper and a high amount of zinc, the composition of this alloy can vary greatly depending on its use and currently three types of bronzes are recognized [7]:

1. statuary bronze which contains roughly copper 97%, tin 2% and 1% of zinc
2. architectural bronze which has a high amount of zinc, nearly 40%, small amounts of lead 3%, the rest being copper 57%
3. commercial bronze is composed of 90% copper and 10% zinc

Pure bronze has a pinkish tint, close to that of salmon [7], however this is very rarely observed as bronze usually forms patinas or corrosion products on the surface giving it a color that can be anything from dark green to light brown.

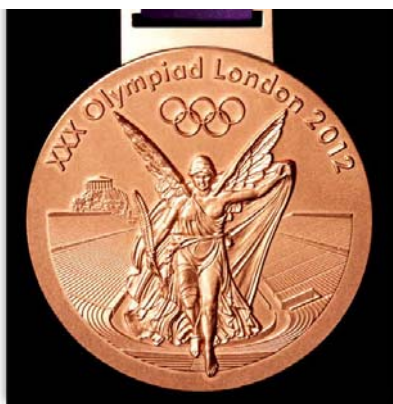


Fig 10. Olympic bronze medal showing the natural color of bronze [8]



Fig. 11. Bronze sculpture with a bluish green oxide patina formed on the surface[9]

The problems involving the corrosion of bronze and the subsequent degradation of the object come from the reactivity of copper and the other alloying elements. While in the original bronze alloy the components are in their metallic form, except for impurities, this is not their most stable state and they tend to oxidize with the formation of various salts. The chemical reactions they undergo to, lead to the formation of corrosion product layer (“patinas”), which in some cases prove very efficient at protecting the alloy.

In regards to what techniques can be used on bronze in order to obtain the desired properties, bronze can either be cast or wrought [10]. While in the case of casting the alloy is handled while in liquid form and then let to cool in an appropriate mould, in the case of working it is in solid state and mechanical operations are performed on it.

Whether the metals are pure or alloyed is one of the most important aspects regarding the casting of ancient metals, determining the type of crystal growth that can occur [10]. In regards to bronze we not only have to consider that it in itself is an alloy (therefore it undergoes constitutional undercooling [11]) but also the fact that ancient smelting techniques did not always provide impurities-free raw materials. Because of this, the vast majority of cast ancient bronzes present a dendritic structure.

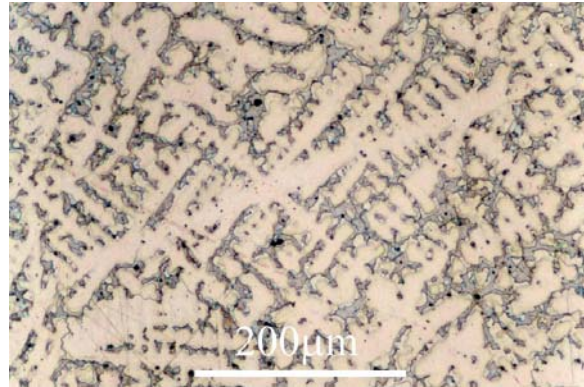


Fig. 12. Dendritic structure of a bronze alloy[12]

The dendritic structure exhibits tiny fernlike growths [10] inside the grains, as can be seen from figure 12. . The size of the dendrites (dendrite arm spacing) is influenced by the cooling rate of the alloy, the faster the cooling the smaller the dendrites [10]. Arms of dendrites can be primary secondary or tertiary as can be seen in figure 13.

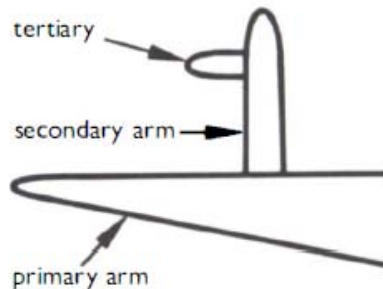


Fig. 13. Dendritic structure showing the primary, secondary and tertiary arms[10].

Dendritic growth is frequently accompanied by coring, which is a form of microsegregation that occurs during casting [10]. It results due to the non-equilibrium solidification and difference in solidification temperature of components or impurities in alloys and metals. As a consequence of microsegregation, the regions of the dendrite that were first solidified have the highest content of the higher melting point component. Its concentration will

decrease in the newer section of the dendrite as they expand leading to a compositional gradient [10] from the center of the dendrite to the surface. Dendrites that display this feature are referred to as cored and are usually found in bronzes, although a sectioning of the material and a subsequent polish is required in determining whether it is present or not.

In the case of copper, lead or gold, if these metals are devoid of impurities, the casting process may produce an equi-axed nearly-hexagonal grain structure [10]. In this type of structure, the grains are about the same size, their section is roughly hexagonal and their orientation random as can be seen from figure 14. The structure corresponds to an ideal metallic grain or crystal and requires the least amount of energy in its formation, leading it to be an equilibrium structure.

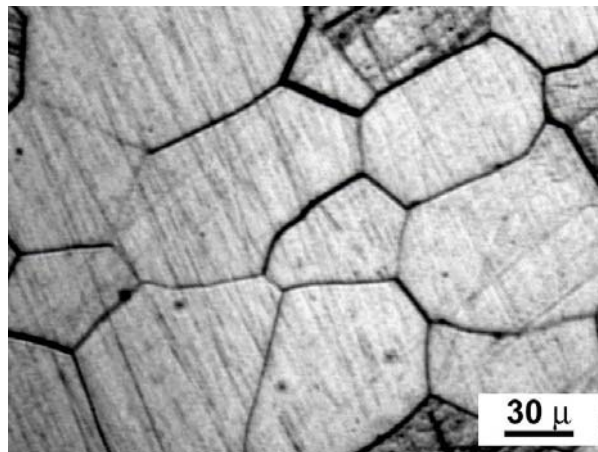


Fig. 14. Micrograph of a polycrystalline metal; grain boundaries evidenced by acid etching. [13]

Another feature that may appear in cast metals is the formation of holes and porosities [10]. This is largely due to the presence of gasses dissolved in the raw materials or due to interdendritic spaces that were not filled up during the cooling process and the subsequent solidification. The dissolved gasses leave the metal during the cooling due to their different solubility in the liquid and solid phases.

In regards to the second technique, working, it involves a combination of methods designed to change the properties of the alloy or metal including hammering, turning, raising and drawing [10]. While the initial orientation of the grains is random, through the process of

working they undergo plastic deformation and become oriented along the material flux direction, as can be seen in figures 15 and 16. This can continue until the grains become too brittle to enable any further operations, the grains being referred to as work-hardened. If the metal or alloy does not have at this time the desired properties, its ductility and malleability are restored by annealing, in the case of copper alloys at temperatures ranging from 500 to 800°C. These cycles of working and annealing may be repeated until one obtains the desired result.

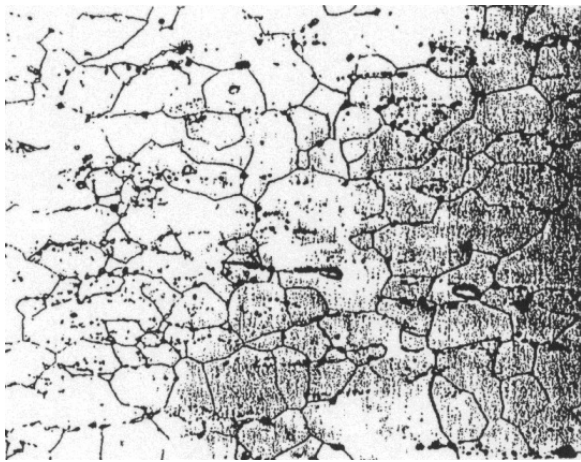


Fig. 15. Micrograph of a cold-worked metal, showing an equiaxed grain structure [14]

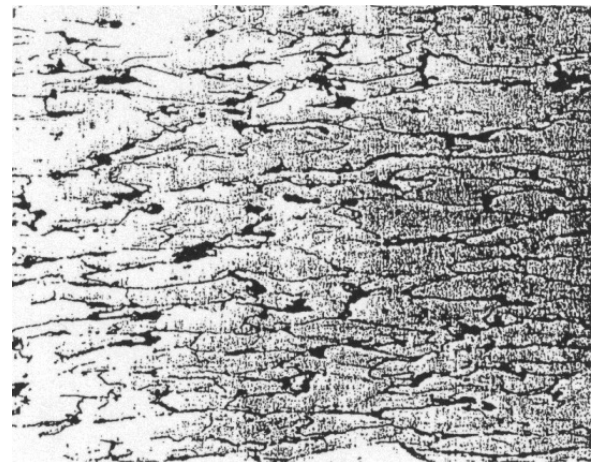


Fig. 16. Micrograph of a cold-worked metal, showing the flattened grains [14]

### **Atmospheric corrosion of bronze**

When used for ornamental and decorative purposes, many bronze objects are displayed in an outdoor urban environment and are exposed to the rain, snow, fog etc. thus being susceptible to atmospheric corrosion. A surface layer of corrosion products called a patina is formed and once established it tends to be extremely stable [15].

The structure and composition of the patina depends both on the composition of the alloy and the atmospheric conditions to which it is exposed. Here one has to take into account a wide range of factors ranging from the alloy microstructure and composition to the amount, type and composition of precipitation, from the exposure time to sunlight and outside temperature to the

various atmospheric pollutants and particles. While the patina components do not reflect the atmospheric composition directly, the corrosion products that possess an optimum set of solubilities, crystal structures, chemical reactivities and formation rates in regards to the atmospheric constituents are favored [15].

Depending on the exposure conditions the overlaying patina can have a different aspect and color that ranges from a pale green to a matte dark, Robbiola et al. [16] were able to link to a specific chemical composition. The authors were also able to determine that the distribution and size of the corroded areas on the surfaces are in relation with the exposure geometry to rainfall (sheltered/unsheltered areas). They found that the corrosion products that mostly correspond to pale green surfaces were exposed to rainfall while the ones which had a dark matte appearance were not directly submitted to the washing effect of rain.

Based on previous research that mentioned that the main process of the Cu/Sn corrosion consists in the selective dissolution of copper, which involves (i) the oxidation of tin resulting in insoluble compounds that remain in the corrosion layers and (ii) the oxidation of copper and dissolution of its ions in the corrosive electrolyte comprised of surface water, the authors [16] were able to consider two ways of evolution for the patina. In the first case (usually corresponding to exposure to stagnant rainwater, in sheltered areas of sculptures) if there is a significant rise in the amount of the copper ions present on the outside surface, a layer of corrosion compounds can precipitate on the internal layer, mostly consisting of Cu (I) oxide (i.e. cuprite) and insoluble tin compounds. This deposition thus will lead to the formation of a protective layer of copper compounds that is able to protect the bronze by decreasing the corrosion rate.

In the other model for patina evolution that the authors propose, the copper ions do not build up in sufficient quantities to form an external layer or its properties do not enable it to protect the bronze, so the resulting corrosion products will consist of a mixture of tin and copper compounds. This case corresponds to the situation in which the surface is directly exposed to rainfall (exposure to the leaching action of the rain in unsheltered areas of the sculpture). The corrosion products will have a porous texture allowing decuprification. Whenever the object will be exposed to rain the metals within the bronze will be submitted to active dissolution leading to a cyclic repetition of the corrosion process causing damage.

While the composition of the patina can vary greatly, as mentioned before, its formation steps can be explained as follows [7]:

1. The first step is dominated by the induction process: oxidation leads to the formation of a dark brown copper (I) oxide film. This step is influenced by the amount and chemical composition of atmospheric pollutants and by the time of wetness, angle of exposure and temperature determined by precipitation. In particular, if there is a high enough concentration of sulfide compounds in the atmosphere, the patina will change dramatically and its protective properties will be significantly altered. The rate of oxidation has also been observed to affect the durability of the patina: corrosion products that have been formed over a longer period of time are much more resistant to deterioration.
2. In the second step, the outer metal layer is converted to copper sulfate. This generally is generally found on the surfaces with the most severe exposure and is caused when, in the absence of oxygen, the moisture trapped by the atmospheric particles allows for electrolytic reactions to occur. As a result, thin light green patches appear on the exposed areas.
3. In contrast to the previous steps, the run-off streaking and scab formation occurs at a slower rate but its consequences are none the less significant. Differential weathering of the corrosion products leads to streaking and uneven discoloration up to the point where black areas and scabs are formed on the surface.
4. In the next step, microscopic particles containing chloride are deposited on the surface. The presence of the chloride ions below a crust or a barrier coating allows for corrosion to continue beneath the surface.
5. The last step is the complete conversion of all exposed surfaces to the bright blue-green copper sulfate in the final stages of corrosion. In this phase of active corrosion the usual green coloration of bronze with lime-green color and a matte texture appears.

In their paper [17], de la Fuente and colleagues were able to identify some common constituents of bronze patinas formed when their specimens were exposed to atmospheric corrosion:

1. Cuprite ( $\text{Cu}_2\text{O}$ ) – insoluble in water but slightly soluble in acid.

2. Brochantite ( $\text{Cu}_4(\text{SO}_4)(\text{OH})_6$ ) – nearly always the most common component of the green patina formed on copper after long atmospheric exposures.
3. Antlerite ( $\text{Cu}_3(\text{SO}_4)(\text{OH})_4$ ) – Not uncommon as a patina constituent. It is stable in more acidic conditions than brochantite. There is some evidence that antlerite may occur at earlier stages of the patination process than brochantite. More recently, antlerite has been found on the copper skin of the Statue of Liberty. It is suggested that acid rain is converting brochantite to the less protective antlerite, which is more susceptible to erosion.
4. Posnjakite ( $\text{Cu}_4(\text{SO}_4)(\text{OH})_6 \cdot \text{H}_2\text{O}$ ) – may co-exist with or undergo transformation to brochantite because of its structural similarity (hydrated form of brochantite).
5. Atacamite ( $\text{Cu}_2\text{Cl}(\text{OH})_3$ ) – soluble in weak acid. It has been found to be as abundant or more abundant than brochantite in the patinas formed near the sea, due to the influence of sea-salt aerosols. It is not found on specimens exposed for short times.
6. Paratacamite ( $\text{Cu}_2\text{Cl}(\text{OH})_3$ ) – its presence is transitory and it eventually converts to atacamite. It is not found in patinas corresponding to long exposures.
7. Malachite ( $\text{Cu}_2(\text{CO}_3)(\text{OH})_2$ ) – atmospheric conditions do not favor the formation of this type of patina, but this basic carbonate is sometimes unexpectedly found in practice.
8. Gerhardtite ( $\text{Cu}_2(\text{NO}_3)(\text{OH})_3$ ) – also found in some locations.

Krätschmer and colleagues [18] investigated 39 exposure sites using quantitative X-ray powder diffraction analysis on patina, still adherent to the substrate, that was up to 8 years old. Their investigations allowed them to deduce a general scheme that describes the evolution of the copper patina including altogether 8 compounds. The scheme is presented in figure 17.

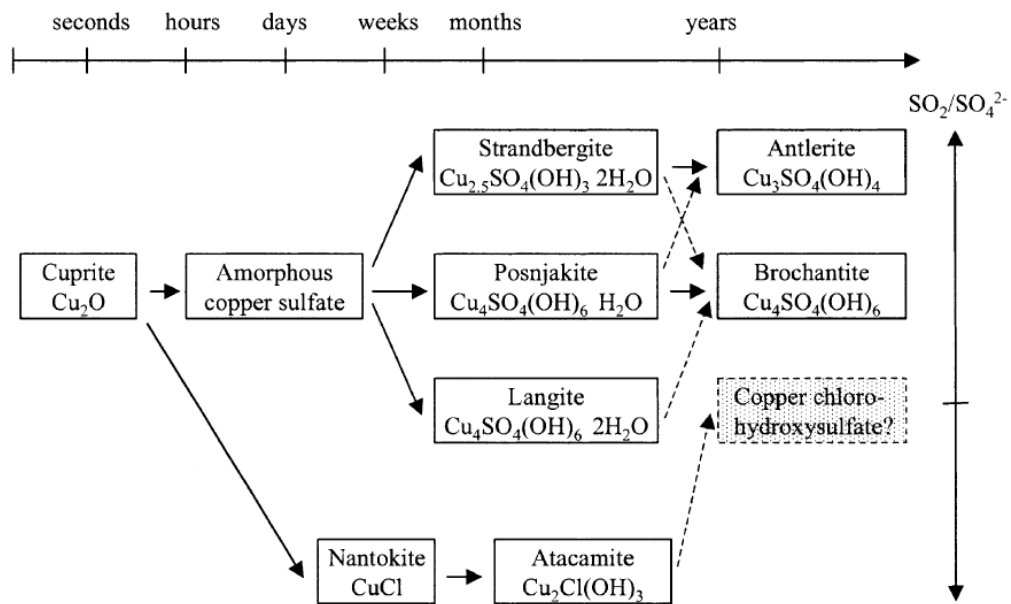


Fig. 17. A general patina evolution scheme of sheltered copper in a sheltered geometry in different environments as a function of time. [18]

As regards the metals released from the bronze alloy, the most reactive major component zinc suffers from a preferential dissolution to copper [19]. Copper itself will undergo a preferential dissolution in respect to tin, making the patina a surface that is rich in insoluble tin oxides with a lower content of copper than the original bronze (“decuprification”).

### Protective treatments for bronze corrosion

Despite the fact that the corrosion process can sometimes have an esthetically pleasing effect on bronze statues and artifacts through the formation of the usual patina, like on the Statue of Liberty which has a beautiful blue-green color, it is none the less destructive and causes damage to those objects. Even more in the cases where the corrosion products have an undesired color or texture or flake off compromising the appearance of the artwork, considerable effort and resources have to be used in order to limit the damage. For these reasons, the development of protective treatments for metal corrosion and bronze in particular has been of great interest for scientists and conservation experts.

Usually, the protective treatment consists of a double layer coating, the inner one consisting of benzotriazole (BTA) derivatives and an outer layer of acrylic resins or microcrystalline wax. While BTA has been proven to be very effective in the protection of copper objects, its effectiveness for bronze items has been lower. Furthermore this class of compounds is known to have toxic effects on the environment and BTA itself is believed to be carcinogenic. It is for these reasons that silane coatings are investigated as a protective treatment for bronze and gilded bronze objects [19], [20].

The authors found that 3-mercaptopropyl-trimethoxy-silane (abbreviated PropS-SH) has the best performance in decreasing the corrosion of bronzes in chloride solutions [20]. The coating was applied on the metal surface in the hydrolyzed form which immediately adsorbs, through the formation of hydrogen bonds between the silanol (SiOH) groups of the silane and the metal hydroxyls (MeOH) found on the surface of the metal due to oxidation in the presence of air. After the application phase, the coating is cured at room or higher temperature for a period ranging from 10 to 60 days. During this time, two main chemical reactions occur at the level of the silane coating. As a result of the reaction between the silanol and metal hydroxyls, metallo-siloxane groups are formed allowing for a good adhesion of the coating to the metal. Also the silanol groups from one PropS-SH molecule may interact with the ones of another leading to the formation of siloxane bonds SiOSi, in what is the beginning of a polymerization process. The behavior of the coating was confirmed using FTIR measurements that are presented in figure 18.

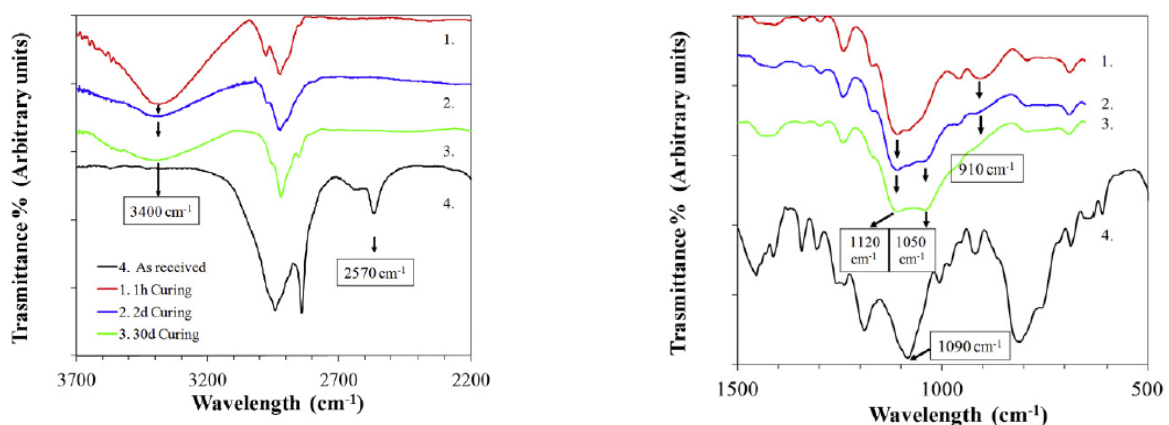


Fig. 18 FTIR spectra recorded by specular reflectance on PropS-SH-pre-treated bronze specimens, after different curing times (spectra 1–3); as a reference, the FTIR spectrum of as-

received PropS-SH is also reported (spectrum 4): (left) wavenumber range 3700–2200  $\text{cm}^{-1}$ ; (right) wavenumber range 1500–500  $\text{cm}^{-1}$  [20].

In figure 18 we are clearly able to distinguish that the spectrum of the fresh PropS-SH is the only one that presents a band at 2570  $\text{cm}^{-1}$ , which the authors attributed to SH stretching. This band disappears in the spectra of the cured coatings due to the formation of thiolate bonds.

The hydrolization process is evidenced by the presence of the band at 1090  $\text{cm}^{-1}$ , characteristic of the Si-OC stretching in the fresh PropS-SH spectrum. It disappears in the case of the cured films and instead a band at 3400  $\text{cm}^{-1}$ , characteristic of Si-OH bonds is present. This new band becomes shallower as curing increases and more Si-O-Si bonds are formed by condensation.

The results also showed that, after a 30 day curing cycle, the reticulation of the silane film is still incomplete. For this reason the authors suggest a 10 day curing period when carrying out research in order to have an acceptable timeframe for obtaining results and a 60 day period when used on artifacts.

Further studies are focused on improving the performance of the PropS-SH coating by the addition of nanoparticles, that provide nucleation centers, in order to determine a better reticulation of the film. The nanoparticles will also target the different exposure to which the bronze will be subjected to - for rain conditions adding cation releasers like  $\text{CeO}_2$  and  $\text{La}_2\text{O}_3$  (with an active inhibiting efficiency) is investigated, whilst for UV exposure  $\text{TiO}_2$  was considered as an additive for its anti-UV activity.

### **Gilded bronze corrosion**

In regards to gilded bronzes, the main form of corrosion that affects them is galvanic corrosion, also called bimetallic corrosion. Galvanic corrosion occurs when metals with different potential are in direct contact due to the presence of an electrolyte (such as the water condensation film that forms on metal surfaces during atmospheric exposure)[21]. If the metals

in contact have different electrochemical potential, a current will flow from the more electronegative anode to the more electropositive cathode, causing corrosion of the anode as can be seen from figure 19.

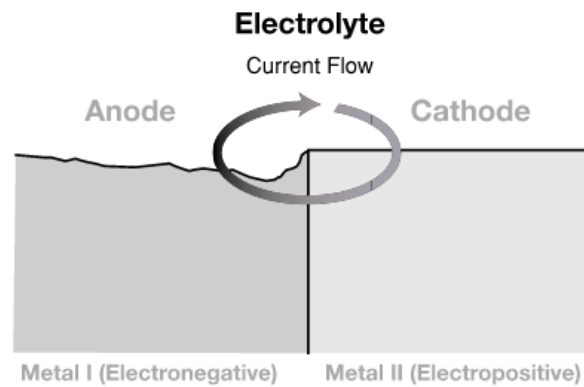


Fig. 19 Method of galvanic corrosion[22]

In general the reactions which occur are similar to those encountered on single uncoupled metal, the attack rate however is increased sometimes dramatically [21].

The effect of coupling together the two metals is that the corrosion rate of the anode is increased while that of the cathode is reduced, in some cases even suppressed.

The basic requirements necessary to cause galvanic corrosion are:

1. The first element needed is an electrolyte that bridges the two metals. The electrolyte may or may not be aggressive to the individual metals and may be in form of a bulk volume of solution, a condensed film or a damp solid.
2. The next requirement is an electrical connection between metals which usually involves direct physical contact.
3. A difference in the potential of the two metals that is large enough to provide a significant galvanic current.
4. A sustained cathodic reaction (e.g. the reduction of environmental species) on the more noble of the two metals.



corrosion. The electrical connection between the two metals is ensured through direct physical contact as the gold layer has been deposited on the surface of the bronze alloy.

### **Gilded horses of St. Mark's Basilica in Venice**

Alunno-Rossetti and Marabelli [23] studied corrosion products and encrustations on the surface of the gilded horse of St. Mark's Basilica in Venice in order to define some aspects in conservation of the statues in outdoor exposure. The scientist were interested also to obtain information in order to understand the mechanism of deterioration (figure 20)



Fig. 20. Gilded horses inside St. Mark's Basilica [24]

The Horses of Saint Mark, also known as the Triumphal Quadriga, is a set of four bronze horses originally part of a monument depicting a quadriga (a four-horse carriage). The four horses, which adorned the hippodrome of Constantinople, were transported to Venice by order of Doge Enrico Dandolo in 1204. The sculptures date from classical antiquity and have been attributed to the 4th century BC greek sculptor Lysippos [25]. These horses were gilded by the mercury-amalgam procedure, with an additional superimposed gold leaf about 8  $\mu\text{m}$  thick.

Preliminary tests of two samples, one in the Istituto Sperimentale dei Metalli Leggeri (ISML), Novara and the other in the Istituto Centrale del Restauro(ICR) have determined the chemical composition reported in Table 2.

The casting defects found in this statue were very numerous. The layer of gilding is no longer visible in various areas and, where is still present, it is either supported by the corrosion products or it is embedded inside and hidden by these products.

	<i>First sample</i>	<i>Second sample</i>
Copper %	97.2	94.4
Tin %	1.2	3.6
Lead %	1.0	1.7
Iron %	0.1	not analysed

Table 2 The chemical composition of the gilded horses (St. Mark's Basilica, Venice) [23].

The scientists carried out three type of analysis: X-Ray diffraction to analyze the solid state, conductivity measurement to obtain the soluble salt and chemical analyses to detect soluble and insoluble chloride, sulphates, copper, lead.

The percentage of soluble salts was obtained by a coulometric titration of the chloride ion in the aqueous extract, while insoluble chlorides were obtained by dissolving them in a solution of acetic acid and nitric acid and submitting the extract to the coulometric titration. Copper and lead were determined by electrolysis after dissolution of the sample with nitric acid and the total sulphate turbidity was assessed using the liquid after electrolysis and filtration.

The results of these experiments showed the following [23]:

1. The horses from St. Marc Basilica contain no trace of basic copper carbonate (malachite). This chemical compound is unstable and decomposes in polluted atmosphere with sulphur dioxide..
2. Lead and copper sulphate are the main components of the corrosion products resulting from marine environment of Venice.
3. The rain water has the effect of leaching out the patina, removing the soluble salts and rendering the residue more porous and crumbly.

4. A soluble chemical compound, copper sulphate pentahydrate (brochantite) was detected.
5. The patina, partially soluble, supports the gold layer, the corrosion products forming a layer in equilibrium with the environment; this layer can be partially leached and becomes porous. This kind of patina cannot be protective at all as it proved to be fragile during the washing procedure with a brush and distilled water.

The concluding remark of the author is that, during conservation procedures, it is necessary to avoid those chemicals which can penetrate the patina and dissolve it and those procedures that can damage the patina supporting the gold.

### **Gilded bronze statue Marcus Aurelius**

The equestrian monument of Marcus Aurelius, is one of the most famous bronze monuments of antiquity. The statue was erected in 175 CE. It was created according to the characteristic iconography to celebrate of a military victory of the emperor (Fig. 39).



Fig. 21. The monument of Marcus Aurelius after restoration [26]

In 1981, following a series of in situ examinations the statue of Marcus Aurelius was transferred to a laboratory of the Istituto Centrale per il Restauro in Rome [26]. The researchers, lead by Fiorentino, performed tests in order to identify the alteration products and to that extent some sixty samples were taken from the internal and external structure of the sculpture. The samples were chosen according to specific characteristics such as color – dark green, light green, gray, whitish, yellowish, light blue, black, earthy – as well as their physical characteristics such as smooth and compact or powdery and voluminous.

The researchers were able to identify, in the light and dark-green samples, brochantite as the most common mineral identified, while anglesite was found to be predominant for grey samples. In regards to the grey samples, in some of them atacamite predominated, while in others cassiterite was found. The blue samples showed the presence of chalcantite and gypsum and feldspar were also found on the surface.

The scientists were not able to characterize the extremely widespread black ablations found on the surface as these corrosion products did not provide clear diffraction patterns. Gypsum and copper oxalate were found in many samples of the yellowish corrosion products while cupric chloride, in a typical pitting formation, was found in the internal walls of the casting.

These tests revealed the extensive surface sulfation caused by urban pollution, an the obvious accumulation of airborne particles that retained humidity in some areas, encouraging cyclic corrosion involving cupric chloride.



Fig. 22. Typical alternation of light and dark areas of surface corrosion[26]

## Gilded Egyptian Osiris

In their 2002 paper [27], Scott and Swartz Dodd examined a gilded Egyptian bronze Osiris. The heavily corroded statue showed to have been originally gilt with gold leaf and inlaid with blue glass. It presents a very unusual patina that comes from the very specific conditions to which the statue was subjected to.



Fig. 23. Gilded bronze Osiris (USC 5047) from the collections of the University of Southern California. Frontal view. Copyright Bruce Zuckerman, West Semitic Research Collection. Scale in cm. Height 255.1 mm.[27]



Fig. 24. Gilded bronze Osiris (USC 5047) View of the back with extensive alteration to chalconatronite at the base and at the shoulders. Scale in cm.[27]



Fig. 25. Detailed view of the region between the crossed arms which retains remnants of the gilded surface. Part of the corrosion crust can be seen which comprises dark green atacamite and light blue chalconatronite, with occasional cuprite pustules, which have formed over the atacamite and chalconatronite surface. Magnification  $\times$  110. [27]

As can be seen from figure 25, the gilding is especially well preserved in the region of the crossed arms and is present as detached flakes within a thick crust of corrosion products. The corrosion crust appears as a thick, dark green mineralized layer, incorporating rounded quartz grains on the exterior surface, together with chalky-blue patches of corrosion that protrude beyond the dark green patina [27].

The dark green corrosion crust, situated on top of a layer of cuprite, shows cracks in many areas, revealing deeper green layers with cuprite below them as well. The presence of these cracks suggests a periodic repetition of hydration and dehydration, a cycle common in severely corroded bronzes associated with the presence of chlorides in the soil. A chalky-light blue corrosion layer that locally varies in colour, ranging from very pale to deep blue, was found overlying the green crust and intercalated with it. In some regions, dark red-brown to black pustules erupt from this green surface and occur as isolated excrescences within that layer. The authors however were not able to find the usual light blue powdery corrosion products associated with the alteration of the bronze [27].

X-Ray fluorescence analysis of the artifact yielded the composition of the bronze presented in table 3 that is typical of Iron Age Egyptian figurines.

element	Fe	Ni	Cu	Sn	Pb	Sb
weight %	0.4	0.03	86.7	7.3	4.5	0.1

Table 3. Composition of the bronze of the Egyptian Osiris figurine

XRF analysis of the gilding probably applied in the form of a leaf showed the presence of Cu. This does not mean that the element was added to gold in the manufacturing of the gold leaf and it could very well be found there due to diffusion of copper into the gold surface from the underlying metal. We present in table 4 the composition of the gold leaf.

element	Au	Cu	Ag
weight %	91.3	15	3.7

Table 4. Composition of the gold layer

In situ XRD studies showed that the light blue patches of corrosion are chalconatronite and the dark green corrosion crust that covers the entire figure is atacamite. Examination of the brown pustules also confirmed the presence of atacamite. In order to determine the presence of the brown coloration, a sample was crushed, mounted, and analyzed with polarized light showing that the atacamite crystals were tipped with cuprite.

### **1.3. The Paradise Door by Ghiberti**

Completed over the course of 27 years between 1425 and 1452, the Paradise Door, the East door of the Florence Baptistery, is a Renaissance masterpiece and one of the most famous sets of bronze sculptures in the world. The door consists of two double doors, each side being adorned with 5 gilded bronze panels, that depict scenes from the Old Testament [28]. The panels are encased in a bronze frame and are surrounded by vertical and horizontal friezes. Currently the panels displayed on the Baptistery door are copies of the originals that have been moved to the Museo dell' Opera del Duomo. There they are currently kept in a dry air atmosphere (RH <20%) with slightly positive overpressure, in order to ensure their conservation.



Fig. 26. Paradise Door [29]



Fig. 27. David panel [29]



Fig. 28. Cain and Abel panel [29]

According to literature [29], from the time of its installment up to 1945, the Paradise Door has not received any cleaning treatments. The maintenance of the masterpiece consisted of surface washing with water and the occasional protection with varnishes based on oil and wax [28]. From 1945 to 1966, the door was washed regularly in an attempt to remove the dirt that had accumulated on the surface. After the 1966 flood, the door began experiencing an accelerated corrosion phenomena and it was decided that tests and in depth analysis was required in order to formulate a strategy for the protection of the door.

While undesired, the flood also presented an opportunity to researchers, as due to the damage sustained in the event, the panels on the bottom of the door became detached from the bronze frame that holds them. Thus the panel depicting the Scenes from the Life of Joseph was brought to the laboratory of the Opificio delle Pietre Dure in order to perform analyses.

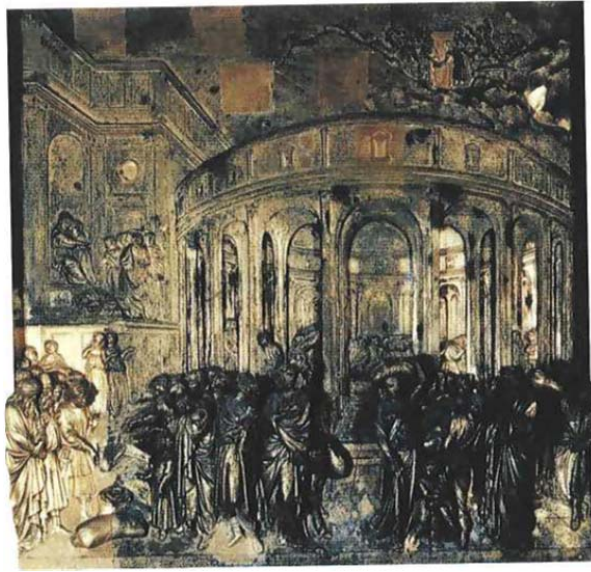


Fig. 29. Scenes from the Life of Joseph panel [30]

The first analyses on the door were performed by Panseri and Leoni and separately by Cesareo and Marabelli[28]. The scientists were able to establish that the bronze panels were executed using a quaternary alloy of copper (Cu, Sn, Zn, Pb) with a low content of alloying metals resulting in a reduced fluidity in the melt and hence numerous defects in the casting. They were also able to show that the method of applying the gold film was mercury amalgam gilding. The composition of the alloy is presented in table 5.

Panel	Cu	Sn	Pb	Zn
I.S.M.L. panel	93.7	2.2	1.3	1.8
I.C.R. framework	81.0	1.47	4.3	13.23
I.C.R. panel	91.42	1.52	2.57	4.47

Table 5. Composition of quaternary alloy of Paradise Door. The difference in values was attributed to the use of different instrumental methods and to different sampling points [28].

The sample was examined using binocular microscope and the authors were able to distinguish several types of material and surface corrosion phenomena: grey-black deposit materials, pointed aggregates of grey-green and green-blue corrosion products, extensive areas

with dark brown patina, corrosion phenomena relating to sharp edges of the relief, micro-blistering and losses of the gold and greenish/reddish coverings of the gold [28]. Among these, only the first three were analyzed as the rest proved impossible to be sampled by the researchers.

The grey-black deposit materials were first analyzed using a mineralogical microscope and were discovered to be a heterogeneous aggregate containing: crystals of calcium sulphate and light green crystals of copper salts, irregular black particles of carbon, crystals of  $\alpha$ -quartz [28]. In the IR spectra of the organic residue extracted with trichloroethylene the researchers were able to attribute bands to gypsum  $\text{CaSO}_4$  and silicates. XRD studies of the residues resulting from the extraction were able to determine the existence of gypsum and  $\alpha$  quartz as major components.

The samples of the pointed aggregates were characterized using XRD and the researchers found that they were mostly copper corrosion products. The predominant compounds were identified as cupric sulphateanthelite  $\text{CuSO}_4 \cdot 2\text{Cu}(\text{OH})_2\text{O}$  and copper nitrate  $\text{Cu}_2(\text{OH})_3(\text{NO}_3)_2$  [28]. The researchers state that these barely soluble salts derive from the electrochemical corrosion of the bronze and that they undergo a gradual process of solubilization and recrystallization on the surface.

The next two surface corrosion phenomena were identified as gypsum and carbonaceous particles that determined a roughness of the surface that favors the deposition of atmospheric particles [28].

Based on the analyses performed the authors are able to determine that the door has come to its current state as a result of two processes: corrosion and deposition.

In regards to the corrosion phenomena hypothesize that it involves several stages[28]: an initial attack of bronze in contact with the gold layer, a second phase in which the primary corrosion products undergo transformations as a result of water in the atmosphere and acidic products on the surface and finally diffusion of the copper salts to the surface.

The first stage is due to the electrochemical couple of gold and bronze, in which gold behaves like the cathode and bronze like the anode. As moisture from the surrounding environment and the occasional salt impurities could act as an electrolyte, the process that

ensures is the oxidation of the copper and the other alloying elements of the bronze. The products of this are copper oxides and compounds of the other elements that accumulate at the interface between the bronze and the gold layer [28].

In the second stage, atmospheric pollutants containing sulphur and nitrogen oxides react with the bronze patina, leading to its chemical modification. Soluble compounds are formed and this new patina no longer has protective properties. This type of corrosion has a tendency to take place in regions where the gold has a higher porosity. The resulting effect is a blistering of the gold film that sometimes even leads to its rupture and flaking off.

The final stage involves cycles of solubilization, migration and recrystallization through the porous gold film of the copper salt, diffusing to the surface and leading to the formation of aggregates and of a greenish film [28].

While being a separate phenomenon, the deposition of atmospheric particles may also lead to an increase in the rate of corrosion by rendering the surface rough and receptive [28]. The particles themselves may not be completely inert as their porosity and roughness allows for a better absorptivity of the sculpture surface, enabling an increase in electrochemical corrosion.

Based on these observations, chemical cleaning tests were performed using 3 types of cleaning solutions containing: ion exchange resin "Rm", a combination of salts of EDTA ( $\text{EDTANa}_2$  and  $\text{EDTANa}_4 \cdot \text{AH}_2\text{O}$ ) and a mixture of a solution of a Rochelle salt (sodium potassium tartrate) and micronized silica. In order to compare the performance of the cleaning solutions, the quantities of cupric ions dissolved in successive washings with distilled water and the conductivity of each wash were measured. All the cleaning solutions had a pH of 7 and the samples received two applications of 10 minutes.

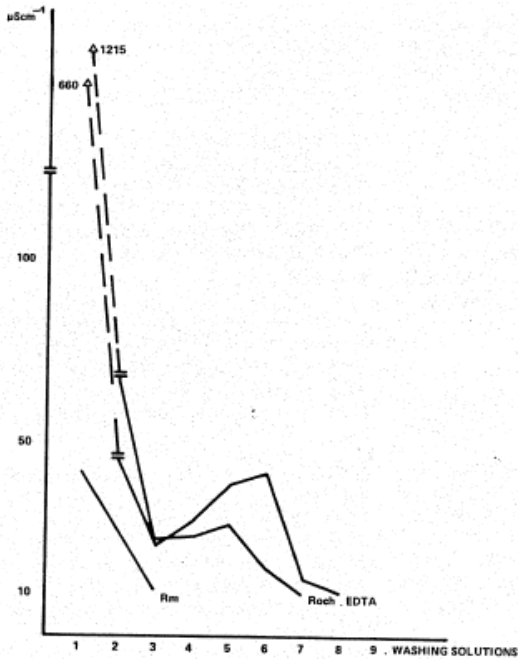


Fig. 30. Graph of the conductivity of the wash-water fractions after the application of resin Rm, Rochelle salt, and EDTA salt [28]

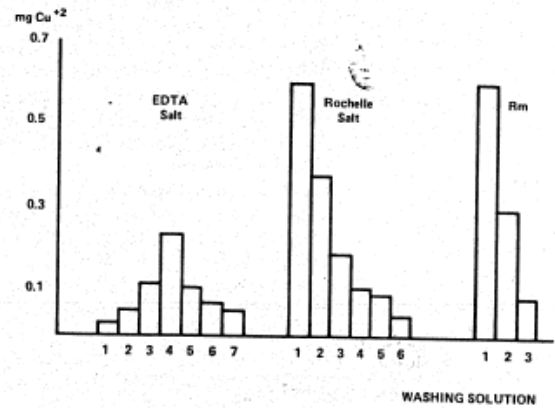


Fig. 31. Analysis of the cupric ion present in the wash water fractions after application of the cleaning agents [28]

The researchers were able to observe that neither applications of the cleaning solution resulted in the detachment of the gold layer.

Further studies on the condition of the Paradise Door were made by Emilio Mello by use of SEM, Auger spectroscopy and metallographic microscopy. The metallographic microscopy studies showed that, while the amalgam was being spread on the bronze surface, it formed accumulations in depressions and that the gold layer presented an increased porosity [30]. The author was able to conclude that the amalgam had a pasty consistency which leads to a higher amount of gold in surface pits as can be seen from figures 32 and 33.

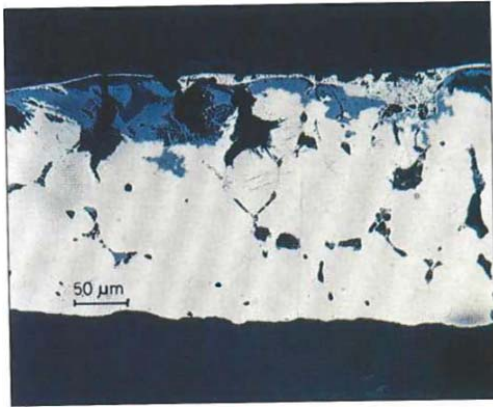


Fig. 32. Micrograph of a bronze cross-section of a gilt bronze sample of Paradise Door [30]

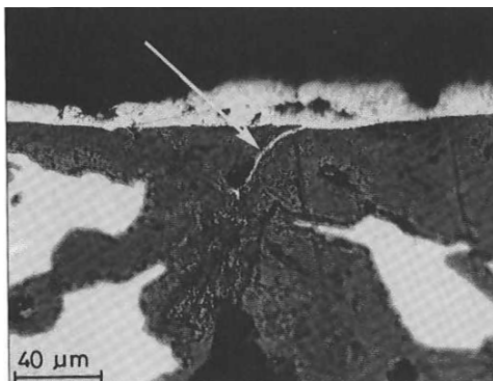


Fig. 33. Micrograph of the gilt bronze sample (the arrow points for gold located in a surface fissure)[30]

The SEM analysis of the sample determined that the gold layer presents a porous texture and that the bubbles were formed when mercury was leaving the amalgam as a result of heating, as can be seen from figure 27.

Ion bombardment excavations and Auger spectroscopy analyses were carried out in order to obtain an in depth perspective of the sample and the presence of mercury was identified in the gold layer [30]. As mercury was not present in the outside layers that contained dust and corrosion products, the researchers were able to establish that its provenance was from the use of



Fig. 34. Scanning electron micrograph of a fracture section of the gilt bronze sample. Magnification is of 1000x [30]

fire gilding and not from environmental pollutants. Another aspect that was pointed out was the presence of a little gold-copper diffusion that is in agreement with other comparative and archeological samples.

In order to conduct reparations as well as determine when and how the casting was executed, Ferretti and Siano [31] performed XRF studies on the panels of Abraham(IV), Isaac(V), Joseph(VI), Moses(VII) and David(IX). In order to obtain semi quantitative information, 230 measurements were performed on the back side of the panels in the main casting zones as well as in the repair areas [28], as can be seen from figure 28. Alongside the main XRF analysis, micro-samples of approx. 100mg were retrieved from the main panels and were investigated using AAS.

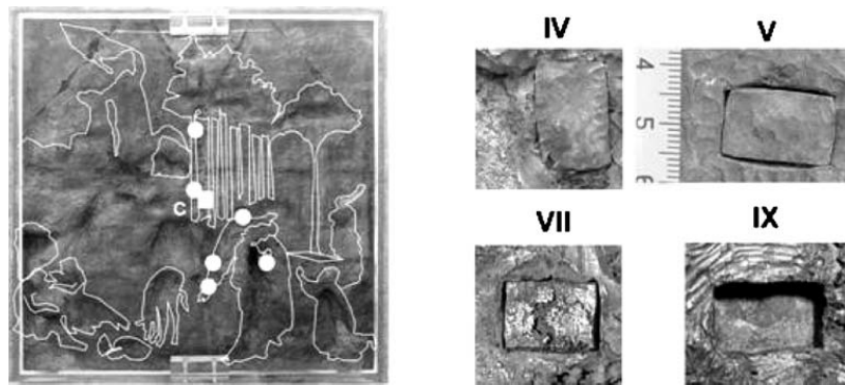


Fig. 35. Examples of analyzed surfaces – on the left the backside of the Abraham panel, with the spots indicating the repair sites and on the right the main repair plug [31]

The analysis revealed the presence of Cu, Sn, Zn, Pb, Fe, Ag, Sb, As and while the first four are characteristic of a quaternary alloy of copper the remaining ones can be correlated to the source of the raw materials. The compositions of four of the panels are presented in table 2.

Panel	Cu	Sn	Pb	Zn	Fe	Ni	Ag	Sb
IV (Abramo), AAS	91.93	1.82	1.25	3.46	0.54	0.19	0.03	0.41
IV (Abramo), XRF	–	2	1	3	–	–	–	–
V (Giacobbe), AAS	92.91	2.53	1.43	1.54	0.46	0.20	0.04	0.52
V (Giacobbe), XRF	–	3	1	2	–	–	–	–
VII (Mosè), AAS	93.51	0.13	1.14	3.78	0.13	0.14	0.06	0.13
VII (Mosè), XRF	–	0.2	2	4	–	–	–	–
IX (David), AAS	95.19	0.70	0.84	1.10	0.38	0.17	0.05	0.50
IX (David), XRF	–	1	3	2	–	–	–	–

Table 6. Composition in weight % of the main alloy of the panels, as measured by atomic absorption spectroscopy and average XRF line intensity analysis.

Using these results as well as those coming from the count-rate scatter plots of Sn-Zn and Sn-Pb from the main body of the panels, the authors were able to discriminate and group the alloys in two categories, determining that panels VII and IX have a higher Pb to Sn ratio than IV, V and VI and that there is a decrease of the Zn to Sn ratio from panels VII to IX, IV and VI [31]. This information along with observations on the casting repairs allowed the authors to speculate that panels VII and IX were cast before the others panel, VII probably being the oldest one.

While a chemical cleaning treatment was applied on the door's panels when they were out of the frame, the friezes surrounding the panels could not undergo the same type of treatment because their removal from the frame could prove damaging. This is the reason why an approach using laser treatment in the cleaning of the door became most appealing. The subsequent laser cleaning treatment performed on the door will be presented in part 4 of the introduction.

#### **1.4. Laser cleaning of bronzes/gilded bronzes**

The best method for caring for patinas always includes regular cleaning and waxing, which is important to both the appearance and longevity of the bronze. Consequently, surface cleaning not only improves appearance, but preserves materials as well. Thus cleaning is usually the first step involved in the various processes employed in the restoration of an artwork. It is one of the most difficult operations which must be performed in order to ensure the preservation of a deteriorating art object.

There are many different kinds of cleaning methods and techniques used in conservation. The conservation expert needs to choose between final appearance of the object and the surface layers which must be retained and that the cleaning process does not damage the object. The loss of surface detail can reduce the aesthetic appeal of an artifact and in extreme cases can lead to its deterioration. Also, chemical-based cleaning techniques leave residues within the material which can cause long-term problems. Chemical methods as solvents, acids or enzymes can dissolve contaminants and even remove the original surface of the artifact. There are also a significant numbers of objects needing conservation, to which traditional cleaning techniques cannot be applied.

Laser cleaning can be considered one of the most important contributions of physics to the conservation of artworks; it is an application of laser ablation. Laser ablation is a process in which a laser beam is absorbed at the surface of a material, determining a sudden transition of its solid phase to another phase (gas, vapor, plasma) if the energy density overcomes a certain level defined as the threshold [32]. Laser cleaning becomes a real alternative to mechanical and chemical techniques to remove contaminants from a large set of materials which are environmentally costly. It has been considered as a promising technique to directly ablate contaminants without altering properties of the material in numerous applications [33], [34]. Compared to conventional mechanical or chemical methods, laser techniques have the benefit of a versatile and selective process of removing specific substances using appropriate laser parameters, such as wavelength, frequency, and intensity.

Laser cleaning depends on the parameters of the laser irradiation and on the physical and chemical properties of the surface. The most important cleaning parameter is the energy density (fluence) of the laser beam; this fluence must be high enough to remove the contaminant layers but low enough to prevent damage the substrate. Other parameters are wavelength, pulse length and transport medium characteristics. When a laser beam interacts with a surface, the major part of the incident energy is absorbed and the remainder is reflected. Strong absorption of energy leads to rapid heating of the surface contaminants and ablation occurs. If the fluence is increased above a certain point, some of the material will be heated to a sufficiently high temperature to cause it to vaporize. When the contaminant has been removed, further pulses may not cause any damage to the reflective metal surface.

Preservation of the undamaged surface of the artworks during the laser cleaning is associated with the selection of the optimal laser parameters. Depending on the laser parameters, the laser cleaning can produce three kinds of photo-induced phenomena: photochemical processes (direct bond breaking and photo-dissociation), photo-thermal processes (evaporation by heating and heat conduction) and photo-mechanical processes (plasma formation, fast expansion and shock wave propagation). Depending on the properties of the sample and on the irradiation conditions, such as wavelength and pulse duration, one of them may become dominant.

The thermal diffusion length  $z$  produced by photo thermal effect, depends on the duration of the laser pulse  $\tau$  and on the diffusivity  $D$  [35]:

$$z = \sqrt{2D\tau}$$

Here the diffusivity  $D$  is:

$$D = \frac{K}{\rho c_p}$$

where  $K$  is the thermal conductivity,  $\rho$  and  $c_p$  are the density and the specific heat of the material, respectively.

Using short duration laser pulse, the heating propagation becomes short also corresponding to the depth of the layer which could be cleaned.

The photomechanical effect is represented by the mechanical coupling coefficient,  $C$

$$C = \frac{P}{I}$$

where  $P$  is the pressure created by the shock wave provoked by laser interaction and  $I$ , intensity of laser beam.

The laser action in the long laser pulse range results in melting, evaporation and sputtering of the surface layer. The photo-mechanical effect induced by the Q-switched regime generates pressure pulses with amplitude of up to hundreds of bars. The shock waves can produce mechanical damage to the surface of delicate artworks and to their artistic surface. The cleaning process implies the use of an appropriate thickness for the layer and an appropriate laser energy density. As stated by Siano and coworkers, working on the Porta del Paradiso by Lorenzo Ghiberti [36], an increase in the length of pulse with a fluence of  $0.15 \text{ J/cm}^2$  from 6 ns to 100 ns causes a reduction in the peak temperature from over  $450 \text{ }^\circ\text{C}$  to below  $150 \text{ }^\circ\text{C}$ . An extended pulse length reduces the pressure spike, and in the case of microsecond pulses practically does not cause any thermal stresses which act on the substrate material. In a typical laser-cleaning, an expected temperature of about  $370^\circ\text{C}$  together with the high pressure due to the vaporization of

the water of up to a few hundred atmospheres can produce substrate damage. However, this peak temperature exists only for a very short time, and most material surfaces show no damage after a few pulses [37].

Two types of laser cleaning have been reported in the literature: with or without the presence of a thin liquid film, usually water; this means dry or wet cleaning. In dry laser cleaning most of the incident energy can be absorbed on a surface allowing selective cleaning by control of the laser wavelength and this technique is useful when the substrate and contaminant layer have different laser absorption characteristics. However, in case of encrustations, better cleaning efficiency can be achieved by choosing a laser wavelength that is strongly absorbed by the surface together with a thin water film. Water sprayed onto the surface before the laser irradiation will penetrate into the contaminant where it will be rapidly heated by the laser leading to explosive vaporization of the water and in an efficient particle removal from the surface.

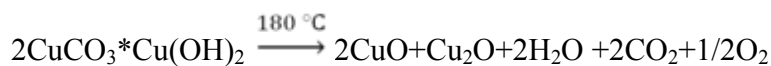
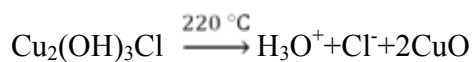
The first research studies on the application of laser technology to art restoration were performed in the late 1970s by John Asmus and co-workers [37], [38]. A great number of studies were reported over the last two decades in journals, proceedings and books about the effectiveness of laser ablation and the advantages by comparison with traditional cleaning techniques. Now at least 300 Nd:YAG lasers (neodymium doped yttrium aluminum garnet or  $\text{Nd:Y}_3\text{Al}_5\text{O}_{12}$ ) are operative in laboratories in all Europe and abroad. Laser cleaning has been used successfully in several conservation applications and has great potential as an effective alternative to many traditional methods of cleaning [39]. These are some examples of Nd:YAG lasers [40]:

1. Q-switched Nd:YAG laser - QS
2. Long Q-switched Nd:YAG laser -LQS
3. Short pulse free running Nd:YAG laser- SFR
4. Free running Nd:YAG-FR

Laser cleaning offers advantages over traditional cleaning methods involving chemical or mechanical action as follows: non-contact (because energy is delivered in the form of light), localization and selectivity (interaction directed only with specific compounds), versatility by wavelength variation, controlled removal (a specific thickness of material can be removed and,

most important, preservation of surface relief (being sensitive enough to preserve the fine details). In addition, this procedure has low environment impact because no hazardous chemical or solvent are involved. For all that, the big disadvantage of this technique is a large initial investment cost [34],[37].

Bronze objects are exhibited to different stages of corrosion. Metal corrosion is a process of chemical dissolution when cations migrate from the metal substrate and react with available anions to form the metal salts that constitute tarnish layers and corrosion crusts (see also section 1.2.). The character and chemical makeup of the bronze corrosion products depend on the nature of the substrate and the environment to which it is exposed [41]. In most of the cases the surface is covered by green calcareous accretions (malachite -  $\text{CuCO}_3 \cdot \text{Cu}(\text{OH})_2$ ) that overlaid the oxidation patina (cuprite -  $\text{Cu}_2\text{O}$ ). Systematic irradiation tests allowed demonstrating that SFR laser heating at sufficiently high fluences induces ablation and local phase transformation of unstable copper minerals such as chlorides and carbonates; the chemical reactions of interest are the following [42]:



A wide range of imaging and spectroscopy-based techniques is nowadays available for analysis of laser cleaning of art objects from optical microscopy, infrared reflectography, thermography, to scanning electron microscopy (SEM), confocal microscopy coupled with laser profilometry, atomic force microscopy (AFM), FTIR (Fourier Transform Infrared Spectroscopy) and Raman microscopy (micro-FTIR, micro-Raman), X-ray spectrometry, ion beam analyses (IBA), LIBS (laser-induced breakdown spectrometry) etc. [43],[44],[45],[46][47].

### **Laser cleaning of archeological bronze artifacts**

Pini and coworkers [48] were the first who used laser cleaning on excavated metal objects. Fragmented metal artifacts were selected from archaeological site of San Gaetano di Vada, Livorno, Italy (Roman Imperial Age) with various alterations. The type of alteration strongly depended on the material (lead, tin, silver or bronze) and the type of soil that hosted

each object (sands, clay deposits, originating from collapsed buildings, etc. Bronze samples have surface covered by malachite including silicates that completely overlaid the oxidation patina, the thickness of the alteration layers varying from a few hundreds of microns up to 2.5 mm.

Prior to laser cleaning tests, all the samples were washed in distilled water to remove incoherent deposits of earth and sand. During cleaning tests, laser irradiation was accompanied with the application of distilled water, in order to cool the sample surface and to enhance laser light coupling in the materials; in this case coupling in the encrustation is significantly larger than that of cuprite, favoring a higher cleaning rate. For bronze cleaning two types of laser were found to be most suitable:

- SFR laser, having pulse duration of 20  $\mu$ s and 1-2J energy per pulse
- QS laser, having pulse duration of 2-10ns and 0.5-1J energy per pulse

In both cases, the laser emitted at a fundamental wavelength of 1064 nm.

Fig. 36 shows a comparison between laser cleaning, manual cleaning and not cleaned of three parts of a bronze plate with a sequence of holes along the circular edge and two slight parallel grooves.

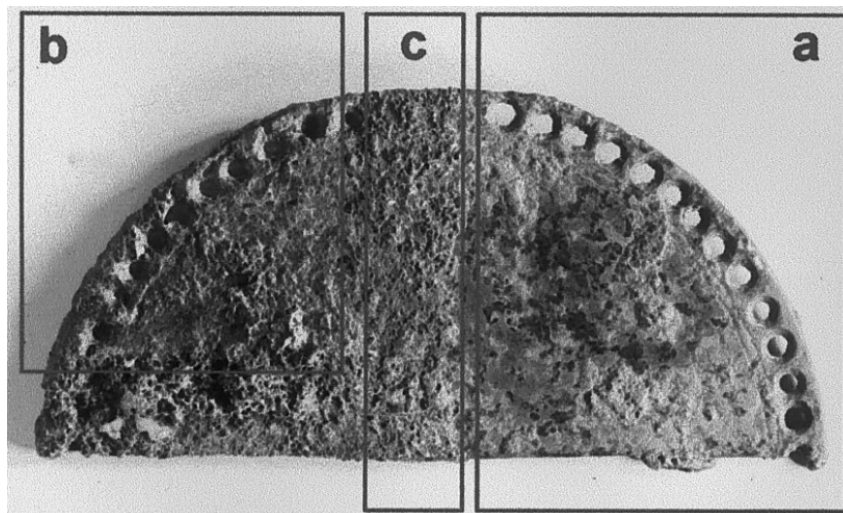


Fig. 36. Decorated bronze plate: (a) cleaned by SFR Nd:YAG laser; (b) cleaned manually by a scalpel; (c) not cleaned [48]

On bronze artefacts, laser cleaning by Q-switched Nd:YAG laser and SFR Nd:YAG lasers produced a selective ablation of the alteration layers that permitted the preservation of the oxidation patina, without exposing the metallic substrate. Laser irradiation was effective at removing the outer calcareous and siliceous encrustations from bronze objects but was markedly reduced when the underlying copper oxide layer was reached. Fig. 37 is an example of a bronze object when, after cleaning operations, the object was adequately restored, leaving the lower oxidation patina almost intact.

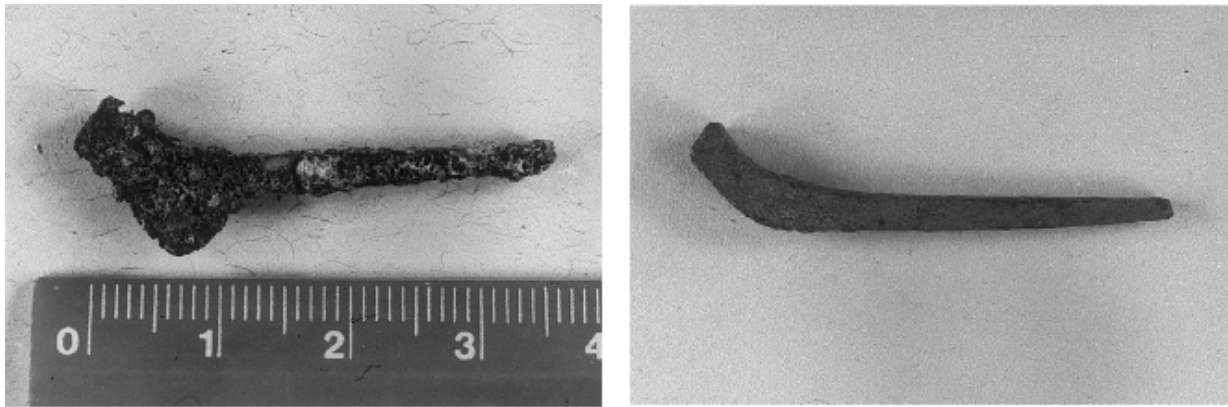


Fig. 37. Bronze clamp before and after laser cleaning [48]

The author's conclusions are that laser emission with short pulse duration is generally preferable to avoid heat damage to the surface of metals especially for the cleaning of metals with a low melting temperature, such as lead and tin, characterized by very low heat capacitance. This technique can be used also for silver objects whenever the cleaning has to be carried out up to the complete removal of oxides. In these cases, Q-switched Nd:YAG lasers with duration in the nanosecond region gave the best results, at fluences in the range  $0.4\text{--}1.0\text{ J/cm}^2$ . For the bronze objects, the SFR Nd:YAG laser of longer pulse duration seemed more suitable, providing safe and effective cleaning operations at fluence values in the range  $2\text{--}10\text{ J/cm}^2$ . This system provided enough control to stop the cleaning at the level of the cuprite, avoiding direct exposure of the metal substrate.

### Laser cleaning of coins

Yang Sook Koh thesis [37] presents the results on the cleaning of oxides from copper alloy surfaces (similar coins) using also Nd:YAG laser. This laser can be operated at 532 nm in the pulsed mode to clean the oxide layer from a selection of similar coins. The coins were in one of three conditions: a) dry; b) wet on the surface; c) submerged beneath 1.0 mm of water.



Fig. 38. A typical cleaned sample of the coins. One quadrant (a) remains uncleaned, quadrants (b) and (d) have been cleaned once by the laser, quadrant (c) has been cleaned twice with overlapping raster patterns at 90° to each other [37].

From figure 38 we can see that the results obtained from this experiment were very good. These optical photographs reveal a bright, completely cleaned surface. In addition it demonstrates that the pulse frequency needs to be optimized to achieve the best cleaning results.

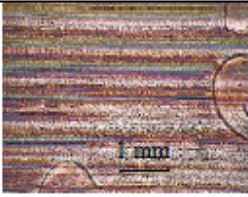
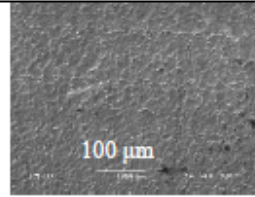
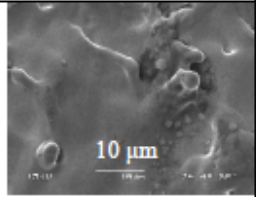
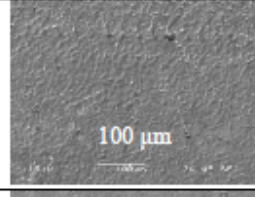
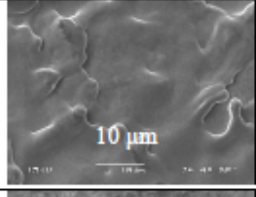
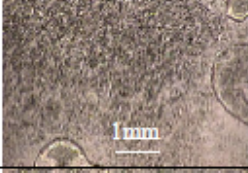
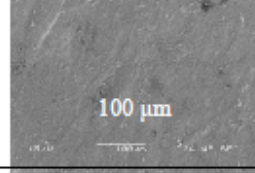
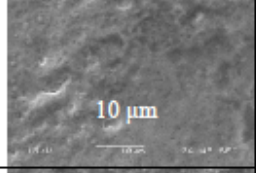
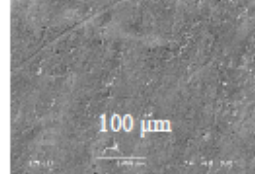
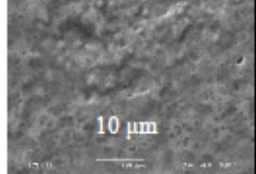
	Quadrant	Optical photos	SEM	SEM
<b>Sample 4</b> Laser power 35 W Pulse length 55 nS Pulse frequency 3000 Hz Raster speed 100 m/s	c			
	b			
<b>Sample 5</b> Laser power 75 W Pulse length 75 nS Pulse frequency 7000 Hz Raster speed 100 m/s	c			
	b			

Fig. 39. Optical and scanning electron microscopy of two coins cleaned with different pulse conditions [37]

To achieve cleaning without surface damage wet and submerged samples are used in order to suppress surface melting by using water as a coolant. In all cases, wet, dry or submerged, the surface of the coin was either covered in droplets (low power) or melt (high power). Nevertheless, in nearly all cases the coins were brightly cleaned and the surface alterations (melting or droplets) were only observable with the help of electron microscopy.

Figure 40 presents a direct comparison of the effect of the laser on the dry, wet and submerged under 1.0 mm of water samples.

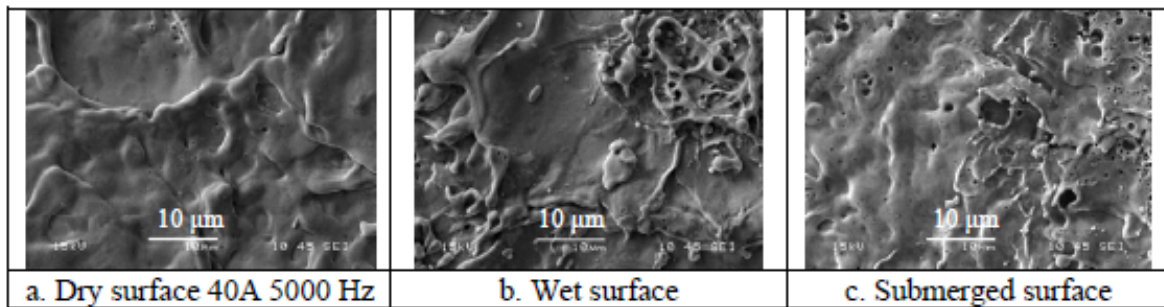


Fig. 40. High magnification SEM photographs of laser irradiated surfaces in the (a) dry, (b) wet and (c) submerged conditions [37]

The main conclusion is that Nd:YAG lasers can be used to remove oxides from copper coins but there is always a residual alteration of the coin surface. Either the surface of the coin is melted or the oxide surface is transformed into small droplets of metal which adhere to the coin surface. These effects are generally microscopic and only visible at high magnification.

Laser cleaning tests were carried on bronze coins also by Buccolieri and coworkers [35]. Sample surfaces presented a thin greenish alteration layer together with soil deposits. Experimental results about the laser cleaning of bronze coins show that the pulsed lasers can be used safely as a powerful tool to remove the patina of bronze coins.

UV and visible laser actions are able to remove the greenish patina from the surface of the coins more than 80 %.

### **Laser cleaning of burial jewelers from XII to XIII century**

Garbaz and coworkers [49] tested the laser cleaning process for two archaeological objects made of copper alloys, a bow and a ring (Fig. 41) from the cemetery located in the garden complex of Wilanow Palace in Warsaw and date from XII to XIII century ( these objects, with ornamental longitudinal grooving, were part of burial jewelers).

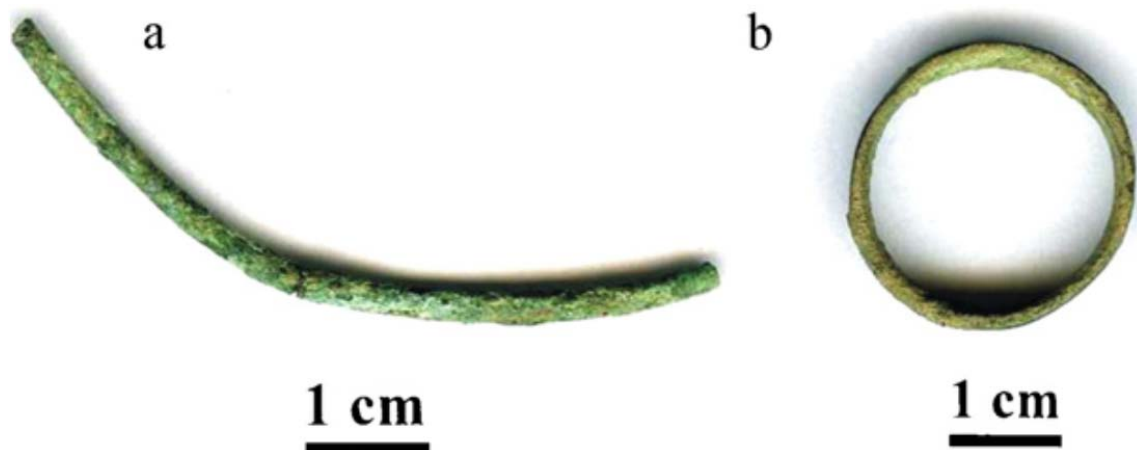


Fig. 41. Archaeological artworks: (a) bow, (b) ring [49]

The structure and chemical composition of these artifacts, as well as the corrosion products were studied using a variety of analytical techniques. The samples were investigated before and after the cleaning processes. The composition of the corrosion deposits was determined using Raman spectroscopy and SEM technique.

Laser cleaning tests of the these objects were conducted using long pulses ranging from 100 $\mu$ s to 1 ms obtained from the Nd:YAG laser which was in a free running regime, and also using short nanosecond pulses generated in the QS Nd:YAG, both working at the wavelength of 1064 nm.

The topography of the bow incrustation is presented in Fig.42.

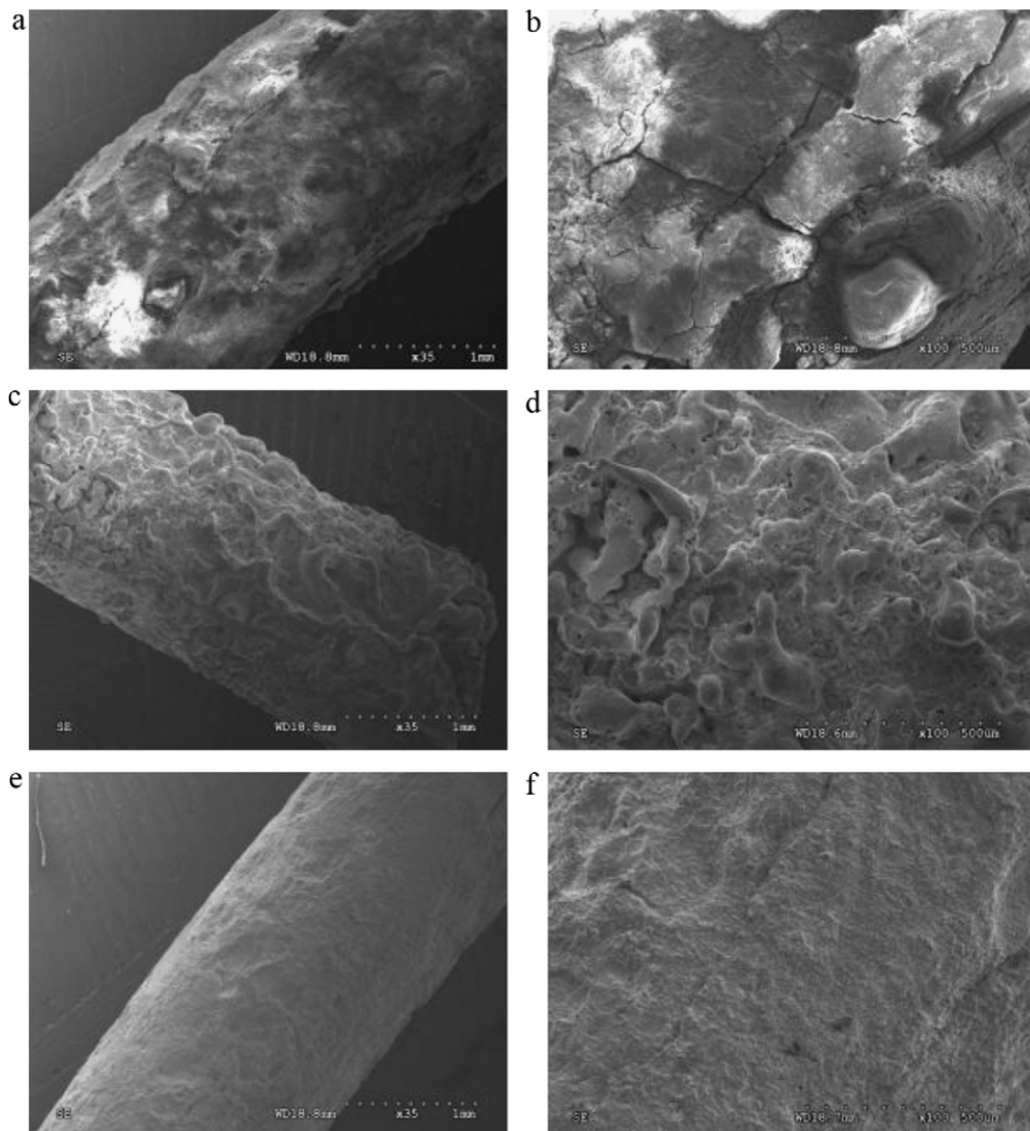


Fig. 42. SEM images of the bow surface in as received state (a and b) and after laser cleaning with microseconds (c and d) and nanoseconds laser pulses (e and f), [49]

From the figure above we can see that after laser cleaning the external corrosion layers were removed and the surfaces are relatively smooth. The observations of cleaned regions show they were slightly re-melted.

The elemental analysis of the corrosion layers present at the surface of both archaeological objects is similar. The main components of the sublayers are carbon, oxygen,

copper, and phosphorous (indicating: copper carbonates, phosphates, and/or oxides). Small amounts of aluminum, chlorine, calcium, and potassium were also detected. Raman spectroscopy results revealed the presence of a mixture of several copper compounds: sampleite, antlerite, malachite and cuprite, in both objects; in addition it reveals the presence of azurite in the ring and posnjakite in the bow. Raman spectra for the bow and the ring are presented in Fig. 43.

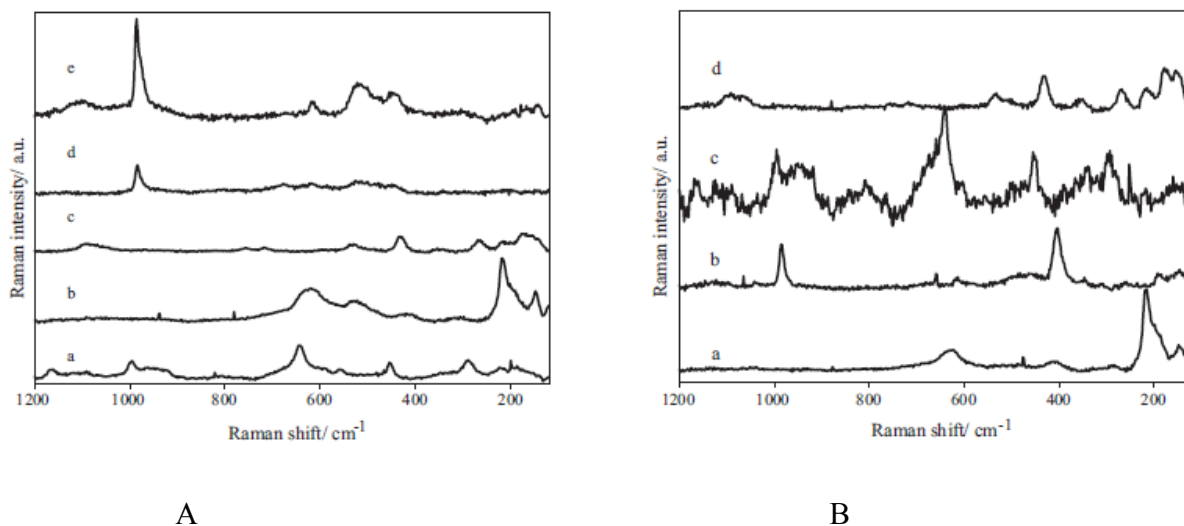


Fig. 43. A- Raman spectra of various corrosion products detected on bow: (a) sampleite, (b) cuprite, (c) malachite, (d) antlerite, (e) antlerite and posnjakite ; B-(a) cuprite, (b) azurite and antlerite, (c) sampleite, (d) malachite [49]

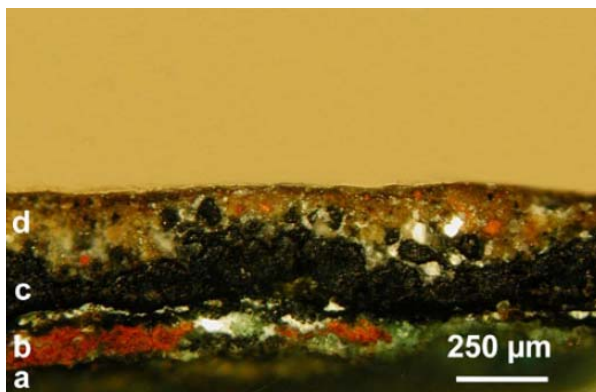
The authors noted that the chemical composition of the ring, after surface cleaning with nanoseconds pulses, is not the same as after cleaning with microseconds pulses. The ring surface cleaned with shorter laser pulses is mainly composed of copper and oxygen; this means that copper oxide is present. This is in agreement with the observations of the cleaned area made with the naked eye because the color of the cleaned area was brown, which is the color of copper oxide - cuprite. The authors conclusions that the use of a laser generating long pulses in the range of 100 $\mu$ s–1ms, leads to irreversible damage to the layers of copper based substrates of archaeological objects. In the case of nanosecond pulses generated in the QS regime of the Nd:YAG laser, they would also cause local damage even if the minimal energy density of the laser is used. Thus it is necessary a good selection of the duration of the laser pulses in the ranges

of tens and hundreds of nanoseconds when the metal artwork be subjected to high temperature gradients and mechanical stress.

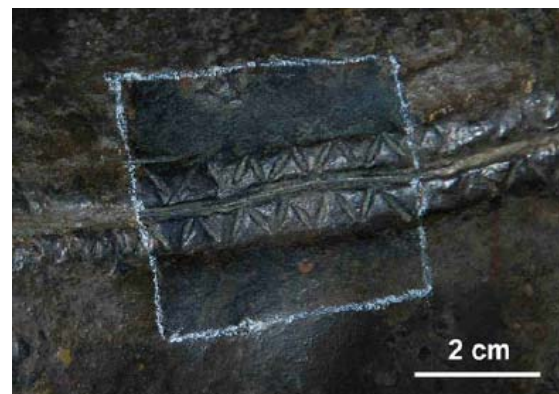
### Laser cleaning of Arringatore statue

The Arringatore is an Etruscan large bronze life-size statue (height 180 cm) found in XVI century near the Lake Trasimeno in Middle Italy. It is acquired by the Grand Duke Cosimo I in 1566, but dated between II–I centuries b.C. [42]. This statue is a man dressed in the typical roman toga, with fine sandals on his feet, and one raised arm that seems to ask silence of a crowd.; he seems be a orator. Based on his pose and clothing, he must have been an important political figure in his city, which might have been Perugia.

XRD, FTIR and stratigraphic analyses showed the following compounds: bronze substrate, copper minerals, mainly including cuprite and chlorides, an irregular tenorite-rich black layer, also including cerussite, cassiterite, and chlorides and organic-matrix intentional patination; the tenorite layer could represent evidence of the original ancient patination (Fig. 44A).



A



B

Fig 44. A-The stratigraphy of the Arringatore statue: an organic binder patination (**d**), a black tenorite layer (**c**), corrosion minerals(**b**), and bronze substrate (**a**); B-Laser-assisted cleaning test (laser treatment then scalpel) carried out on the right shoulder of the Arringatore, [42]

To clean the organic-matrix patination, water-assisted SFR laser irradiation at operative fluencies around  $2 \text{ J/cm}^2$  was used and then mechanically using a scalpel and brush finished the cleaning (Fig. 9. B).

The bust of the Arringatore restored is displayed in Fig. 45.



Fig. 45. The bust of the Arringatore after cleaning [42]

From this figure can see that the laser cleaning leads to a final appearance slightly darker than before cleaning but with a more readable surface and a reduction of corroding agents. The Arringatore also offered the possibility to apply laser irradiation to remove undesired incoherent copper minerals after mechanical cleaning.

### **Laser cleaning of the outdoor objects**

Evaluation of the laser cleaning of an outdoor object (a bronze bell), dating from the second half of the 600 was performed by Buccolieri and coworkers [41](Fig. 48).



Fig.46. Photo of the bronze bell used for this study of laser cleaning, [43]

The authors used a UV laser working at 248 nm and a pulse duration ranging from 20 to 30 ns. As we said earlier, in the operations of laser cleaning of metal artifacts, knowledge of the ablation threshold associated with the metal matrix is essential, in order to avoid possible mechanical damage as well as any noble patina present. The ablation rate as a function of the used laser fluence forms a linear trend: the ablation threshold was determined graphically by evaluating the value for which the ablation rate is void. Fig.47 shows the patterns obtained experimentally for a bronze sample. The value of ablation threshold is equal to  $1.8 \pm 0.3 \text{ J/cm}^2$ .

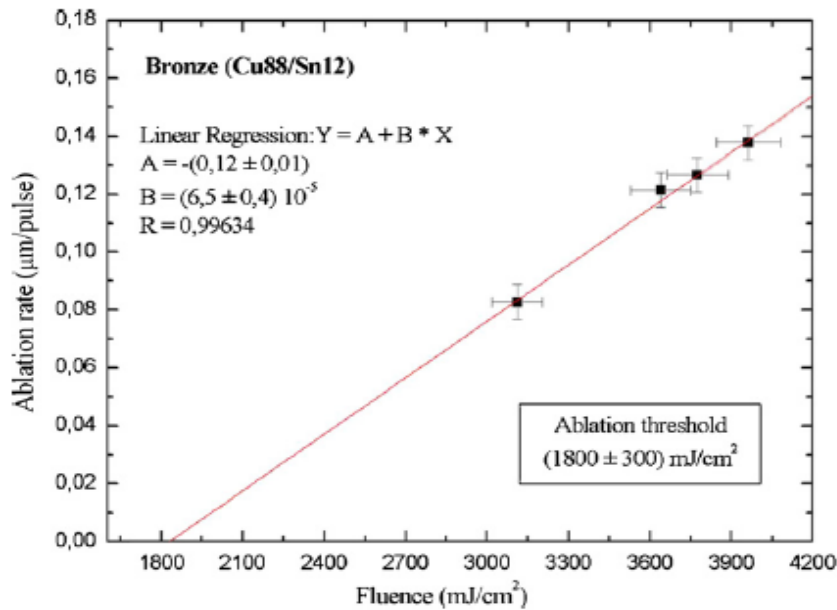


Fig. 47. Laser ablation rate as a function of laser fluence [43]

The bell was subjected to four subsequent laser ablations, in which the fluence per pulse, was the order of  $0.7 \text{ J/cm}^2$  and the area irradiated corresponded to a rectangular laser spot of about  $0.14 \text{ cm}^2$ . Experimental results show that the UV laser cleaning technique is an effective tool to remove some of the most common compounds of alteration of the ancient bronze artifacts, namely basic salts containing copper sulfate and calcium carbonate deposits. Quantitative analysis indicate that in the course of laser cleaning treatments a gradual reduction and controllable of concentration of sulfur and calcium is registered.

Rode and coworkers [33], [34] used ultrafast lasers which generate very short, powerful pulses extending from a few femtoseconds (fs) to the picosecond region (ps), i.e  $10^3$ – $10^5$  times shorter than the nanosecond pulses, currently applied to heritage conservation; Fig. 13 reveals the difference between the two domains.

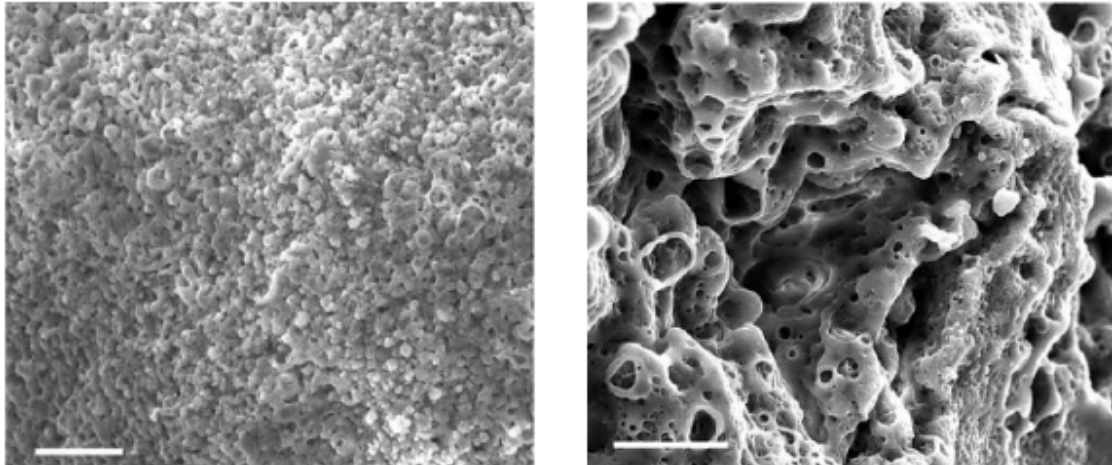


Fig.48. SEM images in the case of 150-fs pulse cleaning (left) and 60-ps pulse (right). The fs-ablated object is smooth while the 60-ps one shows cavities in the surface, indicating high thermal impact. The scale bars are 10- $\mu$ m long in both images [33]

#### **Laser cleaning of the simulated corrosion patina**

To study laser cleaning Barone and coworkers [51] simulated the corrosion chloride patina on bronze surfaces treating the sample with HCl. The experiments were conducted on a series of commercial bronzes with dimensions of 1 cm  $\times$  2 cm and a thickness of about 0.5 cm (Fig. 48 a). The patina obtained in this way is different to natural patina because it is composed only by cupreous chloride but it is the responsible of bronze degradation and therefore must be eliminated in cleanness process. Each sample was immersed in a solution of HCl 37% for 190 h and afterwards they were heated at about 120 °C to evaporate the residuals of HCl. On the sample we can observe the formation of a patina of bronze disease with a thickness of about 300  $\mu$ m (Fig.48 b). Then each sample was submitted to cleaning procedure by laser ablation in air and in marine water. Laser cleaning was performed using a Nd:YAG laser working at the second harmonic (532nm) and a energy of 300mJ/pulse (Fig. 49 c, d).

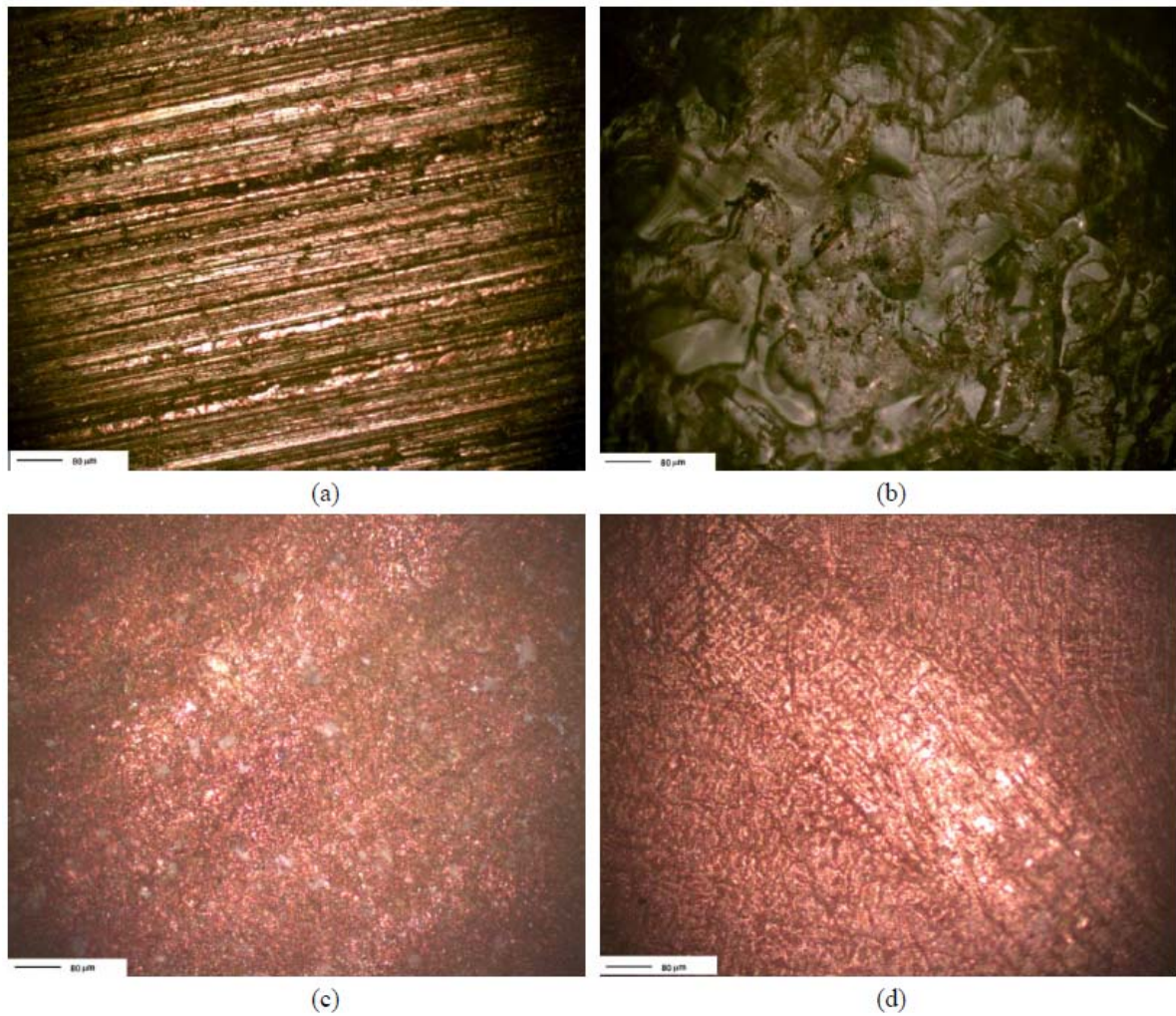


Fig.49 (a) Optical images of commercial bronze sample; (b) bronze disease patina obtained by HCl treatment; (c) samples after laser ablation in air and (d) marine water [51]

Laser ablation process for 2 h in both marine water and air reduces the patina to a few microns and the process is most effective in marine water; in air laser cleaning leads to adsorption of air oxygen and carbon corresponding to a progressive “carbonization” of sample. In addition, laser cleaning conducted in marine water offers the possibility to clean the bronzes directly in marine archeological sites removing the possibility of damaging it due to movement.

Studies of the stimulated of bronze patina in ambient atmosphere using LIBS were also reported by Elhassan and coworkers [52]. Finally, LIBS analysis was carried on three real metal

objects and the spectra obtained have been used to estimate the type and elemental composition of the alloys based on the calibration curves produced with the reference alloys.

Electrochemical testing of laser treated bronze surface was also recently performed by Yilbas and coworkers [53]. Using SEM-ED and X-Ray diffraction, the authors argue that the laser cleaning improves the corrosion resistance of the treated surface.

### **Laser cleaning of the special plate from *DeBraak* shipwreck**

Bartosz Dajnowski [54] successfully performed the laser cleaning of a special plate, known as gudgeon which is from H.M.S (His Majesty's Sloop of War) *DeBraak*. This ship sank along the Delaware coast in 1798 but the shipwreck was discovered in 1984. This plate is a part of a ship rudder assembly. Ropes or chains run through the loops of a plate and are connected to the starboard and port side of the ship stern; chains of *DeBraak* ship were from of copper alloy to prevent loss of the rudder.

The object was examined using X-ray fluorescence, SEM-EDS, Raman spectroscopy and both copper and iron corrosion products were identified. Optimal laser cleaning was obtained using a LQS laser at 1064nm and 100ns and a SFR laser with 60-130 $\mu$ s, at various fluencies. After laser cleaning the plate was treated with 3% benzotriazole in ethanol and afterwards with a protective was coating.

### **Laser cleaning of gilded bronze**

#### **Laser cleaning methodology for *Porta del Paradiso* by Lorenzo Ghiberti**

Much work, begun in the 1980, led to a chemical approach based on washing with sodium potassium tartrate (Rochelle salt). Up to 1985 four of these damaged panels were dismantled and three of them restored but the door still remain at the Baptistery.

The last panels were restored after 1990 when the original door was brought to the OPD (Opificio delle Pietre Dure), the institution responsible for art restoration. An unsolved problem

is dismantling because this procedure might be dangerous for these objects which are very fragile. In addition, the restoration must be non-invasive [55].

Siano and coworkers [53], [36], [56], [32], [42], [57], [58], improved the cleaning on the panel entitled *Storie di Noè*, using laser cleaning. Their study was carried out in two steps:

1. Optimization of the laser cleaning methodology through a good selection of the laser source and operating parameters
2. Integrated cleaning tests of the optimized laser treatment with Rochelle salt.

In their paper Siano and coworkers [36] described the cleaning methodology for gilded bronze objects from “Porta del Paradiso”, being “the first time a well recognized masterpiece was treated with laser cleaning” as said Siano himself. For this masterpiece, the authors introduced a novel laser called Long Q-Switching (LQS) Nd:YAG which has an adjustable pulse duration ranging from tens of nanoseconds to microseconds [42].

The characterization of the state of conservation was derived by analyzing encrustation material and very small gilding fragments that were unwillingly detached during the dismantling of the panel and the cleaning operations [36].

The bronze sculptures of the door were gilded by the mercury-amalgam technique described earlier (section 1.1.). The typical thickness of the gilding film observed by SEM microscopy was between 3 and 9  $\mu\text{m}$ .

The black-greenish encrustation covering the gilded panel surface contains gypsum, earthy materials, oily substances, carbon black and various copper corrosion compounds (Fig.50), as results of XRD, FT-IR and chromatography show.

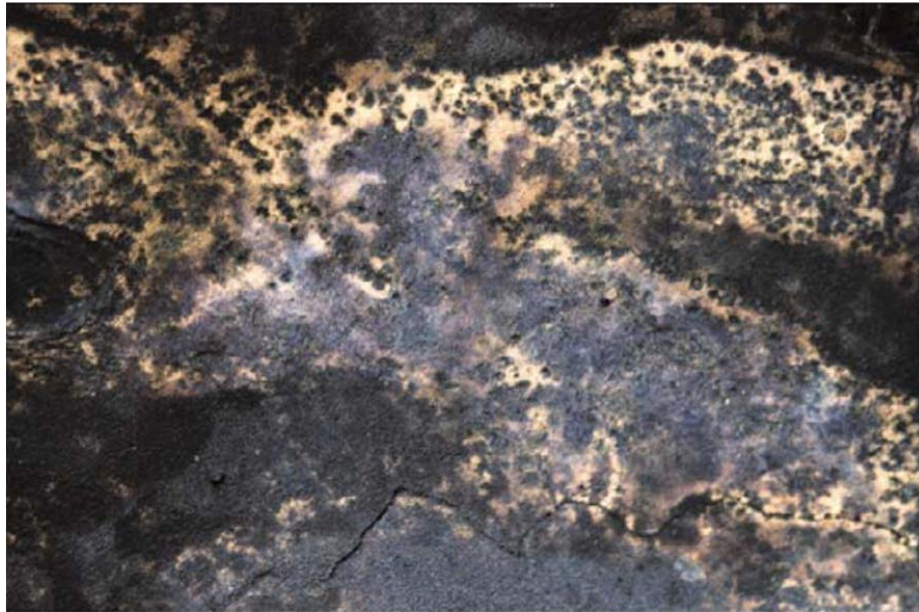


Fig 50. Typical encrustation on the gilding surface [36]

Three main layers can be distinguished above the bronze substrate: encrustation (E), gold film (G) and the underlying cuprite (C). The encrustation thickness is very inhomogeneous and increases in correspondence with micro blisters and gold losses.

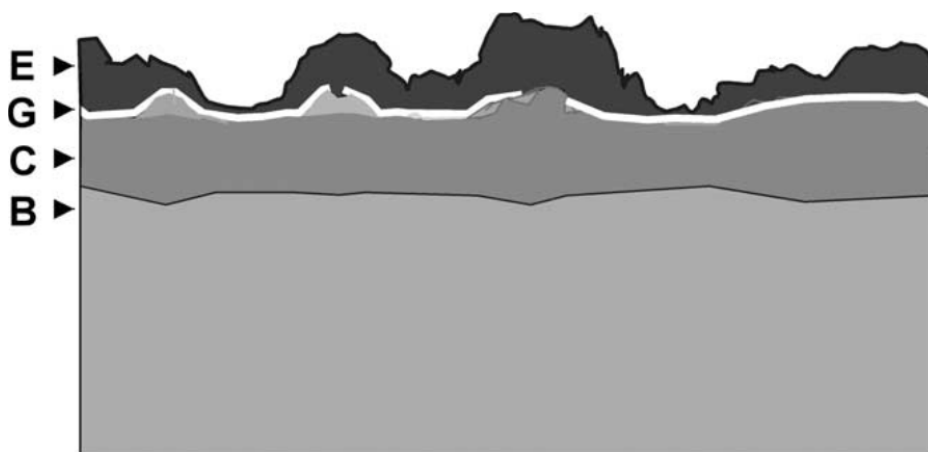


Fig. 51. Schematic representation of the stratigraphic layers: encrustation (E), gilding (G), cuprite (C), bronze substrate (B), [36]

The main scopes of the cleaning are:

1. Safe cleaning of the gilding, i.e. without any thermal or mechanical injuries to the gold film.
2. The safeguard of cuprite spots and the color of the cuprite (reddish brown), procedure which gives an important limitation to the laser irradiation. Laser cleaning, occurring at relatively low fluences is accompanied by surface greying, likely associated with an oxidation process, which transforms cuprite ( $\text{Cu}_2\text{O}$ ) into an incoherent distribution of tenorite ( $\text{CuO}$ ) as usually observed during laser cleaning of archaeological objects.
3. Minimization of the thermal effect of the gold film i.e maximum temperature of the gold film to be lower than  $357^\circ\text{C}$ .

The thermal problem of laser cleaning consists in the heating of the encrustation during ablation, and the direct heating of the gold film, always occurring during the finishing phase of the laser cleaning treatment. The water-assisted irradiation can reduce the cleaning temperature, increase the greyish threshold of cuprite and the undesired reddening of the gilding.

The temperature increase in the gold film is associated with a short pulse as Fig.52 shows

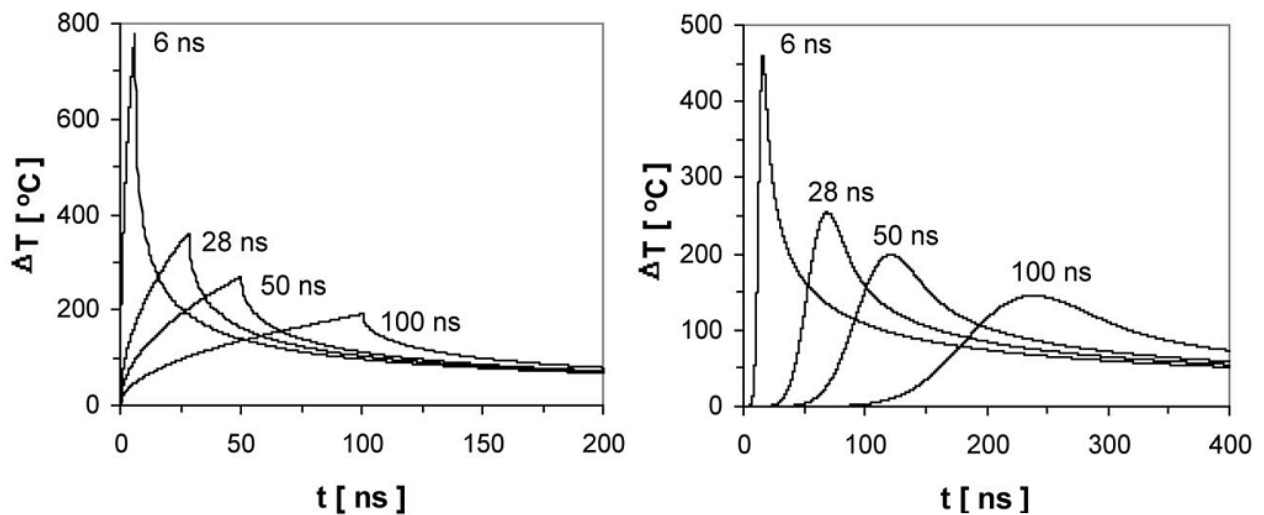


Fig. 52. Temperature rises associated with different pulse durations for top-hat (left) and Gaussian (right) pulse shapes, [36]

Cleaning tests on the *Storie di Noé* panel were performed by a fibre coupled QS laser with a pulse duration of 28 and 50 ns and fluences of 500 mJ/cm<sup>2</sup> and 600 mJ/cm<sup>2</sup> for encrustations. In a single site the cleaning threshold for a 20 μs pulse duration (provided by a further Nd:YAG laser) resulting a fluence of 3.5 J/cm<sup>2</sup>. The long pulse provides a temperature rise to 690 °C. This temperature rules out the possibility of performing cleaning with 20 μs pulse duration because of the possible thermal effects both with water vaporization underneath the gold film and with the possible direct melting effects. Operative fluences and thermal distributions associated with the short pulses were below the critical values for these effects and also for mercury vaporization, as can be observed in Fig.53 for a pulse width of 28 ns.

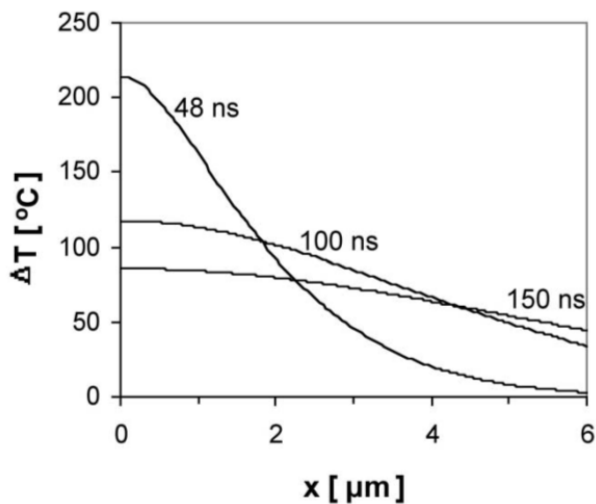


Fig.53. Representation of the thermal wave propagation inside the gold film at different time delays with respect to the beginning of the laser irradiation, [36]

The damage threshold of the gold surface was about 2.3 J/cm<sup>2</sup> for a pulse of 28 ns and 3.1 J/cm<sup>2</sup> for 50 ns; this means a critical temperature of about 660–980 °C.

Microscopic observations of the cleaned areas evidenced a complete removal of the encrustation and the high selectivity of the laser cleaning. Neither thermal nor mechanical injuries to gilding nor cuprite blackening were observed on the cleaned surfaces [36], [39], (Fig.54)

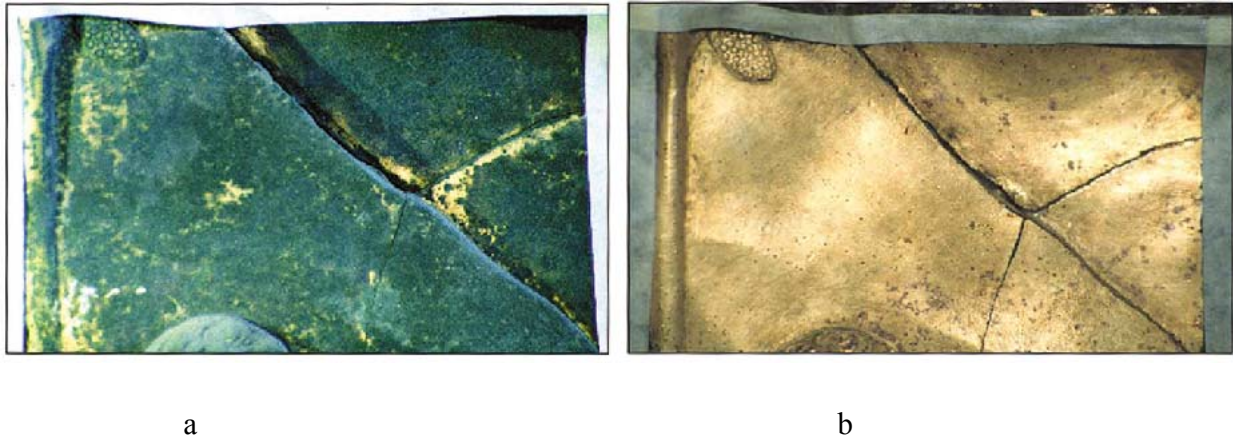


Fig. 54. Example of a laser cleaned area: a-before; b-after [36]

The authors concluded that the pulse is the most critical parameter and the most convenient range is 30–100 ns; this is the reason they used a pulse duration of 28 ns but in the future they will be enlarge this domain to 50–150 ns. The pulse duration has to be very precisely selected for each task because it determines the time for the localized heating. “Sometimes a long heating is harmful and sometimes a short heating is harmful” as Siano said.

Matteini and coworkers [58] reported the cleaning methodology based on integrated chemical and laser techniques. This cleaning procedure is appropriate for cleaning of gilded sculptural elements of the door frieze, without them being dismantled from the bronze framework.

The method included application of neutral solutions of sodium potassium tartrate by poultices or atomization and QS laser cleaning. Chemical and physical characterization diagnostics of the cleaned surfaces were employed to assess the effectiveness of the various cleaning methodologies under testing. The restorer treatment with 35% aqueous Rochelle salt solution provided a complete cleaning of the flat areas of sites 3 and 4, from the figure but they were less effective on the deep encrustation of the main scene (sites A and B).

The neutral solution employed in order to differentiate copper oxides from other copper compounds has a low rate with respect to the more aggressive alkaline solution usually employed

for archaeological findings. The surface cleaning by optimized QS Nd:YAG laser cleaning was effective in the complete removal of the encrustation.

This integrated procedure also provided, in the case of the flat area, an increase of reflectance of the gold surface in comparison with the stand-alone laser treatment (Fig. 55).

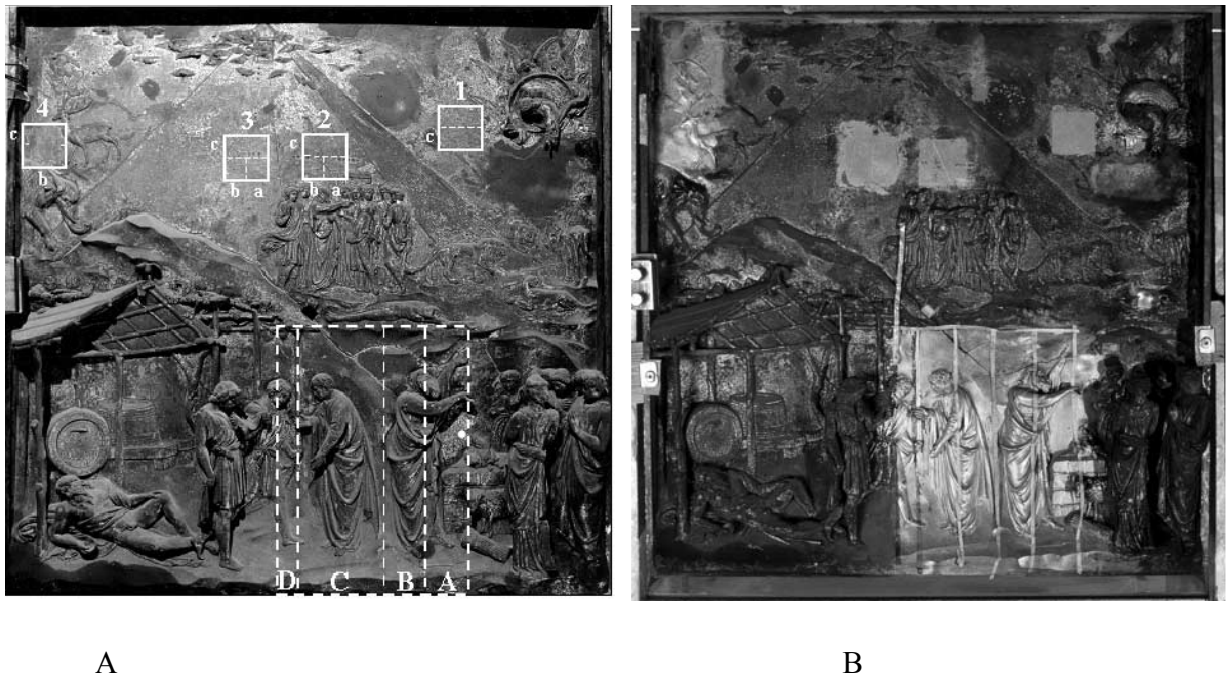


Fig. 55. Storie di Noè (Porta del paradiso) ; A-before restoration; B-after partial cleaning [58]

Thus, application of the two techniques provides better cleaning results and larger safety ranges when compared with the stand-alone treatments.



Fig. 56. Storie di Noè (*Porta del paradiso*) after cleaning [59]

This investigation allowed the definition of an integrated cleaning procedure that can be used to complete the cleaning intervention of the *Porta del Paradiso*.

Other results of restoration are given in Fig. 57.



a



b

Fig.57. a-A frieze of the *Porta del Paradiso* by Lorenzo Ghiberti during the laser cleaning intervention [30]; b- Lorenzo Ghiberti's self portrait on the Gate of Paradise, during laser cleaning [60]

### Laser cleaning of gilded putto

Many researchers studied a bronze metal gilded putto from the Wilanów Palace gardens façade decorations (Fig. 58), due to sculptor Disqenue from Rome and dated as from the end of the 17th century [61].



Fig. 58. Pair of gilded bronze putti from the Wilanów Palace garden façade: (a) putto with torch, above-microscopic photograph of damage to the putto's wing; (b) putto with laurel, left side: microscopic photographs of damage to the fruit and leaf [61].

Prior to analyses, sections of each object were removed, embedded in a Meliodent epoxy resin and polished. The elemental composition of the encrustations was tested using a SEM



Identification of several corrosion compounds by Raman spectroscopy revealed the green copper salt to be antlerite, which can be found below and above the metallic layers. Cuprite has been identified as the red compound, and the grey salts there are probably silver compounds (silver sulfates). Silver compounds were not identified in Raman spectra, but ions of Sand Ag have been found during microchemical analysis. For laser cleaning a Nd:YAG laser operating at the fourth harmonic 266 nm, 11.2 mJ and 4 ns was used.

Halina Garbacz and coworkers [49](Garbacz et al., 2010) tested the laser cleaning process for putto with torch. The base metal of the putto figure with a torch is a copper-zinc alloy, with 11 – 20 % of zinc and a small quantity of added lead (0.2 – 1.4)%. The structure of the layers is presented in the polished cross section (Fig. 61a) and LIBS stratigraphic measurements (Fig. 61b).

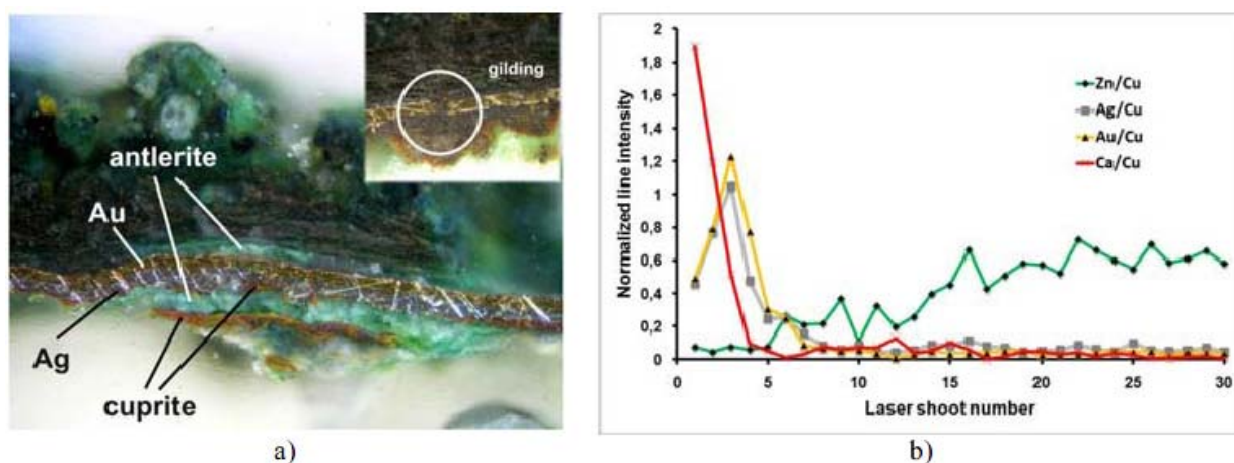


Fig. 61. Layered structure of the bronze putto surface: (a) cross-section; (b) LIBS stratigraphy of main elements, [49]

Raman spectrometric measurements also identified the existence of antlerite and cuprite. The grey compounds visible in the photo in the top right hand corner of Fig. 61a are silver compounds.

Laser cleaning tests of the copper sheets were conducted using long pulses ranging from 100  $\mu$ s – 1 ms that were obtained by the Nd:YAG laser in FR laser regime, and also using short nanosecond pulses generated in the QS laser regime at 1064 nm.

The evaluation of cleaning process was carried out also using SEM- EDS technique. In all locations laser cleaning revealed gilding or the putto surface. Parts of areas revealed a smooth surface of the gilding composed of gold with up to fifteen percent of silver and copper.

Because in the case of a delicate gilding typical nanosecond pulses (6 – 17 ns) generated in the QS regime of the Nd:YAG laser could cause local damage and surface melting (Fig.62) to the gold layer even if the minimal energy density of the laser, the authors propose enlarging the domain of pulsewidth to 100 – 1000 ns.

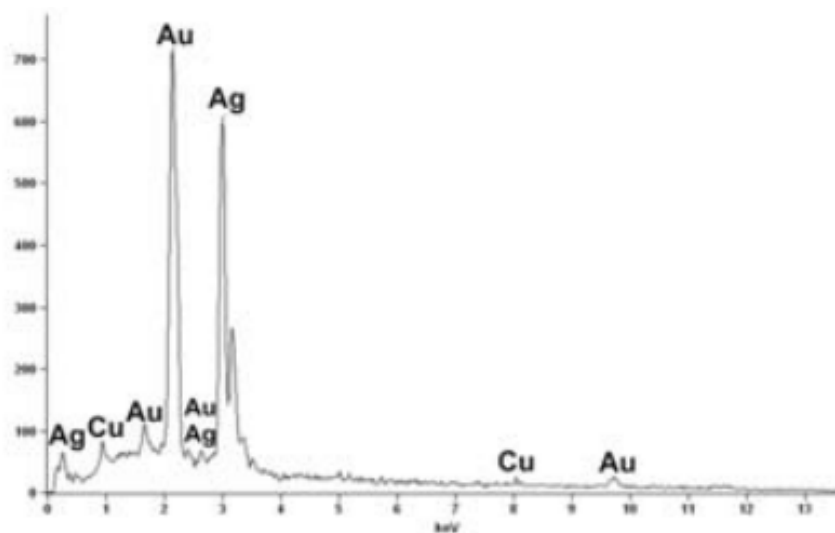


Fig. 62. Composition of melted fragment [49]

This gilded artifact was studied also by Andrzej Koss and Jan Marczak [62]. Raman Spectra of the corrosion layers for putto with laurel are presented in Fig. 63. Raman spectra of the corrosion layers also have been identified as antlerite and cuprite.

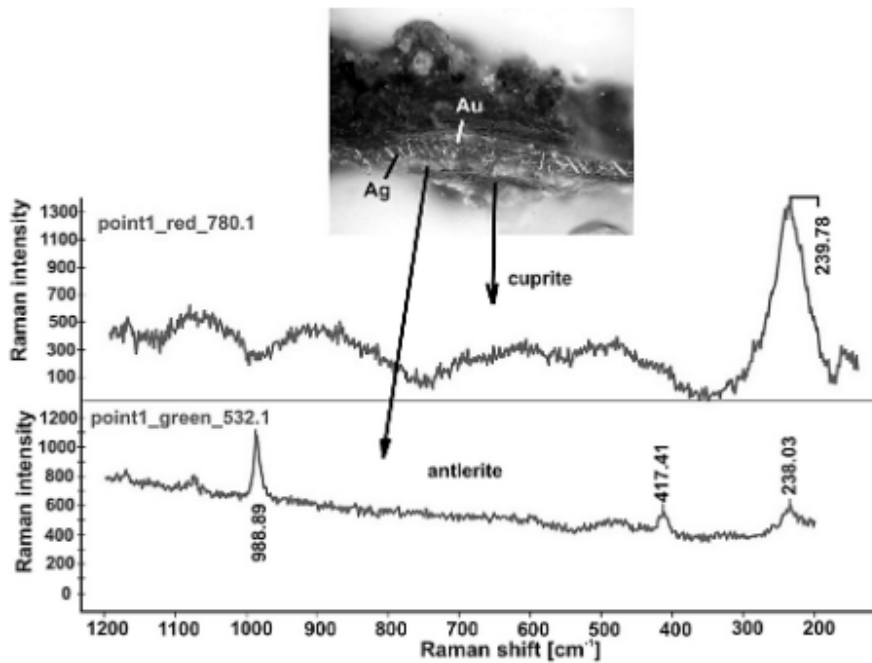


Fig. 63. Raman spectra of corrosion layers near the putto gilding. Small photograph shows the section of gilding. Identified metals and compounds are indicated by lines and arrows [62].

Grey salts, which were not identified in Raman spectra, as indicated by supplementary SEM-EDS analysis (right side of the Fig. 64), are cerargyrite ( $\text{AgCl}$ ).

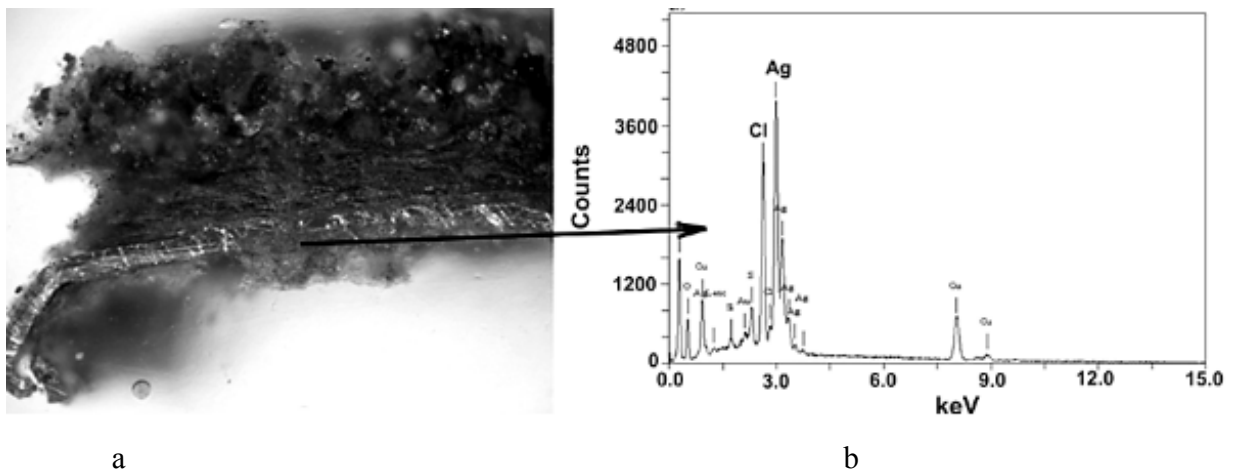


Fig. 64. a) Section of putto gilding damage with developed area of grey corrosion near Ag layer; b) SEM - EDS spectrum of corrosion in the point indicated by black arrow and identified as cerargyrite [62]

A comparative analysis of chemical and laser cleaning for gilded bronze objects was reported by Lee and coworkers [63]. They studied four samples from gilt-bronze artifacts of the Proto–Three Kingdoms Period of Korea in the 4 b.C–5bC based on the amalgam technique of about 1–3 $\mu$ m thickness of gold layer (Fig. 65)

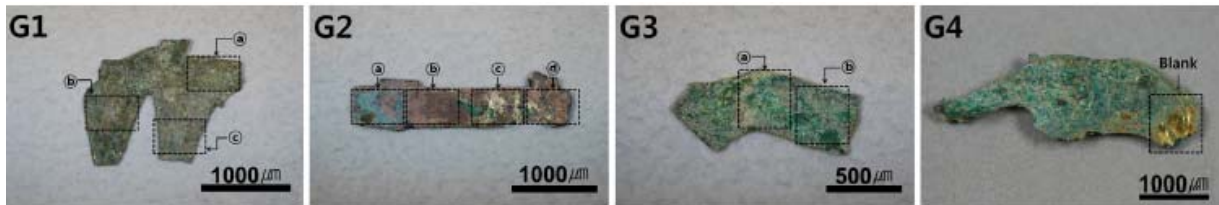


Fig. 65. Samples for laser cleaning (G1, G2), chemical cleaning (G3), blank (G4), [63]

Laser used for this experiment was a QS Nd:YAG laser with an energy output of 160–800 mJ with 1064 nm wavelength and 10 ns of pulse length. As for chemical method, 5% formic acid (in distilled water) was absorbed into super absorbent polymer and then it was placed on top of gilt-bronze sample until the corrosion product was removed.

In the laser conditions of 3–5 pulses having a fluence of 1.59–2.39 J/cm<sup>2</sup> using 1064 nm laser wavelength, the copper corrosion products were removed successfully, and exposed the gold layer. However, the gilt layer was damaged. In the case of chemical cleaning, the copper corrosion products were not removed uniformly and due to acid solvents, the substrate metal was softened and the gilt layer was separated. Analyzing the surface of gilt-bronze specimens with SEM-EDS after cleaning, melting was observed due to high temperatures of laser irradiation and when chemical solvent was used, organic solvents remained on the surface. Although copper corrosion products were removed by laser cleaning, brown residue remained in some samples (Fig. 66)

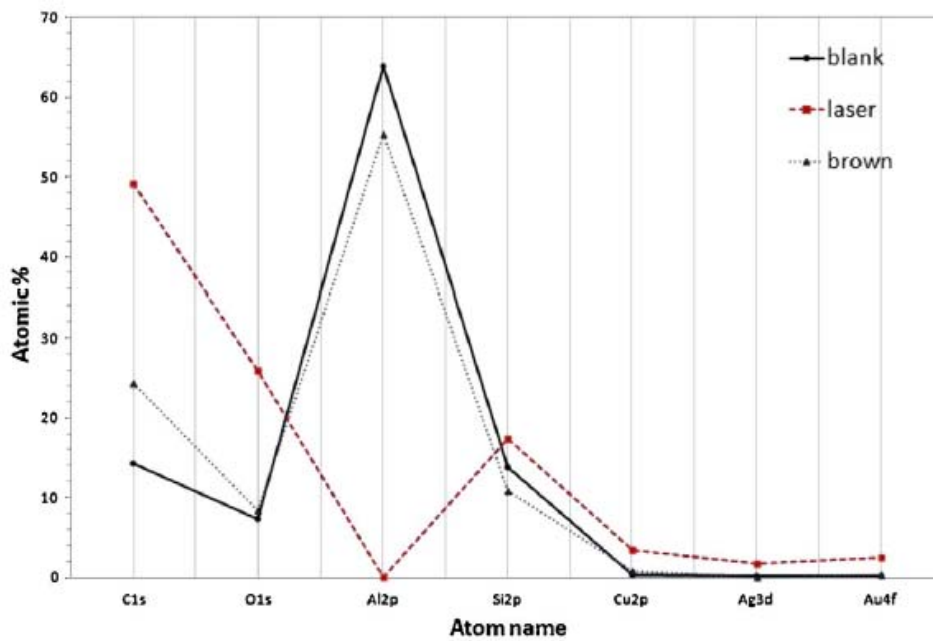


Fig. 66. Comparing the atomic content (%) of the blank surface, the clean surface, and the brown residues after laser irradiation [63]

A special gilded bronze object laser cleaned was a 12th century gilded copper cross with a wooden core found in the church of San Miguel, San Esteban de Gormaz, Spain [64] (Fig. 67).

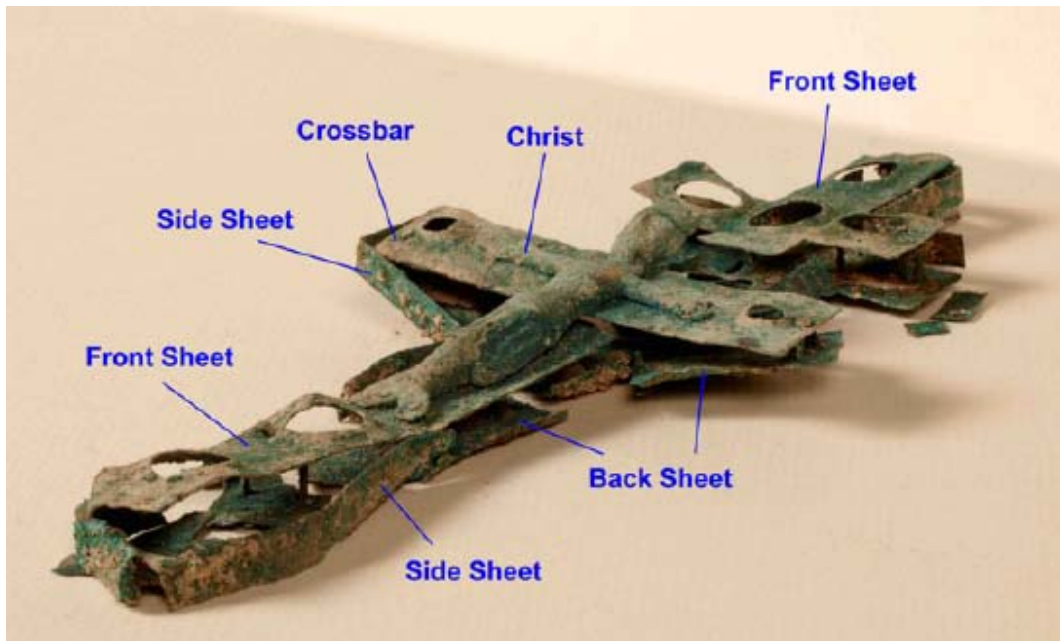


Fig. 67. The San Esteban de Gormaz cross with all its component metallic parts[64].

Ion Beam Analysis (IBA) and PIXE (Particle-induced X-ray emission) indicated that the metal sheets are made of copper, always associated with small quantities of As and that the three nails examined are made of bronze; the gold content is higher on the Christ figure. This is the most important part of the object, deserving therefore to be the richest one; it was certainly made and gilded separately from the copper sheets.

Finally, laser ablation sampling coupled to inductively coupled plasma–mass spectrometry (LA–ICP–MS) has a strong analytical performance in trace element determination [65] in cultural heritage (Fig. 68).

Cultural heritage represents a bridge between the contemporary society and the past populations, and a strong collaboration between archaeologists, art historians and analysts may lead to the decryption of the information hidden in an ancient object. Quantitative elemental compositional data play a key role in solving questions concerning dating, provenance, technology, use and the relationship of ancient cultures with the environment. The scientific investigation of an artifact should be carried out complying with some important constraints: above all the analyses should be as little destructive as possible and performed directly on the object to preserve its integrity.

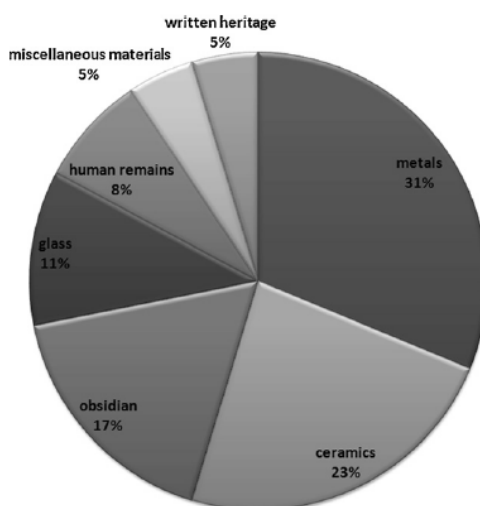


Fig. 68. Relative percentage of the materials investigated by LA–ICP–MS in cultural heritage published on international journals by the end of August 2008 [65]

## **2. Materials and methods**

### **2.1. Accelerated corrosion test**

The efficiency of the organosilane coating in the protection of gilded bronzes was evaluated on the basis of accelerated ageing tests.

In the current work, a dropping test that mimics the action of acid rain on unsheltered areas of outdoor monuments was employed. The ageing method was described in detail in previous work [66] and a short description is reported in section 2.3. The ageing period for the samples in the current work was a TOW(time of wetness) of 30 days.

The dropping test was used in order to obtain samples with comparable morphology and composition to gilded bronzes exposed in outdoor conditions. These were then used as the substrate on which the organosilane coatings were applied.

### **2.2. Tested material: quaternary gilded bronze and organosilane coating (PropS-SH +nanoparticles)**

The composition of the bronze, cast in stone moulds and then fire-gilded, is similar to those of Renaissance artefacts (Cu: 91.9/Zn: 2.9/Sn: 2.4/Pb: 1.0/Sb: 0.8 wt%). The bronze specimens showed a dendritic microstructure of cored alpha solid solution, typical of as cast bronzes, with Sn-rich precipitates in the interdendritic spaces. Lead globules were present in the interdendritic spaces and residual porosity/shrinkage cavities were uniformly distributed in the samples.

Fire-gilding was carried out after acid pickling of the cast bronze surface, according to the recipe by Cellini in his treatises on goldsmithing and sculpture (1568). The pickled surface was covered with Au-Hg (1:8) amalgam paste and then heated by a free flame so as to vaporize Hg. Subsequently, the gilded surface was burnished by an agate tool, in order to densify the porous layer and produce a smooth and shiny surface. Fire-gilding was carried out by the artisan goldsmith Dott. A. Pacini in Montepulciano (SI).

The organosilane coating that was used in this study is 3-mercapto-propyl-trimethoxy-silane that is referred in this current work by its acronym PropS-SH. Figure 1 on the next page displays the structural formula of the compound.

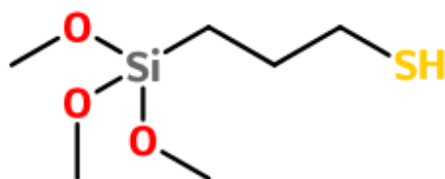


Fig. 1. Structural formula of 3-mercaptopropyl-trimethoxy-silane(PropS-SH)

The PropS-SH was applied on the substrate by dip-coating as was performed at the University of Ferrara, Corrosion and Metallurgy Centre “A.Daccò”. Details on the application method are described in section 2.5.

Before accelerated ageing tests, the surface of the bronze specimens was washed with deionized water and degreased with acetone.

In the current work, in order to assess the efficiency of the PropS-SH coating different types of samples were investigated. Table 1 lists the types of investigated samples and the acronyms by which they are referred in this work.

Acronym	Sample condition
G	Gilded
GP	Gilded and coated with PropS-SH
GD	Gilded and aged
GDP	Gilded, aged and coated with PropS-SH
GDPC	Gilded, aged and coated with PropS-SH with CeO <sub>2</sub> nanoparticles

Tab 1. Summary of samples exposed to dropping tests (for an ageing period of 30 days)

### 2.3. Weathering method: dropping test

The samples underwent cycles of exposure to artificial acid rain solution in order to simulate outdoor corrosion. The cycles consist of periods when the artificial acid rain solution is dripped onto the samples and periods when the samples are allowed to dry. The aim of this type of test is to expose the samples to conditions similar to severe runoff.

The dropping test was used to investigate the behavior of the propS-SH coating when applied on two kinds of substrate: as-gilded and prepatinated. In the case of the as-gilded samples, the coating is applied on the as-gilded samples and afterwards these are subjected to the accelerated ageing conditions. In the case of prepatinated samples, the uncoated as-gilded bronze coupons are subjected to an ageing cycle and only afterwards are coated with PropS-SH and the aged again.

Within the installation designed for the ageing test the samples are placed at a 45° angle on plastic supports. A peristaltic pump drips artificial acid rain solution (described in section 2.5.) on the samples by means of capillary tubes. The runoff solution is collected in canisters in order to determine the volume. Small amounts of the solution are stored in lab bottles in order to be analyzed. The solution is acidified with HNO<sub>3</sub> 65% suprapur in order to prevent absorption of metals on the interior of the bottles and dissolve any metal complexes present.



Fig. 2. Dropping test setup



Fig. 3. Samples mounted on support

The Cu and Pb content in the runoff solution was analyzed through Atomic Absorption Spectrometer Perkin Elmer PinAAcle 900Z, provided with Transversely Heated and longitudinal Zeeman background correction.

## 2.4. Artificial acid rain solution

Based on natural rain collected during the winter months at Bologna weather station, an artificial acid rain solution was prepared. The solution contains the ions detected in natural rain and was prepared using analytical grade reagents and bidistilled water. The composition of the acid rain solution is presented in table 2.

Conductivity (20°C)	37.92 ± 0,09 μS/cm
pH	4.27 ± 0,01
Cl <sup>-</sup>	1.24 ± 0,04 mg/L
NO <sub>3</sub> <sup>-</sup>	1.02 ± 0,02 mg/L
SO <sub>4</sub> <sup>2-</sup>	1.94 ± 0,02 mg/L
CH <sub>3</sub> COO <sup>-</sup>	0.23 ± 0,02 mg/L
HCOO <sup>-</sup>	0.04 ± 0,02 mg/L
NH <sub>4</sub> <sup>-</sup>	0.86 ± 0,03 mg/L

Tab 2. Properties and constituents of artificial acid rain solution

## 2.5. Application of coating on pre-patinated samples

As mentioned before the samples were protected with the PropS-SH coating at the University of Ferrara, in the Centro di Corrosione “A. Daccò”.

The application of the organosilane coating involves the following steps:

- Preparation of a solution containing 90% ethanol, 5% water and 5%PropS-SH
- hydrolysis of the solution over the course of 1 month
- immersion of the samples into the hydrolyzed solution for a period of 1 hour
- removal of the samples from the solution
- curing at room temperature for 10 days

As mentioned before in section (1.2 – gilded bronze corrosion) the main reaction involved in fixing the coating on the metal surface is the elimination of a H<sub>2</sub>O molecule between Me-OH on the bronze surface and the Si-OH in the solution. Another important reaction also

occurs through the formation of copper-thiolate bonds between the copper on the surface of the sample and the SH groups of the PropS-SH.

In regards to the PropS-SH coatings with added nanoparticles, they were obtained by dispersion of 250 ppm of CeO<sub>2</sub> nanoparticles with a nominal size lower than 25nm. The CeO<sub>2</sub> nanoparticles provide nucleation centers for the reticulation of the coating and also act as Ce<sup>2+</sup> cation releasers [67].

### **3. Accelerated ageing in runoff conditions for corrosion investigations of fire gilded bronzes and assessment of the protective efficiency of PropS-SH**

In this chapter, the results of accelerated ageing tests, carried out on fire-gilded bronzes (with/without a protective organosilane coating based on PropS-SH) in runoff conditions, will be reported. The aim of the work is both to (i) investigate corrosion of fire-gilded bronze in accelerated ageing conditions, and (ii) to assess the protectiveness of PropS-SH towards fire-gilded bronzes.

To the second aim, both the direct application of the organosilane coating on the as-gilded bronze (as reported in section 1 and 2) and the application of the silane coating on a corroded, fire-gilded substrate (section 3) was considered. The latter option, in fact, is more representative of real conservation interventions, where cleaning procedures remove the disfiguring accretions of corrosion products from the gilded surface but do not remove the corrosion products at the gold/bronze interface. In order to produce a representative, corroded gilded bronze substrate, the accelerated ageing method described in section 2.3 was used. Therefore, accelerated ageing in runoff conditions was used here both for “pre-patination” of the gilded bronze and for assessing the protective efficiency of PropS-SH.

#### **3.1 Samples before corrosion testing**

##### **3.1.1 As gilded bronzes**

The as-supplied gilded samples (before exposure tests) show two main surface morphologies (Fig. 1a): smooth areas (where the burnishing procedure successfully compacted the gilded layer after Hg evaporation) and porous areas (where the depth of the grooves on the bronze surface, due to mechanical polishing, was too high to allow full densification of the gilded layer by burnishing). The correlation between surface morphology and compactness of the gilded layer was confirmed by FIB cross section observations in a previous work [68], as shown in Figure 1b,c.

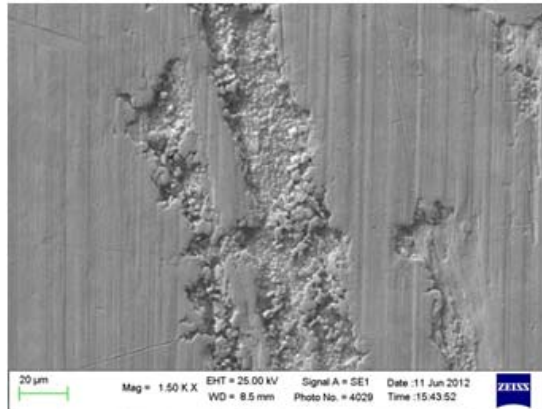


Fig. 1a. BSE image of the surface of as-supplied gilded sample showing the smooth areas on the sides and the porous area in the center [68]

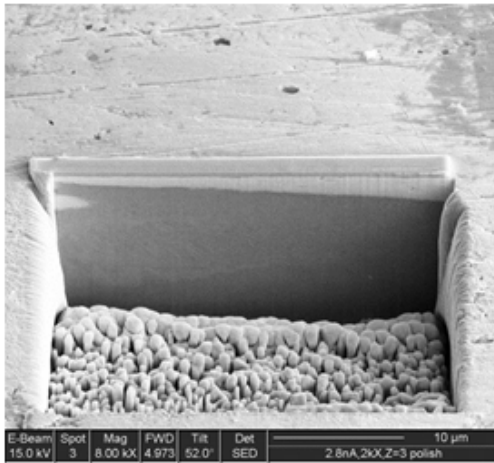


Fig. 1b. BSE image of FIB excavation of smooth area of as-supplied gilded sample [68]

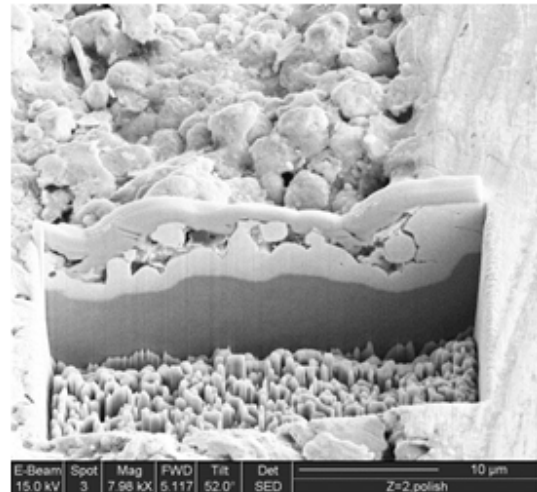
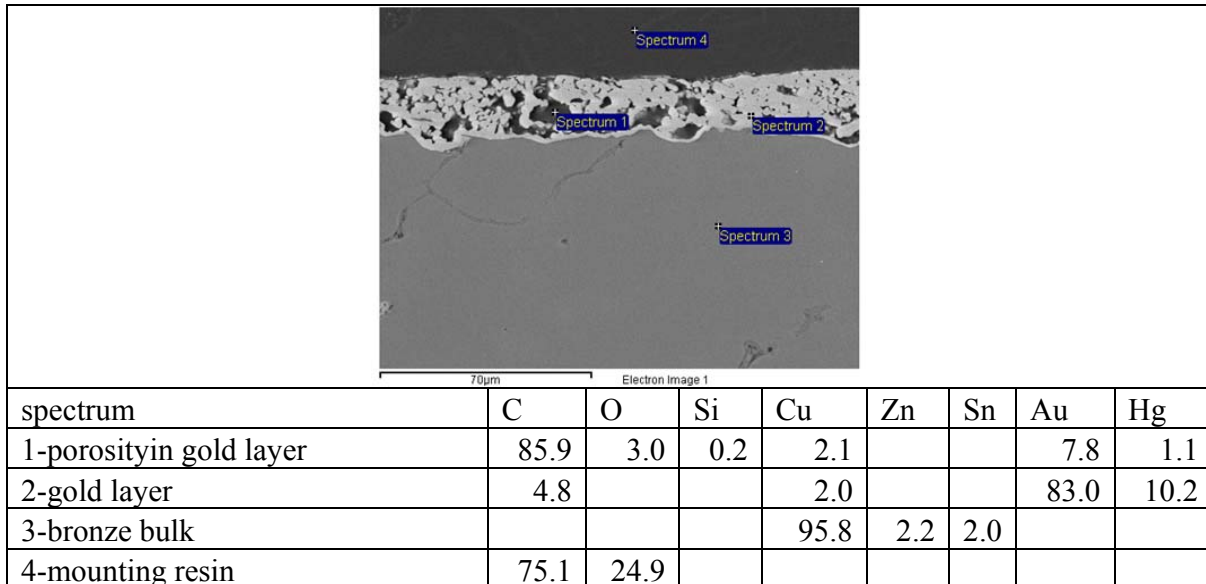


Fig. 1c. BSE image of FIB excavation of porous area of as-supplied gilded sample [68]

This morphological feature has a key role in influencing the corrosion behavior of the gilded bronze, because the presence of pores and cavities in the areas where the gilded layer is less compact (even though with a higher thickness), may stimulate the corrosion of the bronze substrate, due to the gold/bronze galvanic coupling[2-3].

### 3.1.2. As-gilded bronze coated with PropS-SH

The gilded bronze samples that were coated with PropS-SH, as described in section 2.5, were investigated using SEM and FIB. These studies were useful in getting a better understanding of how the coating is distributed on the surface of the gilded bronze samples.



Tab. 1. Elemental composition (measured by EDS, wt%) of different regions from a cross section of a PropS-SH coated gilded bronze sample (GP)

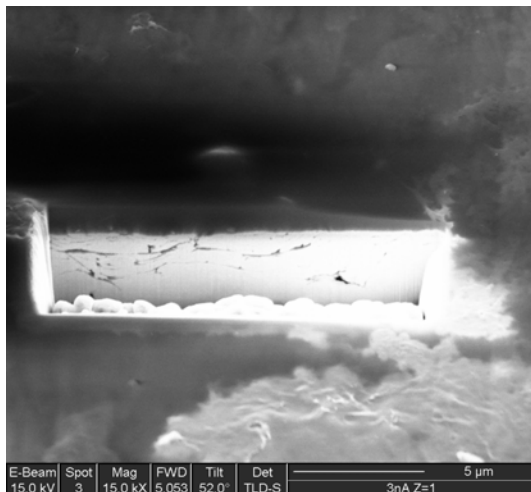


Fig. 2. BSE image of FIB excavation of PropS-SH coated gilded bronze sample (the PropS-SH coating (dark grey layer on top of the bright gold layer) is about 1.6 µm thick in the thickest area.

Based on the data in tables 1,2 and figure 2-3, we can state that the coating has a tendency to accumulate in the grooves and porosities of the gold layer. The coating is quite

uneven on the surface of the gold layer, its thickness ranging from 0 to 2  $\mu\text{m}$  in smooth areas of the surface, while in grooves it can reach 4  $\mu\text{m}$ .

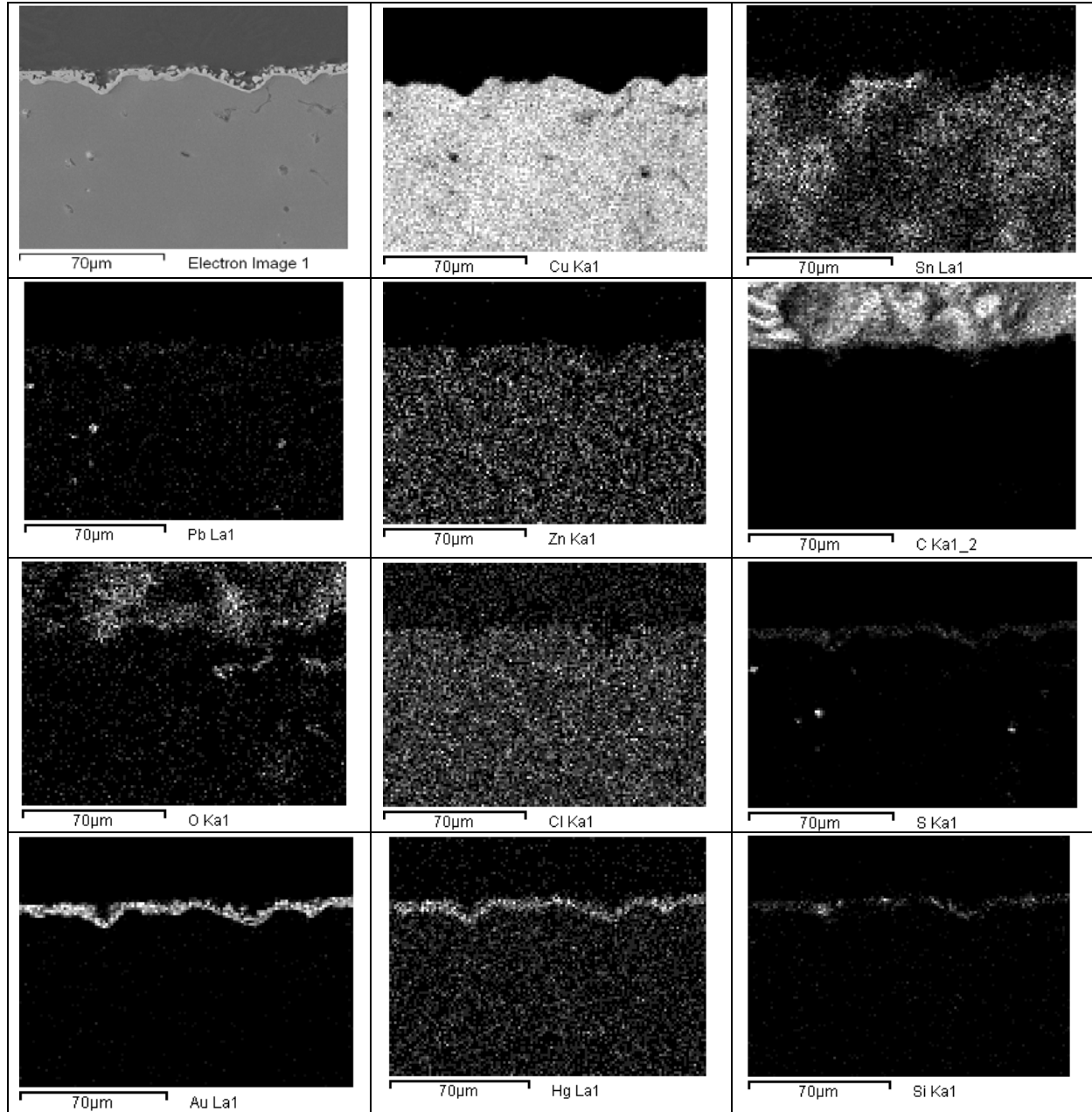


Fig. 3. BSE image and X-Ray maps of PropS-SH coated gilded bronze (cross-section)

### 3.2. Samples (as-gilded) after corrosion testing

In the first ageing cycle, the so-called “pre-patination cycle”, two as-gilded bronze samples and one gilded bronze sample that was coated with PropS-SH were used. In regards to the coated sample, it was used to determine the efficiency of the PropS-SH on as-gilded bronzes. Concerning the as-gilded samples, one was used as a reference while the other became the substrate for applying the PropS-SH in the second ageing cycle (section 3.3).

The as-gilded samples were aged for 30 days as described in section 2.3. Macro images and size measurements of these samples are available in table 2.

Sample type	G – gilded bronze coupon	G – gilded bronze coupon	GP – Gilded bronze coupon coated with PropS-SH
Image			
Length(mm)	38.11	48.00	37.70
Width(mm)	13.60	14.50	13.44
Height(mm)	6.33	6.83	7.13

Tab 2. The images and measurements corresponding to the samples that were aged.

### 3.2.1. Assessment of the ability of the accelerated ageing test to simulate real corrosion conditions

Upon completion of the pre-patination cycle, the uncoated gilded bronze samples were cut and mounted in resin, in order to be investigated using SEM in cross-section. The cross-sections of samples obtained by accelerated ageing were compared to the cross-sections of real gilded bronze artefacts. SEM observations showed that the accelerated ageing process succeeded in forming a corrosion layer comparable to the one observed on a fire-gilded bronze sample from the frame of the altar in the Chapel of Our Lady of the Fire, Dome of Forlì (by the sculptor G. Giardini, 1706), as can be seen from figure 4. A more detailed characterization of the sample from the Chapel of Our Lady of the Fire is reported in section 3.2.3.

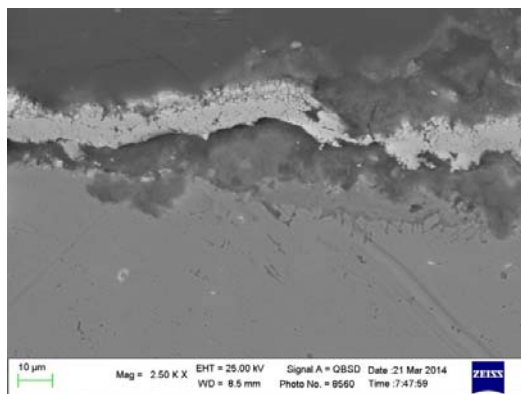


Fig. 4a. BSE image of sample cross section from Altar, Our Lady of the Fire, Dome of Forlì, Italy (by Giovanni Giardini, 1706)

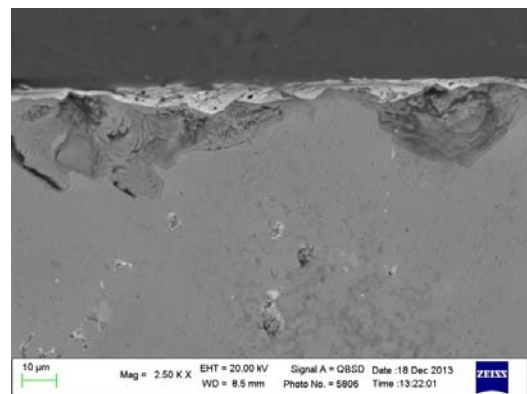


Fig. 4b. BSE image of cross section of artificially aged gilded bronze sample

### 3.2.2. Evaluation of the influence of exposure time on corrosion morphologies

In a previous work [1], the results of a short 10 day ageing cycle were reported. A comparison between the corrosion sites present in the two types of samples showed a more advanced corrosion process for the 30 day ageing cycle, as can be seen from figure 5.

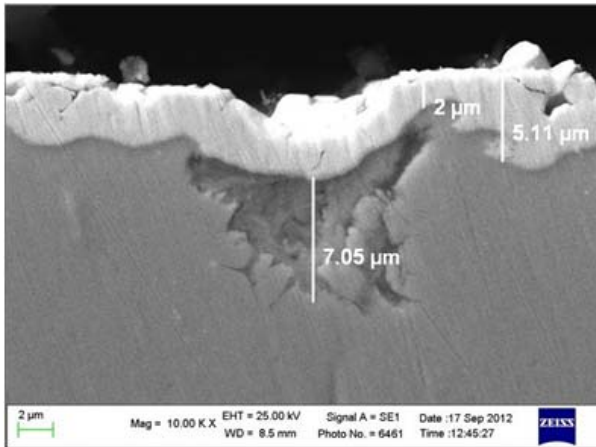


Fig. 5a. BSE image of cross section of 10 day aged gilded bronze sample[68]

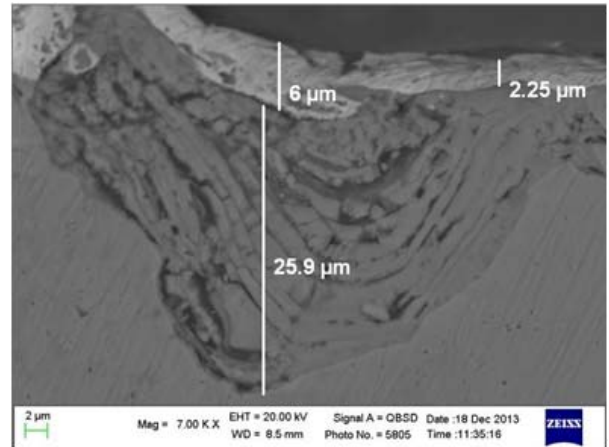


Fig. 5b. BSE image of cross section of 30 day aged gilded bronze sample

The 30 day ageing cycle was also able to reproduce the morphology present in the samples taken from the Porta del Paradiso (Baptistry of Florence, by L.Ghiberti, 1425-1452), as can be seen from figure 6. For these reasons, in the current study, the 30 day ageing cycle was used, in order to investigate corrosion processes of fire-gilded bronze and assess the protective effectiveness of the PropS-SH coating.

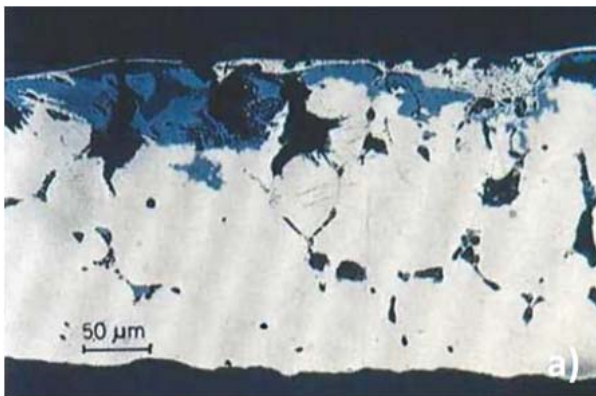


Fig. 6a. Fire gilded bronze from Ghiberti's Porta del Paradiso (cross-section) [30]

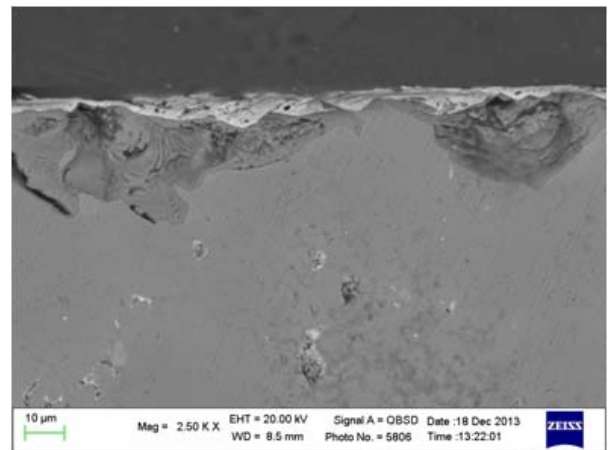


Fig. 6b. BSE image of cross section of 30 day aged gilded bronze sample

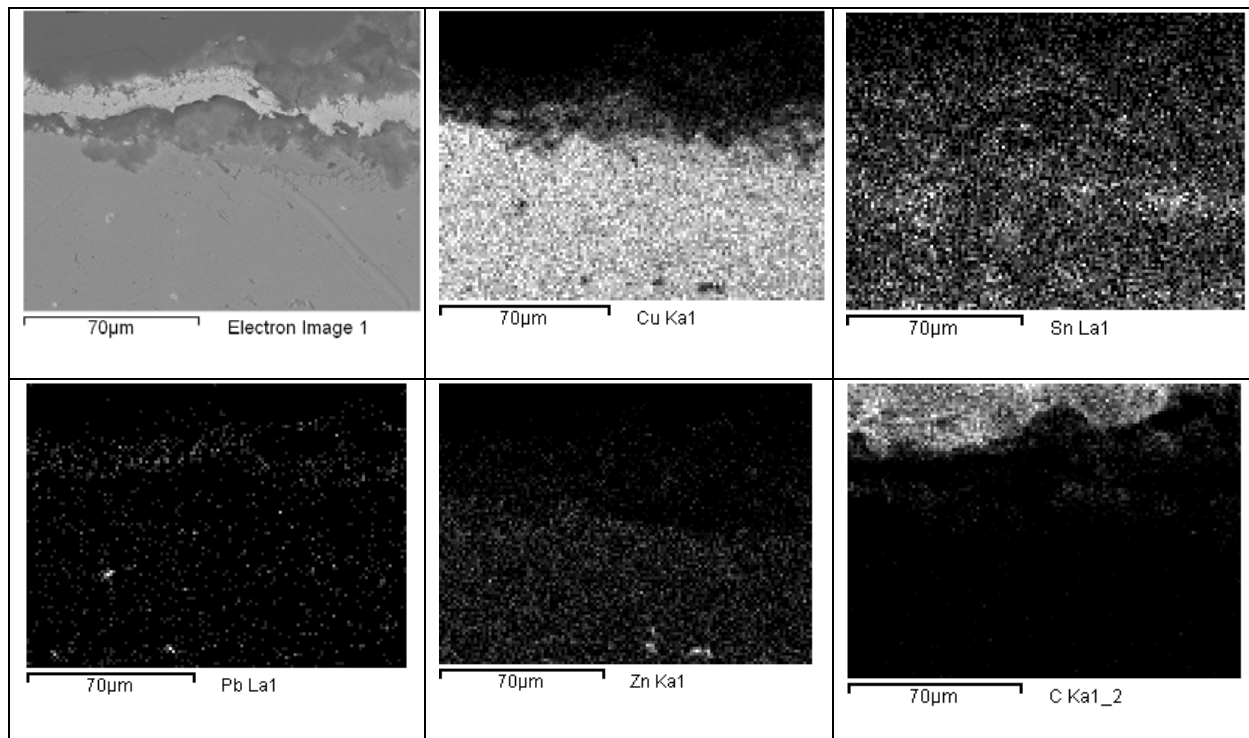
### 3.2.3. Case study (Our Lady of the Fire, 1707)

An important part of the current study was the comparison of our artificially aged samples with reference material from fire-gilded bronze heritage artifacts. This came in the form of samples from the altar of the chapel of Our Lady of the Fire in the Dome of Forlì, Italy. The gilded bronze samples were taken from the altar frames shown in figure 7.



Fig. 7. Area of the altarpiece from which the samples were collected

SEM-EDS analyses (X-ray maps of elemental distribution) of the cross section are reported in figure 8. The X-ray maps show the presence of a fire-gilded layer (gold and mercury are both present in the gold-rich layer, which is indicative of the fire gilding technique as discussed in section 1.1). Furthermore, a corrosion layer involving at least three sub-layers of different types of corrosion products, two beneath the gold layer and one above it, can be observed. The corrosion layer is also highlighted by the presence of oxygen and chloride ions.



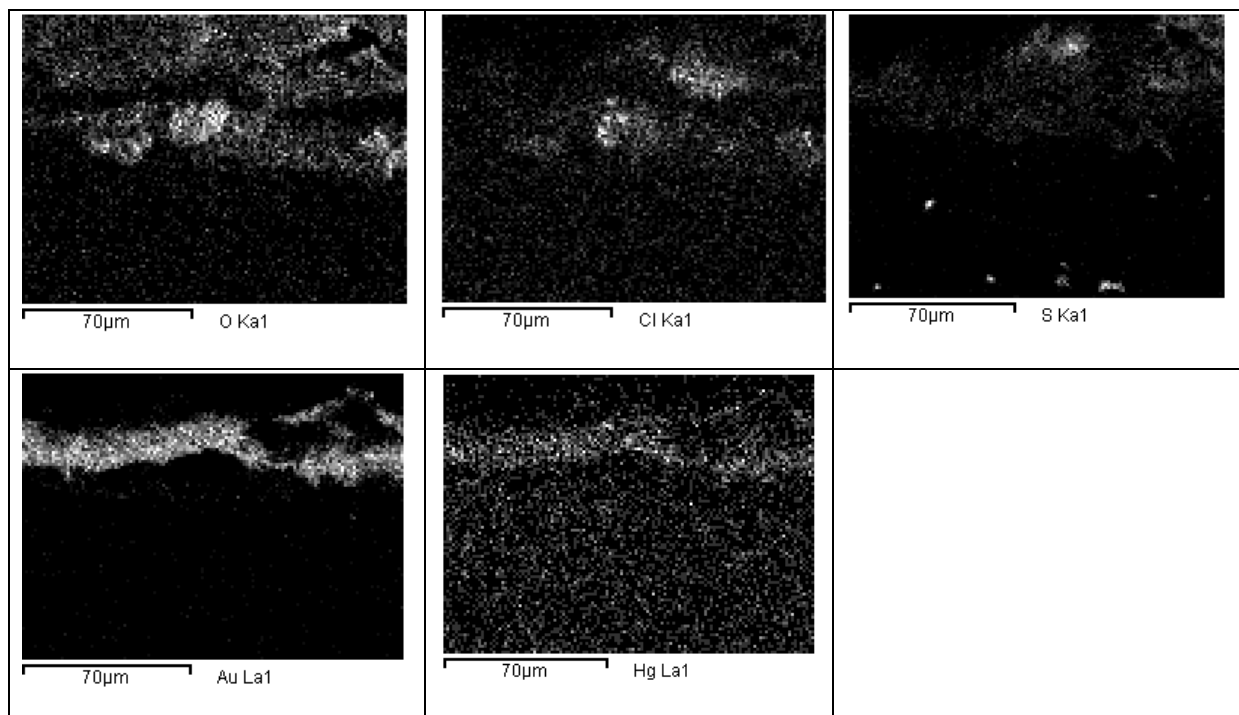
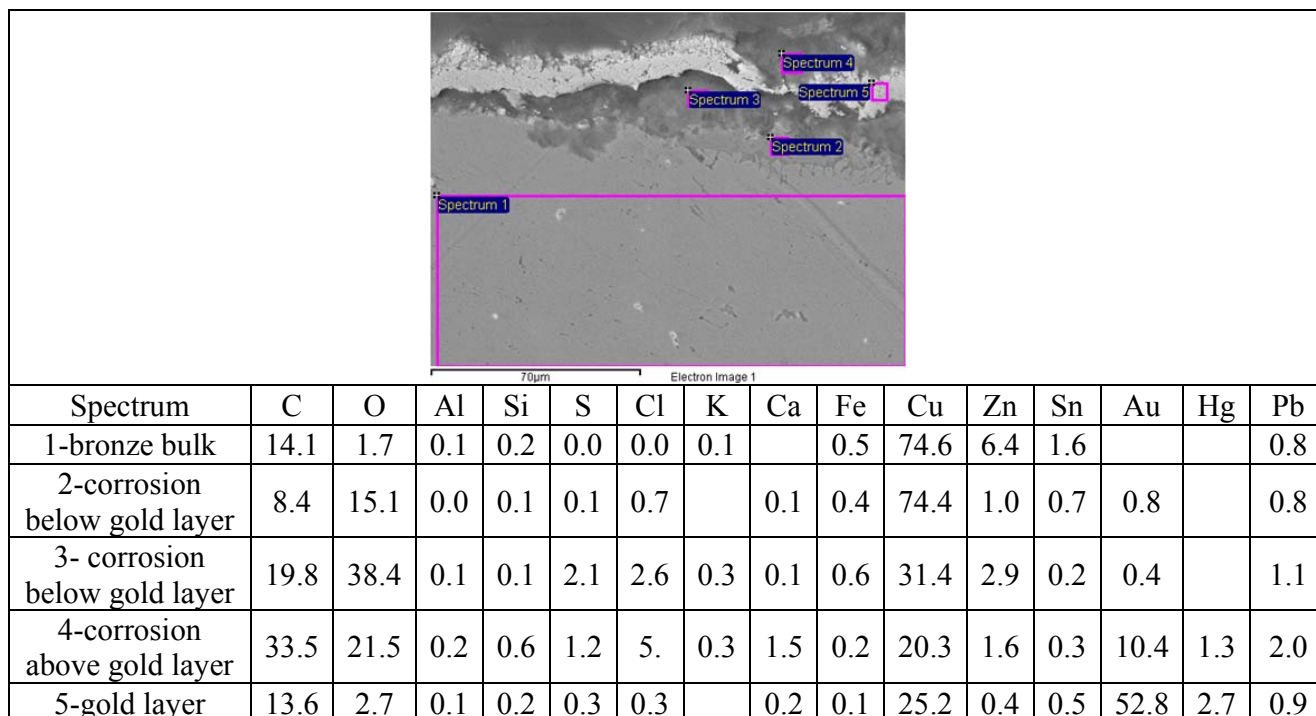


Fig. 8. BSE and X-Ray maps of a corrosion site in a sample from the Chapel of Our Lady of the Fire from Forli



Tab 3. Elemental composition (measured by EDS, wt%) of different regions in the sample from the Chapel of Our Lady of the Fire from Forli

The most external corrosion layer (above the gold layer) mostly contains C (due to the presence of the mounting resin), Ca and K (from environmental deposition) O, S and Cl (from atmospheric aggressive pollutants). The presence of elements related with corrosion phenomena tends to decrease on going from the external surface towards the bulk (bronze substrate). However, the X-ray maps in Fig. 8 clearly show the presence of Cl mostly at the corrosion/metal interface (which is typical of corrosion processes involving chlorides [21]) and a Sn-enriched area, again at the corrosion/metal interface: also this is a typical feature of bronze corrosion, due to decuprification (as discussed in section 1.2).

On the basis of the elemental composition data provided by table 12, different areas within the sample were selected and studied using  $\mu$ Raman spectroscopy in order to identify the various compounds within the corrosion layers.

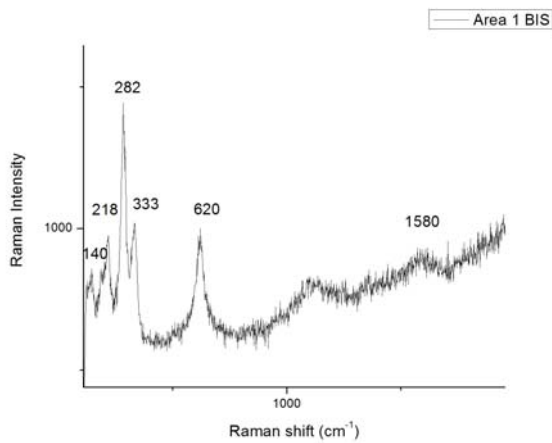


Fig. 9a.

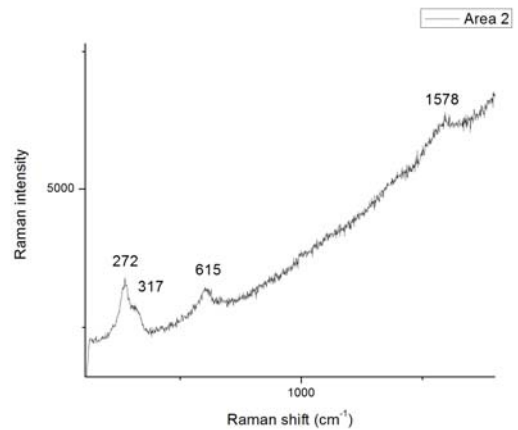


Fig. 9b.

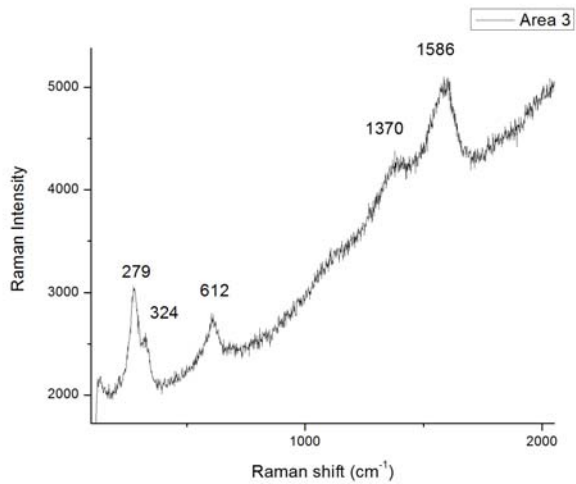


Fig. 9c.

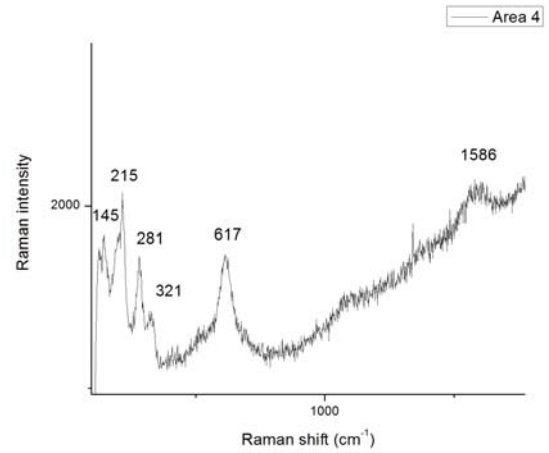


Fig. 9d.

Fig. 9 Raman spectra of the corrosion products recorded in cross-section (sample from the Chapel of Our Lady of the Fire)

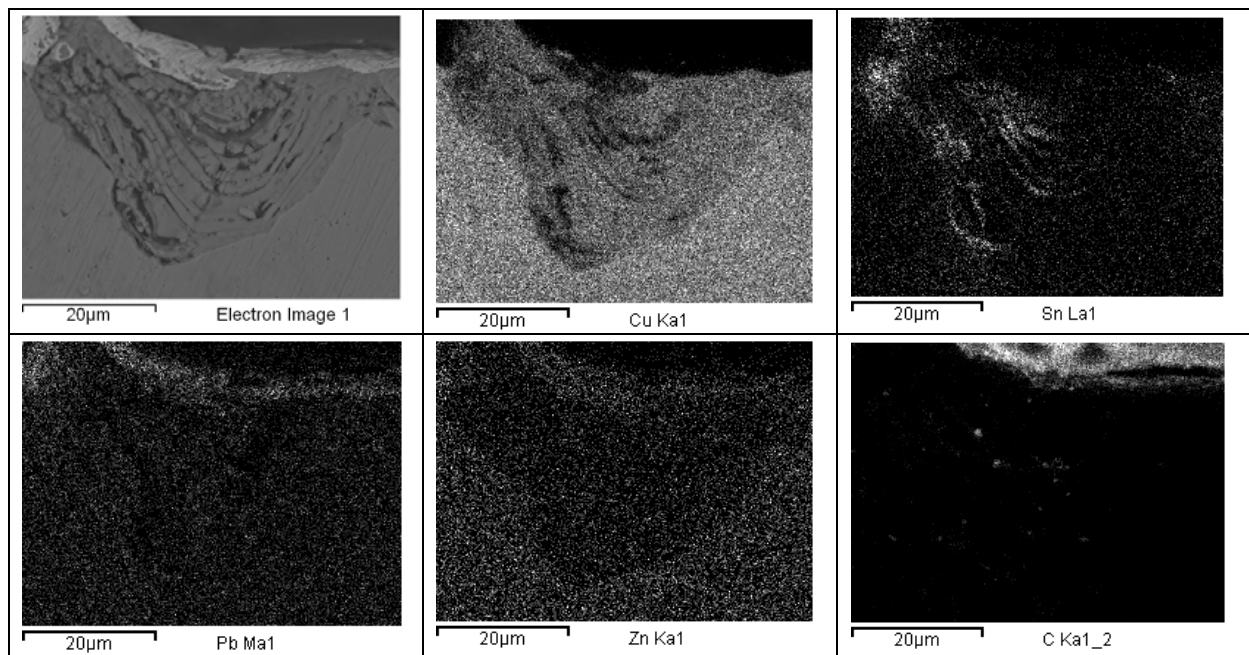
The  $\mu$ Raman analysis of the sample was able to identify bands characteristic of the following compounds: tenorite at 620, 330 and 270  $\text{cm}^{-1}$ , cuprite at 640, 150 and 220  $\text{cm}^{-1}$  and amorphous carbon probably due to environmental contamination at 1580  $\text{cm}^{-1}$  [69], [70], [71].

- Fig 9a: tenorite, cuprite and amorphous carbon
- Fig 9b: tenorite and amorphous carbon
- Fig 9c: tenorite, cuprite and amorphous carbon
- Fig 9d: tenorite and amorphous carbon

The presence of tenorite ( $\text{CuO}$ , a typical high temperature oxidation product of  $\text{Cu}$  [68]) is probably due to heating of the sample during the life of the artifact, because during Raman analyses care was taken to avoid thermal degradation by controlling the power of the laser source. The most frequently detected corrosion product is cuprite ( $\text{Cu}_2\text{O}$ ), whilst it was not possible to detect  $\text{Cu}$  sulphates or chlorides (notwithstanding the presence of  $\text{S}$  and  $\text{Cl}$  in the layers, as demonstrated by EDS analyses).

### 3.2.4 Uncoated samples

The SEM-EDS maps of the uncoated gilded bronze sample shown in figure 10 show the presence of corrosion products at the interface between the gold layer and the bronze substrate, as in the historical artifact. No products were observed above the gold layer due to exposure conditions (i.e. runoff). The artificially patinated bronze shows a lower amount of copper and zinc in the corrosion products than in the undamaged alloy, due to selective dissolution of these elements. As a consequence of decuprification, we can also observe the typical relative Sn enrichment, as discussed in section 12. Oxygen is present in a higher amount in the corrosion layer than in the bronze substrate, while lead is present in a higher amount in the gold layer (due to interdiffusion effects that will be the subject of further investigations).



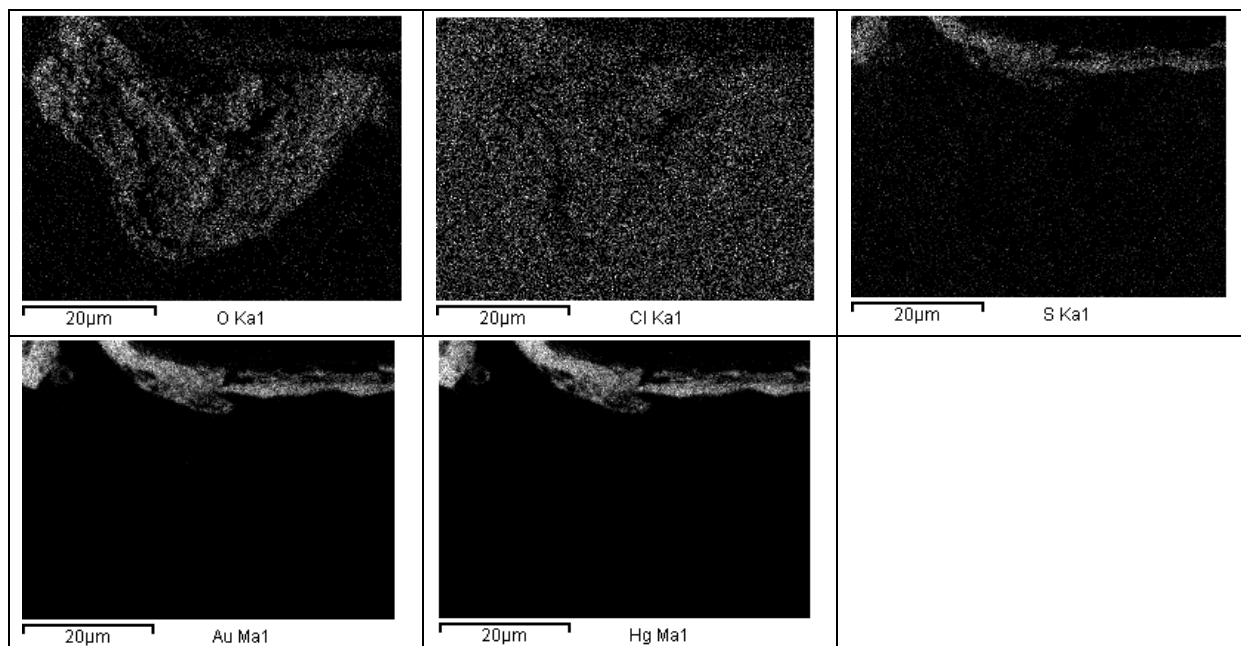
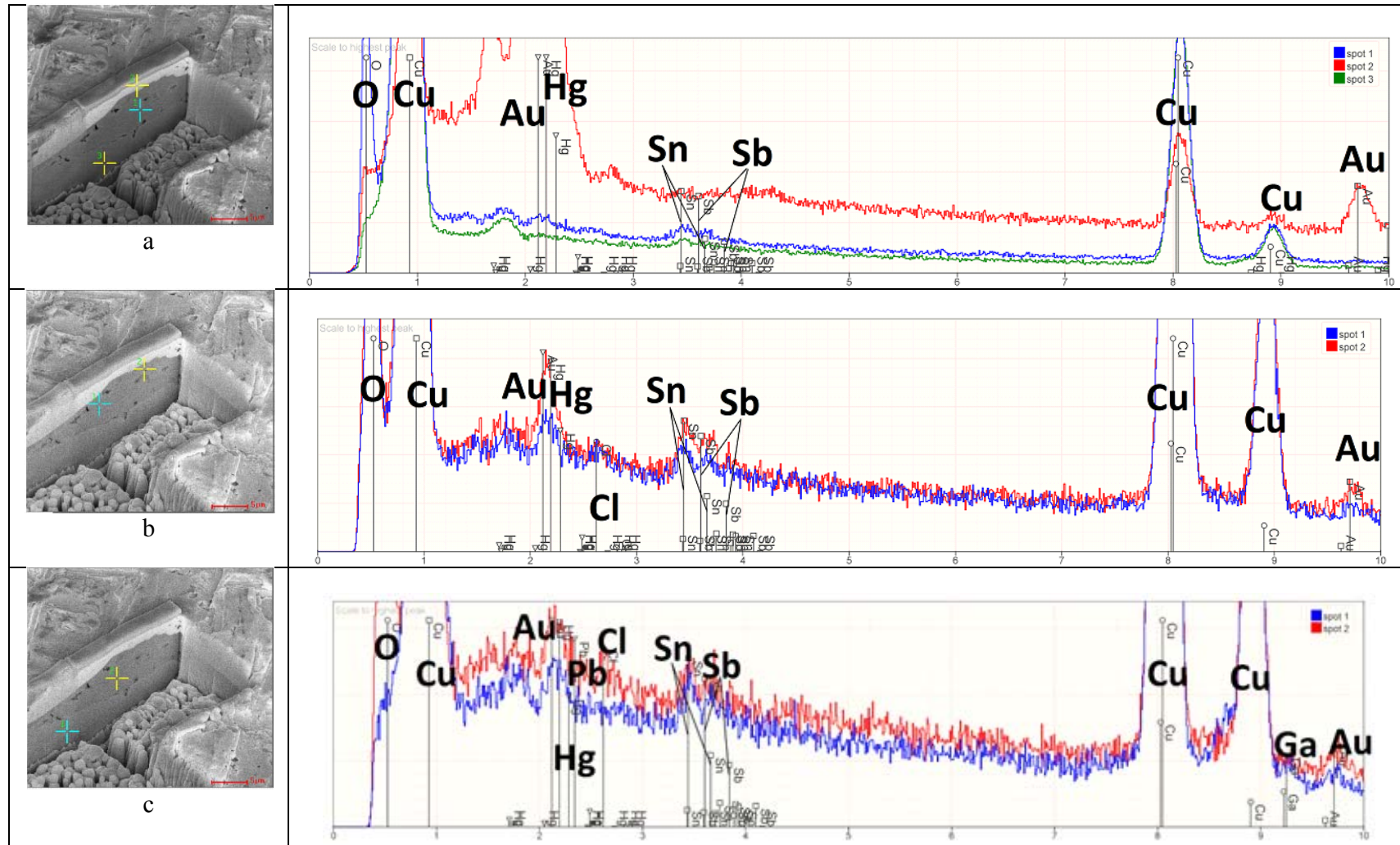
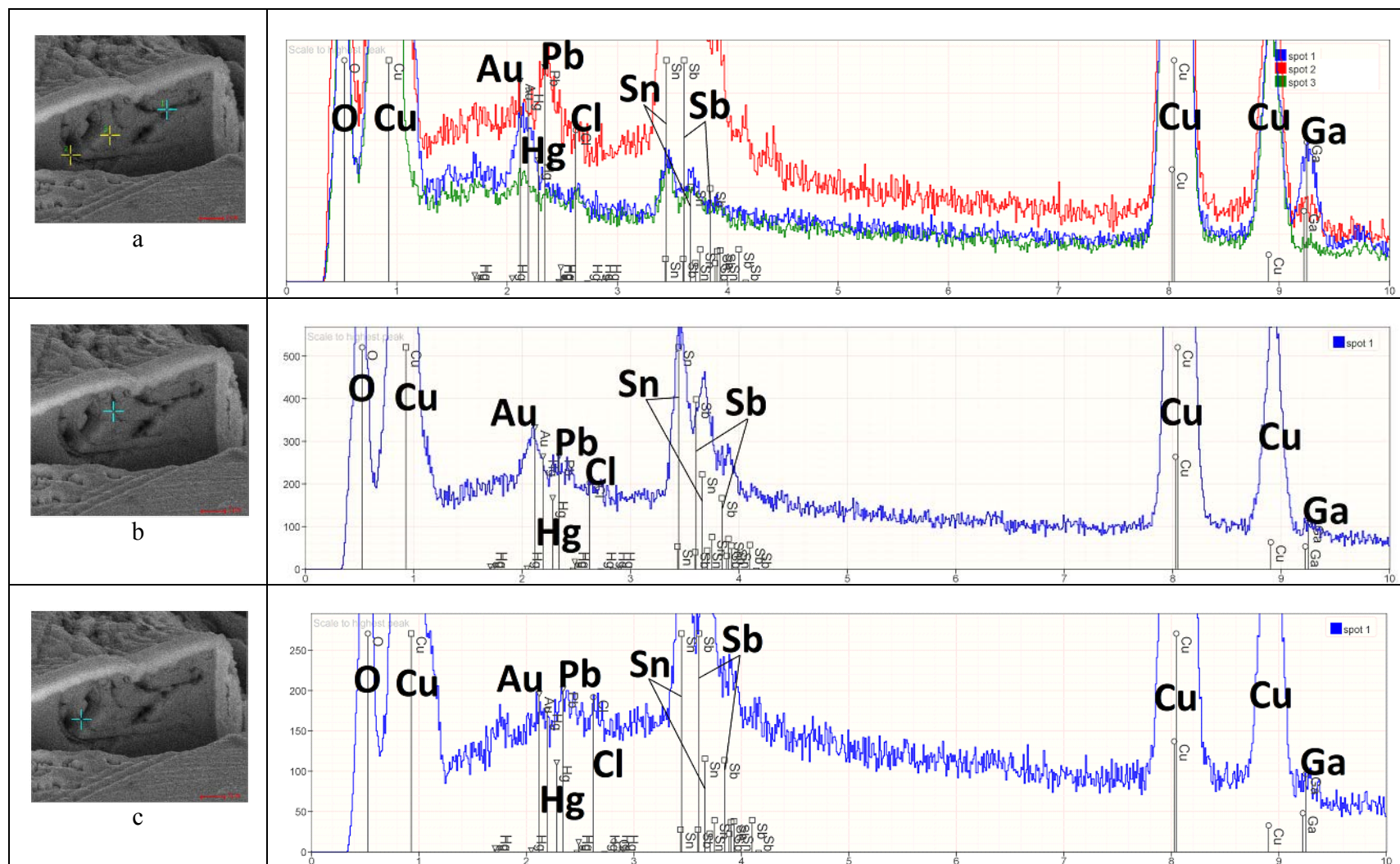


Fig. 10. BSE and X-Ray maps of a corrosion site in an uncoated gilded bronze sample, after accelerated ageing by dropping test (TOW=30 days).

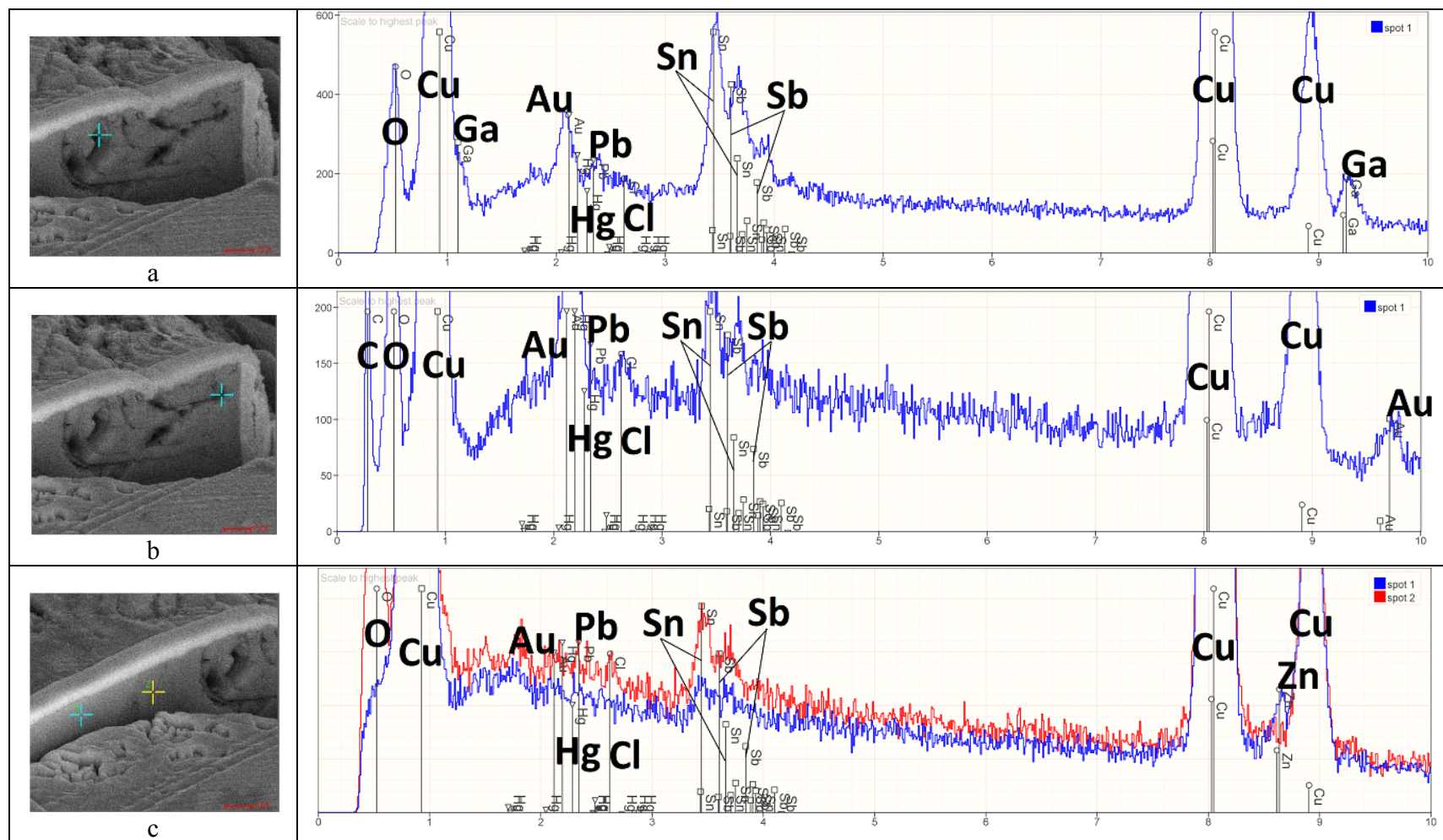
FIB studies were performed on the uncoated sample, allowing for a better understanding of the corrosion process at the level of the bronze-gold interface. EDS results of analyses carried out on cross-sections obtained by FIB milling on the uncoated gilded bronze sample, aged for 30 days of TOW are presented in tables 4-6.



Tab 4. EDS spectra of different regions in the excavations of the uncoated gilded bronze sample, after accelerated ageing by dropping test (TOW=30 days).



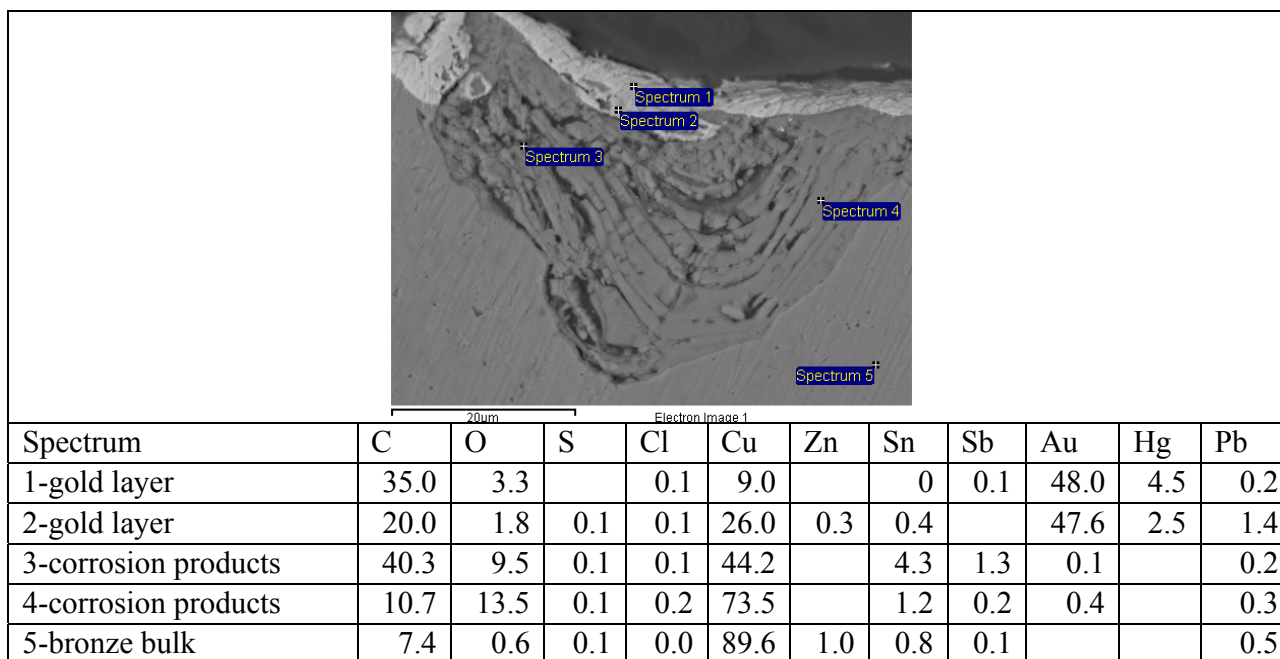
Tab 5. EDS spectra of different regions in the excavations of the uncoated gilded bronze sample, after accelerated ageing by dropping test (TOW=30 days).



Tab 6. EDS spectra of different regions in the excavations of the uncoated gilded bronze sample, after accelerated ageing by dropping test (TOW=30 days).

EDS data in Table 4a allow the comparison of the localized elemental composition in the gold layer (spot 2), in the corrosion layer at the interface between gold and bronze (spot 1) and in the bronze substrate (spot 3), showing the presence of high amounts of O in the corroded layer (as demonstrated also by data in Table 4b). The analysis of the corrosion layer (spot 2 in Table 4c) also detected the presence of Cl. The comparison of different areas within the corrosion layer (Table 5 and 6) showed the presence of residual Pb-rich areas around the holes due to preferential Pb dissolution (Pb being anodic to the Cu-rich matrix [21]), particularly in Table 5c. EDS data in Table 6c pointed out also another typical feature of bronze corrosion, that is frequently observed in bronze monuments [16] and that was observed also in the sample from the Dome of Forli (section 2.3): the formation of Sn-rich areas due to decuprification.

The similarities in the uncoated and historic sample continue at the level of the elemental composition presented in table 7. Again the bronze bulk presents a higher amount of copper and zinc, while in the corrosion the proportion of oxygen and tin increases.



Tab 7. Elemental composition (measured by EDS, wt%) of different regions in uncoated gilded bronze sample (G) after accelerated ageing by dropping test (TOW=30 days).

The  $\mu$ Raman analysis of this sample was heavily influenced by the presence of the mounting resin and by the fluorescence that it brings as it can be seen from figures 11a-c and 12.

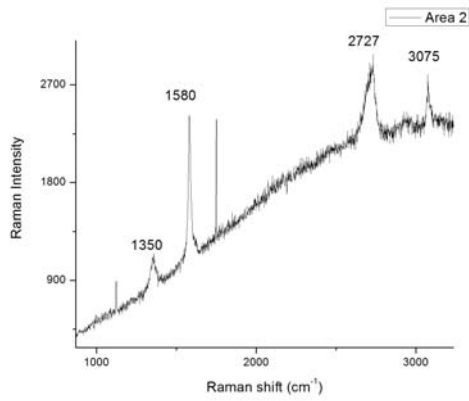


Fig. 11a.

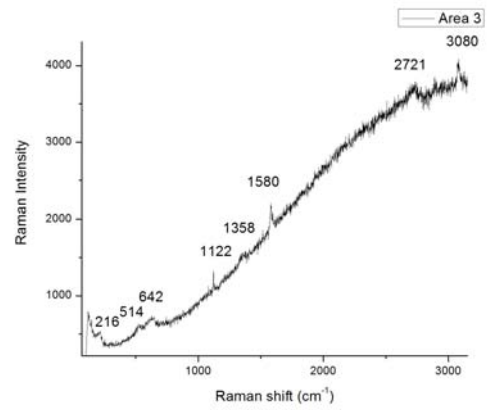


Fig. 11a.

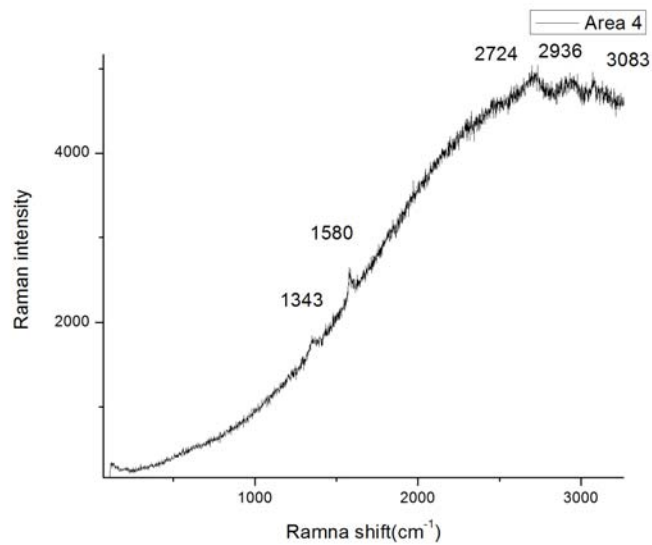


Fig. 11c.

Fig. 11. Raman spectra of the corrosion products from the gilded bronze sample after accelerated ageing by dropping test (TOW=30 days).

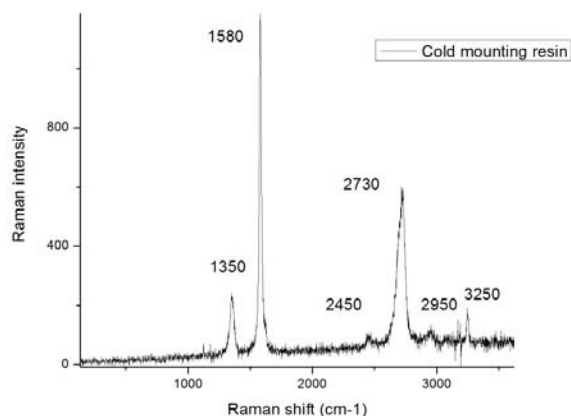


Fig. 12. Raman spectrum of cold mounting resin

In all the spectra acquired from the sample aged for 30 days, the main bands are at wavenumbers corresponding to the mounting resin. Figure 11c is the only one that provides information about the nature of the corrosion products. Here the presence of cuprite in the layer of the corrosion products is confirmed by the bands at 640, 510, 215cm<sup>-1</sup>[69], [70], [71].

### 3.2.5. PropS-SH coated sample

In regards to the as-gilded sample coated with PropS-SH, the comparison with the cross section of an uncoated sample provides us with valuable information about the protectiveness of the organosilane coating. The morphology of the two types of samples is different: in the case of the sample coated with PropS-SH, the corrosion sites appear to be much smaller in size and in number as shown in figure 13.

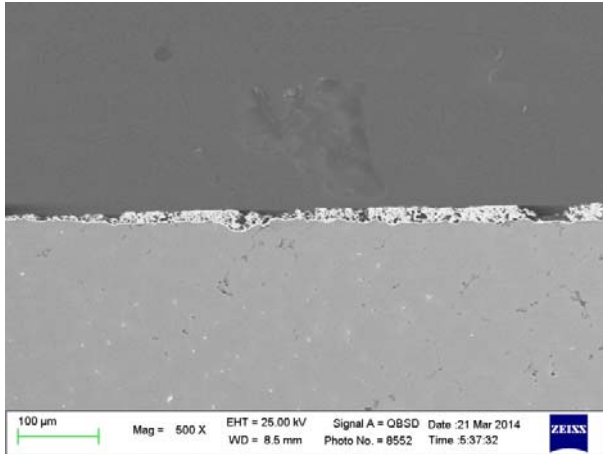


Fig. 13a. BSE image of gilded bronze sample coated with PropS-SH, after accelerated ageing by dropping test (TOW=30 days).

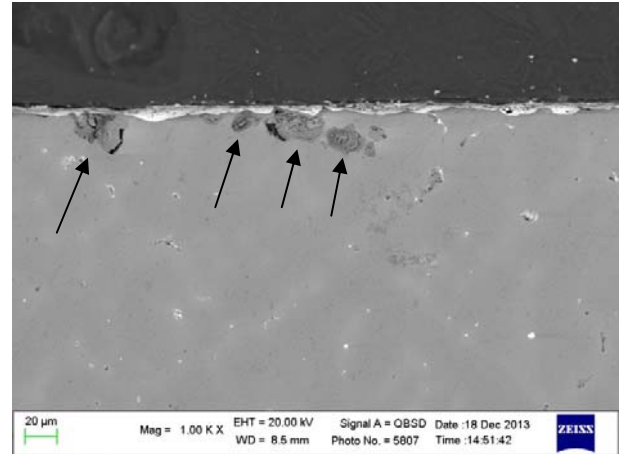


Fig. 13b. BSE image of uncoated gilded bronze sample, after accelerated ageing by dropping test (TOW=30 days). Localized corrosion sites are indicated by arrows.

The difference in morphology is highlighted also by the BSE and X-Ray maps presented in figures 14-16. The uncorroded bronze bulk, consisting of a high amount of copper and low amounts of lead (in the form of insoluble globules), microsegregated tin and zinc is the defining feature coming out of these figures. Gold and mercury are present in the fire-gilded layer, while the typical elements related to corrosion are not present in the sample. In fact, carbon and oxygen are located only in the region of the mounting resin (Fig. 14-15) or in an intergranular corrosion area (Fig. 16).

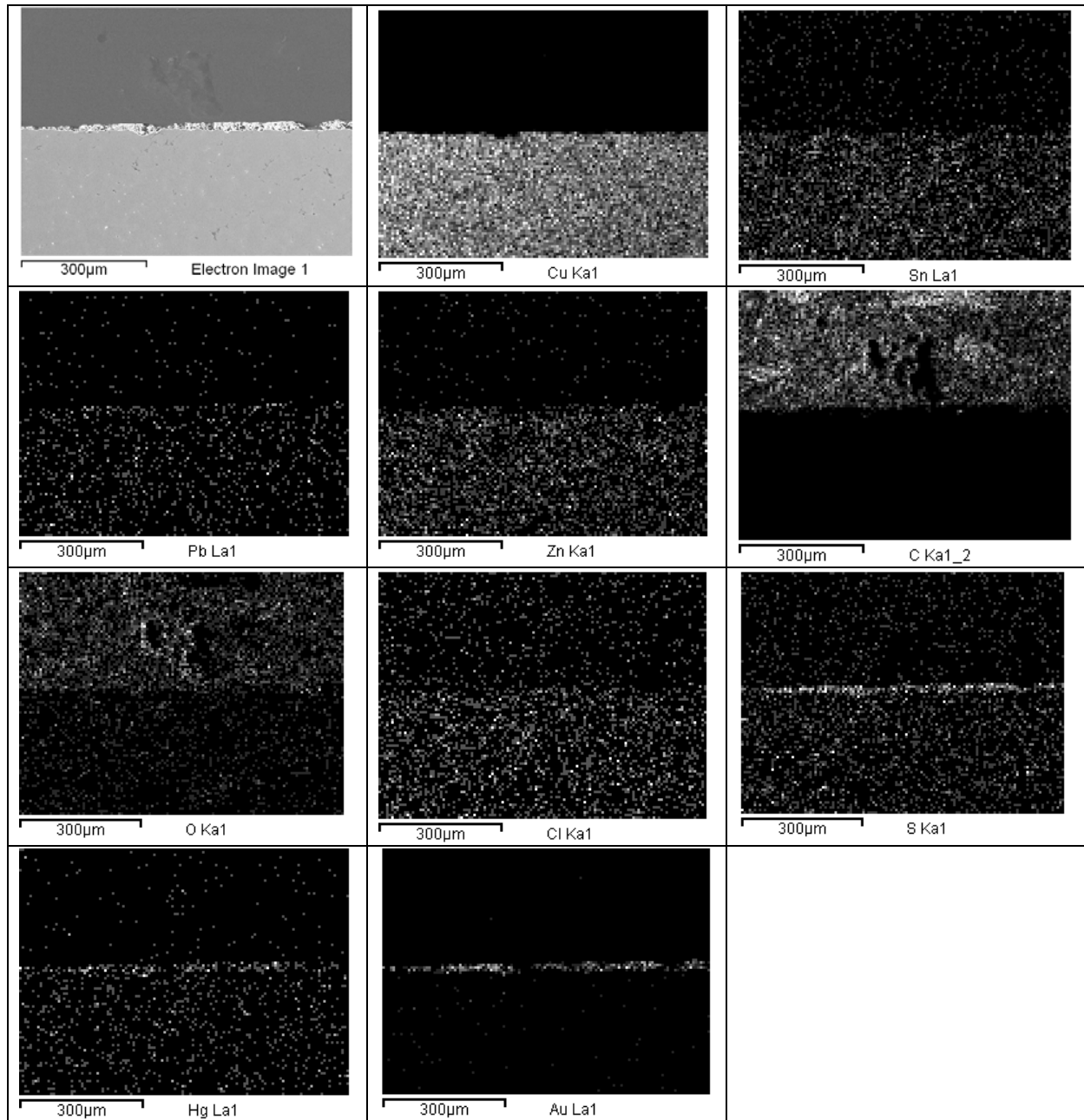


Fig. 14. BSE and X-Ray maps of a gilded bronze sample coated with PropS-SH, after accelerated ageing by dropping test (TOW=30 days).

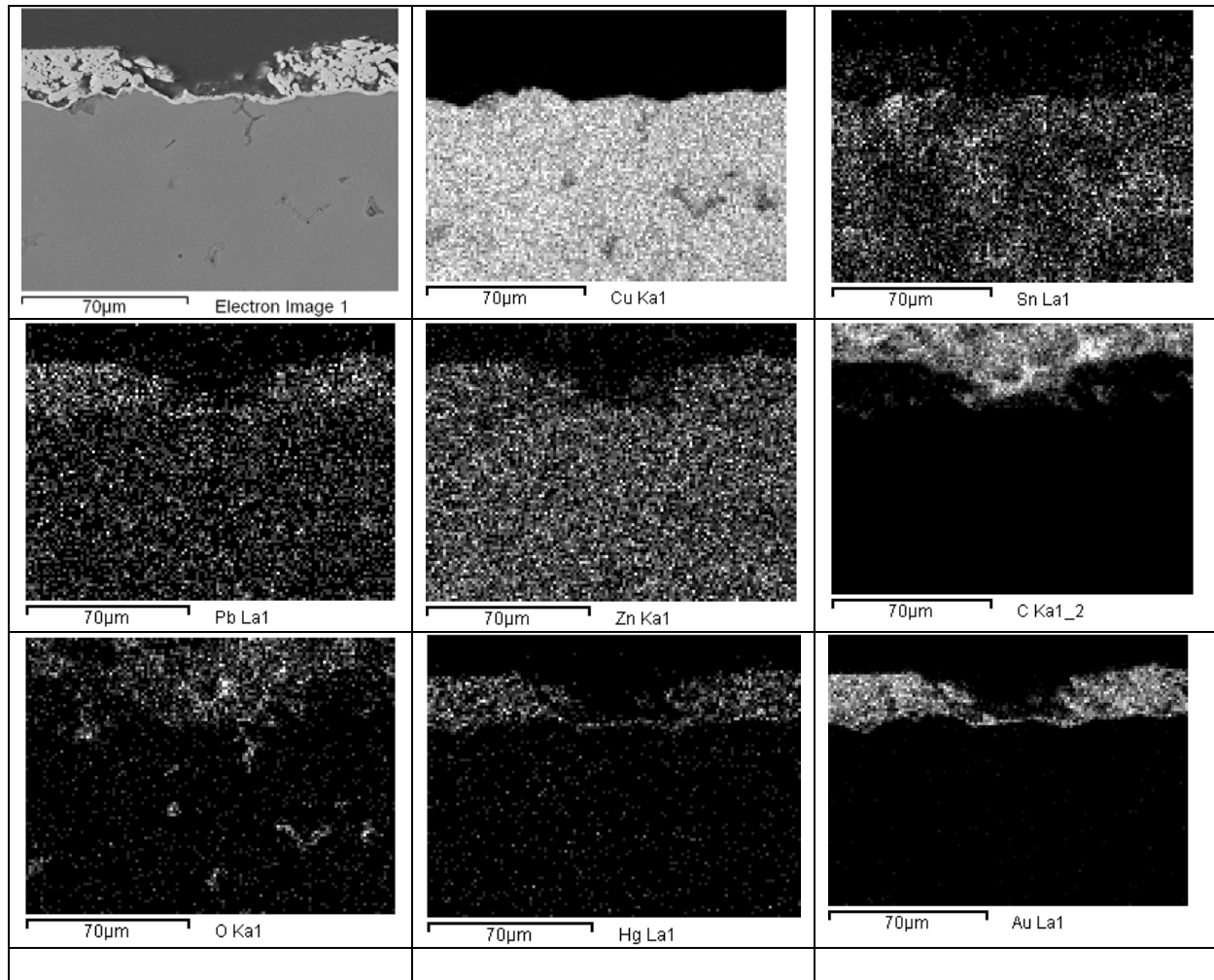


Fig. 15. BSE and X-Ray maps of a gilded bronze sample coated with PropS-SH, after accelerated ageing by dropping test (TOW=30 days).

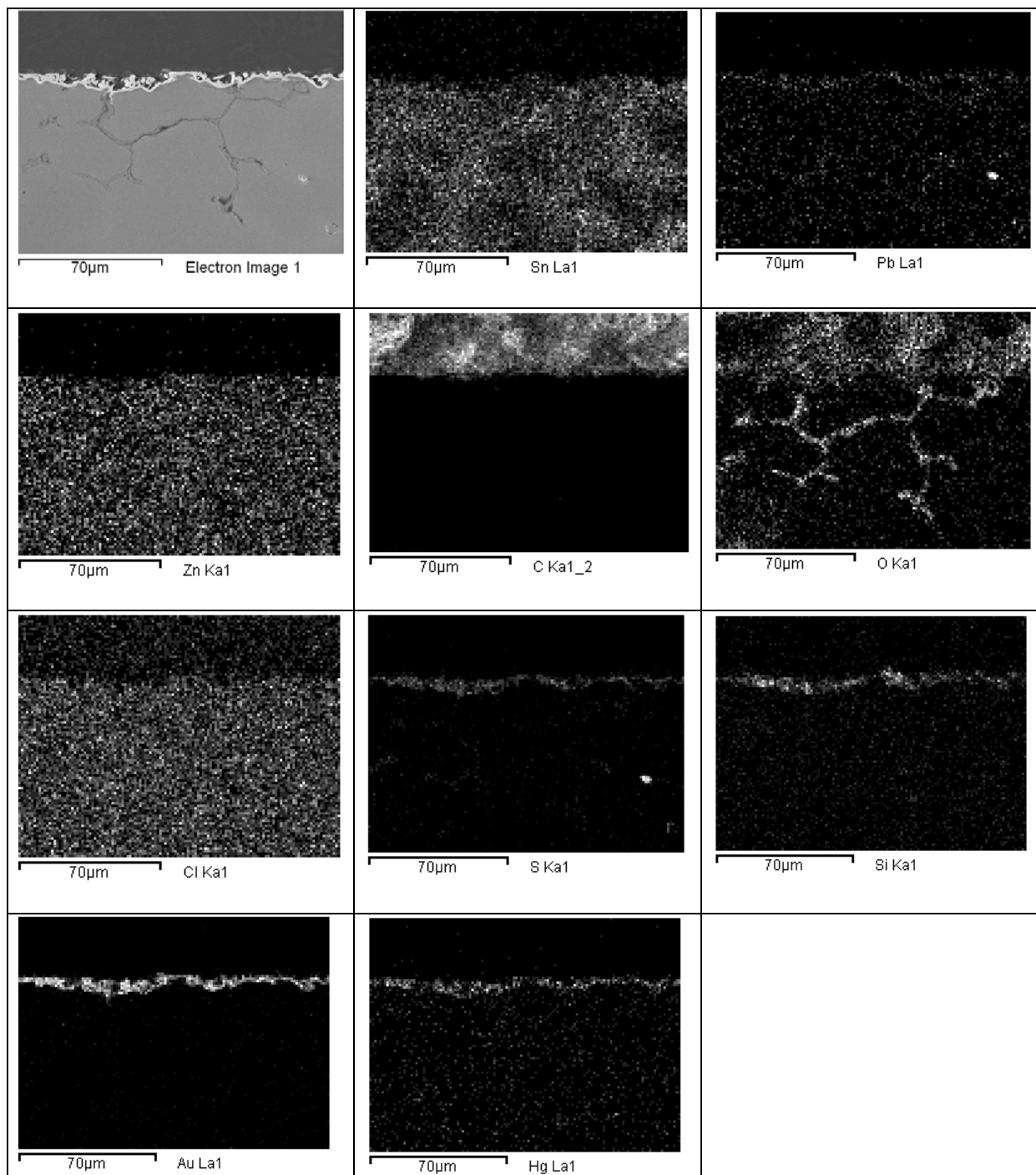
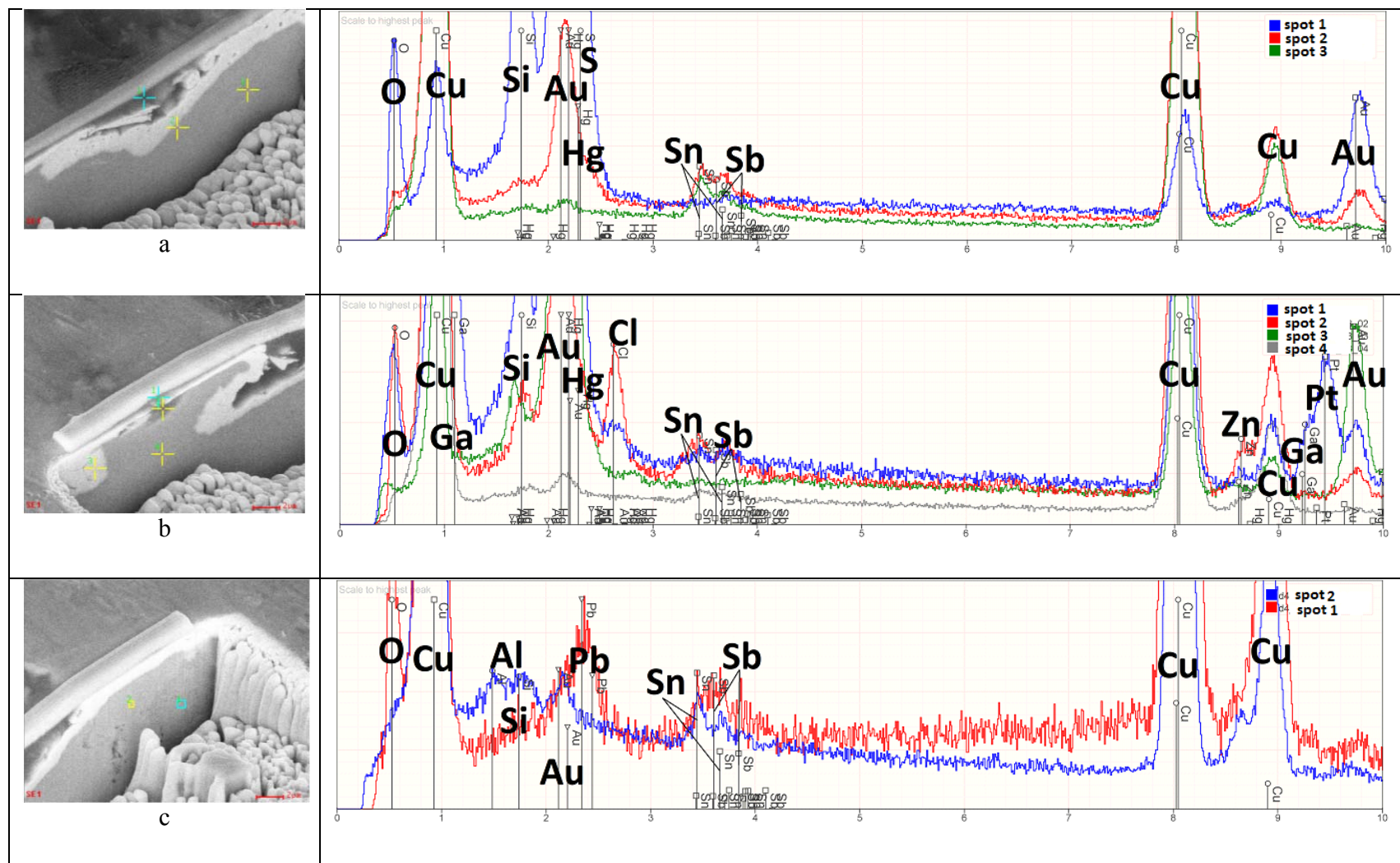
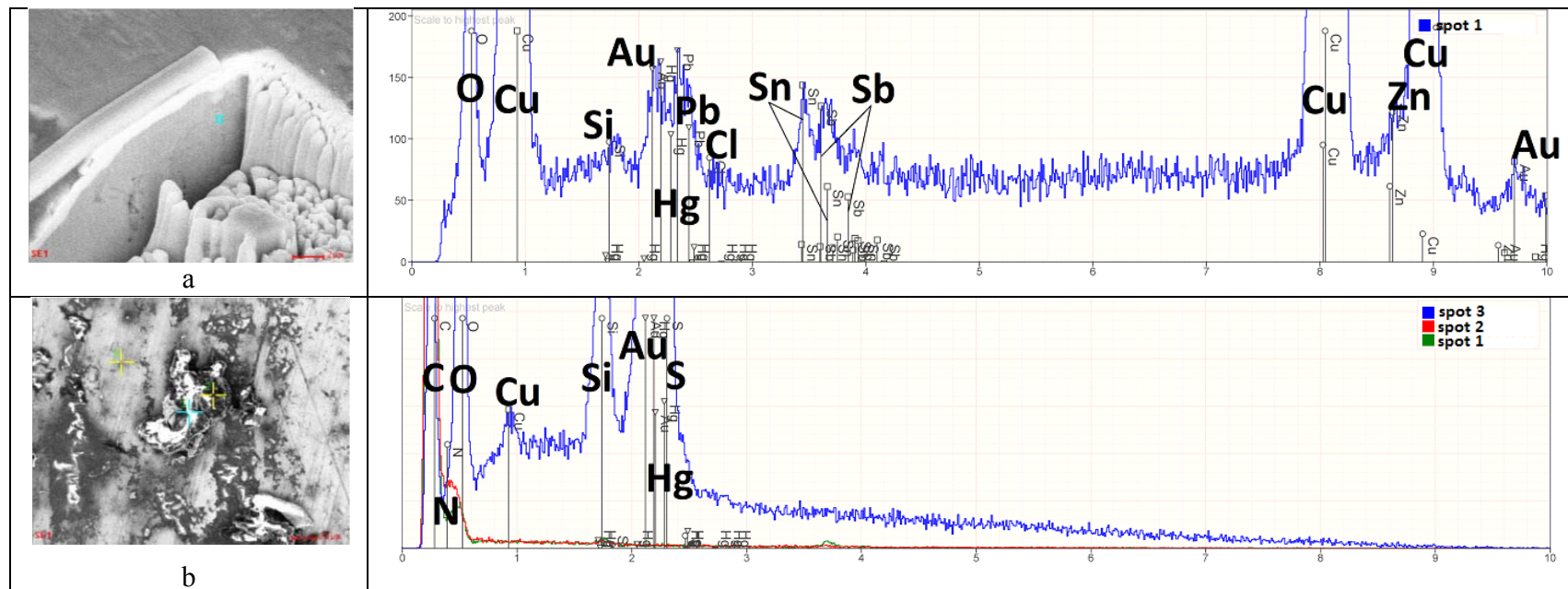


Fig. 16. BSE and X-Ray maps of a gilded bronze sample coated with PropS-SH, after accelerated ageing by dropping test (TOW=30 days).

FIB studies on the PropS-SH coated sample allowed the determination of the thickness of the coating and the comparison with the uncoated sample.



Tab 8. EDS spectra of different regions in the excavations of the gilded bronze sample coated with PropS-SH, after accelerated ageing by dropping test (TOW=30 days).



Tab 9. EDS spectra of different regions in the excavations of the gilded bronze sample coated with PropS-SH, after accelerated ageing by dropping test (TOW=30 days).

The EDS data in Table 8a show that the thin black layer above the gilded layer contains Si and S (therefore it corresponds to the PropS-SH layer). Data in Table 8b highlights the presence of an extremely small localized corrosion attack (point 2) where a higher Cl content than in other locations was detected. The zone in Table 8c and Table 9a shows a Pb-rich area in the alloy, located on the side of the FIB section. EDS data in Table 9b show that the surface of the sample is slightly contaminated (presence of C-rich islets, likely originating from the plastic bag for sample handling).

As mentioned previously, the FIB studies enabled us to observe the thickness of the coating layer in different regions on the surface of the samples. The size varies from 0.2  $\mu\text{m}$  to 2  $\mu\text{m}$  in the smooth areas of the surface, while in the grooves it can reach up to 4  $\mu\text{m}$  as can be seen from figure 17.

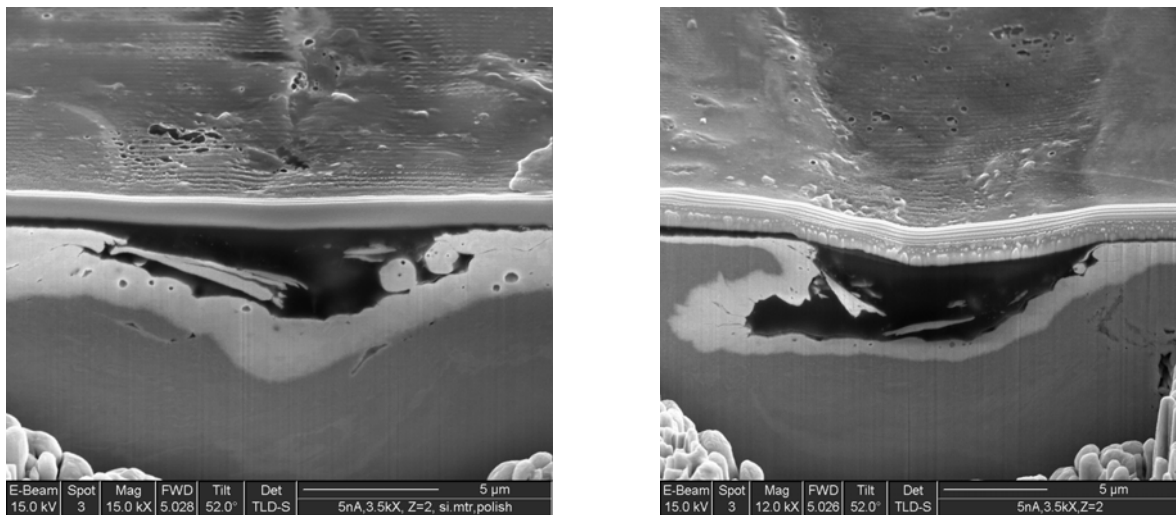
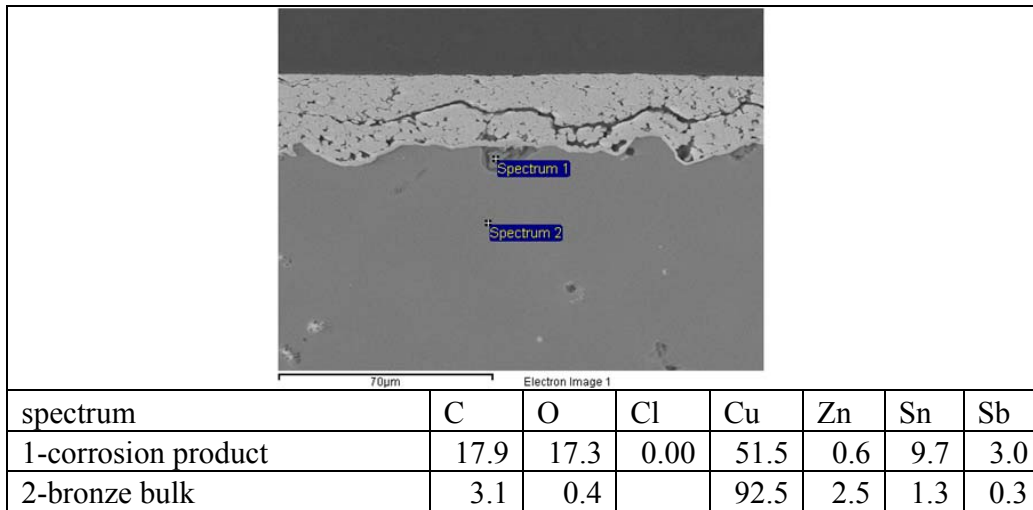


Fig. 17. SEM images of excavations of the gilded bronze sample coated with PropS-SH, after accelerated ageing by dropping test (TOW=30 days).

A qualitative assessment on the protective effectiveness of the coating was also derived from the FIB studies, as we were able to find a corrosion site in the case of the uncoated sample, while in the case of the coated one we were not (with the exception of spot 2 in Table 8b). Another small localized corrosion attack (with Sn enrichment and small amounts of Cl) was identified by SEM/EDS analyses in cross section on the PropS-SH coated sample, as shown in Table 10. However, the size and number of corroded areas at the gold/bronze interface is definitely lower in the PropS-SH coated- than in the uncoated gilded bronze.



Tab 10. Elemental composition (EDS, wt%) of different regions in gilded bronze sample coated with PropS-SH (GP) after accelerated ageing by dropping test (TOW=30 days).

### 3.2.6. Gravimetric measurements and metal release (as-gilded samples)

Gravimetric measurements of the samples were taken during each dry period of the ageing cycle in order to monitor their mass evolution. The values obtained for the coated sample were compared to the average of those obtained for the uncoated samples.

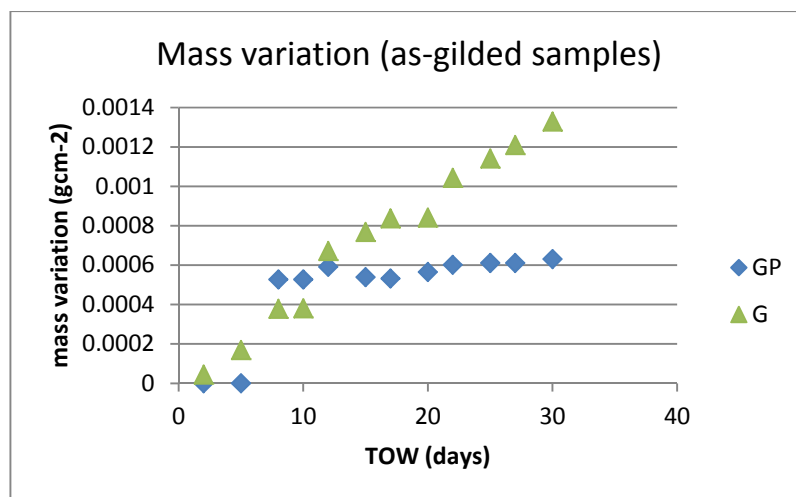


Fig. 18. Negative mass variation (mass loss) per unit area of GP (gilded and protected with PropS-SH) and G (gilded) samples as a function of the time of wetness (TOW)

The mass variation graph in Fig. 18 shows that the PropS-SH coating is able to limit mass loss of the bronze when applied on the as-gilded bronze surface. Fig. 18 shows that the mass loss of gilded uncoated samples (G) increases with a linear trend, whilst the PropS-SH coated sample (GP) shows a decrease of the slope after the first 10 days. However, it must be noticed that there was an interruption in the exposure test between the first 10 days and the last 20 days, which might have improved the protective properties of the silane coating due to increased reticulation.

During accelerated ageing, the evolution of the samples was also followed by monitoring the evolution of the metal release in the leaching solution of artificial acid rain. Graphite-Furnace Atomic Absorption Spectroscopy was used in order to determine the amount of metals released by each sample.

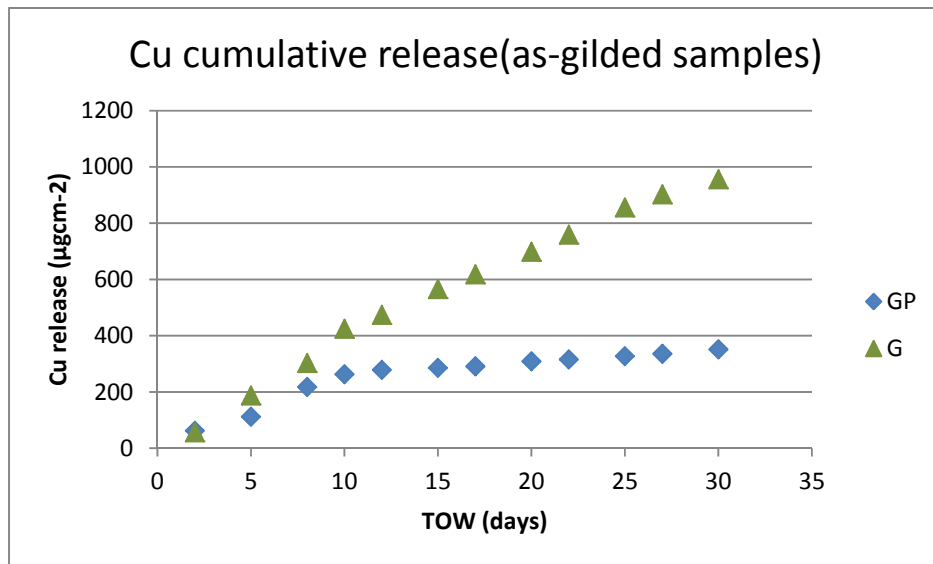


Fig. 19. The cumulative Cu release of GP(gilded and protected with PropS-SH) and G(gilded) samples, normalized to the surface, as a function of the time of wetness(TOW)

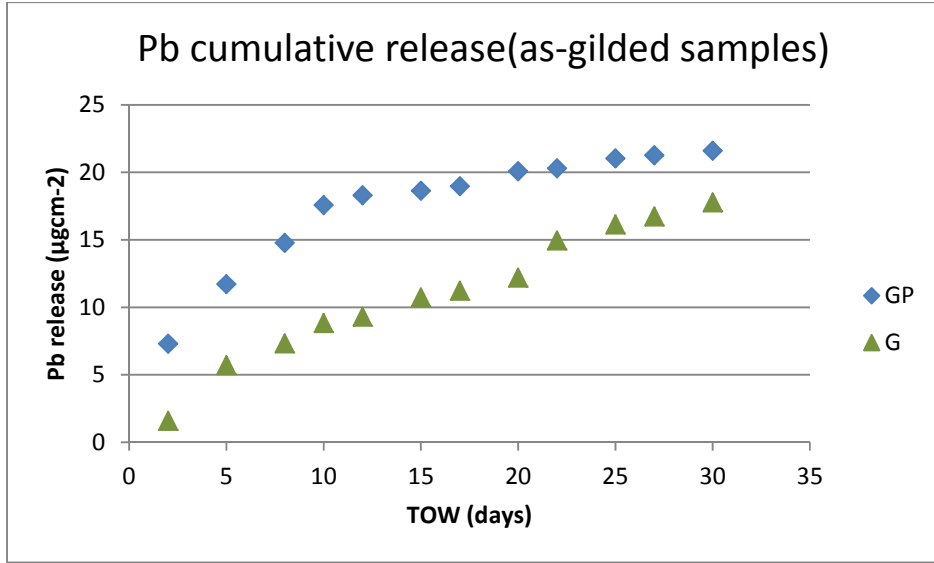


Fig. 20. The cumulative Pb release of a GP(gilded and protected with PropS-SH) and G(gilded) samples, normalized to the surface, as a function of the time of wetness(TOW)

The lowest values of Cu release (fig. 19) are measured for the GP sample (as-gilded, coated PropS-SH), indicating that the PropS-SH coating is able to limit Cu release when applied on the as-gilded bronze surface, in agreement with mass variation data of Fig.19. Conversely, PropS-SH is not able to limit Pb release (as already observed for non-gilded [20]).

### 3.3. Samples (pre-patinated) after corrosion testing

Sample type	Reference (unaged sample)	GD – gilded aged for 30 days	GDP – gilded aged for 30 days and coated with PropS-SH	GDPC – gilded aged for 30 days and coated with PropS-SH + CeO <sub>2</sub>
before				
after				
Length (mm)		48.00	38.11	41.90
Width (mm)		14.50	13.60	14.02

Tab 11. Pictures of the gilded bronze samples before and after the ageing process.

#### 3.3.1. Surface and cross section analysis

In regards this ageing cycle (the so-called “second” ageing cycle, dedicated to assess the protective efficiency of PropS-SH when applied on a corroded gilded bronze substrate, produced by using accelerated ageing as a pre-patination method), as mentioned before (section 3), the two uncoated samples were again use: one as a substrate for applying the PropS-SH on a prepatinated

surface, while the other as a reference. Another previously aged sample was used as a substrate for applying the PropS-SH coating which contained CeO<sub>2</sub> nanoparticles. Table 21 on the previous page displays pictures of the samples before and after this “second” ageing cycle.

No significant surface morphology variation was observed on the macroscopic scale (which is not surprising, due to the localization of corrosion at the gold/bronze interface, at least in the first step of the degradation process), apart from a few green-white streaks appearing on the surface of the GDPC sample.

In general, the application of PropS-SH and PropS-SH+CeO<sub>2</sub> on the gilded bronzes, both non-prepatinated and prepatinated, does not induce appreciable colour variations. Significant color variations do not occur also during the ageing of the coated samples, as shown by data in Table 12, where color variation values  $\Delta E$  are reported, considering that in the field of Cultural Heritage,  $\Delta E \geq 3$  is considered as the perceptibility threshold [69].

Specimen	Color variation after	
	coating	Ageing 30 days TOW
Gilded bronze		$\Delta E=4.6$
Gilded bronze	PropS-SH $\Delta E=1.1$	$\Delta E=3.0$
Gilded bronze	PropS-SH + CeO <sub>2</sub> $\Delta E=2.6$	
Prepatinated		$\Delta E=3.9$
Prepatinatedandcoated with PropS-SH	PropS-SH $\Delta E=2.9$	$\Delta E=2.2$
Prepatinatedandcoated with PropS-SH + CeO <sub>2</sub>	PropS-SH + CeO <sub>2</sub> $\Delta E=6.2$	$\Delta E=0.7$

Tab. 12. Color variation table

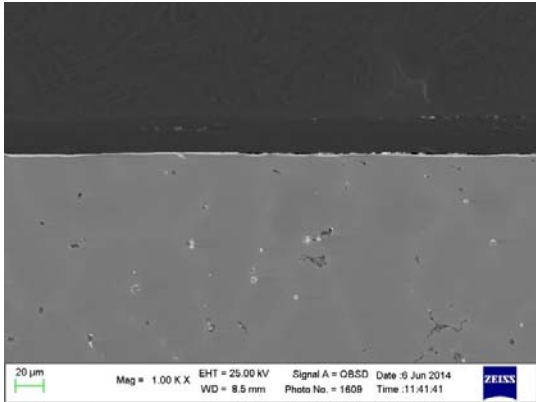


Fig. 21a. SEM image of cross section of GD(aged gilded sample, uncoated) showing a continuous gold layer with few imperfections

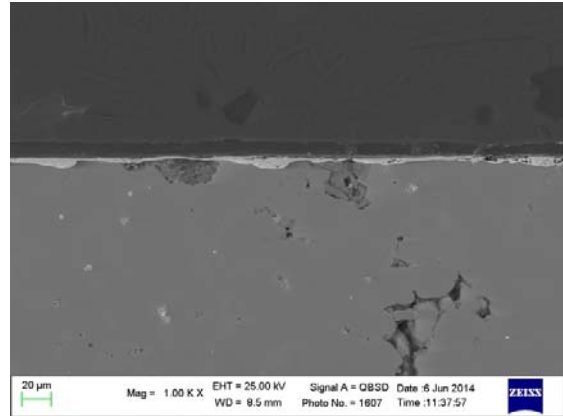


Fig. 21c. SEM image of cross section of GDPC (aged gilded sample, coated with PropS-SH + CeO<sub>2</sub>) showing a porous gold layer and corrosion sites

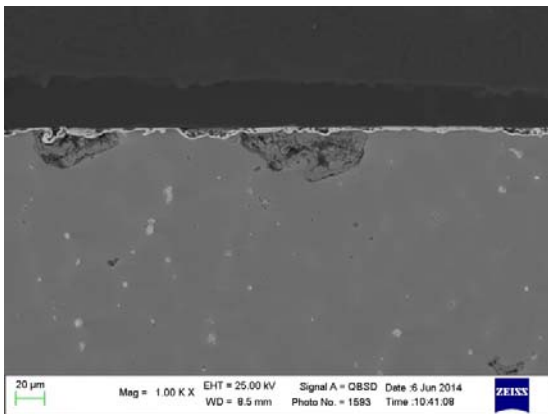


Fig. 21b. SEM image of cross section of GDP(aged gilded sample, coated with PropS-SH) showing a porous gold layer and corrosion sites

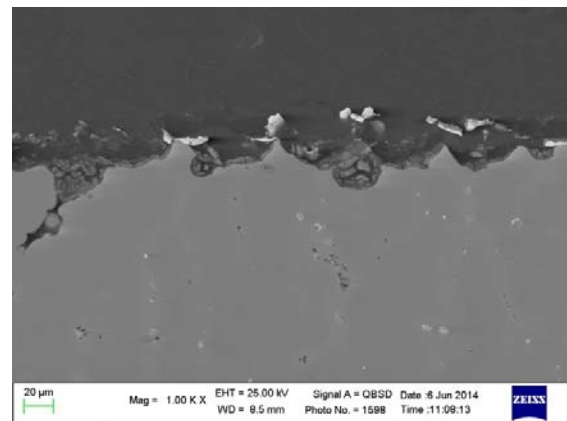
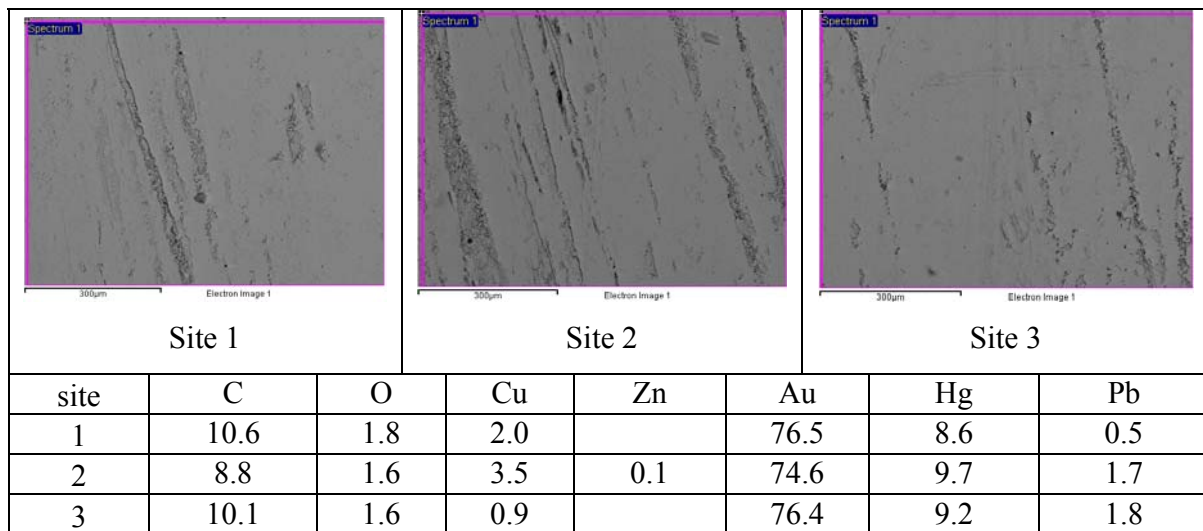


Fig. 21d. SEM image of cross section of GDPC (aged gilded sample, coated with PropS-SH + CeO<sub>2</sub>) sample showing a very discontinuous gold layer and extensive corrosion

When discussing the data collected in this cycle, certain specifications have to be made regarding the morphology of the samples involved in this study. The GDP(aged gilded bronze, coated with PropS-SH) and GDPC(aged gilded bronze, coated with PropS-SH + CeO<sub>2</sub>) samples presented a gilding that was much less naturally protective than the GD(aged gilded bronze, uncoated) sample, where the gold layer was thin but with less pores and discontinuities than in the other samples, as shown by figure 21a-d.

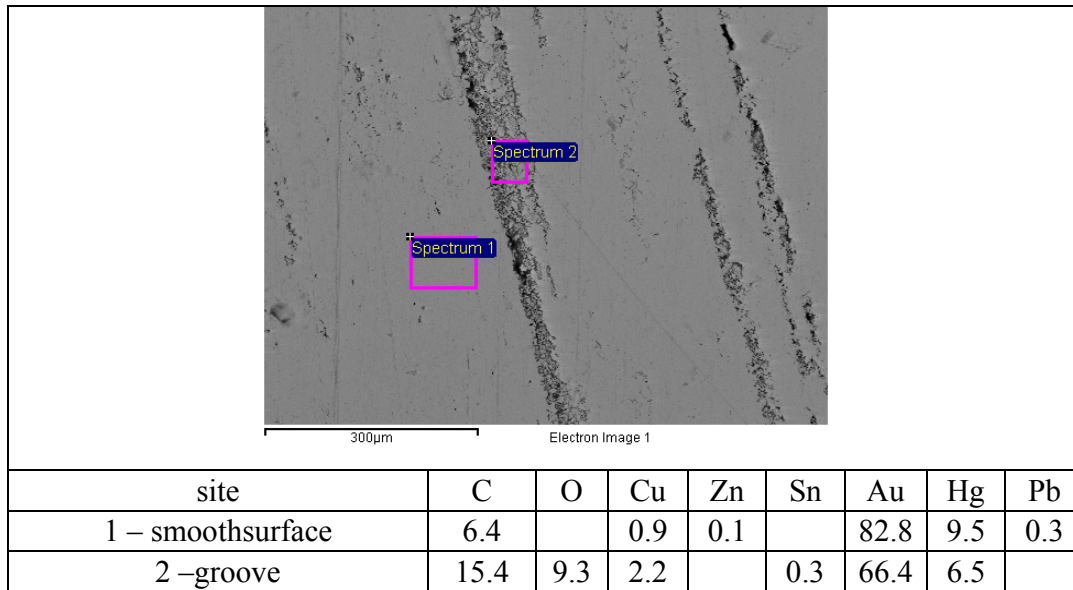
These very heterogeneous morphologies of the fire-gilded layer surely affect the corrosion behavior of the samples (i.e a very protective gold layer may lead to overestimation of the protective efficiency of the silane coating), but they are representative of the real conditions when considering a historic fire-gilded bronze artifact.

The surface morphologies (SEM) and elemental compositions (EDS) of the samples at the end of the last ageing cycle, followed by cross-section observation, are discussed in the following text.

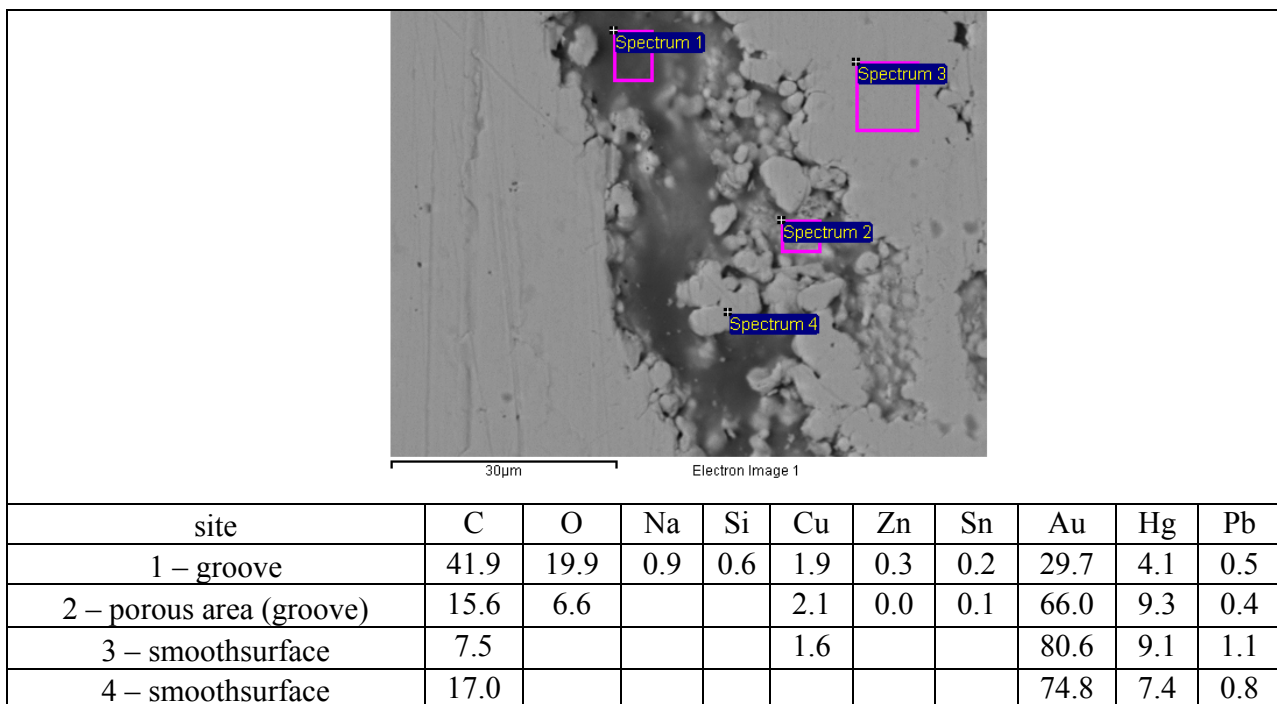


Tab. 13. BSE images and the corresponding elemental composition (EDS, wt%) of the surface of the uncoated gilded bronze sample (GD), after accelerated ageing by dropping test (TOW=60 days)

In the case of the uncoated gilded sample (GD), the EDS surface analysis in the three sites in table 13 show comparable situations, while tables 14 and 15 allows us to compare the results collected in the smooth areas (where the gilded layer was compacted by burnishing) and in the porous areas (i.e. the grooves, where the gilded layer was not accessible to the burnishing tool). In the porous areas, the lower amounts of gold and mercury correspond to higher amounts of carbon and oxygen, probably due to deposition of organic compounds from the synthetic acid rain during the ageing cycle.



Tab. 14. Elemental composition (EDS, wt%) of different regions from the surface of uncoated gilded bronze sample (GD), after accelerated ageing by dropping test (TOW=60 days)



Tab. 15. Elemental composition (EDS, wt%) of different regions from the surface of uncoated gilded bronze sample (GD), after accelerated ageing by dropping test (TOW=60 days)

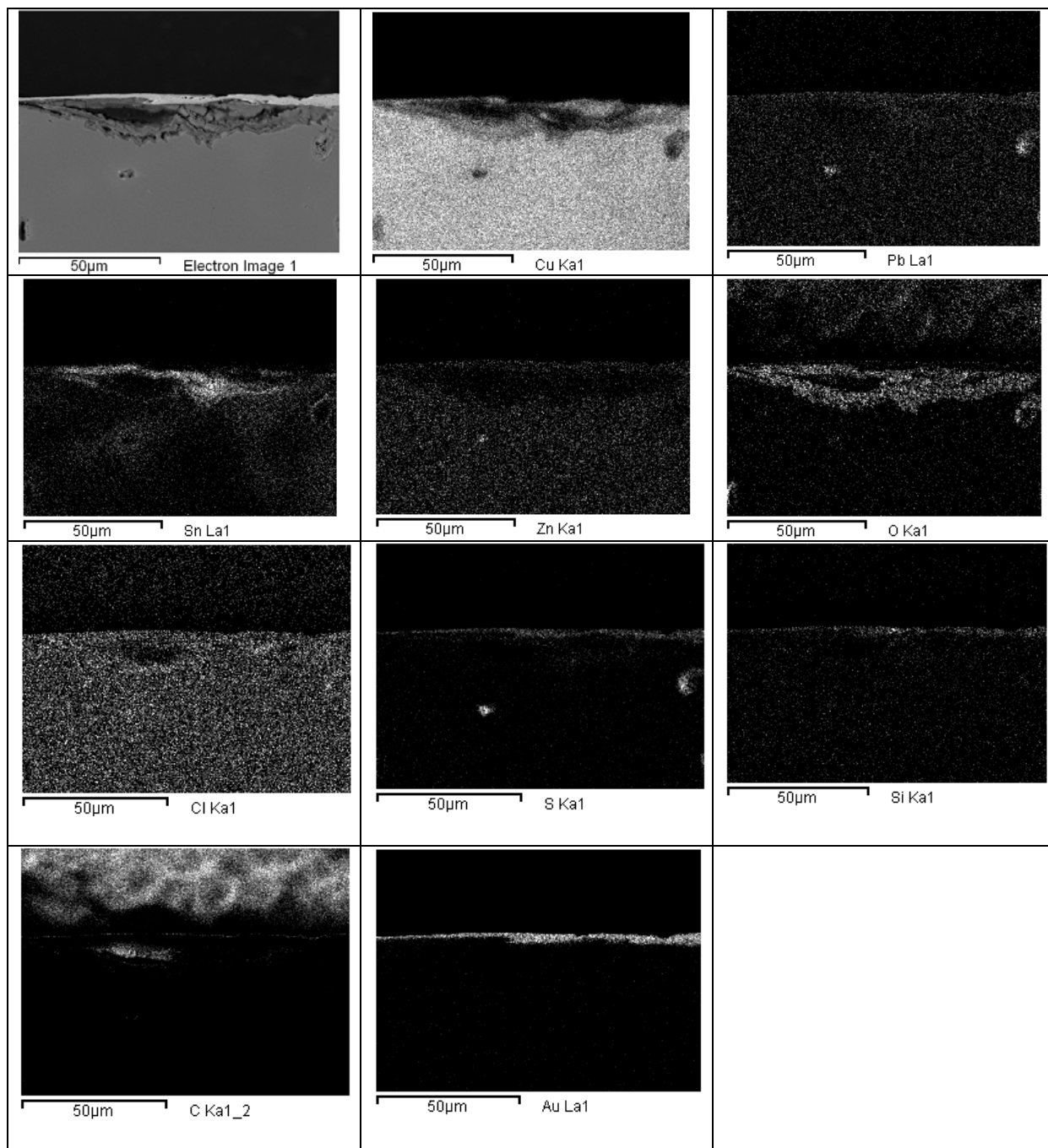
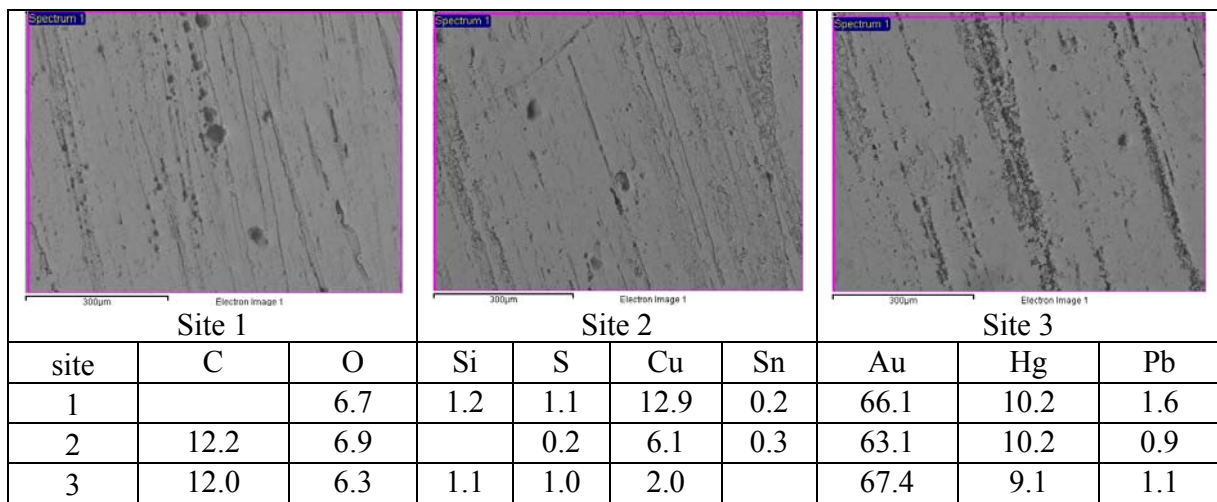


Fig. 22. BSE and X-Ray maps of a corrosion site in an uncoated gilded bronze sample (GD), after accelerated ageing by dropping test (TOW=60 days). Cross-section observation.

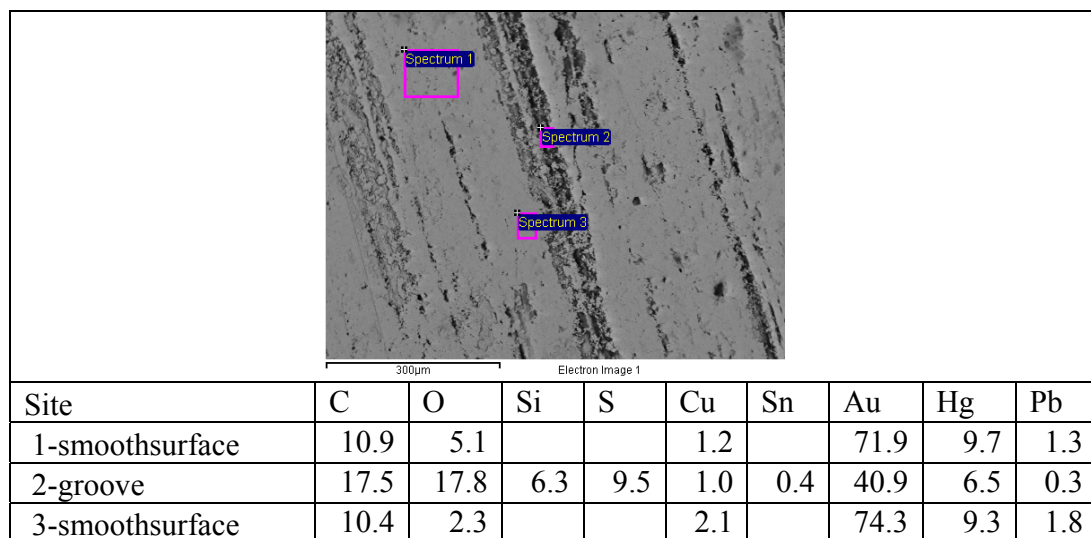
The EDS X-ray maps of the uncoated gilded bronze (GD, reference sample) aged for 60 days (Fig. 22), shows a morphology comparable to the one aged for 30 days. The map also shows a very thin but compact gilding layer, that was able to protect the bulk of the bronze from

corrosion in most of the section. The silicon and sulphur are not due to the PropS-SH, as this sample was uncoated but from the mounting and polishing procedure. This shows the need for FIB studies (FIB milling being much less invasive than conventional metallographic procedures) in this type of research.

Surface morphology and composition and cross section observation of the PropS-SH coated sample (GDP) are reported in Table 16-17.



Tab.16. BSE images and the corresponding elemental composition (EDS, wt%) of the surface of GDP(aged gilded sample, coated with PropS-SH and aged another 30 days)



Tab.17. Elemental composition (EDS, wt%) of different regions from the surface of the GDP(aged gilded sample, coated with PropS-SH and aged another 30 days)

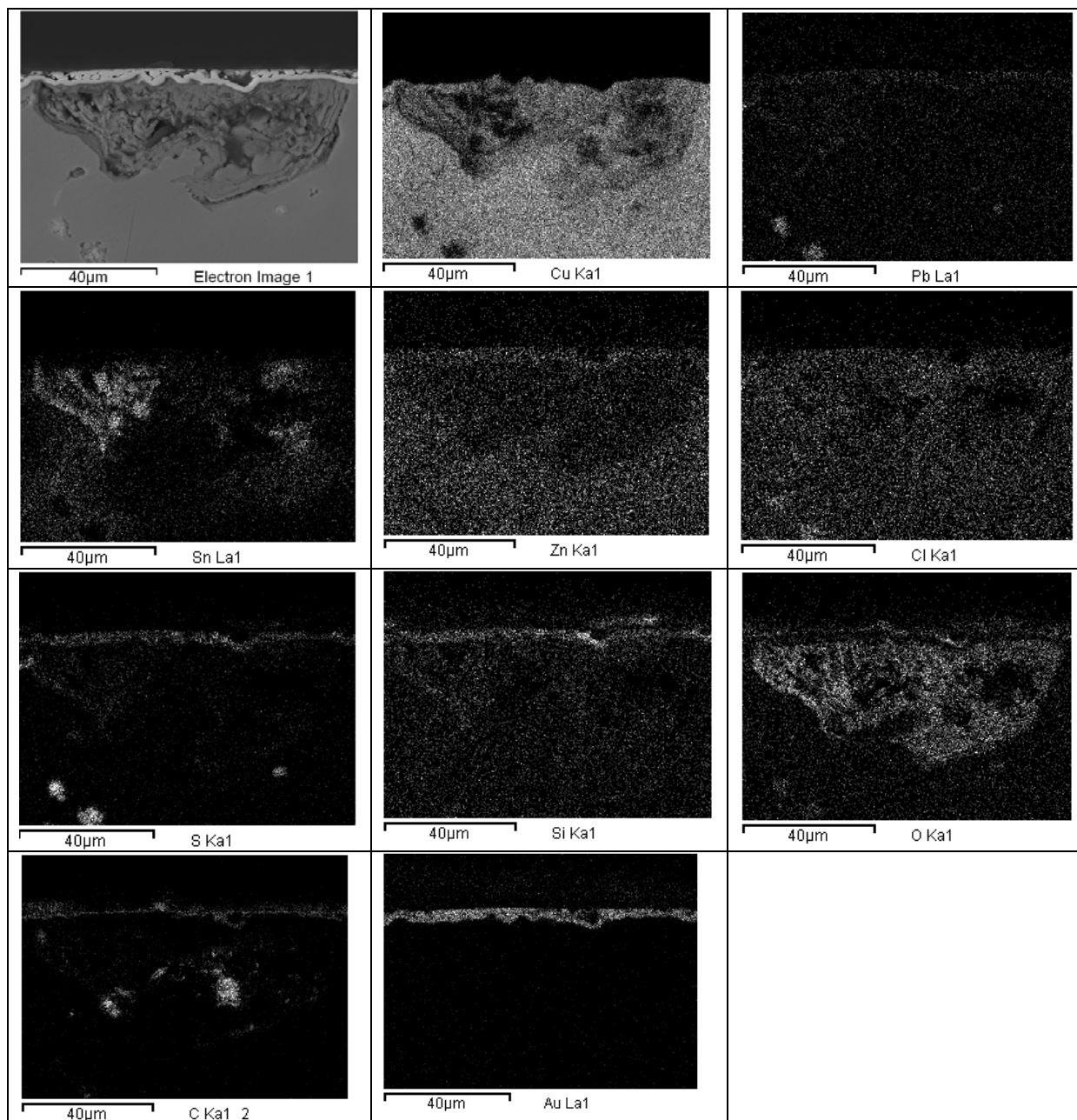


Fig. 23. BSE and X-Ray maps of a corrosion site in the GDP(aged gilded sample, coated with PropS-SH and aged another 30 days)

The composition of the surface of the aged sample protected with PropS-SH (GDP) showed the presence of silicon and sulphur, coming from the organosilane layer, which was not significantly damaged by exposure in runoff conditions. Table 17 clearly shows that the

PropS-SH coating tends to accumulate in the grooves of the gilded surface, as site 2 presents lower amounts of gold and mercury and higher ones for silicon, oxygen, carbon and sulphur.

The X-ray maps of the cross section of sample GDP (Fig. 23) show that corrosion craters are present also in this case, at the interface between gold and bronze. It is not possible to define if these craters are due to the “pre-patination” step or if were formed (or enlarged) due to the final ageing cycle.

Also  $\mu$ Raman studies were conducted in different areas in the corroded sites of the aged gilded bronze coated with PropS-SH. The spectra are displayed in figures 24a-e.

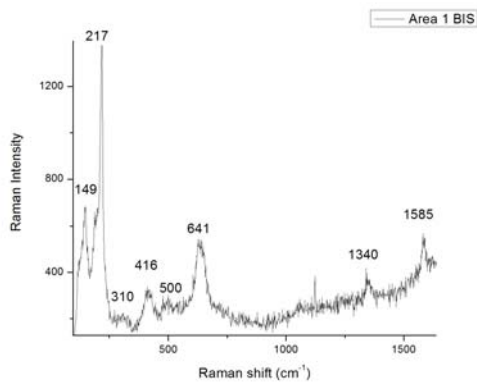


Fig. 24a.

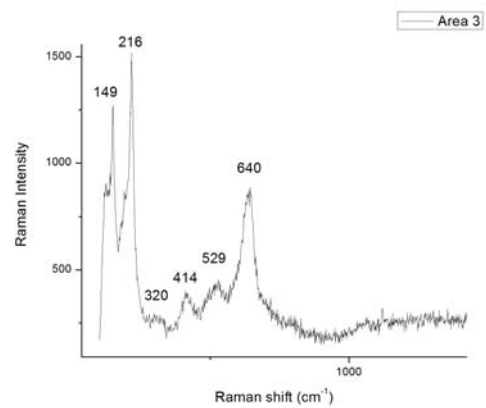


Fig. 24c.

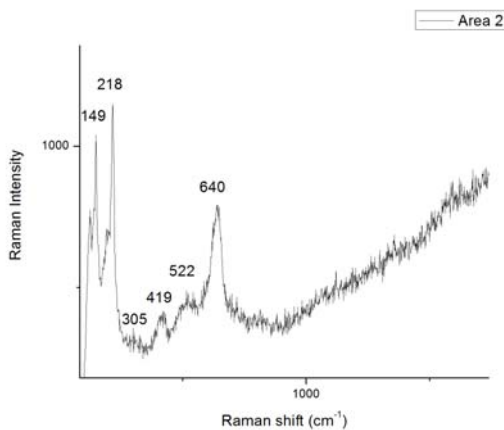


Fig. 24b.

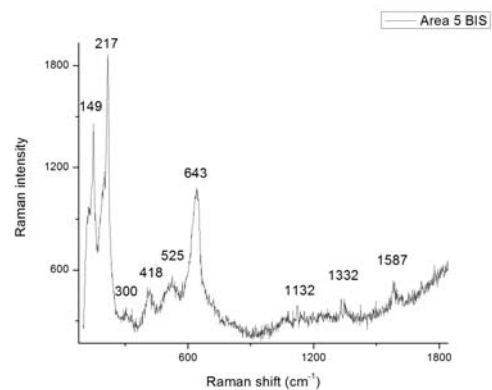


Fig. 24d.

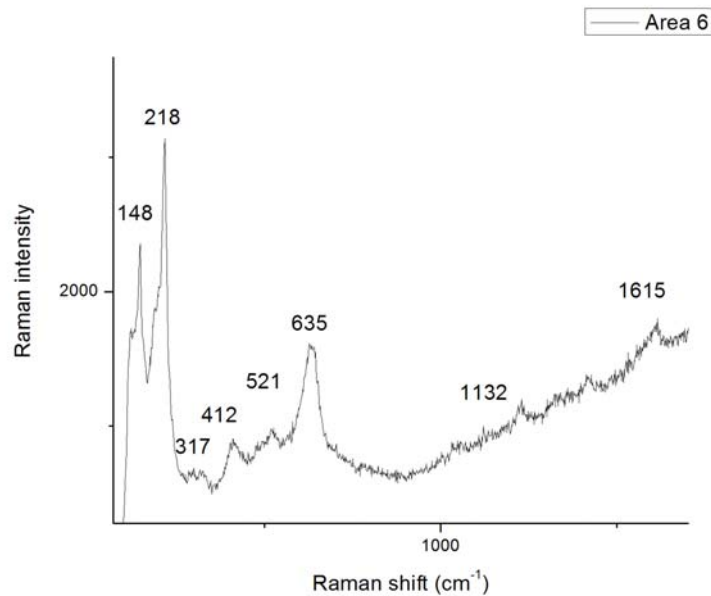


Fig. 24e.

Fig. 24. Raman spectra of the corrosion products from different regions in the GDP(aged gilded sample, coated with PropS-SH and aged another 30 days)

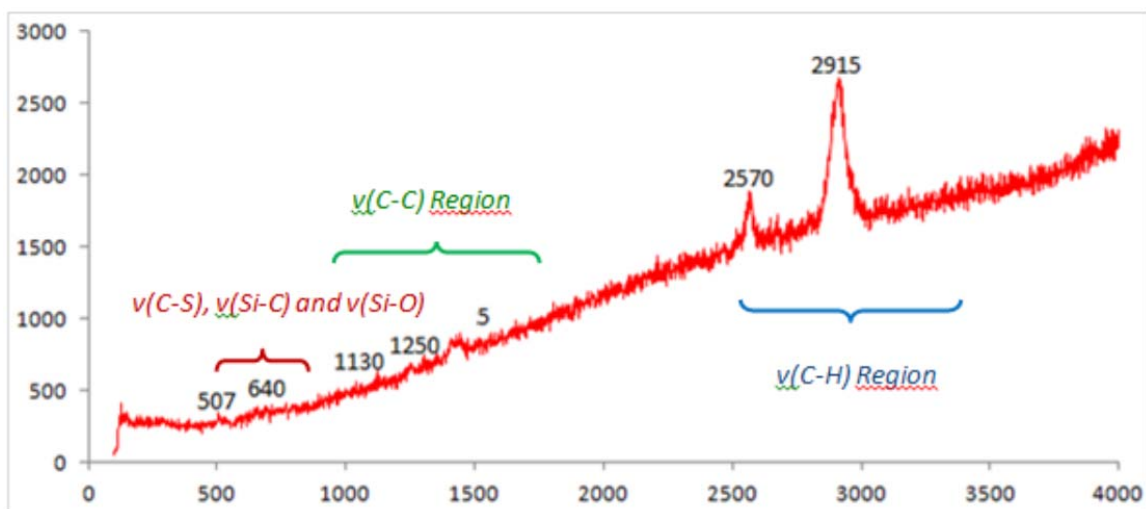


Fig. 25. Raman spectrum of PropS-SH (used as a reference)[74]

Based on the Raman spectrum of the PropS-SH recorded in a previous work [74] and on the spectrum of the mounting resin shown in section 2.5, we were able to attribute the following

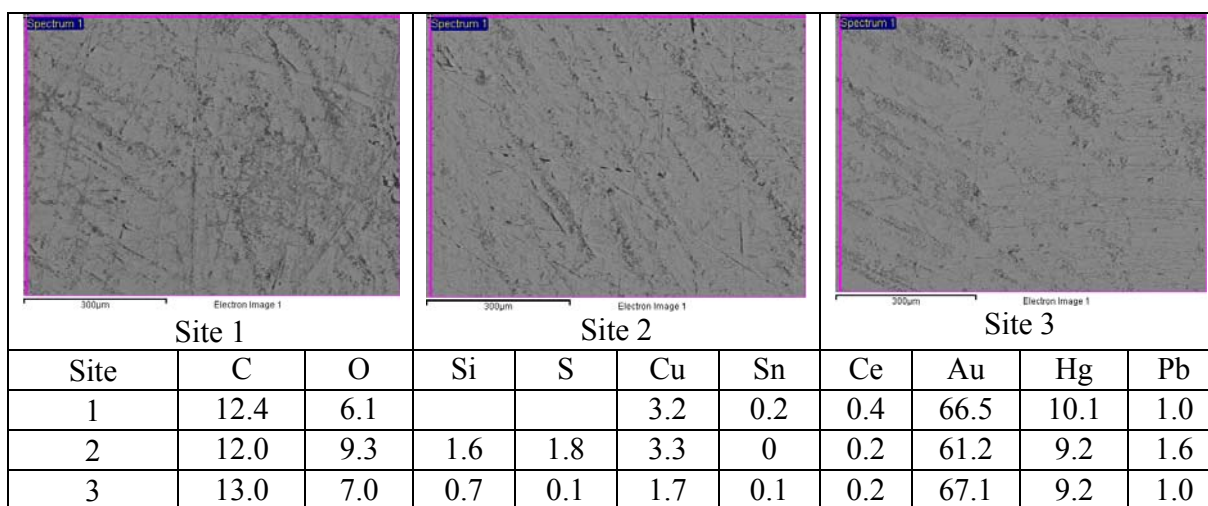
bands: 640, 520, 415, 305, 217 and 149  $\text{cm}^{-1}$  to cuprite, 1130, 1230  $\text{cm}^{-1}$  to the PropS-SH coating and 1580  $\text{cm}^{-1}$  to the mounting resin.

In each figure the bands correspond to the compounds as follows:

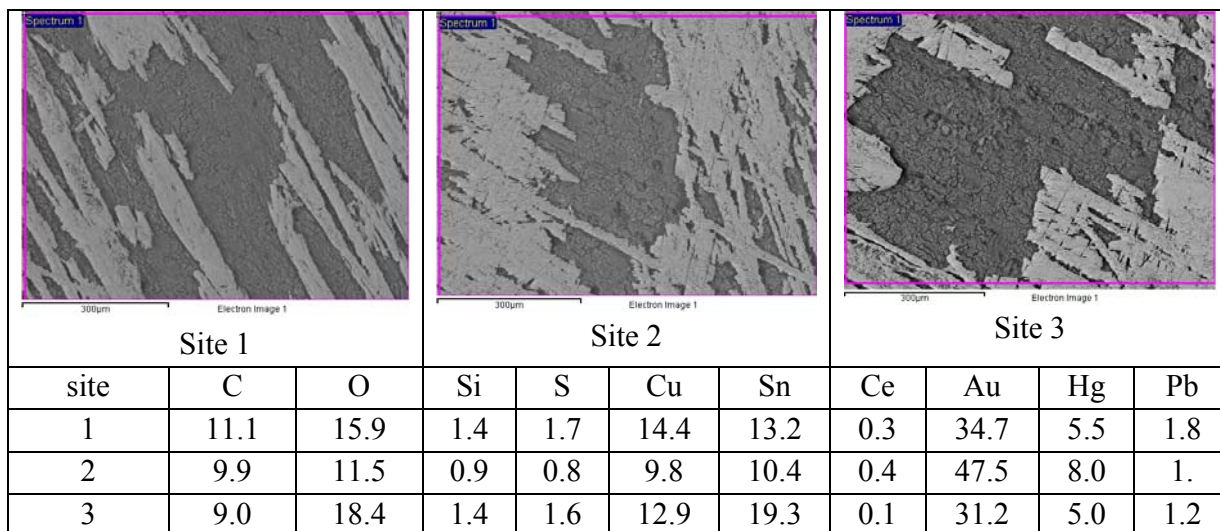
- Fig. 22a: cuprite, PropS-SH and mounting resin
- Fig. 22b: cuprite
- Fig. 22c: cuprite
- Fig. 22d: cuprite, PropS-SH and mounting resin
- Fig. 22e: cuprite, PropS-SH and mounting resin

Therefore, the main corrosion product identified in the corrosion craters of sample GDP is cuprite, as already observed in the “pre-patinated” substrate (section 3.2.5.).

Surface morphology and composition and cross section observation of the PropS-SH +  $\text{CeO}_2$  coated sample (GDPC) are reported in Table 18-21. Tables 18 and 19 show regions with different surface morphologies. While in one case the gold layer is continuous (Table 18), in the other (Table 19) it appears broken up and covered with corrosion products. These areas correspond to the white-green streaks observed in macroscopic images (Table 11).

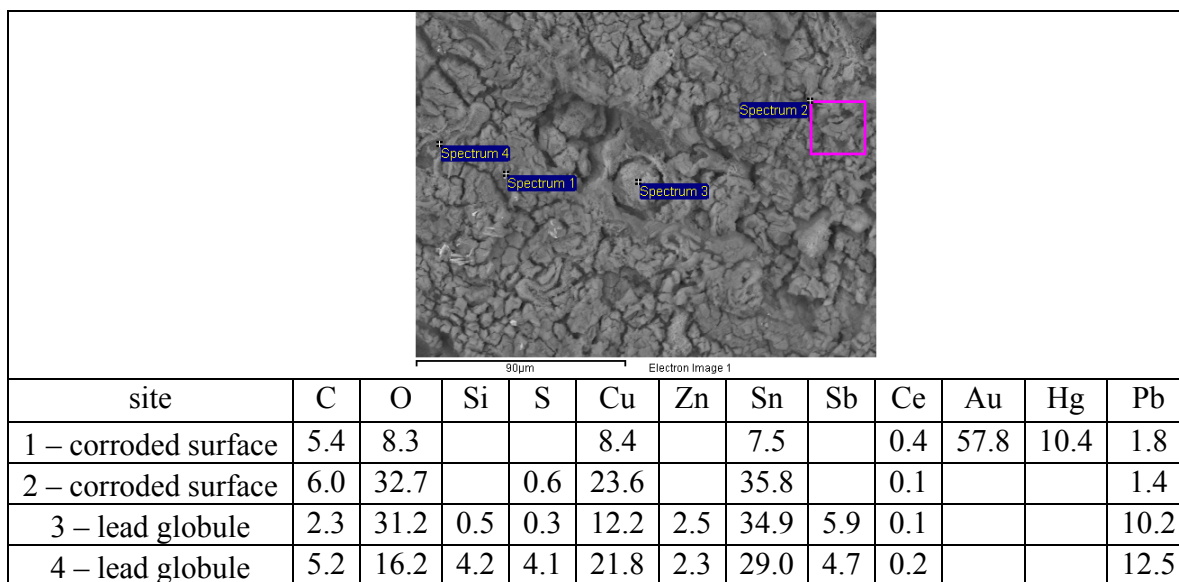


Tab. 18. BSE images and the corresponding elemental composition (EDS, wt%) of the surface of the GDPC(aged gilded sample, coated with PropS-SH+ $\text{CeO}_2$  and aged for another 30 days)sample where the gold layer is continuous

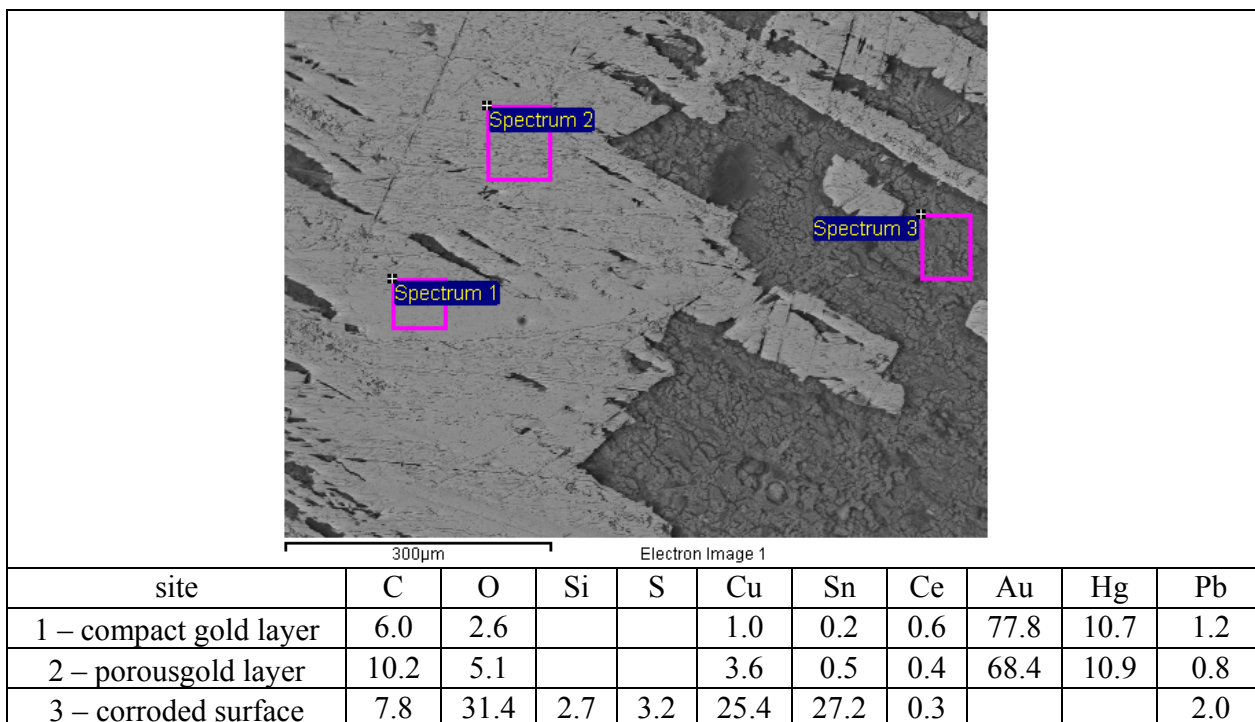


Tab. 19. BSE images and the corresponding elemental composition (measured by EDS, wt%) of the surface of the GDPC(gilded aged for 30 days, coated with PropS-SH and CeO<sub>2</sub> and aged for another 30 days)sample where the gold layer is discontinuous

Higher magnification details with the corresponding EDS localized analyses, recorded in the areas where the gold layer is discontinuous and covered by corrosion products, are shown in Table 20-21.



Tab. 20. Elemental composition (measured by EDS, wt%) of different regions from the surface of the GDPC(gilded aged for 30 days, coated with PropS-SH and CeO<sub>2</sub> and aged for another 30 days)sample where the gold layer is discontinuous



Tab. 21. Elemental composition (measured by EDS, wt%) of different regions from the surface of the GDPC(gilded aged for 30 days, coated with PropS-SH and CeO<sub>2</sub> and aged for another 30 days)sample where the gold layer is discontinuous

High amounts of O and Sn are observed in the most corroded areas. In general, Ce(from the PropS-SH + CeO<sub>2</sub> coating) can still be detected on the coated surface, even in the more corroded areas, whilst Si and S tend to decrease beyond the detection limit. Also Au (from the gilded layer) is seldom detected in the most corroded areas, either because the gold layer was too damaged and detached from the corrode surface, or because it is completely covered by a thick layer of corrosion products. FIB milling will be used for ascertaining the sequence of layers in the corroded areas.

Based on the information provided in table 21 we are able to compare three types of regions from the damaged area of the GDPC sample. The “porous gold layer” area shows a lower amount of gold and a higher amount of copper and oxygen, indicating that in that region the deposition of organic compounds from the ageing solution. The “corroded surface” area has a composition which is quite different from that of the bulk bronze, with a high amount of oxygen

and the amounts of copper and tin being almost equal, meaning that the alloy has suffered decuprification and tin enrichment in that region.

In regards to the EDS X-ray map of the GDPC sample shown in figure 24, we can observe that it displays a similar corrosion morphology and elemental distribution as the one coated only with PropS-SH (Figure 26). The main difference appears when taking into account Ce in the coating, that shows a higher concentration the region above the gold layer.

The presence of certain elements in the cross-section can be affected by the preparation method: C, with a strong signal in the region of the mounting resin also appears in the corrosion layer. This may again be due to the mounting in resin and the polishing procedure.

The signal of silicon in the region of the fire-gilded layer may come from the PropS-SH coating while at the same time it may be due to the SiC particles used in the polishing procedure (as observed for the uncoated sample, Fig. 26). PropS-SH may also not be the source of the sulphur depicted in the SEM-EDS maps, as its signal overlaps with lead which is known to accumulate in the gold layer.

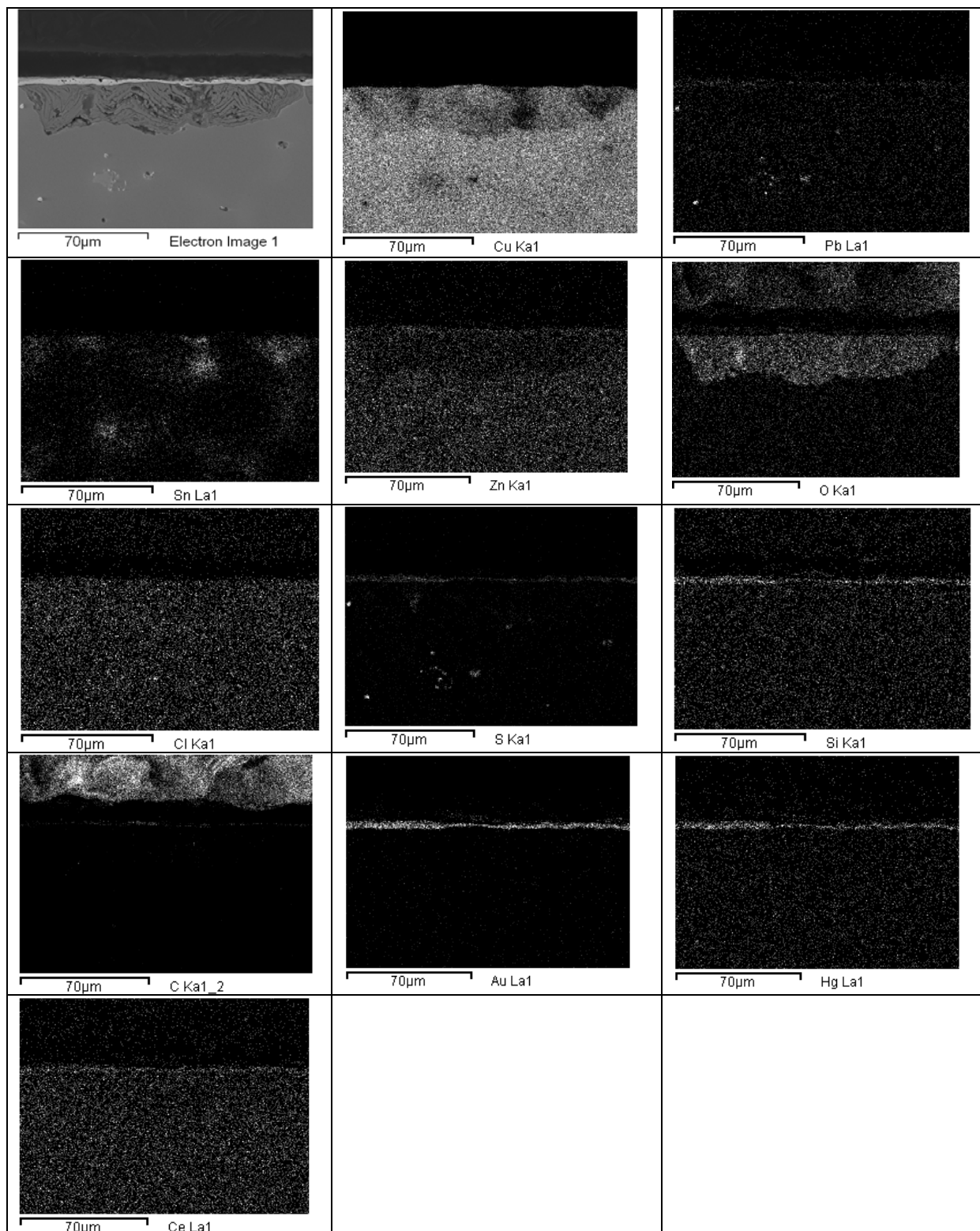


Fig. 26. BSE and X-Ray maps of a corrosion site in the GDPC (gilded aged for 30 days, coated with PropS-SH and CeO<sub>2</sub> nanoparticles and aged another 30 days) sample

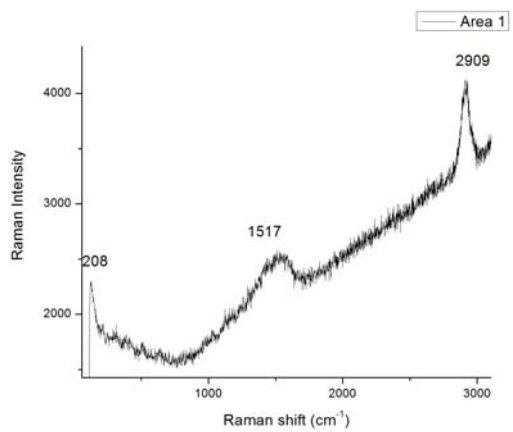


Fig. 27a.

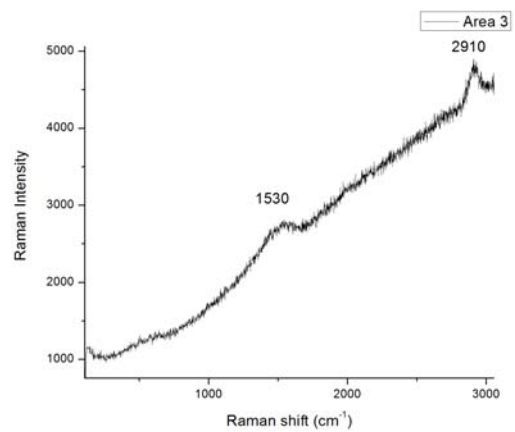


Fig. 27c.

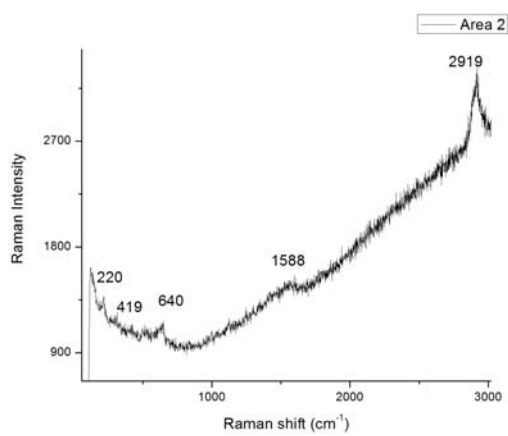


Fig. 27b.

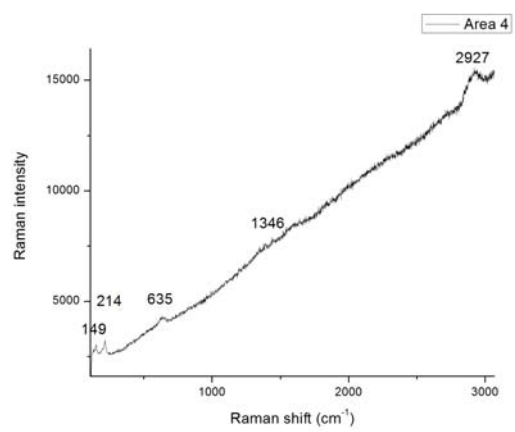


Fig. 27d.

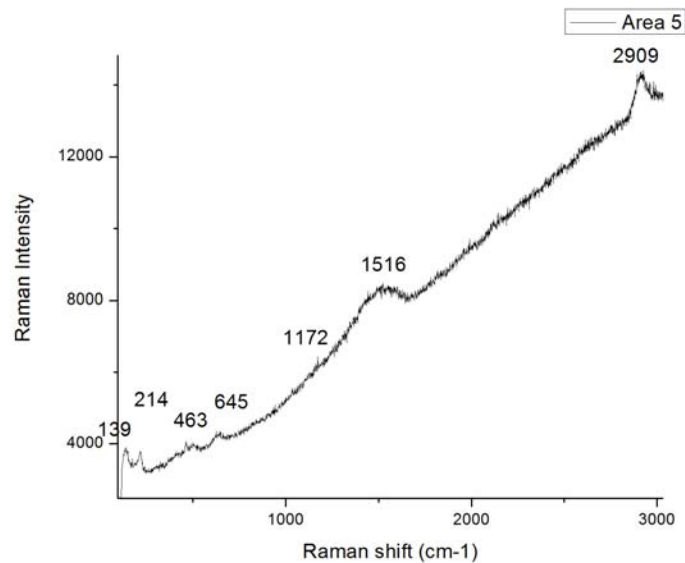


Fig. 27e.

Fig. 27. Raman spectra of the corrosion products from different regions in the GDPC (gilded aged for 30 days, coated with PropS-SH and CeO<sub>2</sub> nanoparticles and aged another 30 days) sample

As in the case of the GD sample, the GDPC sample showed a lot of fluorescence in the Raman spectra. One of the more pronounced features however was the band centered at 2910 cm<sup>-1</sup> that comes from the PropS-SH coating. The band that corresponds to cuprite also appears, with a very low intensity, in figures 27c-e.

In each figure the bands correspond to the compounds as follows:

- Fig. 27a: PropS-SH
- Fig. 27b: PropS-SH
- Fig. 27c: cuprite and PropS-SH
- Fig. 27d: cuprite and PropS-SH
- Fig. 27e: cuprite and PropS-SH

Therefore, also in this case, the main compound detected by Raman in cross-section is cuprite.

### 3.3.2. Gravimetric measurements and metal release (pre-patinated samples)

Again the evolution of the samples was monitored in terms of mass variations and metal release. The results obtained in this cycle are affected by the different morphologies of the gilded layer on which the protective coatings are applied, as discussed in the previous section.

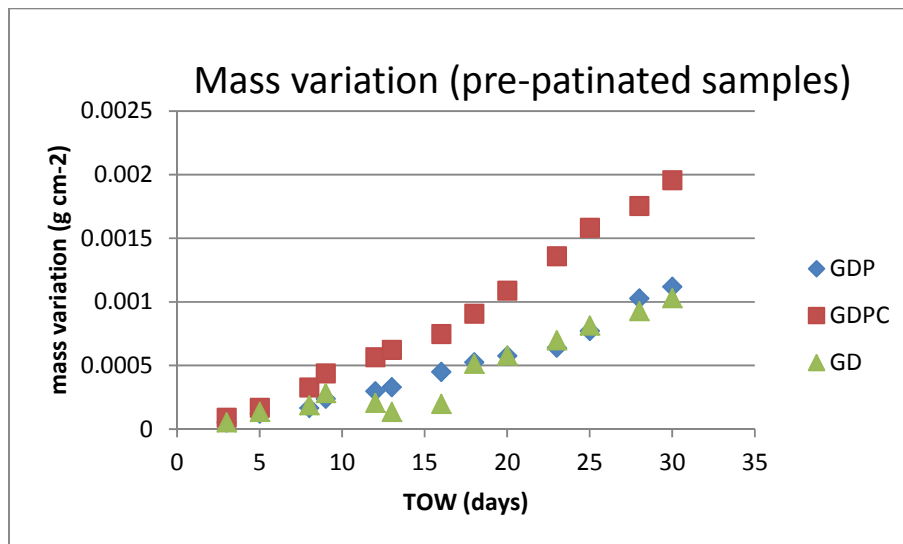


Fig. 28. Negative mass variation (mass loss) of GD (aged gilded, uncoated), GDP (aged gilded, coated with PropS-SH) and GDPC (aged gilded, coated with PropS-SH+CeO<sub>2</sub>) samples during the second ageing cycle, normalized to the surface as a function of the time of wetness (TOW)

The graph in figure 28 shows that the mass loss values of GD and GDP are overlapping, therefore the PropS-SH coating is not able to limit mass variation when applied on pre-patinated gilded surfaces. The GDPC sample shows mass variation values that are even higher than those observed for the uncoated sample (GD). In this case, the influence of the substrate (morphology/porosity of the gilded layer) may have been higher than that of the coating. Further investigations are in progress for a better understanding of this issue.

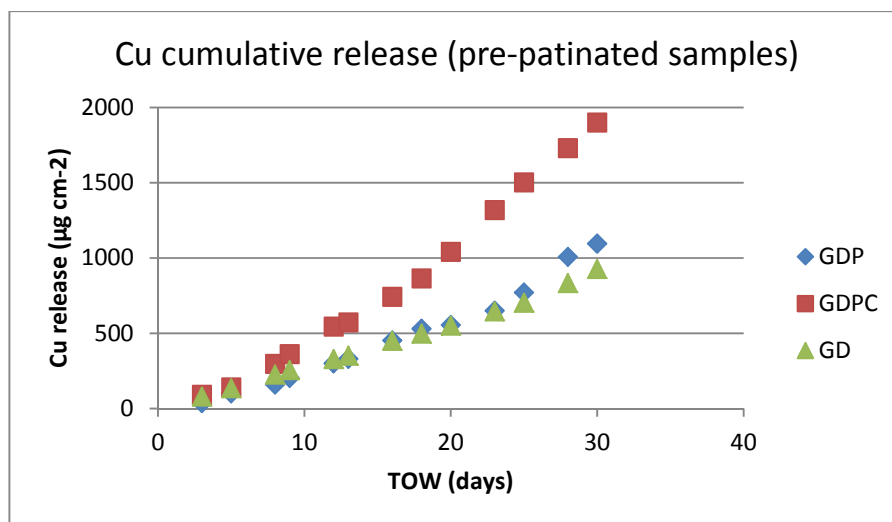


Fig. 29. The cumulative Cu release of GD (aged gilded, uncoated), GDP(aged gilded, coated with PropS-SH) and GDPC (aged gilded, coated with PropS-SH+ CeO<sub>2</sub>) samples during the second ageing cycle, normalized to the surface as a function of the time of wetness(TOW)

The graph in Fig 29 shows that the PropS-SH-based coatings are not able to limit Cu release, when applied on the pre-patinated gilded surface. While the release of copper from the PropS-SH coated sample (GDP) is comparable to the uncoated one (GD, where the gold layer is thin but very compact and continuous, Fig. 29), the Cu release from, GDPC(coated with PropS-SH + CeO<sub>2</sub>) is much higher. Further investigations are needed in order to understand if these results are due to defects in the organosilane film (e.g. low thickness, discontinuities) or to defects in the gilded layer.

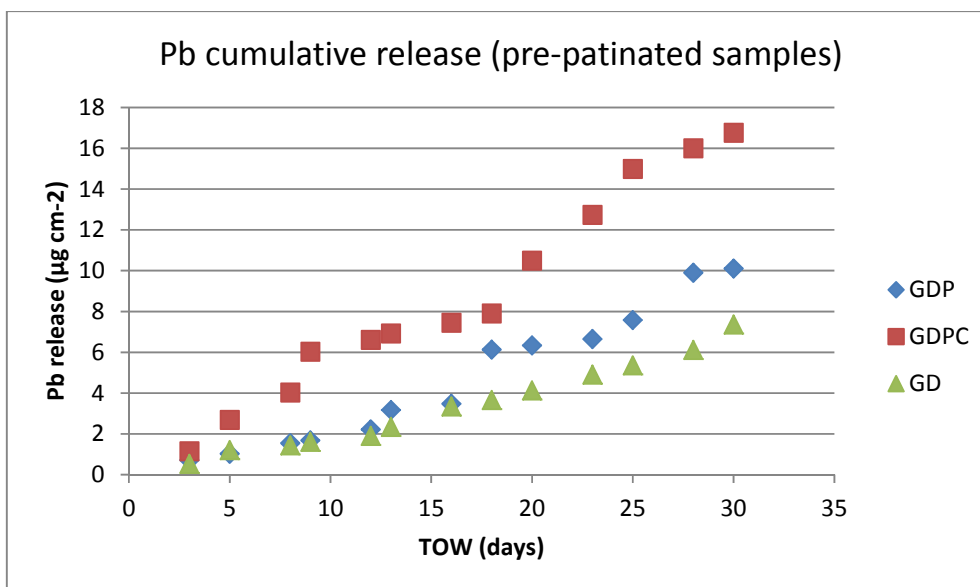


Fig. 30. The cumulative Pb release of GD (aged gilded, uncoated), GDP(aged gilded, coated with PropS-SH) and GDPC (aged gilded, coated with PropS-SH+ CeO<sub>2</sub>) samples during the second ageing cycle, normalized to the surface as a function of the time of wetness(TOW)

In regards to Pb release, we again see that the PropS-SH based coatings are not able to limit the release of this element from the pre-patinated gilded surface to the ageing solution. This behavior was already observed when the PropS-SH coating was applied on the as-gilded surface (section 3.2.5.) as well as in non-gilded bronzes [20], where this behavior may be attributed to weaker interactions between PropS-SH and lead globules in interdendritic areas, enriched with Sn (which also has a weaker interaction with PropS-SH than Cu). In the case of a gilded bronze, the surface/coating interaction mechanism will be the subject of further investigations.

### 3.4. Conclusions

Long-term dropping tests (in runoff conditions) are able to reproduce corrosion morphologies comparable to those observed in reference historical amalgam-gilded bronzes (craters and blisters at the gold/bronze interface).

Therefore, long-term dropping tests can be used both for assessing the protectiveness of coatings as well as for pre-patination of gilded layer before the application of protective coatings, so as to produce substrates that are representative of real conservation interventions.

In the present work, organosilane coatings (3-mercaptopropyl-trimethoxy-silane (PropS-SH)) were applied on both as-gilded and pre-patinated gilded bronze, and then aged by long-term dropping tests (TOW=30 days). The following conclusions can be drawn:

- PropS-SH is able to limit mass decrease and metal release when applied on as-gilded bronze (however, the organosilane coating has a beneficial influence on Cu release only)
- PropS-SH and PropS-SH+CeO<sub>2</sub> are not able to limit mass decrease and metal release when applied on pre-patinated bronze.
- A strong influence of gilder layer thickness and morphology on the overall corrosion process was observed.

## 4. Laser treatment for the removal of aged organosilane coatings

### 4.1 Materials and methods

In the course of this study, gilded bronze samples coated with organosilane coatings underwent a laser cleaning treatment in order to assess the efficiency of the removal of PropS-SH after ageing by accelerated corrosion testing in runoff conditions (dropping test, as described in section 2.3). The first type of sample was a fire-gilded bronze coated with PropS-SH + CeO<sub>2</sub> nanoparticles that underwent a short-term ageing cycle (TOW=10 days). The second type of sample was fire-gilded bronze protected with PropS-SH and aged for a long-term ageing cycle (TOW=30 days).

Paper masks were made from plotting paper and placed on the gilded surface of the bronze samples. Within the paper masks, squares of 4 mm by 4 mm were cut, in order to indicate the sites where to place the laser spot and to facilitate the analysis of the same area before and after laser treatment. 8 squares were cut for 8 laser cleaning tests on each sample. Also, in the gilded bronze sample coated with PropS-SH + CeO<sub>2</sub>, an area outside the paper mask was left available for initial tests, aiming at the identification of the best laser treatment conditions (calibration area). A scheme of the sample and paper mask is available in figure 1.

The laser cleaning treatment was carried out at the Institute of Applied Physics “Nello Carrara” (CNR Sesto Fiorentino (FI)) by Dr. Marta Mascalchi and Dr. Andrea Azeglio Mencaglia. For the spot sites indicated in the paper mask diagram from 1 to 7, a Nd:YAG LQS laser was used. The Nd:YAG LQS laser works at a wavelength of  $\lambda=1064$  nm and pulse duration of  $\tau_L=120$  ns. The variation of the fluence was obtained by using the same laser spot size by and by, only changing the energy by optical filters. In the spot site designated with the number 8, a Er:YAG FR laser was employed, that works at a wavelength of  $\lambda=2940$  nm and pulse duration of  $\tau_L=400$  ns. The visible spots on the laser treated surface were obtained with 5 laser pulses, locally wetting the surface inside the paper mask with ethanol.

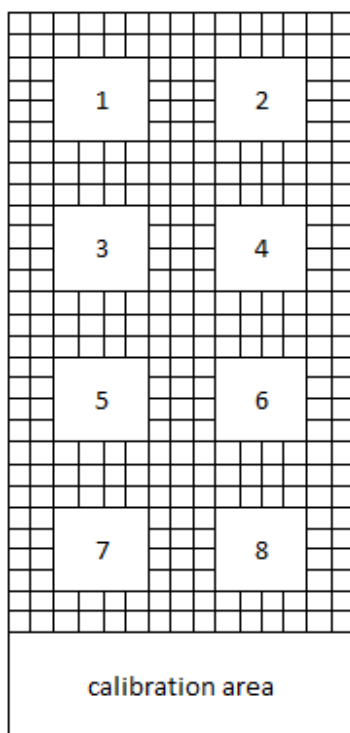


Fig. 1. Scheme of the paper mask placed on the surface of the gilded bronze sample in order to conduct the laser cleaning studies

## 4.2 Results

The efficiency of the laser cleaning treatment was assessed on the basis of SEM/EDS analysis of the surface of the gilded bronze samples, before and after the procedure. The studies aimed to give a qualitative determination of the efficiency in two ways: the first by comparing the chemical composition of the surface before and after the treatment and the second by comparing the surface morphologies.

### 4.2.1. Gilded bronze sample coated with PropS-SH+CeO

Laser cleaning was performed on the gilded bronze coupon that was coated with PropS-SH + CeO<sub>2</sub> nanoparticles and then submitted to dropping test (TOW=10 days). Table 1 shows the sample after the laser cleaning treatment, indicating the type of laser and fluence used in each area where tests were conducted.

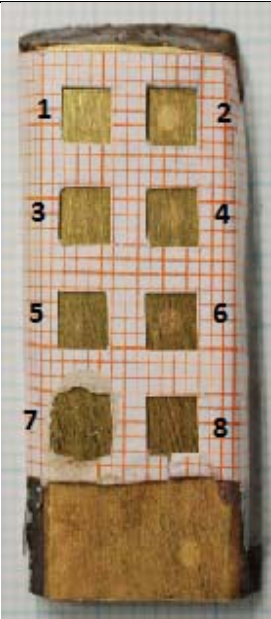
Photo of the laser cleaned sample	Area	Laser	Fluence(J/cm <sup>2</sup> )
	1	Nd:YAG	1.05
	2	Nd:YAG	1.65
	3	Nd:YAG	1.15
	4	Nd:YAG	0.80
	5	Nd:YAG	0.75
	6	Nd:YAG	0.60
	7	Nd:YAG	0.55
	8	Er:YAG	5.65

Table 1. The bronze gilded sample coated with PropS-SH + CeO<sub>2</sub> and aged for 10 days after the laser cleaning treatment, indicating the type of laser and fluence used in each site

As can be seen from the photo in table 1, in some cases (areas 2,4,6), the laser treatment has changed the properties of the gilded bronze surface in a way that is observable with the naked eye. The SEM/EDS studies carried out on the sample aimed to determine if the changes in the surface properties are due only to the removal of the silane coating or due to modifications that affected also the gilding.

In the following figures and tables, SEM images of the treated areas and EDS data for elemental composition (wt%) are compared before (Fig. AN, BN) and after (Fig. CN, DN) the laser treatment in each of the N square areas (with N from 1 to 8 as in Table 1). For most values, a relative standard deviation of about 5% (as a maximum value) can be considered.

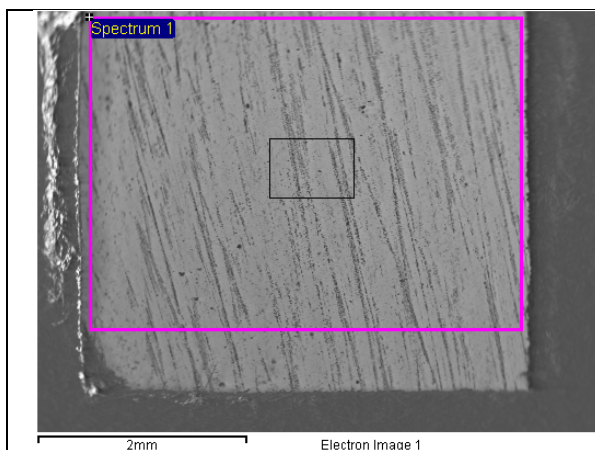


Fig. A1. BSE low magnification image before laser cleaning indicating with a black square where the high magnification image was taken

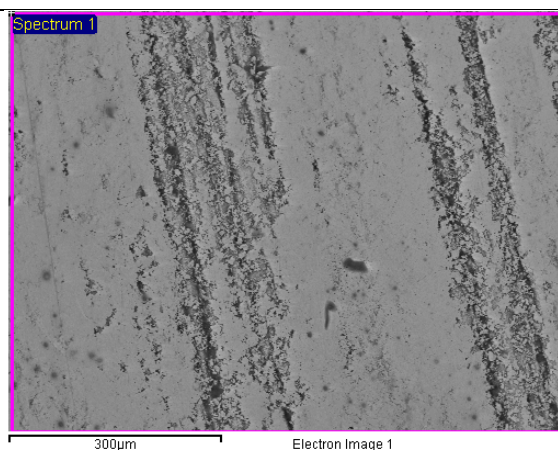


Fig. B1. BSE high magnification image before laser cleaning

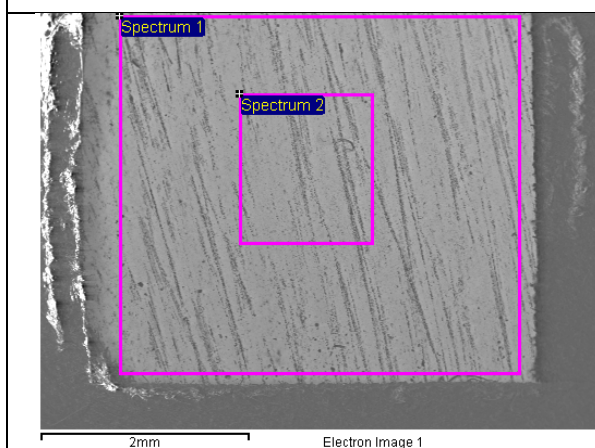


Fig. C1. BSE low magnification image after laser cleaning; spectrum 2 indicates where the spectrum relevant for laser cleaning was taken

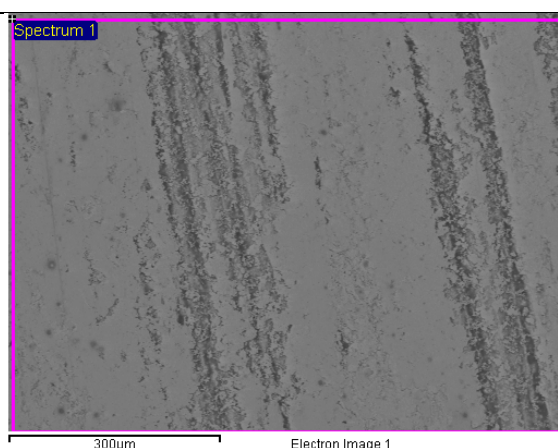


Fig. D1. BSE image of the same area as in Fig. C1. after laser cleaning

<b>Figure</b>	<b>C</b>	<b>O</b>	<b>Si</b>	<b>S</b>	<b>Cu</b>	<b>Zn</b>	<b>Sn</b>	<b>Ce</b>	<b>Au</b>	<b>Hg</b>	<b>Pb</b>
A1	14.2	11.4	1.7	2.2	2.4	0.0	0.1	0.3	59.3	7.4	0.9
B1	12.8	10.3	1.3	1.9	2.7	0.2	0.3	0.2	62.6	6.7	1.2
C1spect. 1	12.7	11.0	1.5	2.5	2.5				61.8	6.7	1.4
C1spect. 2	11.1	10.3	1.3	1.7	2.6			0.45	62.1	7.9	2.4
D1	10.8	11.2		1.4	2.8		0.2		63.8	7.9	1.9

Table 2. Elemental composition (measured by EDS, wt%) of different regions of the 1<sup>st</sup> square within the paper mask(Nd:YAG LQS, fluence 1.05 J/cm<sup>2</sup>) for the sample coated with PropS-SH + CeO<sub>2</sub> aged 10 days

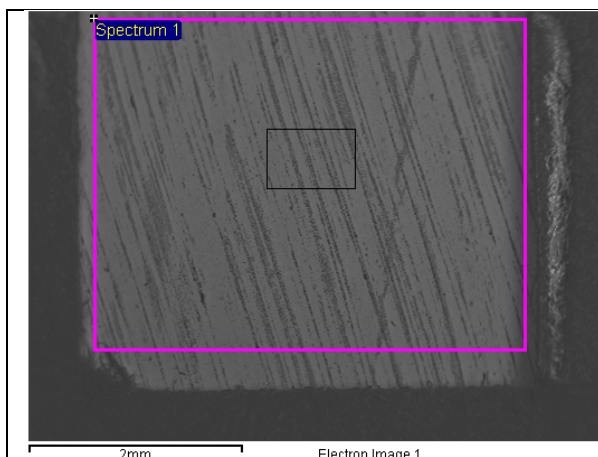


Fig. A2 BSE low magnification image before laser cleaning indicating with a black square where the high magnification image was taken

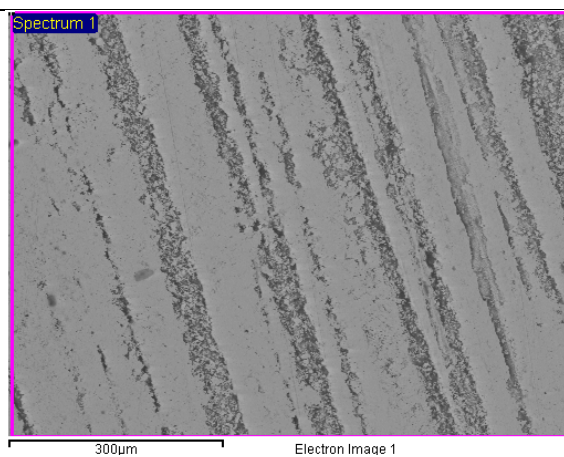


Fig. B2. BSE high magnification image before laser cleaning

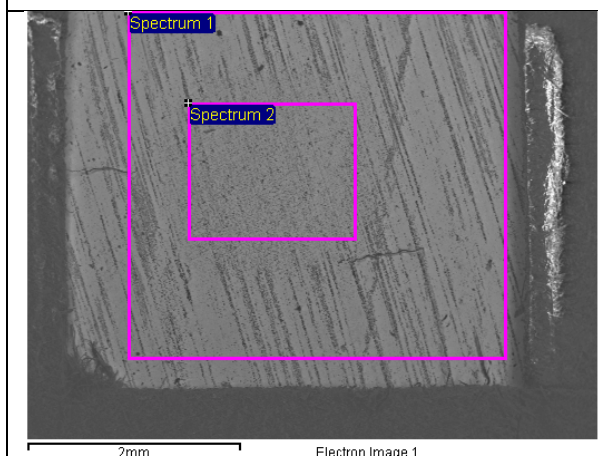


Fig. C2. BSE low magnification image after laser cleaning; spectrum 2 indicates where the spectrum relevant for laser cleaning was taken

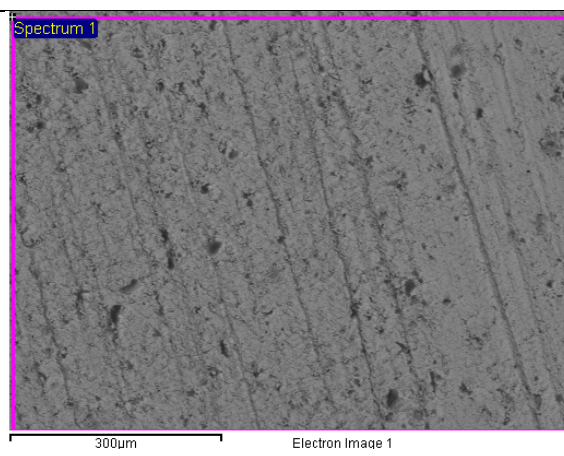


Fig. D2. BSE image of the same area as in Fig. 2. after laser cleaning

Figure	C	O	Si	S	Cl	Cu	Sn	Ce	Au	Hg	Pb
A2	15.2	8.0	0.9	1.0	0.0	2.1	0.0		66.9	6.0	
B2	14.6	8.1		0.5	0.20	2.2	0.3	0.1	64.2	8.6	1.2
C2spect. 1	12.8	8.4		1.1		4.2	0.5		67.7	5.3	
C2spect. 2	9.6	3.8				6.9	0.4	0.0	67.1	9.8	2.5
D2	11.6	3.7				9.4		0.1	67.6	6.4	1.3

Table 3. Elemental composition (measured by EDS, wt%) of different regions of the 2<sup>nd</sup> square within the paper mask(Nd:YAG LQS, fluence 1.65 J/cm<sup>2</sup>) for the sample coated with PropS-SH + CeO<sub>2</sub> aged 10 days

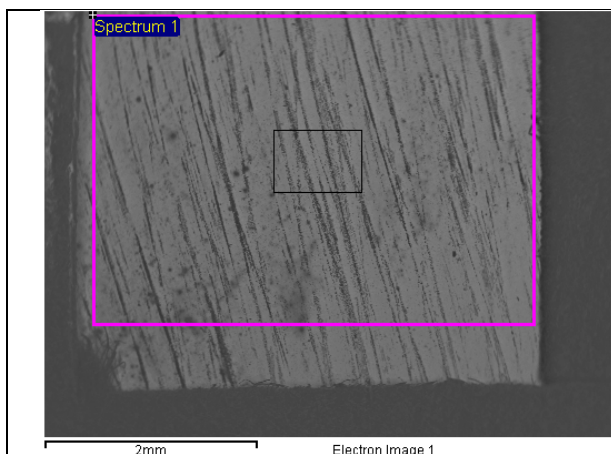


Fig. A3 BSE low magnification image before laser cleaning indicating with a black square where the high magnification image was taken

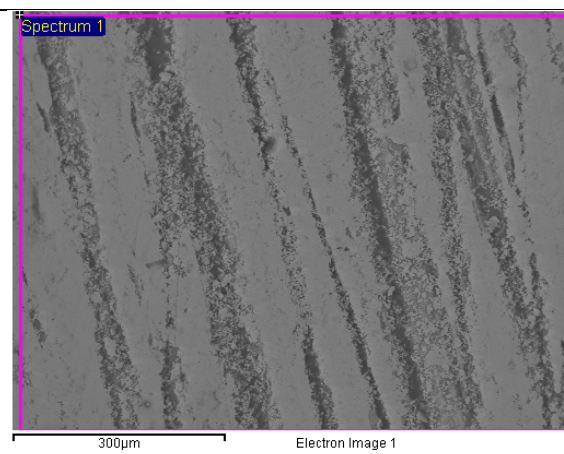


Fig. B3. BSE high magnification image before laser cleaning

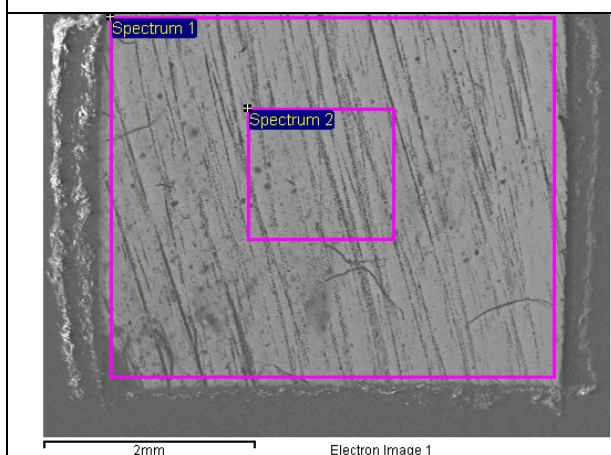


Fig. C3. BSE low magnification image after laser cleaning; spectrum 2 indicates where the spectrum relevant for laser cleaning was taken

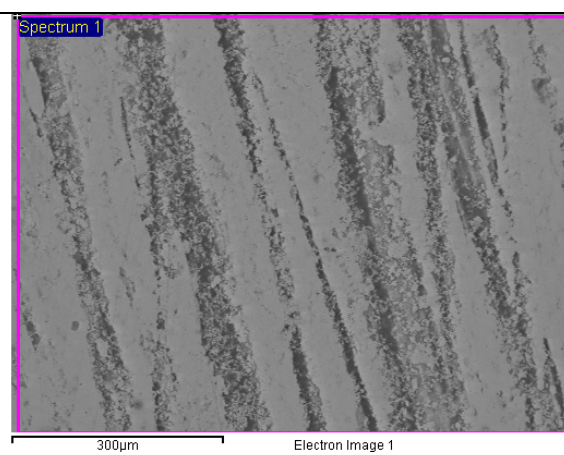


Fig. D3. BSE image of the same area as in Fig. 2. after laser cleaning

Figure	C	O	Si	S	Cl	Cu	Zn	Sn	Ce	Au	Hg	Pb
A3	14.1	12.8	2.6	4.1	0.0	2.6	0.1	0.2		57.3	5.1	1.0
B3	14.3	12.2	2.1	3.0	0.2	3.3		0.2	0.6	58.5	5.4	0.4
C3spect. 1	15.3	15.1	2.5	4.0		2.5			0.2	55.2	4.8	0.5
C3spect. 2	13.5	12.9	2.2	3.1		2.5		0.2	0.1	58.5	5.5	1.6
D3	13.7	12.9	1.7	2.6		3.3			0.1	59.2	5.6	0.9

Table 4. Elemental composition (measured by EDS, wt%) of different regions of the 3<sup>rd</sup> square within the paper mask(Nd:YAG LQS, fluence 1.15 J/cm<sup>2</sup>) for the sample coated with PropS-SH + CeO<sub>2</sub> aged 10 days

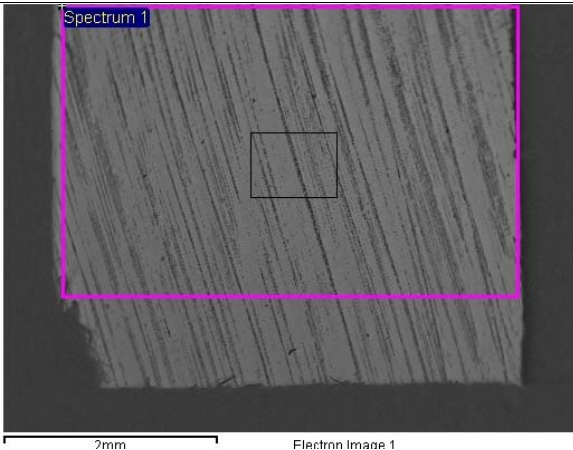


Fig. A4 BSE low magnification image before laser cleaning indicating with a black square where the high magnification image was taken

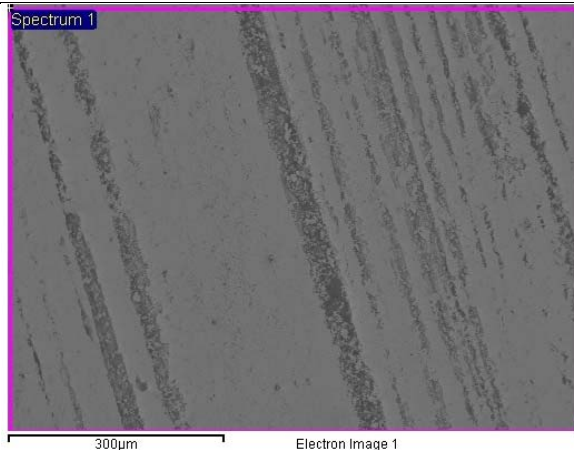


Fig. B4. BSE high magnification image before laser cleaning

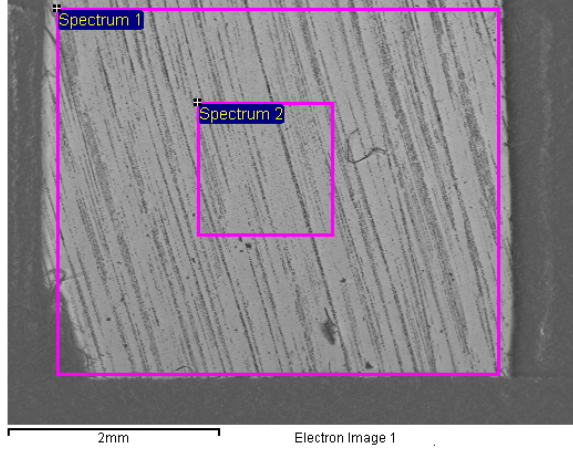


Fig. BSE low magnification image after laser cleaning; spectrum 2 indicates where the spectrum relevant for laser cleaning was taken

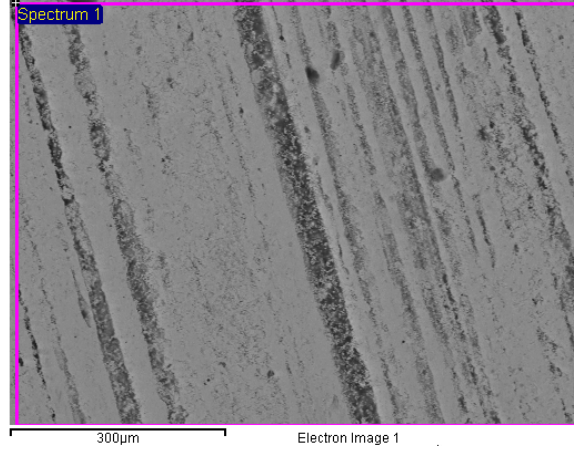


Fig. D4. BSE image of the same area as in Fig. 2. after laser cleaning

Figure	C	O	Si	S	Cl	Cu	Zn	Sn	Ce	Au	Hg	Pb
A4	12.6	11.4	1.7	2.		3.4	0.0		0.1	62.1	6.1	0.5
B4	13.2	9.0	1.4	2.3	0.1	3.8	0.0	0.1	0.3	64.2	4.9	0.6
C4spect. 1	12.7	10.3	1.4	1.3		3.6			0.1	62.6	6.6	1.3
C4spect. 2	11.0	9.0		1.0		4.3		0.2	0.0	65.1	8.0	1.4
D4	11.6	6.4	1.0	1.0		4.3		0.5		66.2	7.5	1.6

Table 5. Elemental composition (measured by EDS, wt%) of different regions of the 4<sup>th</sup> square within the paper mask(Nd:YAG LQS, fluence 0.80 J/cm<sup>2</sup>) for the sample coated with PropS-SH + CeO<sub>2</sub> aged 10 days

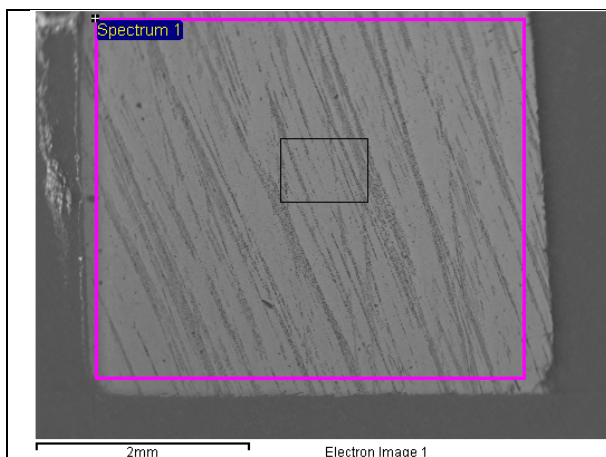


Fig. A5 BSE low magnification image before laser cleaning indicating with a black square where the high magnification image was taken

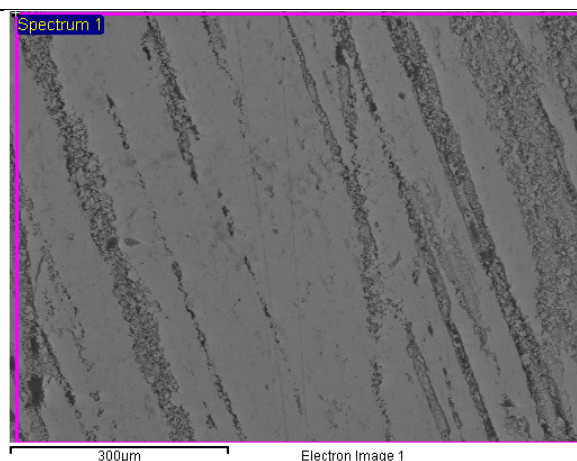


Fig. B5. BSE high magnification image before laser cleaning

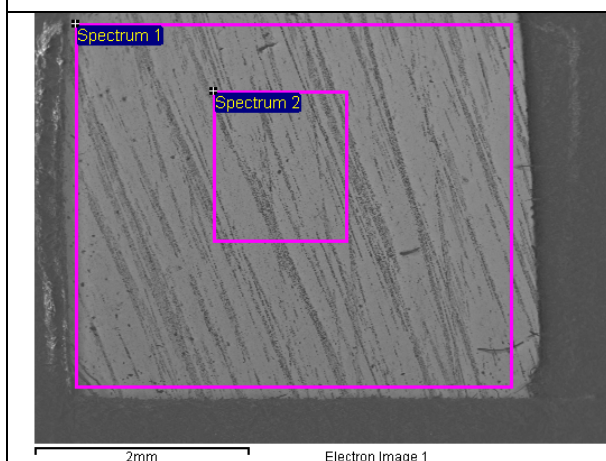


Fig. C5. BSE low magnification image after laser cleaning; spectrum 2 indicates where the spectrum relevant for laser cleaning was taken

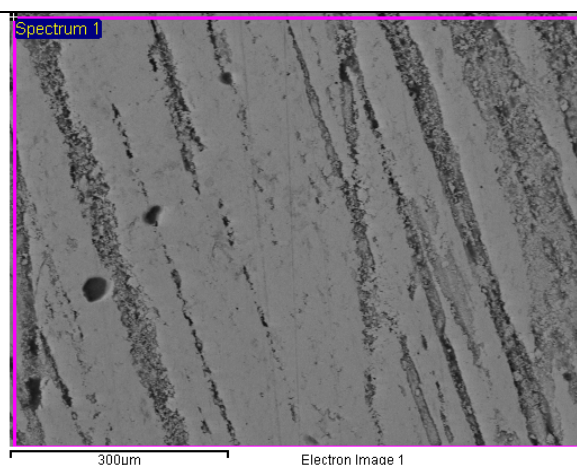


Fig. D5. BSE image of the same area as in Fig. 2. after laser cleaning

Figure	C	O	Si	S	Cl	Cu	Zn	Sn	Ce	Au	Hg	Pb
A5	13.2	9.6		0.5	0.3	3.7	0.1	0.2		62.6	8.4	1.6
B5	13	9.1	1.0	0.7	0.2	4.8	0.0		0.3	61.8	7.6	2.0
C5spect. 1	14.3	9.4	1.1	1.6		3.5		0.2	0.1	64.6	4.7	0.5
C5spect. 2	11.9	9.7		1.0		3.5		0.2		64.8	7.8	1.2
D5	10.6	9.1	1.3	0.8		4.5		0.1		65.7	6.1	1.9

Table 6. Elemental composition (measured by EDS, wt%) of different regions of the 5<sup>th</sup> square within the paper mask(Nd:YAG LQS, fluence 0.75 J/cm<sup>2</sup>) for the sample coated with PropS-SH + CeO<sub>2</sub> aged 10 days

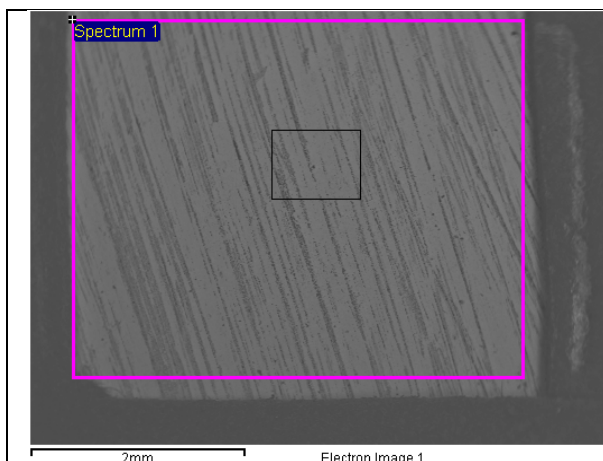


Fig. A6 BSE low magnification image before laser cleaning indicating with a black square where the high magnification image was taken

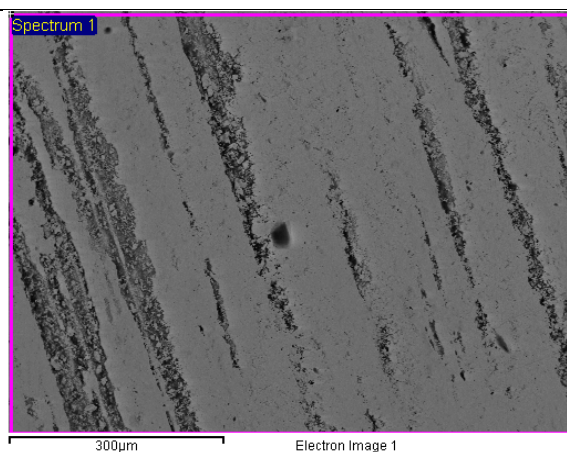


Fig. B6. BSE high magnification image before laser cleaning



Fig. C6. BSE low magnification image after laser cleaning; spectrum 2 indicates where the spectrum relevant for laser cleaning was taken

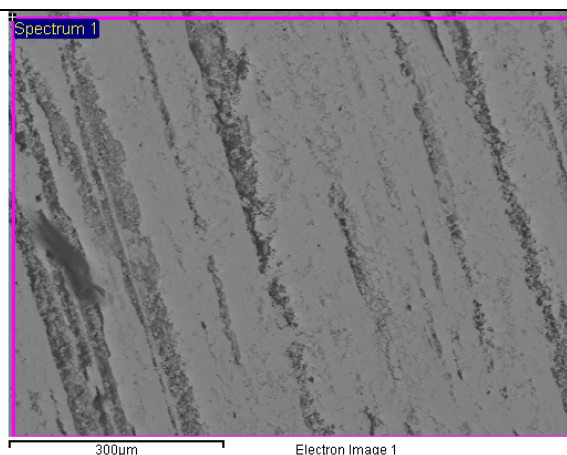


Fig. D6. BSE image of the same area as in Fig. C6. after laser cleaning

Figure	C	O	Si	S	Cu	Sn	Ce	Au	Hg	Pb
A6	11.7	9.0	1.1	1.5	4.4	0.1		66.8	5.3	
B6	12.0	7.4		0.7	3.9	0.2	0.2	66.7	7.7	1.2
C6spect. 1	12.4	8.8		0.8	4.0	0.3		65.7	7.1	1.0
C6spect. 2	10.3	7.8	1.0	1.3	4.7		0.0	67.7	6.1	1.1
D6	11.7	8.2	1.5	4.1			0.3	66.8	6.1	1.3

Table 7. Elemental composition (measured by EDS, wt%) of different regions of the 6<sup>th</sup> square within the paper mask(Nd:YAG LQS, fluence 0.60 J/cm<sup>2</sup>) for the sample coated with PropS-SH + CeO<sub>2</sub> aged 10 days

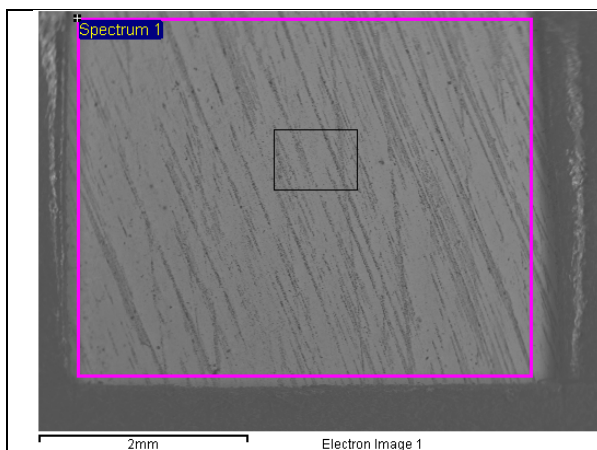


Fig. A7 BSE low magnification image before laser cleaning indicating with a black square where the high magnification image was taken

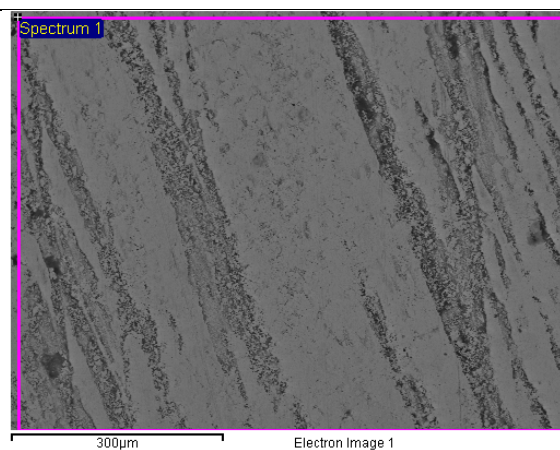


Fig. B7. BSE high magnification image before laser cleaning

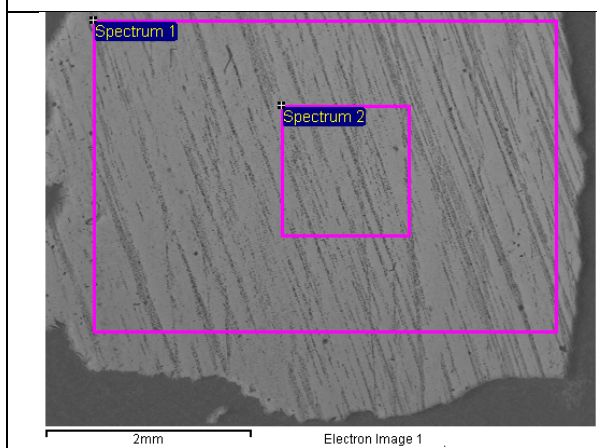


Fig. C7. BSE low magnification image after laser cleaning; spectrum 2 indicates where the spectrum relevant for laser cleaning was taken

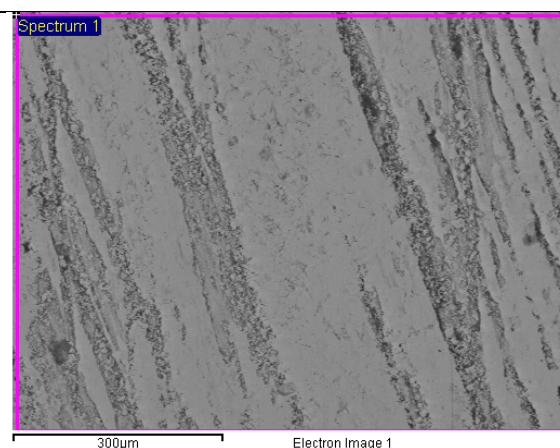


Fig. D7. BSE image of the same area as in Fig. B7. after laser cleaning

Figure	C	O	Si	S	Cl	Cu	Zn	Sn	Ce	Au	Hg	Pb
A7	13.0	10.6	1.1	1.0	0.0	3.4		0.0	0.2	61.6	7.6	1.5
B7	13.3	9.1	1.0	0.8	0.2	3.7	0.0	0.3	0.5	62.7	7.0	1.5
C7spect. 1	12.8	9.9	1.1	2.0		3.4		0.2	0.4	63.6	6.3	0.4
C7spect. 2	11.1	9.2	1.0	0.7		4.0				65.3	7.4	1.3
D7	11.6	10.1	1.1	1.7		3.7		0.4	0.1	65.5	5.3	0.5

Table 8. Elemental composition (measured by EDS, wt%) of different regions of the 7<sup>th</sup> square within the paper mask(Nd:YAG LQS, fluence 0.55 J/cm<sup>2</sup>) for the sample coated with PropS-SH + CeO<sub>2</sub> aged 10 days

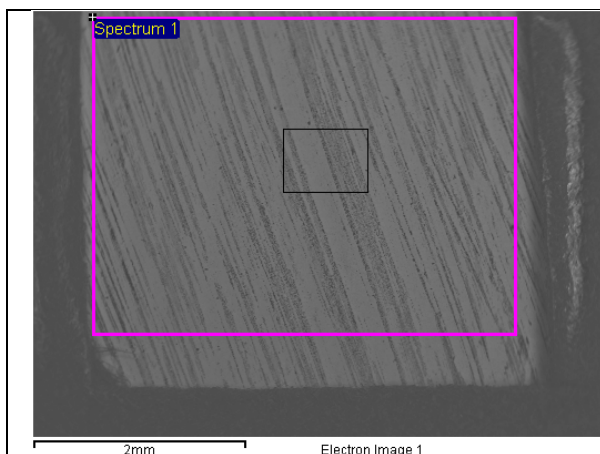


Fig. A8 BSE low magnification image before laser cleaning indicating with a black square where the high magnification image was taken

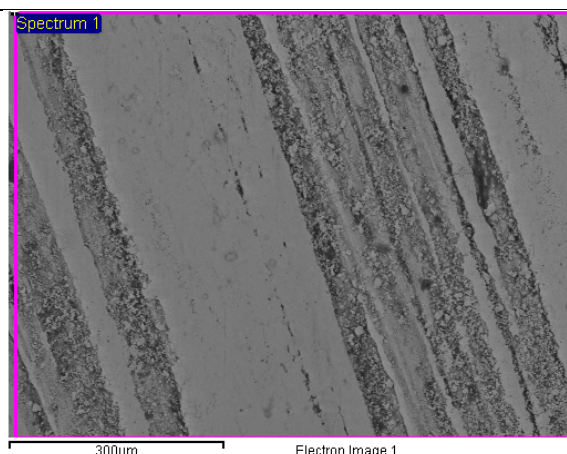


Fig. B8. BSE high magnification image before laser cleaning

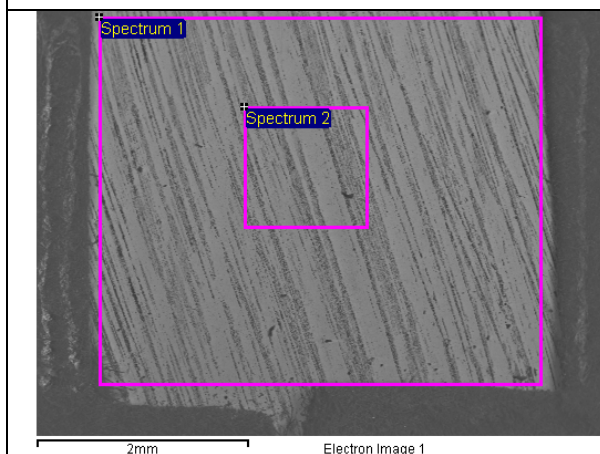


Fig. C8. BSE low magnification image after laser cleaning; spectrum 2 indicates where the spectrum relevant for laser cleaning was taken

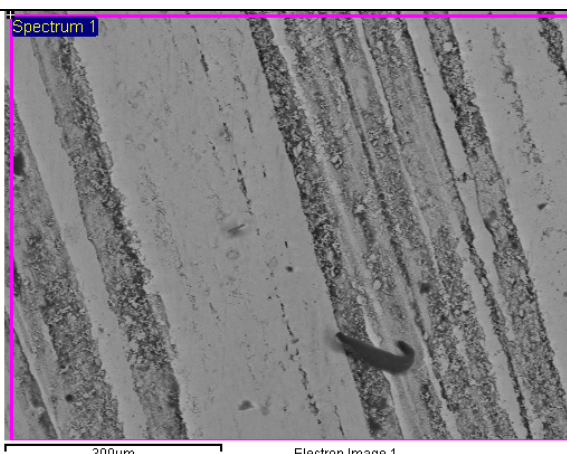


Fig. D8. BSE image of the same area as in Fig. 2. after laser cleaning

Figure	C	O	Si	S	Cl	Cu	Zn	Sn	Ce	Au	Hg	Pb
A8	13.5	9.2		0.8	0.1	5.0	0.0	0.2		63.4	7.2	0.5
B8	14.7	10.0		0.9	0.1	4.9	0.3	0.2		61.4	7.2	0.5
C8spect. 1	12.9	9.0	1.0	0.3		4.2		0.3	0.4	62.1	7.5	2.3
C8spect. 2	12.6	9.6	1.2	1.3		5.2		0.6	0.0	62	6.6	1.1
D8	13.1	11.0	1.2	1.1		4.9		0.4	0.3	62.2	5.5	0.4

Table 9. Elemental composition (measured by EDS, wt%) of different regions of the 8<sup>th</sup> square within the paper mask(Er:YAG FR, fluence 5.65 J/cm<sup>2</sup>) for the sample coated with PropS-SH + CeO<sub>2</sub> aged 10 days

By comparing the spectra in regions corresponding to images of the same magnification, based on the data in Table 2, we cannot observe any changes in the elemental composition of the gilded bronze surface. The only noticeable feature is a slightly higher amount of mercury in the gold layer after the laser treatment.

For the fluence of  $1.65\text{J}/\text{cm}^2$  data displayed in Table 3, obvious changes have occurred at the level of the gilded surface, which can be identified comparing figures B2 and D2. As regards the removal of PropS-SH, EDS data in Table 3 are not conclusive because it was not possible to determine Si (element that can be used as a “marker” of the silane layer) in most areas already before the laser treatment, probably due to the low thickness of the PropS-SH +  $\text{CeO}_2$  coating.

In the case of the third square (fluence of  $1.15\text{J}/\text{cm}^2$ , Table 4), based on the elemental composition data we can observe that the surface has been relatively enriched in mercury, while the amount of silicon and sulphur has lowered after the laser cleaning, indicating the removal to some extent of the PropS-SH coating.

The removal of the PropS-SH is highlighted in the case of the fourth square (fluence of  $0.80\text{J}/\text{cm}^2$ , Table 5), as elements associated with the coating (carbon, oxygen, silicon, sulphur, cerium) are detected in lower amounts after the laser treatment, while those corresponding to the gilding (gold, mercury, lead) are detected in higher amounts, with mercury and silicon showing significant variations.

For the fifth square (fluence of  $0.75\text{J}/\text{cm}^2$ , Table 6) we cannot make any useful observations as the variation in the elemental compositions are quite small and may be influenced by surface contamination.

A comparison of the elemental composition in the surfaces before and after laser treatment (Table 7, fluence  $0.6\text{J}/\text{cm}^2$ , figures A6 and C6 spectrum 2) yields an increase in the amount of mercury and gold present in the surface and a lowering of the amount of silicon, indicating that the coating has been affected by the laser cleaning.

The values of the elemental composition in the case of square seven (Table 8, fluence  $0.55\text{J}/\text{cm}^2$ ) do not show a decrease of Si after laser treatment. S is probably affected also by corrosion, whilst Au slightly increase after the treatment.

In the case of the Er:YAG FR laser, based on the elemental analysis data shown in Table 9, there is no detectable change in the composition and morphology of the gilded surface after laser treatment. There are no variations in S or Au that indicate the removal of the PropS-SH coating.

In order to obtain a clearer picture of the efficiency of the laser cleaning treatment, the percentage variations of silicon (as an indicator of silane removal), gold and mercury (as indicators of gold layer conditions) were plotted for the tests conducted with the Nd:YAG LQS laser. The variations were determined using the following equation:

$$\Delta N\% = \frac{N_{after} - N_{before}}{N_{before}} \cdot 100$$

where the percentage variation of the concentration of element N ( $\Delta N\%$ ) is derived on the basis of the concentration of element N (wt%) measured by EDS in the same area before ( $N_{before}$ ) and after ( $N_{after}$ ) the laser treatment.

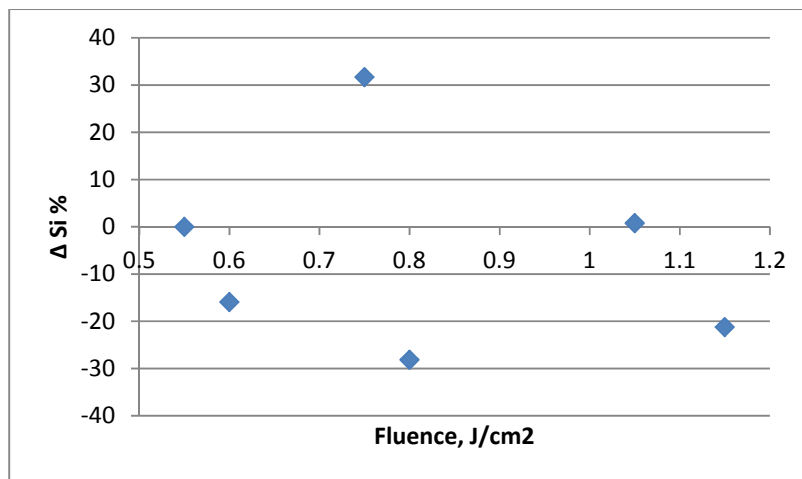


Fig. 2. The percentage variation of Si concentration ( $\Delta Si\%$ ) for the Nd:YAG LQS laser cleaning treatment as a function of fluence for the sample coated with PropS-SH+CeO<sub>2</sub> aged 10 days

Based on the graph above, there is no monotonic trend in the evolution of  $\Delta Si\%$  as a function of fluence. We can observe that for 3 fluence values (0.60, 0.80, 1.05 J cm<sup>-2</sup>), the laser

treatment has managed to remove some of the PropS-SH, as  $\Delta Si\%$  is negative. For the other 3 it has increased, meaning that the laser cleaning has had little or no effect and there might be some environmental contamination.

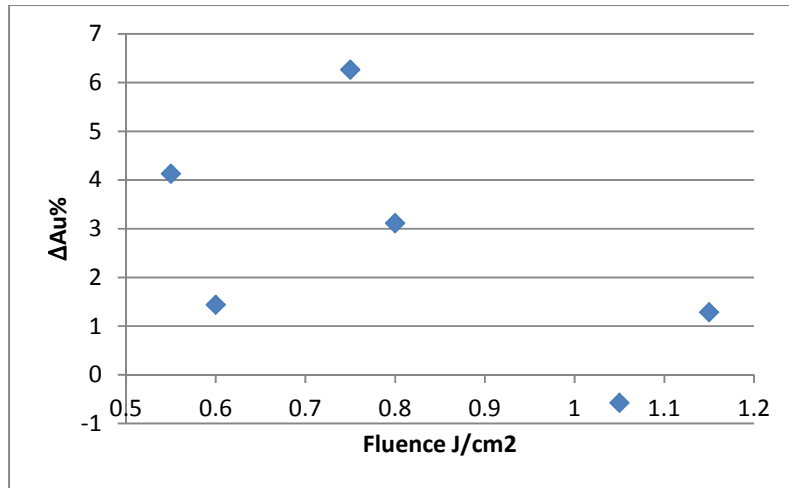


Fig. 3. The percentage variation of Au concentration ( $\Delta Au\%$ ) for the Nd:YAG LQS laser cleaning treatment as a function of fluence for the sample coated with PropS-SH+CeO<sub>2</sub> aged 10 days

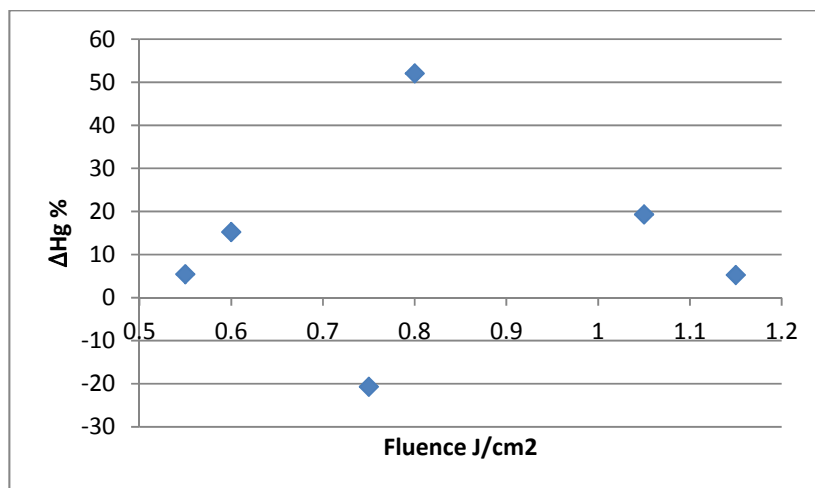


Fig. 4. The percentage variation of Hg concentration ( $\Delta Hg\%$ ) for the Nd:YAG LQS laser cleaning treatment as a function of fluence for the sample coated with PropS-SH+CeO<sub>2</sub> aged 10 days

The percentage variation of Au concentration ( $\Delta\text{Au}\%$ ) data in Figure 3 do not show a clear trend. Most of the values of  $\Delta\text{Hg}\%$  in the graph of Figure 4 are positive, indicating that the concentration of mercury increases after the laser cleaning treatment. These values however cannot be attributed only to the laser cleaning, removing the PropS-SH-based coating, but may be influenced also by the mercury that is “extracted” out of the gold layer due to laser-induced heating.

Based on these results, the morphologies of the “worst” and “best” areas (squares 2 (damage to the gold layer, fluence  $1.65 \text{ J/cm}^2$ ) and 4 (higher  $\Delta\text{Si}\%$ , fluence  $0.80 \text{ J/cm}^2$ ), respectively) were observed using SEM at high magnification.

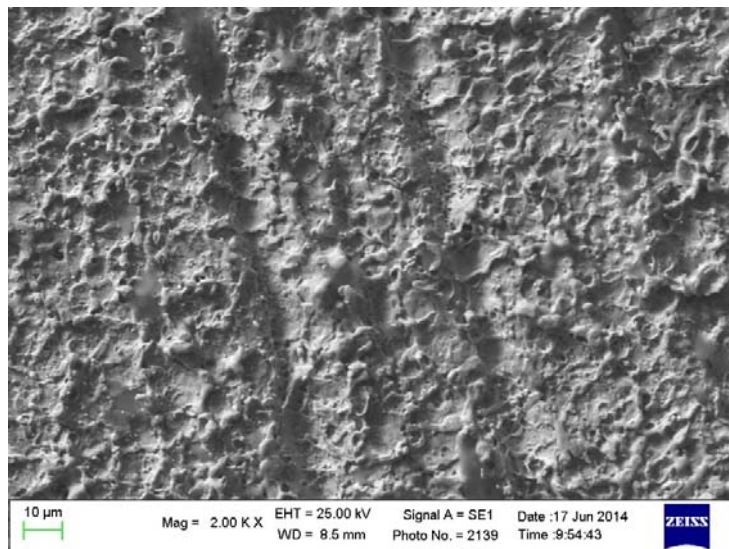


Fig. 5. High magnification BSE image of area 2, (Nd:YAG LQS, fluence  $1.65 \text{ J/cm}^2$ ) for the sample coated with PropS-SH +  $\text{CeO}_2$  aged 10 days

Figure 5 reveals a much altered morphology in area 2 (gold damage). While the silane coating, that has a tendency to accumulate in the grooves, seems to have been removed, the surface of the gilded layer has been modified dramatically also. Melting occurred at the surface level, giving an overall spongy texture which has completely replaced the smooth surface crossed by grooves observed in as-gilded samples (section 3.2.2. figure 5a). The melting is more pronounced than in any of the other sites where the laser was used, probably due to the fact that the fluence used in this site had the highest value.

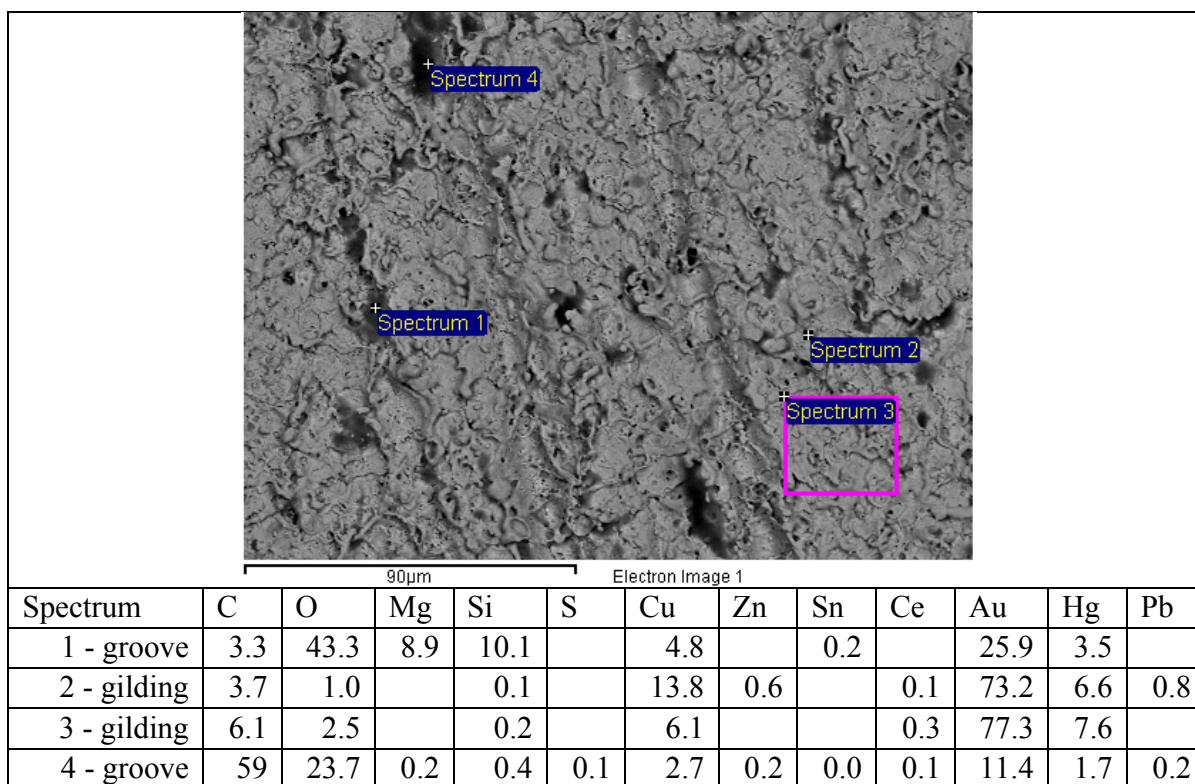


Table 10. Elemental composition of different regions (Nd:YAG LQS, fluence 1.65 J/cm<sup>2</sup>) for the sample coated with PropS-SH + CeO<sub>2</sub> aged 10 days (data for K, Ca, Sb are not shown)

The elemental composition presented in table 10 indicates that the PropS-SH+CeO<sub>2</sub> coating has been removed from the gilded surface. The only areas where it can be found is in the grooves where it is known to accumulate (section 3.2.5. figure 17) and where the thickness of the silane coating can reach several μm. The elemental composition from the other locations indicates that the mercury has been extracted out of the gold layer due to heating.

Also area 4 (with the highest Si removal efficiency, Fig. 2-ΔSi% graph) was investigated by SEM/EDS at higher magnification. In figure 6 we see that the Nd:YAG LQS laser with a fluence of 0.80 J/cm<sup>2</sup> has not affected the gilded surface to the same extent as in area 2. Melting appear to have occurred (Fig. 7), but at a much lower extent than in the previous situation (area 2). The main reason for this behavior seems to be the fact that the fluence at which the laser was used was lower in this case compared to the previous one by a factor of two.

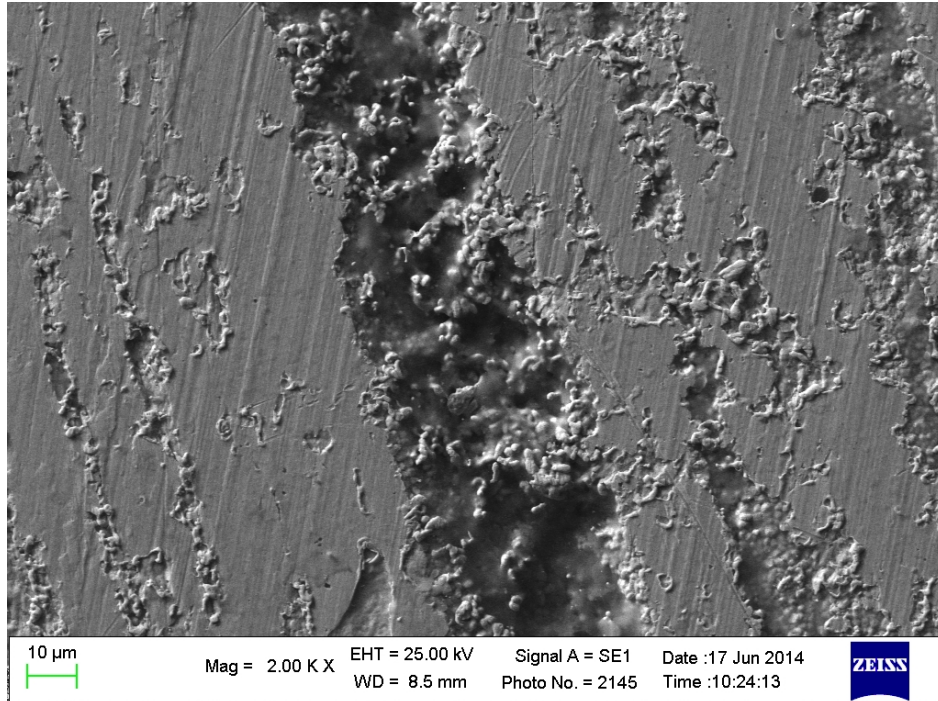


Fig. 6. High magnification BSE image of an area within the second square (Nd:YAG LQS, fluence  $0.80 \text{ J/cm}^2$ ) for the sample coated with PropS-SH +  $\text{CeO}_2$  aged 10 days

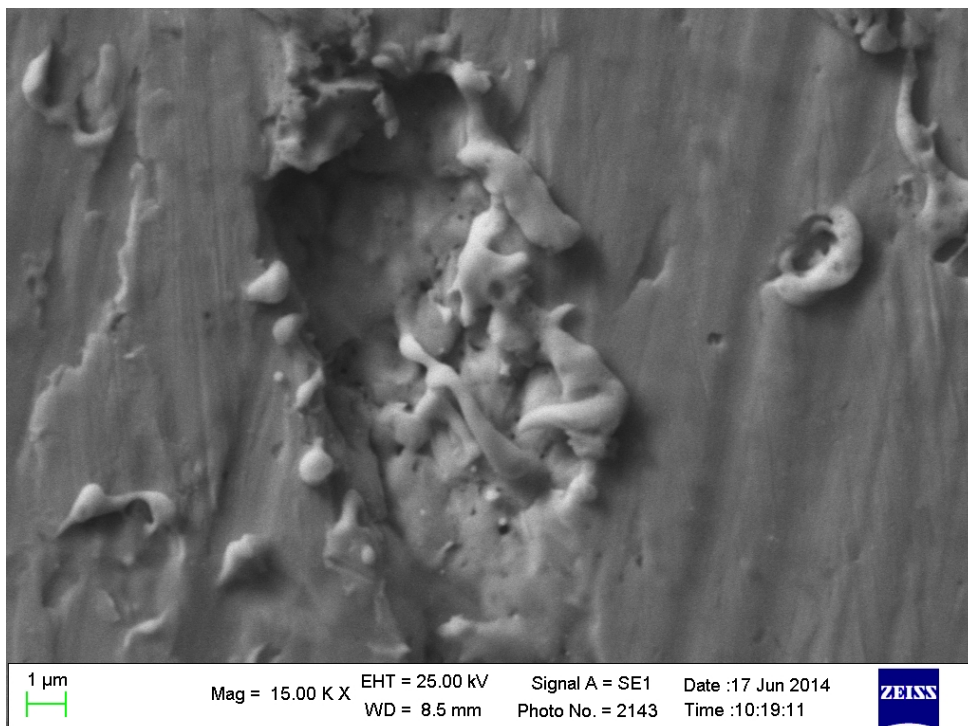


Fig. 7. High magnification BSE image of an area within the second square (Nd:YAG LQS, fluence  $0.80 \text{ J/cm}^2$ ) for the sample coated with PropS-SH +  $\text{CeO}_2$  aged 10 days

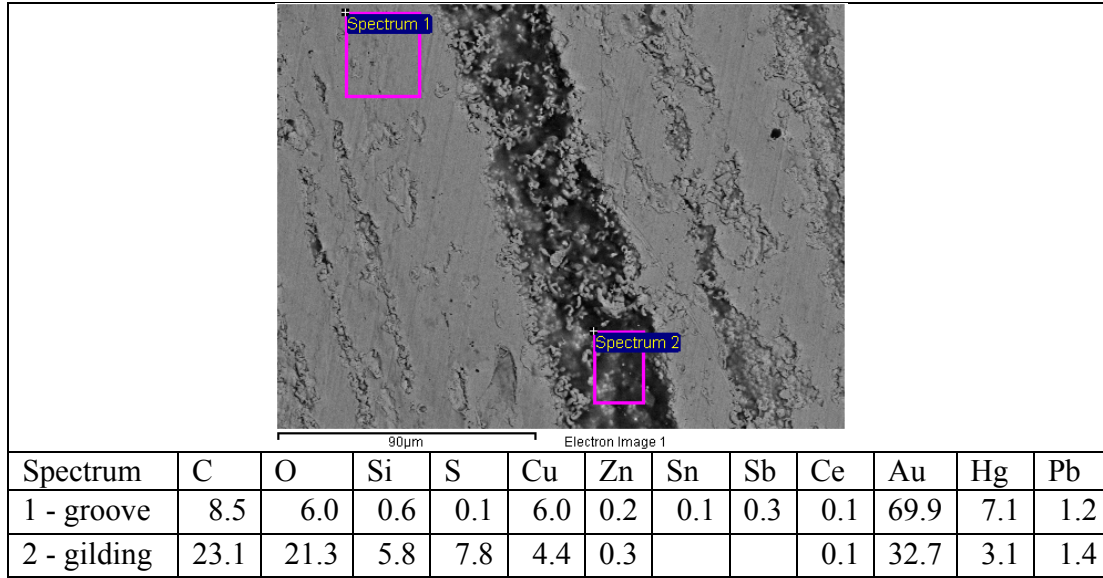


Table 11. Elemental composition (measured by EDS, wt%) of different regions (Nd:YAG LQS, fluence 0.80 J/cm<sup>2</sup>) for the sample coated with PropS-SH + CeO<sub>2</sub> aged 10 days

The elemental composition presented in table 11 indicates, as before, that traces of the PropS-SH coating still remain within the grooves of the gilding layer, even in this area where the decrease of Si concentration is the highest. This can be easily observed as nonmetal elements within the composition of PropS-SH appear in higher amounts within the areas corresponding to the groove.

#### 4.2.2. Gilded bronze sample coated with PropS-SH

Laser cleaning was performed on a fire-gilded bronze coupon that was coated with PropS-SH and then submitted to dropping test for 30 days of wetness. Table 12 shows the sample after the laser cleaning treatment indicating the type of laser and fluence used in each area where tests were conducted.

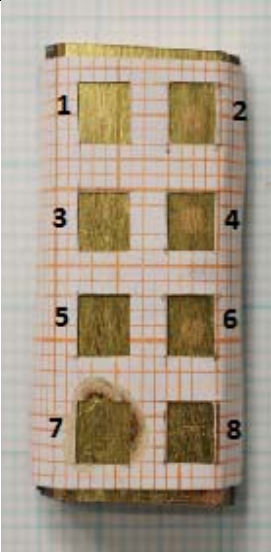
Photo of the laser cleaned sample	Area	Laser	Fluence(J/cm <sup>2</sup> )
	1	Nd:YAG	3.15
	2	Nd:YAG	1.65
	3	Nd:YAG	1.15
	4	Nd:YAG	0.80
	5	Nd:YAG	0.75
	6	Nd:YAG	0.60
	7	Nd:YAG	0.55
	8	Er:YAG	5.65

Table 12. The bronze gilded sample coated with PropS-SH and aged for 30 days of wetness after the laser cleaning treatment, indicating the type of laser and fluence used in each site

For this sample also, SEM images were taken and EDS spectra were collected, characterizing the gilded gold surface before and after the laser the laser cleaning treatment

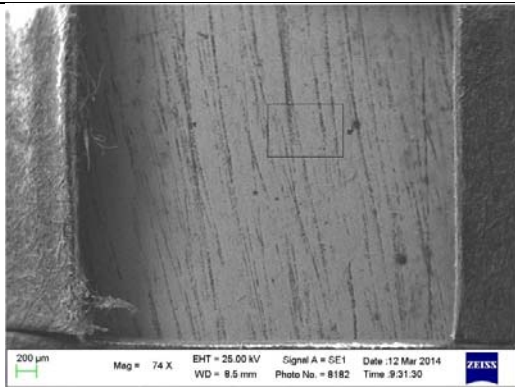


Fig. A9 BSE low magnification image before laser cleaning indicating with a black square where the high magnification image was taken

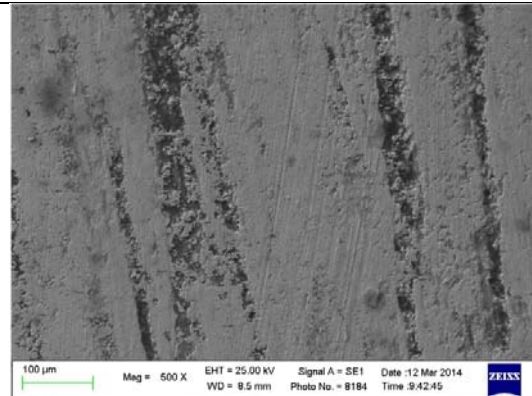


Fig. B9. BSE high magnification image before laser cleaning

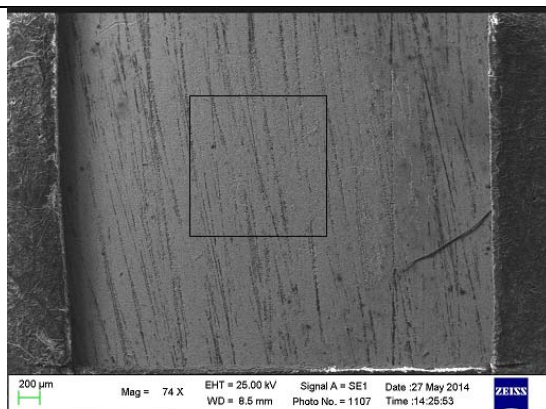


Fig. C9. BSE low magnification image after laser cleaning; spectrum 2 indicates where the spectrum relevant for laser cleaning was taken

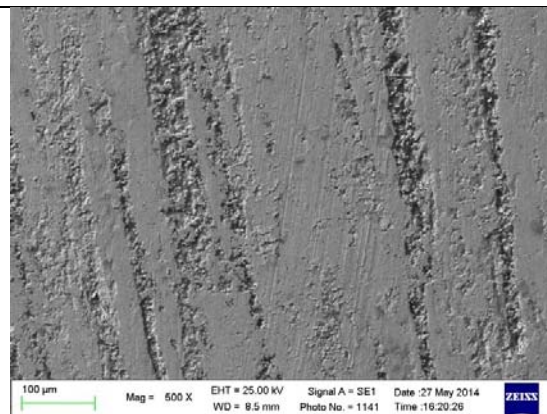


Fig. D9. BSE image of the same area as in Fig. 2. after laser cleaning

Figure	C	O	Al	Si	S	Cu	Zn	Sn	Au	Hg	Pb
A9	21.4	11.2		1.6	2.3	1.3		0.2	54.1	7.1	0.8
B9	23.0	12.3	0.1	1.6	2.5	2.1		0.0	51.4	6.6	0.4
C9spect. 1	13.8	11.2		1.8	2.2	2.5	0.3	0.3	59.3	8.3	0.4
C9spect. 2	12.0	8.5		1.1	0.8	2.5			65.1	8.8	1.3
D9	12.6	9.7		1.0	1.2	2.1			62.6	9.5	1.4

Table 13. Elemental composition (measured by EDS, wt%) of different regions of the 1<sup>st</sup> square within the paper mask(Nd:YAG LQS, fluence 3.15 J/cm<sup>2</sup>) for the sample coated with PropS-SH aged 30 days

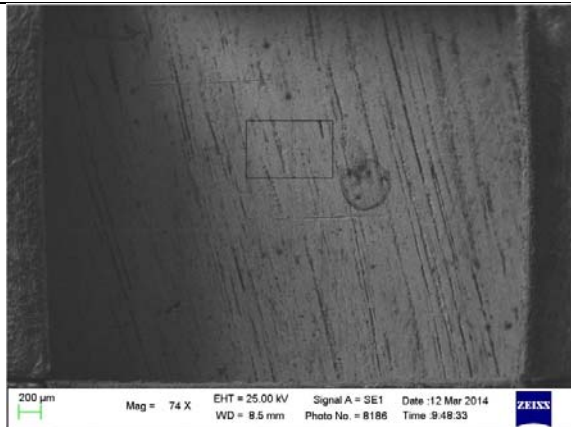


Fig. A10 BSE low magnification image before laser cleaning indicating with a black square where the high magnification image was taken

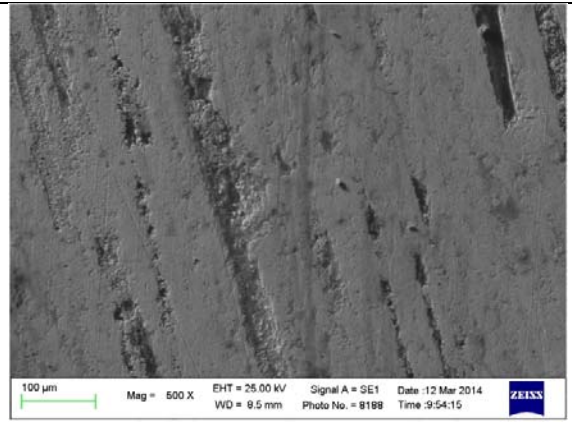


Fig. B10. BSE image of the same area as in Fig. 2. after laser cleaning

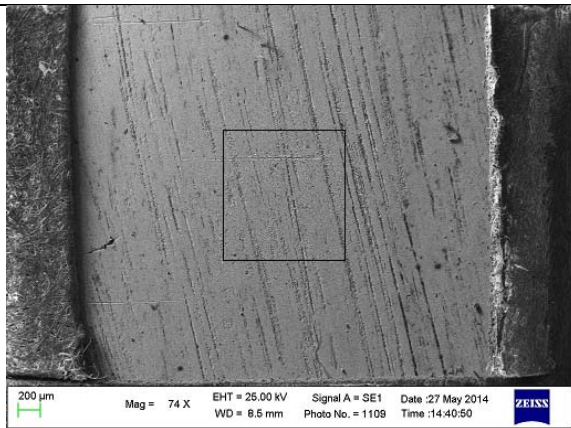


Fig. C10. BSE low magnification image after laser cleaning; spectrum 2 indicates where the spectrum relevant for laser cleaning was taken

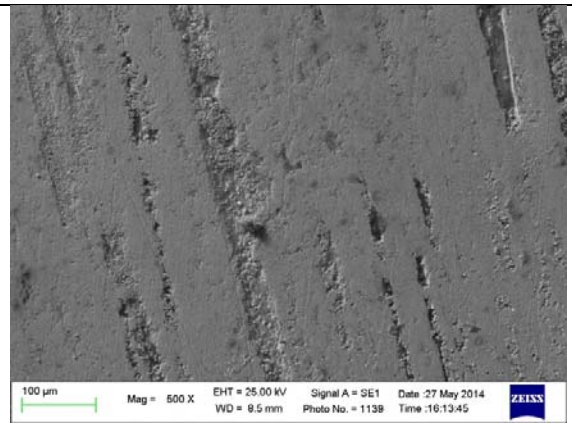


Fig. D10. The same area as in Fig. 2. after laser cleaning

Figure	C	O	Si	S	Cu	Sn	Au	Hg	Pb
A10	20.2	11.0	1.1	1.1	1.9		55.0	8.2	1.5
B10	23.2	11.7	1.3	1.3	2.5	0.2	52.7	6.7	0.4
C10spect. 1	11.7	10.0	1.3	2.0	2.7	0.3	64.4	7.5	0.1
C10spect. 2	10.2	8.8	0.9	0.4	3.4	0.4	64.2	9.7	2.0
D10	10.2	10.8	1.2	1.6	2.3	0.0	65.4	7.9	0.7

Table 14. Elemental composition (measured by EDS, wt%) of different regions of the 2<sup>nd</sup> square within the paper mask(Nd:YAG LQS, fluence 1.65 J/cm<sup>2</sup>) for the sample coated with PropS-SH aged 30 days

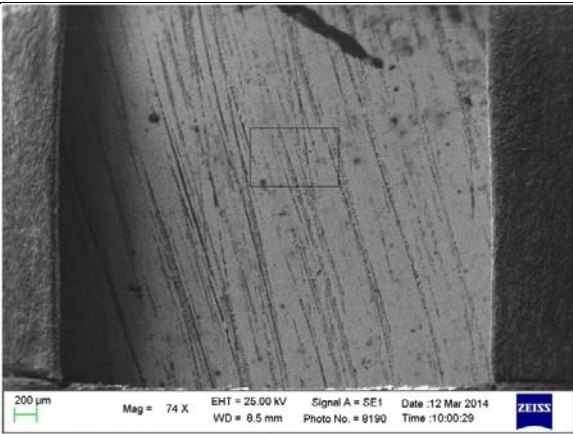


Fig. A11. BSE low magnification image before laser cleaning indicating with a black square where the high magnification image was taken

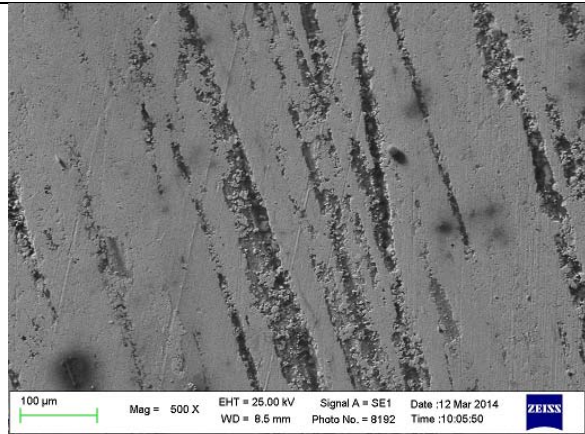


Fig. B11. BSE high magnification image before laser cleaning

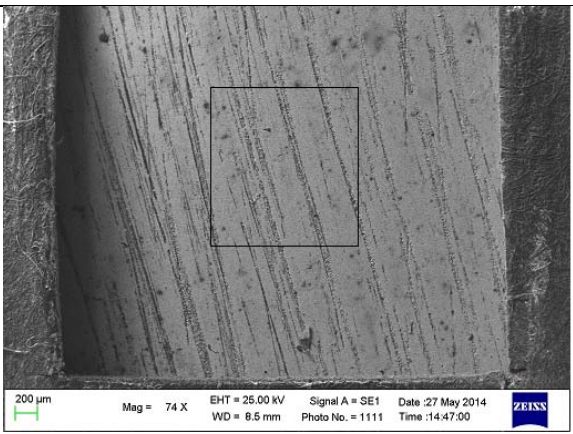


Fig. C11. BSE low magnification image after laser cleaning; spectrum 2 indicates where the spectrum relevant for laser cleaning was taken

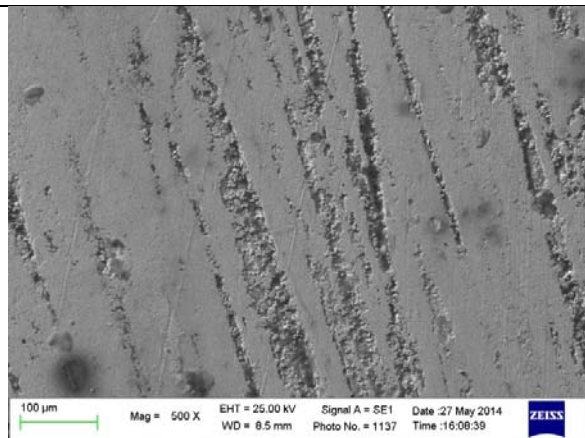


Fig. D11. BSE image of the same area as in Fig. 2. after laser cleaning

Figure	C	O	Si	S	Fe	Cu	Zn	Sn	Au	Hg	Pb
A11	12.9	11.2	2.0	2.9		2.7		0.2	58.	8.8	1.1
B11	17.3	11.6	1.8	2.3	0.4	2.8	0.1		55.2	7.8	0.8
C11spect. 1	15.0	10.3	1.8	2.5		2.6		0.4	57.9	8.4	1.1
C11spect. 2	13.4	10.5	1.5	1.8		2.5		0.1	60.3	8.7	1.1
D11	14.0	11.4	1.5	1.4		2.8			59.6	9.0	0.3

Table 15. Elemental composition (measured by EDS, wt%) of different regions of the 3<sup>rd</sup> square within the paper mask(Nd:YAG LQS, fluence 0.55 J/cm<sup>2</sup>) for the sample coated with PropS-SH aged 30 days

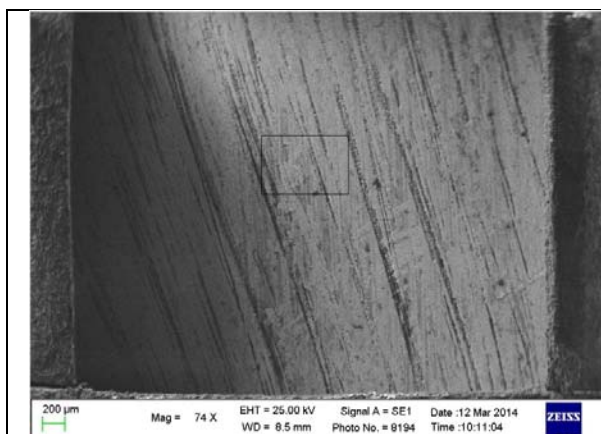


Fig. A12. BSE low magnification image before laser cleaning indicating with a black square where the high magnification image was taken

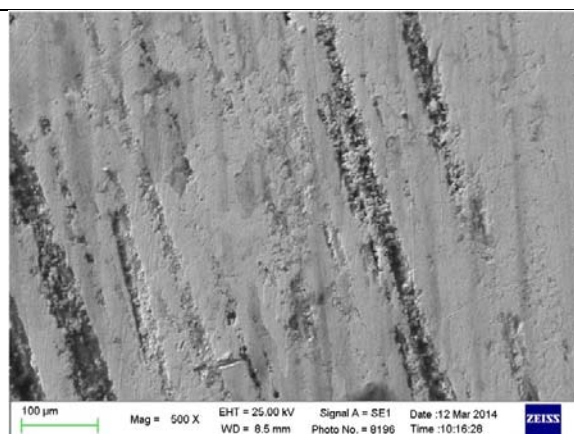


Fig. B12. BSE high magnification image before laser cleaning

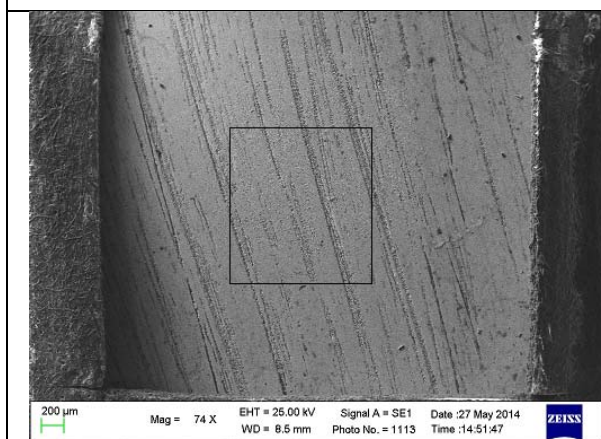


Fig. C12. BSE low magnification image after laser cleaning; spectrum 2 indicates where the spectrum relevant for laser cleaning was taken

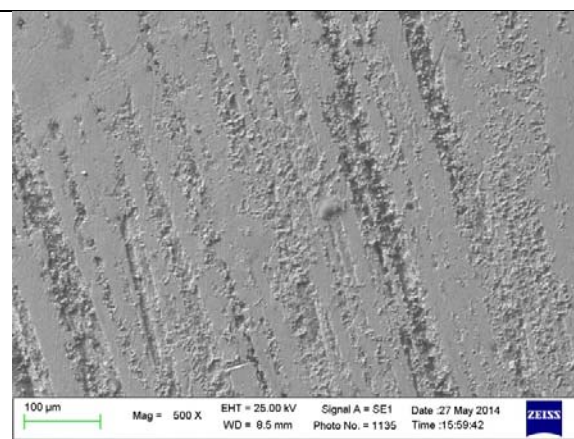


Fig. D12. BSE image of the same area as in Fig. 2. after laser cleaning

Figure	C	O	Si	S	Cu	Zn	Sn	Au	Hg	Pb
A12	27.4	12.4	0.	0.4	2.5		0.1	48.9	6.8	0.9
B12	28.2	13.3	0.8	0.4	2.3	0.1	0.4	47.0	6.7	0.8
C12spect. 1	15.7	9.2		1.3	3.4		0.2	61.0	8.4	0.9
C12spect. 2	11.4	7.8	0.7	0.5	3.0		0.2	66.6	9.1	0.9
D12	10.3	8.7			3.2		0.4	65.5	10.2	1.8

Table 16. Elemental composition (measured by EDS, wt%) of different regions of the 4<sup>th</sup> square within the paper mask(Nd:YAG LQS, fluence 0.80 J/cm<sup>2</sup>) for the sample coated with PropS-SH aged 30 days

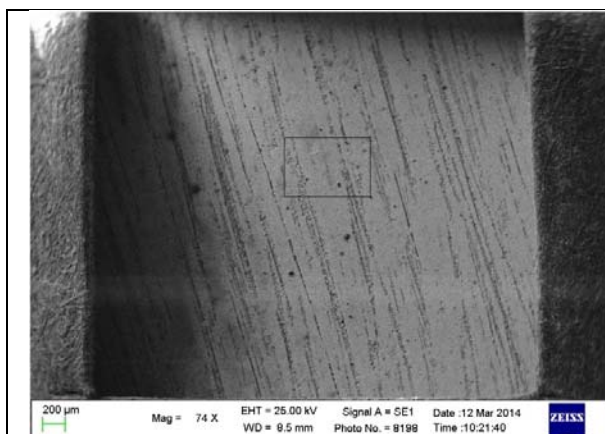


Fig. A13. BSE low magnification image before laser cleaning indicating with a black square where the high magnification image was taken

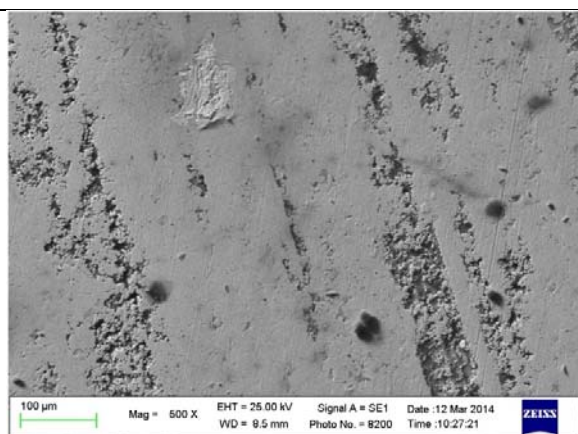


Fig. B13. BSE high magnification image before laser cleaning

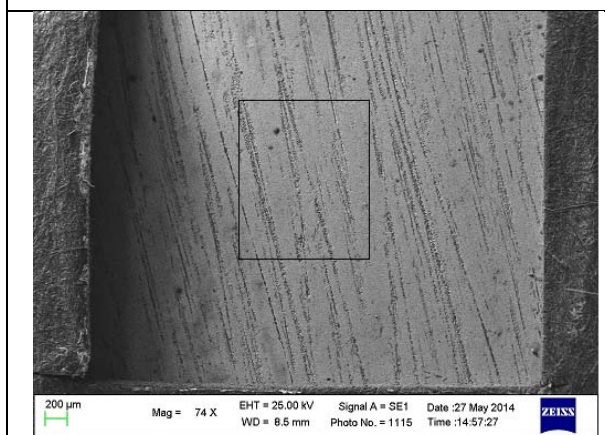


Fig. C13. BSE low magnification image after laser cleaning; spectrum 2 indicates where the spectrum relevant for laser cleaning was taken

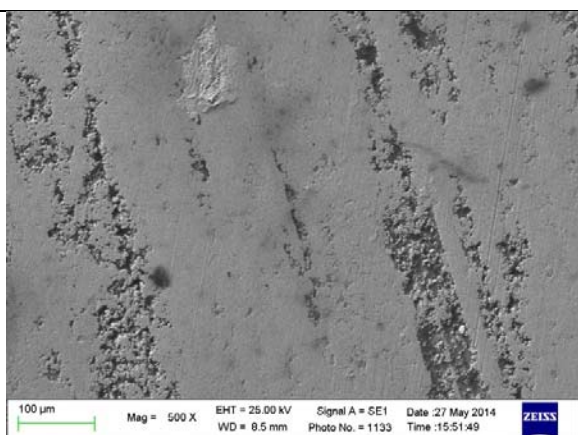


Fig. D13. BSE image of the same area as in Fig. 2. after laser cleaning

Figure	C	O	Al	Si	S	Cu	Sn	Au	Hg	Pb
A13	15.3	11.4	0.2	1.5	2.3	1.1	0.3	59.9	7.3	0.7
B13	15.8	12.8		2.2	2.9	2	0.3	56.7	6.6	0.8
C13spect. 1	15.5	12.3		1.6	2.0	2.2	0.2	56.7	7.9	1.7
C13spect. 2	12.3	10.2		1.4	1.7	2.1	0.2	62.7	8.7	0.6
D13	13.2	11.0		1.7	2.8	1.3	0.3	62.4	6.7	0.6

Table 17. Elemental composition (measured by EDS, wt%) of different regions of the 5<sup>th</sup> square within the paper mask(Nd:YAG LQS, fluence 0.75 J/cm<sup>2</sup>) for the sample coated with PropS-SH aged 10 days

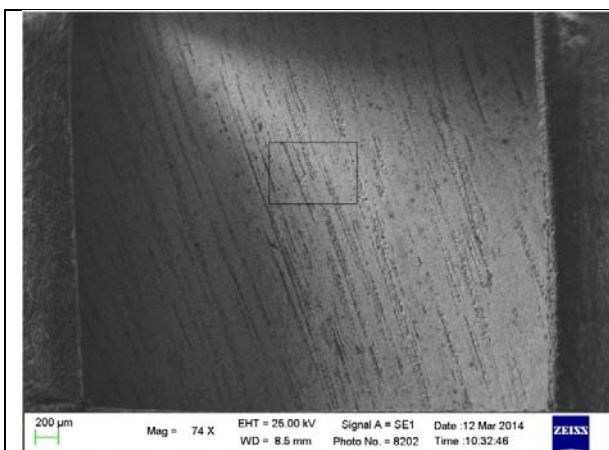


Fig. A14. BSE low magnification image before laser cleaning indicating with a black square where the high magnification image was taken

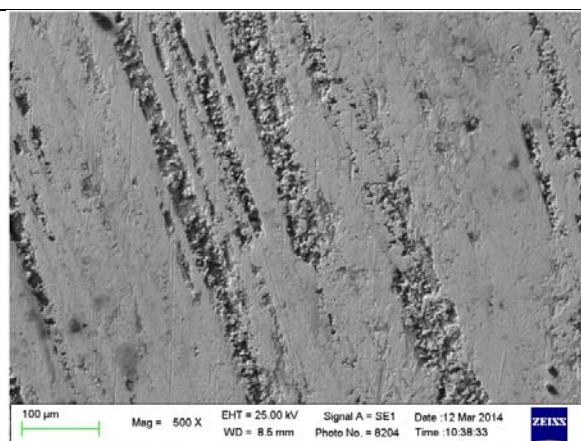


Fig. B14. BSE high magnification image before laser cleaning

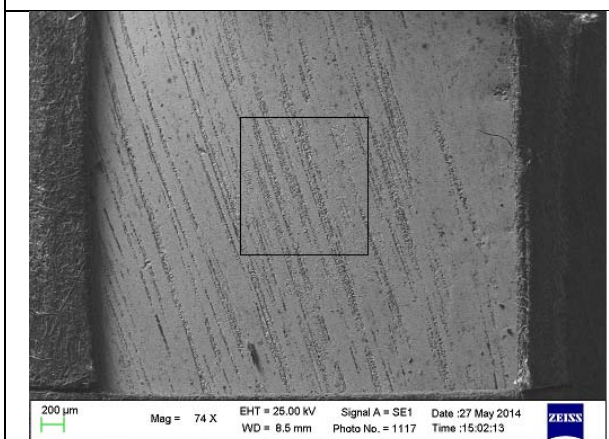


Fig. C14. BSE low magnification image after laser cleaning; spectrum 2 indicates where the spectrum relevant for laser cleaning was taken

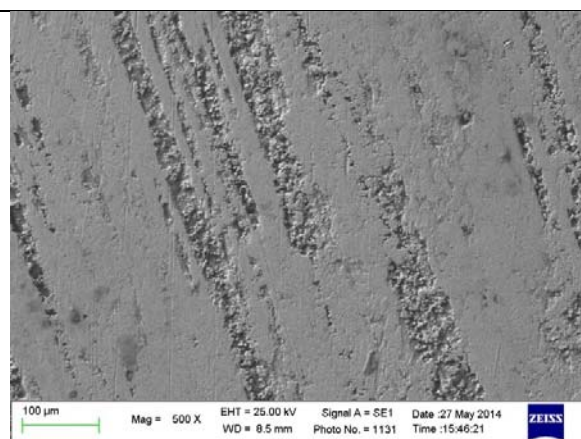


Fig. D14. BSE image of the same area as in Fig. 2. after laser cleaning

Figure	C	O	Si	S	Cu	Zn	Sn	Au	Hg	Pb
A14	20.3	10.9	1.0	0.9	2.3		0.2	55.6	8.1	0.7
B14	20.6	10.5	1.1	1.1	2.6	0.2	0.2	55.2	7.7	0.7
C14spect. 1	10.3	9.6	1.2	1.0	2.9		0.5	63.6	9.1	2.0
C14spect. 2	11.1	8.0	1.1	1.0	2.8			65.8	9.0	1.1
D14	10.9	9.4	1.0	0.8	2.3		0.3	64.2	9.4	1.7

Table 18. Elemental composition (measured by EDS, wt%) of different regions of the 6<sup>th</sup> square within the paper mask(Nd:YAG LQS, fluence 0.60 J/cm<sup>2</sup>) for the sample coated with PropS-SH aged 30 days

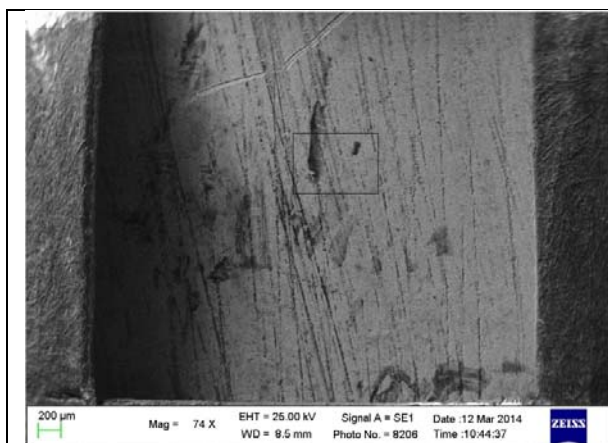


Fig. A15. BSE low magnification image before laser cleaning indicating with a black square where the high magnification image was taken

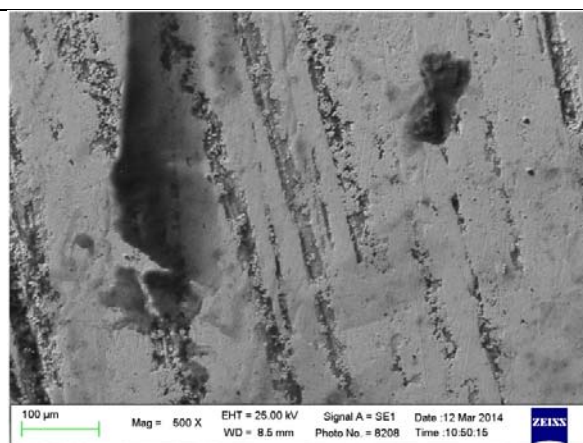


Fig. B15. BSE high magnification image before laser cleaning

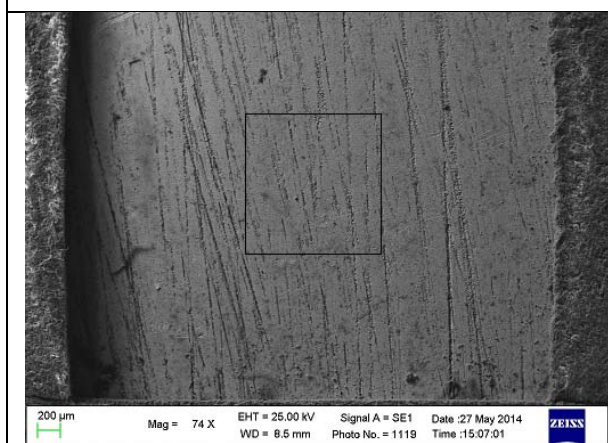


Fig. C15. BSE low magnification image after laser cleaning; spectrum 2 indicates where the spectrum relevant for laser cleaning was taken

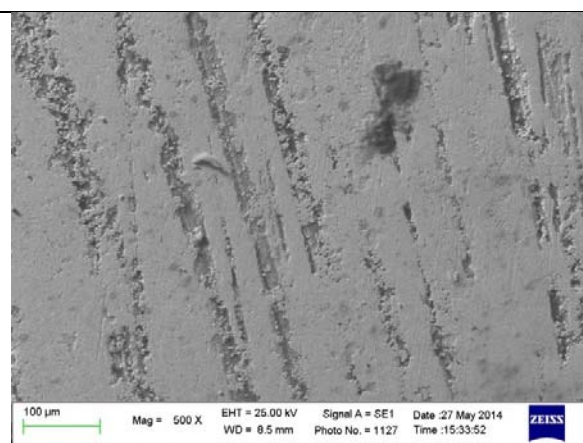


Fig. D15. BSE image of the same area as in Fig. 2. after laser cleaning

Figure	C	O	Si	S	Cu	Zn	Sn	Au	Hg	Pb
A15	29.3	12.7	1.4	2.1	1.6	0.2	0.3	45.9	5.9	0.8
B15	25.1	13.8	2.2	2.7	1.7	0.0	0.4	47.1	6.3	0.7
C15spect. 1	16.9	12.3	2.1	2.3	1.7			56.2	8.5	0.1
C15spect. 2	13.7	12.3	1.6	2.8	1.7			61.0	6.8	0.3
D15	13.4	11.5	1.6	2.5	2.0			0.4	60.7	7.9

Table 19. Elemental composition (measured by EDS, wt%) of different regions of the 7<sup>th</sup> square within the paper mask(Nd:YAG LQS, fluence 0.55 J/cm<sup>2</sup>) for the sample coated with PropS-SH aged 10 days

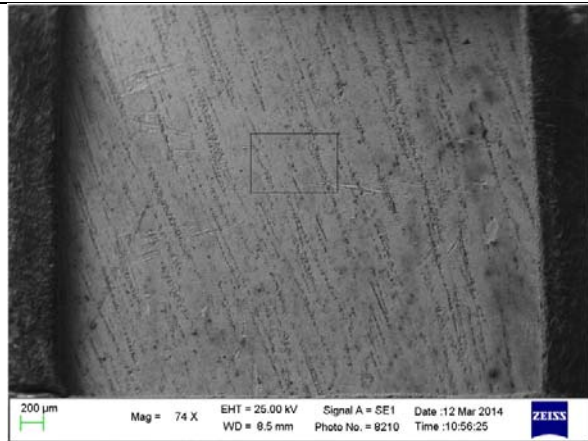


Fig. A16. BSE low magnification image before laser cleaning indicating with a black square where the high magnification image was taken

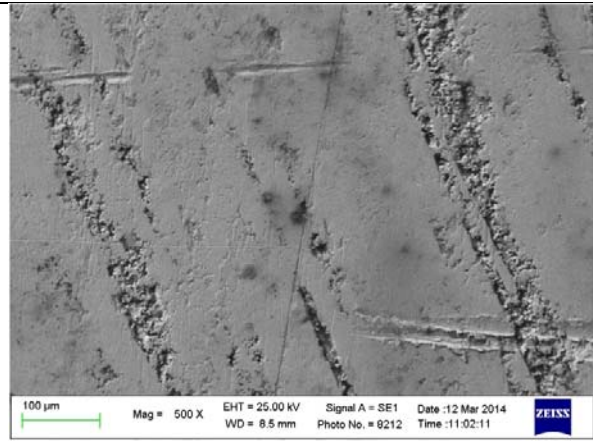


Fig. B16. BSE high magnification image before laser cleaning

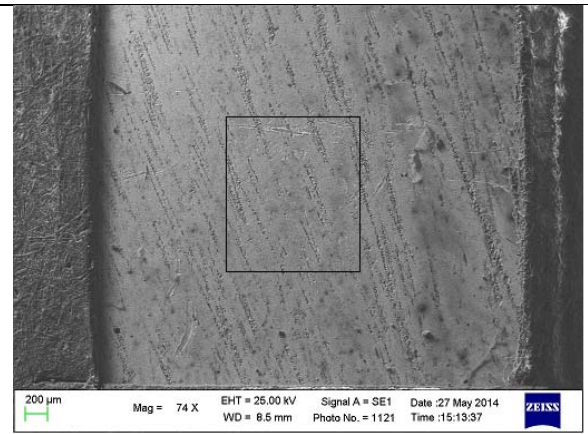


Fig. C16. BSE low magnification image after laser cleaning; spectrum 2 indicates where the spectrum relevant for laser cleaning was taken

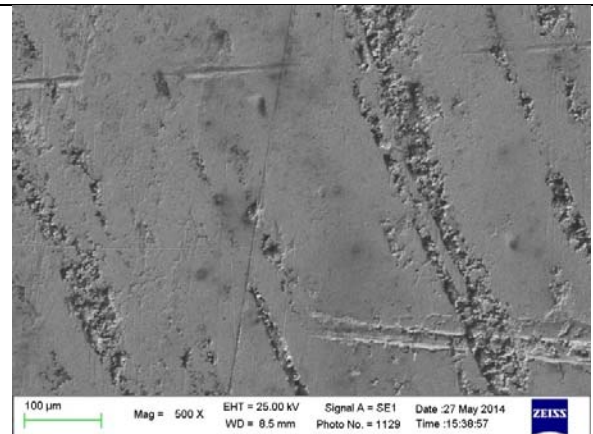


Fig. D16. BSE image of the same area as in Fig. 2. after laser cleaning

Figure	C	O	Si	S	Cu	Sn	Au	Hg	Pb
A16	13.9	11.0	1.4	2.1	1.7	0.1	60.6	8.0	1.2
B16	13.6	11.0	1.5	2.1	2.1	0.3	59.9	8.3	1.3
C16spect. 1	13.3	11.4	1.8	2.0	1.8		57.6	9.7	2.4
C16spect. 2	11.9	11.9	1.8	2.6	1.8		62.1	7.1	0.8
D16	11.2	11.8	1.7	2.5	1.5	0.6	61.0	8.6	1.1

Table 20. Elemental composition (measured by EDS, wt%) of different regions of the 8<sup>th</sup> square within the paper mask(Er:YAG FR, fluence 5.65 J/cm<sup>2</sup>) for the sample coated with PropS-SH aged 30 days

In all regions (tables 13-19) where the laser cleaning was undertaken with the Nd:YAG LQS, the before/after elemental compositions of the gilded surface show comparable evolutions: elements that are associated with the coating and corrosion products (carbon, oxygen, silicon and sulphur) decrease after the procedure. On the other hand, the ones associated with the fire-gilded layer (gold, mercury, lead) increase. Once again the percentage mass variation for the elements of interest (silicon, gold and mercury) were plotted as a function of the fluence for the Nd:YAG LQS laser.

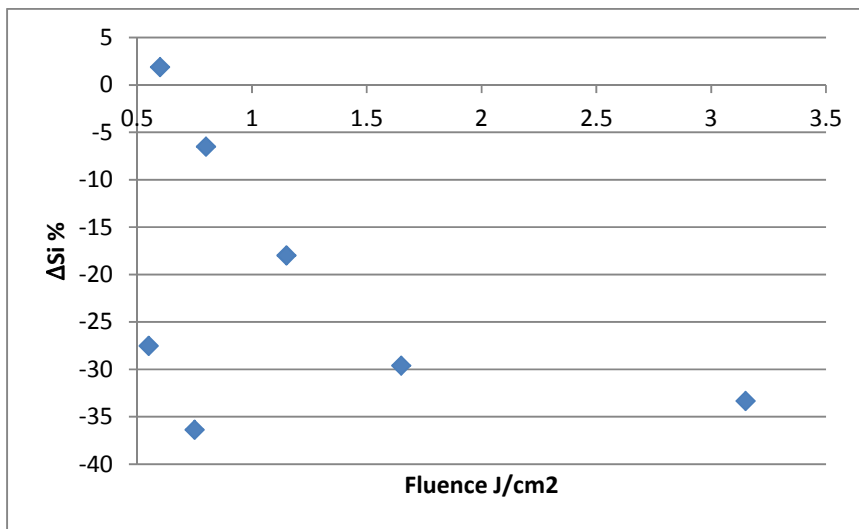


Fig. 8. The percentage variation of Si concentration ( $\Delta Si\%$ ) for the Nd:YAG LQS laser cleaning treatment as a function of fluence for the sample coated with PropS-SH aged 30 days

The silicon percentage variation graph (Fig. 8) shows that, in the case of the sample coated with PropS-SH and aged for 30 days, most of fluences at which the Nd:YAG LQS laser was used have a good performance: when it comes to the removal of PropS-SH, 4 values show a decrease of over 25% in the amount of silicon and only 2 close to 0.

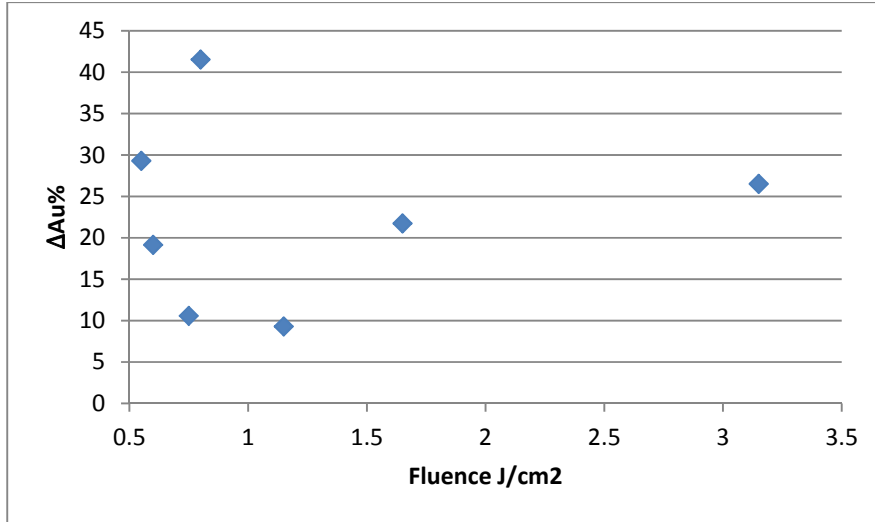


Fig. 9. The percentage variation of Au concentration ( $\Delta Au\%$ ) for the Nd:YAG LQS laser cleaning treatment as a function of fluence for the sample coated with PropS-SH aged 30 days

While in the case of the previous sample all values indicated an increase in the amount of gold mostly below 5% (Fig. 3), for the sample coated with PropS-SH, most values are over 20% (Fig. 9). We can assume that the coating has been removed to a higher extent and that is why the signal we get from gold is more intense.

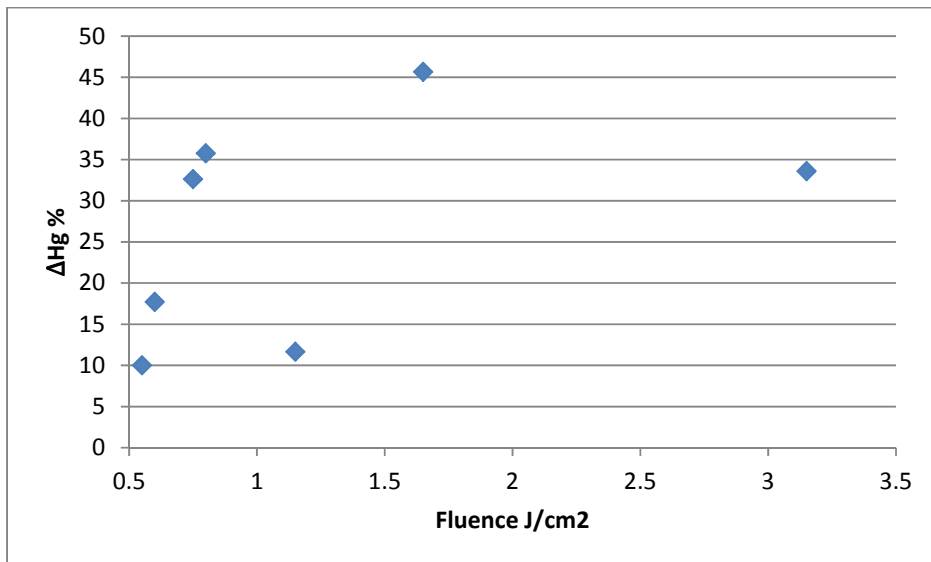


Fig. 10. The percentage variation of Hg concentration ( $\Delta Hg\%$ ) for the Nd:YAG LQS laser cleaning treatment as a function of fluence for the sample coated with PropS-SH aged 30 days

The mercury percentage variation graph (Fig. 10) for the sample coated with PropS-SH and aged 30 days is quite different when compared to the one of gold. We find some points that overlap, meaning that the behavior of the mercury follows the one of the gold, with which it is associated within the gilding layer. Other values for the same fluence are much different, meaning that the mercury may have been affected by heating during the treatment.

The area in the fifth square of the paper mask where the Nd:YAG LQS laser had a fluence of  $0.75 \text{ J/cm}^2$  was investigated at high magnification using SEM-EDS measurements. It was chosen as it showed the highest decrease in the amount of silicon and the lowest increase in the gold.

In figures 11 and 12 we do not observe the melting of the gold layer that we found in figures 5, 6 and 7. Though there is a great discrepancy in the percentage mass variation of gold – 10.6% - compared to that of mercury which is much higher – 32.6% - the morphology of the surface does not appear to be changed by the laser cleaning treatment.

Even though the laser cleaning treatment appears to have removed the PropS-SH coating from the surface of the sample to a higher extent than in the case of PropS-SH +  $\text{CeO}_2$ , the silane coating inside the grooves of the gilded surface was not fully removed (as for the previous sample), as shown by EDS data in Table 21.

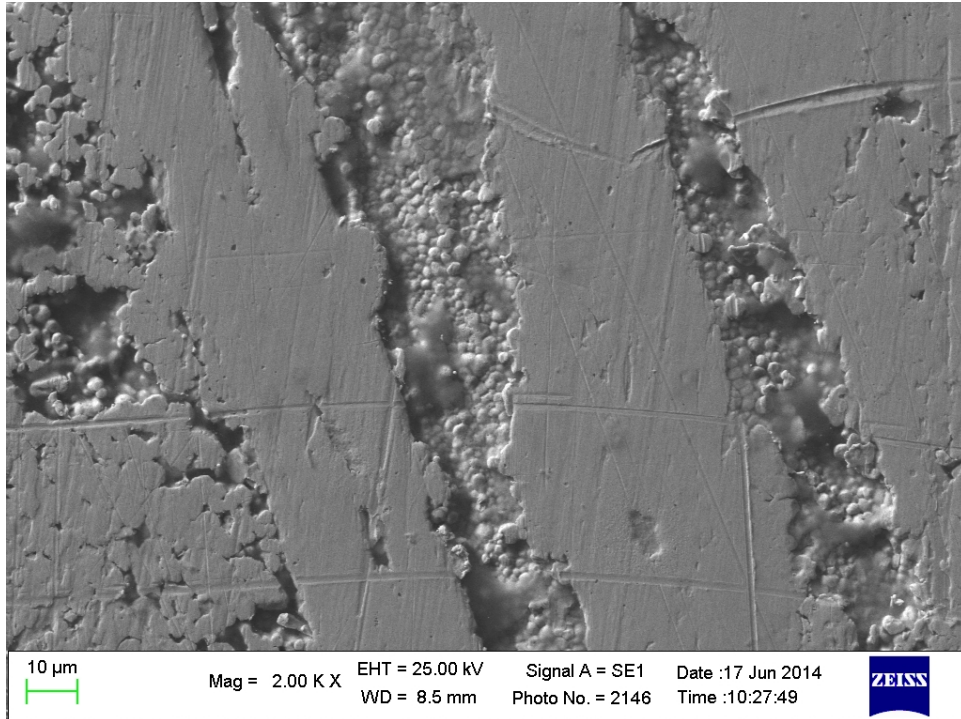


Fig. 11. High magnification BSE image of an area within the second square (Nd:YAG LQS, fluence  $0.75 \text{ J/cm}^2$ ) for the sample coated with PropS-SH aged 30 days

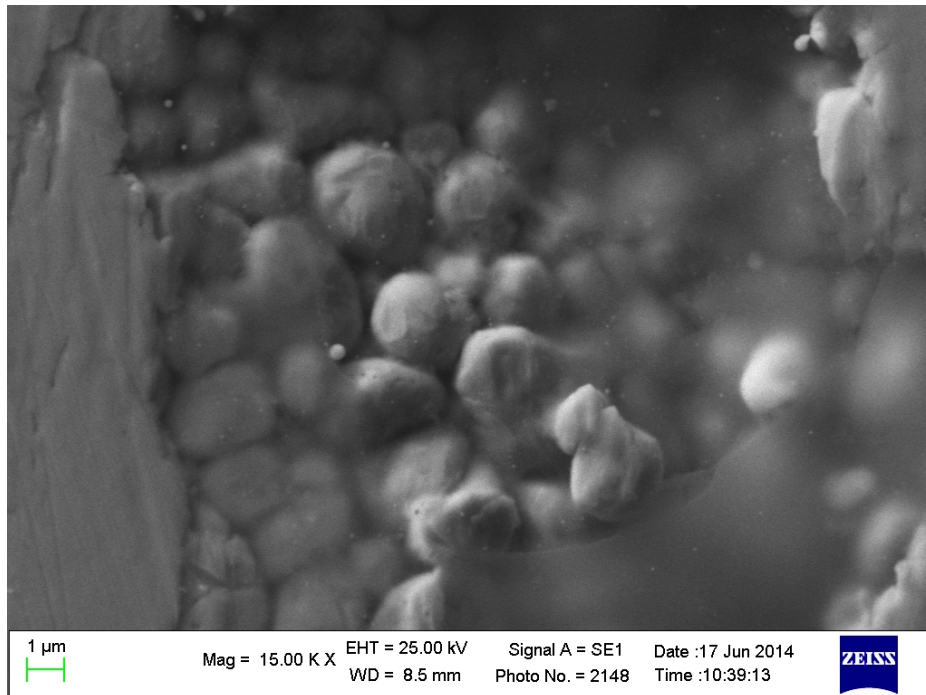


Fig. 12. High magnification BSE image of an area within the second square (Nd:YAG LQS, fluence  $0.75 \text{ J/cm}^2$ ) for the sample coated with PropS-SH aged 30 days

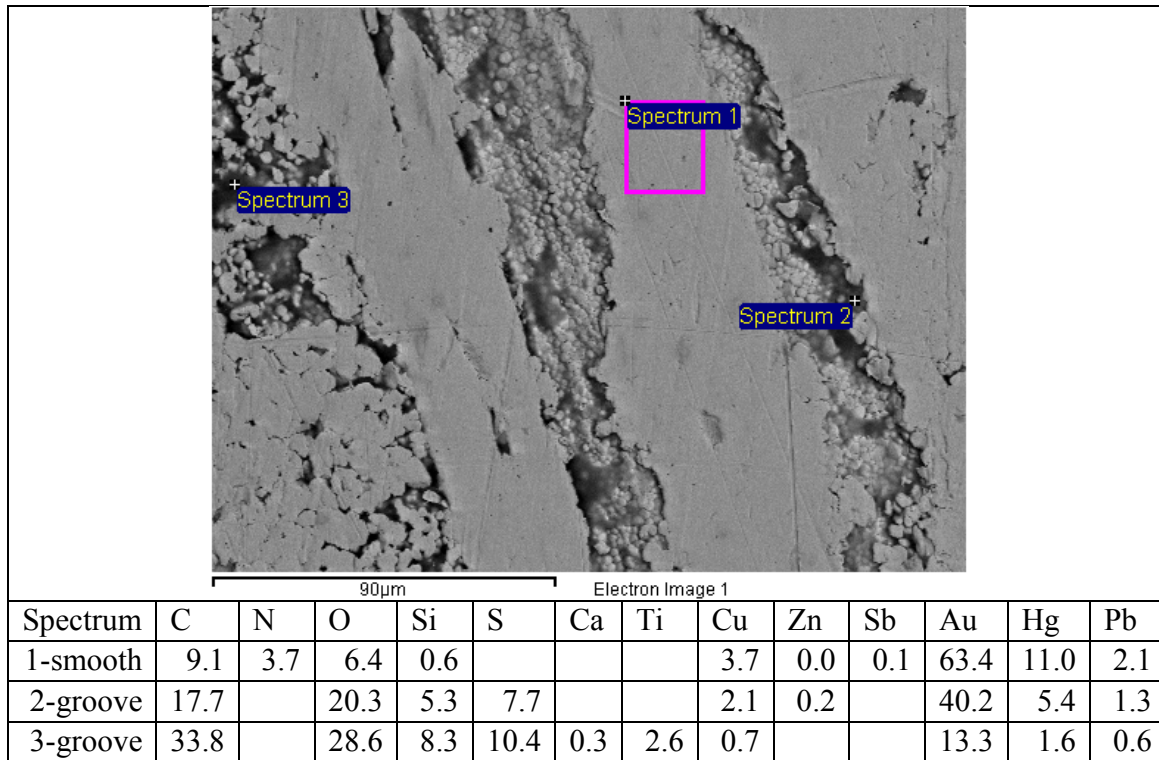


Table 21. Elemental composition (measured by EDS, wt%) of different regions (Nd:YAG LQS, fluence 0.75 J/cm<sup>2</sup>) for the sample coated with PropS-SH aged 30 days

The elemental composition in Table 21 shows that the laser cleaning treatment has cleared the smooth areas of the gilded surface of the PropS-SH coating, while leaving the silane coating in place in the porous grooves.

### 4.3. Concluding remarks

In order to assess the effectiveness of the laser treatment both the chemical composition and the morphology of the gilded surface were taken into account. Over the course of these investigations we have encountered situations that range from melting of the gold layer to cases where the laser has not modified the morphology of the gold surface.

For the sample coated with PropS-SH+CeO<sub>2</sub> and aged for 10 days, the best coating removal was obtained with a fluence of 0.80 J/cm<sup>2</sup>. The laser beam however modified the morphology of the gilded surface due to melting. A fluence of 1.65 J/cm<sup>2</sup> lead to melting of the gold layer, giving the surface a spongy texture. Laser cleaning treatments carried out in these conditions did not yield high removal efficiencies for surfaces coated with PropS-SH+CeO<sub>2</sub>. CeO<sub>2</sub> is reported to help silane reticulation by forming Si-O-Ce bonds [75] and also to act as filler, improving the silane barrier effect [76]): probably the presence of CeO<sub>2</sub> makes the silane layer more difficult to remove. Also the lower ageing time than in the case of PropS-SH made the CeO<sub>2</sub>additivatedcoating less damaged therefore less easy to remove

The sample coated with PropS-SH and aged for 30 days responded better to the laser cleaning and no melting was identified at the level of the gold layer. Two fluence values gave the best results. A fluence of 0.75 J/cm<sup>2</sup> decreased by 36% the amount of silicon on the surface and by 11 % the gold one. The amount of mercury however increased up to 33%, probably indicating that there were modifications to the gold layer. That is why a fluence of 1.15 J/cm<sup>2</sup> could be considered for further investigations, as it decreased the amount of silicon but the increase of gold and mercury is comparable.

As a final remark, the peculiar surface morphology of the fire-gilded surfaces must be taken into account, because it makes the removal of silane from such a complex surface (smooth areas combined with grooves with porous structure) a daunting task.

## References

1. Anheuser K., The practice and Characterization of Historic Fire Gilding Techniques, JOM, November 1997, pp 58-62
2. Darque-Ceretti E., Aucouturier M., Gilding for Matter Decoration and Sublimation. A Brief History of the Artisanal Technical Know-How, International Journal of Conservation Science, 2013, Volume 4, Special issue, pp 647-660
3. Alessandro Pacini, personal communication, 2011
4. <http://www.youtube.com/watch?v=yZbzD6UhdJk>
5. Smit Z., Istenic J., Knific T., Plating of archaeological metallic objects – studies by differential PIXE, Nuclear Instruments and Methods in Physics Research, B, 266, 2008, pp. 2329–2333
6. Chêne G., Bols S., Dupuis T., Marchal A., Mathis F., Garnir H.-P., Strivay D., New external beam and particle detection set-up of Liège cyclotron – First applications of high energy beams to cultural heritage, Nuclear Instruments and Methods in Physics Research, B, 273, 2012, pp. 208–212
7. <http://www.gsa.gov/portal/content/111994>
8. <http://www.azgem.com/newsletters/newsletter-08-12.html>
9. <http://www.sculptorandmoldmaker.com/cold-cast-bronze-sculptures-dog.html>
10. Scott D. A., Metallography and Microstructure of Ancient and Historic metals, The J. Paul Getty Trust, 1991
11. Callister W.D., Fundamentals of Material Science and Engineering, Fifth Edition, John Wiley and Sons, 2001, ISBN 0-471-39551-X
12. <http://core.materials.ac.uk/search/detail.php?id=1522>
13. <http://upload.wikimedia.org/wikipedia/commons/c/cd/CrystalGrain.jpg>
14. <http://www.steeluniversity.org/content/html/eng/default.asp?catid=276&pageid=2081272701>
15. Leygraf C., Graedel T., ATMOSPHERIC CORROSION, WILEY INTERSCIENCE, ISBN 0-471-37219-6

16. Robbiola L, Hurtel L., Nouvelles contributions à l'étude des mécanismes de corrosion des bronzes de plein air : caractérisation de l'altération de bronzes de Rodin, Mémoires et études scientifiques Revue de Métallurgie- Décembre 1991
17. de la Fuente D., Simancas J., Morcillo M., Morphological study of 16-year patinas formed on copper in a wide range of atmospheric exposures, Corrosion Science, 2008, 50, pp 268–285
18. Krätschmer A, Wallinder I. O., Leygraf C., The evolution of outdoor copper patina, Corrosion Science, 2002, 44, pp 425-450
19. Balbo A., Chiavari C., Martini C., Monticelli C., Effectiveness of corrosion inhibitor films for the protection of bronzes and gilded bronzes, Corrosion Science 2012, 59, pp 204-212
20. Chiavari C., Balbo A., Bernardi E., Martini C., Bignozzi M. C., Abbottoni M., Monticelli C., Protective silane treatment for patinated bronze exposed to simulated natural environments, Materials Chemistry and Physics, 2013, 141, pp 502-511
21. Shreir L. L., Jarman R.A., Burstein G.T., Corrosion Metal/Environment Reactions Third Edition, Butterworth-Heinemann, ISBN 0 7506 1077 8
22. [http://www.npl.co.uk/upload/pdf/bimetallic\\_20071105114556.pdf](http://www.npl.co.uk/upload/pdf/bimetallic_20071105114556.pdf)
23. Alunno-Rossetti V., Marabelli M., Analyses of a Gilded Horse of St. Mark' Basillica in Venice: Corrosion Mechanisms and Conservation Problems, Studies in Conservation, 1976 (21), pp 161-170
24. [http://penelope.uchicago.edu/~grout/encyclopaedia\\_romana/circusmaximus/sanmarco.html](http://penelope.uchicago.edu/~grout/encyclopaedia_romana/circusmaximus/sanmarco.html)
25. [http://en.wikipedia.org/wiki/Horses\\_of\\_Saint\\_Mark](http://en.wikipedia.org/wiki/Horses_of_Saint_Mark)
26. Scott, David A., Jerry Podany, and Brian B. Considine, eds. 1994. Ancient & Historic Metals: Conservation and Scientific Research: Proceedings of a Symposium Organized by the J. Paul Getty Museum and the Getty Conservation Institute, November 1991. Marina del Rey, CA: Getty Conservation
27. Scott D. A., Swartz Dodd L., Examination, conservation and analysis of a gilded Egyptian bronze Osiris, Journal of Cultural Heritage, 2002, pp 333-345

28. Fiorentino P., Marabelli M., Matteini M., Moles A., The Condition of the Door of Paradise by L. Ghiberti. Tests and Proposal for Cleaning, *Studies in Conservation*, 1982, 27, pp 145-163
29. Linares G., *L'oro Del Ghiberti, Restauri Alla Porta del Paradiso*, Panini, Modena, 1986
30. Mello E., The Gilding of Lorenzo Ghiberti's Paradise Doors of Paradise, *Golden Bull*, 1986, 19(4), pp 123-126
31. Ferretti M., Siano S., The gilded bronze panels of the Porta del Paradiso by Lorenzo Ghiberti: non-destructive analyses using X-ray fluorescence, *Appl. Phys. A* 90, 97-100 (2008), DOI: 10.1007/s00339-007-4231-2
32. Salimbeni R., Laser techniques for conservation of artworks, *Archeometriai Műhely*, 1, 2006, pp. 34-40
33. Rode A.V., Baldwin K.G.H., Wain A., Delaporte P.H., Ultrafast lasers for conservation of heritage artefacts, *AICCM Bulletin*, 30, 2007, pp. 17-26
34. Rode A.V., Baldwin K.G.H., Wain A., Madsen N.R., Freeman D., Delaporte Ph., Luther-Davies B., Ultrafast laser ablation for restoration of heritage objects, *Applied Surface Science*, 254, 2008, pp. 3137–3146
35. Buccolieri G., Nassisi V., Torrisi L., Buccolieri A., Castellano A., Di Giulio M., Giuffreda E., Delle Side D., Velardi L., Analysis of selective laser cleaning of patina on bronze coins, *Journal of Physics: Conference Series*, 508, 2014, [http://iopscience.iop.org/1742-6596/508/1/012032/pdf/1742-6596\\_508\\_1\\_012032.pdf](http://iopscience.iop.org/1742-6596/508/1/012032/pdf/1742-6596_508_1_012032.pdf)
36. Siano S., Salimbeni R., Pini R., Giusti A., Matteini M., Laser cleaning methodology for the preservation of the Porta del Paradiso by Lorezo Ghiberti, *Journal of Cultural Heritage*, 2003(4), pp 140–146
37. Koh I.S., 2006, Laser Cleaning as a Conservation Technique for Corroded Metal Artifacts, <http://epubl.ltu.se/1402-1544/2006/02/LTU-DT-0602-SE.pdf>
38. Asmus J. F., Thirty-seven years of lasers in the conservation of art, *Rev. Cub. Física*, 27 (1), 2010, pp.3-8
39. Salimbeni R., Zafirooulos V., Radvan R., Verges-Belmin V., Kautek W., Andreoni A., Sliwinski G., Castillejo M., Ahmad M., The European community research concerning laser techniques in conservation: results and perspectives, 2005, [http://www.rtphc.csic.es/issues/9\\_1.pdf](http://www.rtphc.csic.es/issues/9_1.pdf)

40. Folgado Martins M.I., La práctica de la limpieza con láser en materiales metálicos, Valencia, 2012, <https://riunet.upv.es/bitstream/handle/10251/28738/TFM.pdf?sequence=1>
41. Adriaens A., Non-destructive analysis and testing of museum objects: An overview of 5 years of research, *Spectrochimica Acta, Part B*, 60, 2005, pp. 1503 – 1516
42. Siano S., Agresti J., Cacciari I., Ciofini D., Mascalchi M., Osticioli I., Mencaglia A.A., Laser cleaning in conservation of stone, metal and painted artifacts: state of art and new insight on the use of the Nd:YAG lasers, *Appl. Phys. A*, 106, 2012, pp.419-446
43. Fornarini L., Colao F., Fantoni R., Lazic V., Spizzicchino V., Calibration analysis of bronze samples by nanosecond laser induced, breakdown spectroscopy: A theoretical and experimental approach, *Spectrochimica Acta Part B*, 60, 2005, pp. 1186 – 1201
44. Fortes F.J., Cabalín L.M., Laserna J.J., The potential of laser-induced breakdown spectrometry for real time monitoring the laser cleaning of archaeometallurgical objects, *Spectrochimica Acta Part B*, 63, 2008, pp.1191–1197
45. De Giacomo A., Dell'Aglio M., De Pascale O., Gaudiuso R., Santagata A., Teghil R., Laser Induced Breakdown Spectroscopy methodology for the analysis of copper-based-alloys used in ancient artworks, *Spectrochimica Acta Part B*, 63, 2008, pp. 585–590
46. Sandu A.C., Helena de Sa M., Pereira M.C., Ancient ‘gilded’ art objects from European cultural heritage: A review on different scales of characterization, *Surf. Interface Anal.*, 2011, <http://www.afir.org.ro/sica/files/ISI/SIA2011.pdf>
47. Walaszek D., Senn M., Faller M., Philippe L., Wagner B., Bulska E., Ulrich A., Metallurgical and chemical characterization of copper alloy reference materials within laser ablation inductively coupled plasma mass spectrometry: Method development for minimally-invasive analysis of ancient bronze objects, *Spectrochimica Acta Part B*, 79–80, 2013, pp. 17–30
48. Pini R., Siano S., Salimbeni R., Pasquinucci M., Miccio M., Tests of laser cleaning on archeological metal artefacts, *J. Cult. Heritage*, 1 2000, pp. S129-S137
49. Garbacz H., Koss A., Marczak J., Mróz J., Onyszczuk T., Rycyk A., Sarzynski A., Skrzeczanowski W., Strzelec M., Zatorska A., Optimized laser cleaning of metal artworks – evaluation of determinants, *Physics Procedia*, 5, 2010, pp. 457–466
50. Buccolieri G., Nassisi V., Buccolieri A., Vona F., Castellano A., Laser cleaning of a bronze bell, *Applied Surface Science*, 272, 2013, pp. 55– 58

51. Barone P., Stranges F., Barberio M., Bonanno A., Application of Laser Ablation to Cleaning Process of the Corrosion Chloride Patina Formed on Bronze Surfaces in Air and Marine Water, *Journal of Physical Science and Application*, 2013,(3), pp 135-140
52. Elhassan A., Giakoumaki A., Anglos D., Ingo G.M., Robbiola L., Harith, M.A., Nanosecond and femtosecond Laser Induced Breakdown Spectroscopic analysis of bronze alloys, *Spectrochimica Acta Part B*, 63, 2008, pp. 504–511
53. Yilbas B.S., Toor I.H., Malik J., Patel F., Karatas C., Electrochemical testing of laser treated bronze surface, *Journal of Alloys and Compounds*, 563, 2013, pp. 180–185
54. Dajnowski B.A., Laser ablation cleaning of an underwater archeological bronze spectacle plate from H.M.S *DeBraak* shipwreck, *Proc of SPIE, Optics for Arts, Architecture, and Archaeology IV*, 8790, 87901K, 2013, <http://www.deepdyve.com/lp/spie/laser-ablation-cleaning-of-an-underwater-archaeological-bronze-tA5a48dwPO>
55. Siano S., Salimbeni R., The gate of paradise: physical optimization of the laser cleaning approach, *Studies in Conservation*, 46, 2001, pp.269-281
56. Salimbeni R., Zafirooulos V., Radvan R., Verges-Belmin V., Kautek W., Andreoni A., Sliwinski G.,Castillejo M., Ahmad M., The European community research concerning laser techniques in conservation: results and perspectives, 2005, [http://www.rtphc.csic.es/issues/9\\_1.pdf](http://www.rtphc.csic.es/issues/9_1.pdf)
57. Siano S., 2012b, [http://www.enea.it/it/enea\\_informa/events/techitaly2012/04S.SianoIFACCNR.pdf](http://www.enea.it/it/enea_informa/events/techitaly2012/04S.SianoIFACCNR.pdf)
58. Matteini M., Lalli C., Tosini I., Giusti A., Siano S., Laser and chemical cleaning tests for the conservation of the Porta del Paradiso by Lorenzo Ghiberti, *JOURNAL OF CULTURAL HERITAGE*, 2003(4), pp 147s-151s
59. [http://www.santimartiri.prato.it/forum/forum\\_messaggi.asp?IDtit=401&IDpag=1&IDnpage=2&IDtype=1](http://www.santimartiri.prato.it/forum/forum_messaggi.asp?IDtit=401&IDpag=1&IDnpage=2&IDtype=1)
60. <http://news.bbc.co.uk/2/hi/science/nature/8534969.stm>
61. Ciupinski L., Zalesna E.F., Zukowska G.Z., Comparative Laser Spectroscopy Diagnostics for Ancient Metallic Artefacts Exposed to Environmental Pollution, *Sensor*, 10 (5), 2010, 4926-4949
62. Koss A., Marczak J., Evaluation of laser cleaning progress and quality, *Journal of Heritage Conservation*, 32, 2012, pp. 109-114

63. Lee H., Cho N., Lee J., Study on surface properties of gilt-bronze artifacts, after Nd:YAG laser cleaning, *Applied Surface Science*, 284, 2013, pp. 235–241
64. Zucchiatti A., Gutiérrez Neira P.C., Climent-Font A., Escudero C., Barrera M., IBA analysis of a laser cleaned archaeological metal object: The San Esteban de Gormaz cross (Soria-Spain), *Nuclear Instruments and Methods in Physics Research B* 269, 2011, pp. 3115–3119
65. Giussani B., Monticelli D., Rampazzi L., Role of laser ablation–inductively coupled plasma–mass spectrometry in cultural heritage research: A review, *Analytica Chimica Acta*, 635, 2009, pp. 6–21
66. Bernardi E., Chiavari C., Lenza B., Martini C., Morselli L., Ospitali F., Robbiola L., The atmospheric corrosion of quaternary bronzes: the leaching effect of acid rain, *Corrosion Science*, 2009(51), pp 159-170
67. Montemor M.F., Trabelsi W., Lamaka S.V., Yasakau K.A., Zheludkevich M.L., Bastos A.C., Ferreira M.G.S., The synergistic combination of bis-silane and CeO<sub>2</sub>·ZrO<sub>2</sub>nanoparticles on the electrochemical behaviour of galvanised steel in NaCl solutions, *Electrochim. Acta* 53 (2008) 5913–5922.
68. Serena Bassini (2011). Bronzi e bronzi Dorati esposti all’azione della pioggia: corrosione ed inibizione, Corso di Laurea Magistrale in Chimica Industriale University of Bologna.
69. Ospitali F, Chiavari C., Martini C., Bernardi E., Passarini F., Robbiola L., The characterization of Sn-based corrosion products in ancient bronzes: a Raman approach, *Journal of Raman Spectroscopy*, 2012, 43, 1596–1603
70. Li Y., Zhang G.F., He Y. Y., Hou X. D., Electrical Double Layer Model and Thermodynamic Coupling for Electrochemically Deposited Hydrogenated Amorphous Carbon Films, *Journal of the Electrochemical Society*, 2012(159), H918-H920
71. <http://rruff.info/tenorite/display=default/R120076>
72. D.A.Scott, *Copper and Bronze in Art*, Getty Publications, Los Angeles, 2002
73. C.M. Grossi, P. Brimblecombe, R. Esbert, F.J. Alonso (2007). Color changes in architectural limestones from pollution and cleaning. *Color Res. Appl.*, Vol. 32, pp.320 – 331

74. Marie Cordier (2013). Outdoor bronze conservation: assessment of protective treatments by accelerated aging and of treatment removal procedures by laser cleaning, *Advanced Spectroscopy in Chemistry* master thesis, University of Bologna
75. M.F. Montemor, R. Pinto, M.G.S. Ferreira, Chemical composition and corrosion protection of silane films modified with CeO<sub>2</sub> nanoparticles, *Electrochim. Acta* 54 (2009) 5179–5189
76. A. Phanasgaonkar, V.S. Raja, Influence of curing temperature, silica nanoparticles- and cerium on surface morphology and corrosion behavior of hybrid silane coatings on mild steel, *Surf. Coat. Technol.* 203 (2009) 2260–2271